Multiphysics Design of Integrated Modular Motor Drives

Abdalla Hussein Rashad Mohamed

Doctoral dissertation submitted to obtain the academic degree of
Doctor of Electromechanical Engineering

Supervisors

Prof. Peter Sergeant, PhD - Prof. Hendrik Vansompel, PhD

Department of Electromechanical, Systems and Metal Engineering
Faculty of Engineering and Architecture, Ghent University

October 2021

GHENT UNIVERSITY

Multiphysics Design of Integrated Modular Motor Drives

Abdalla Hussein Rashad Mohamed

Doctoral dissertation submitted to obtain the academic degree of
Doctor of Electromechanical Engineering

Supervisors
Prof. Peter Sergeant, PhD - Prof. Hendrik Vansompel, PhD

Department of Electromechanical, Systems and Metal Engineering
Faculty of Engineering and Architecture, Ghent University

October 2021

GHENT
UNIVERSITY

Members of the Examination Board

Chair

Honorary Prof. Ronny Verhoeven, PhD, Ghent University

Other members entitled to vote

Prof. Frede Blaabjerg, PhD, Aalborg Universitet, Denmark

Prof. Frederik De Belie, PhD, Ghent University

Prof. Jeroen De Kooning, PhD, Ghent University

Prof. Chris Gerada, PhD, University of Nottingham, United Kingdom

Prof. Omar Hegazy, PhD, Vrije Universiteit Brussel

Supervisors

Prof. Peter Sergeant, PhD, Ghent University

Prof. Hendrik Vansompel, PhD, Ghent University

Preface

This thesis is the output of two research projects out of four projects I had to work on during my four years at EELAB. During this time, I learned a lot about modelling and control of electric motor drives. A word of thanks and appreciation should be directed to everyone contributed to the success of this work.

I would like to say thank you for my promoters, Prof. Peter Sergeant and Prof. Hendrik Vansompel for proofreading and finding financial resources for my work.

I would like to thank all the members of the examination board: prof. Frede Blaabjerg, prof. Chris Gerada, prof. Frederik De Belie, prof. Omar Hegazy, and prof. Jereon De Kooning for the effort they exerted and the time they spent in reading and evaluating my thesis. Their comments were indeed valuable to the thesis. Reading their reports of very high admire and appreciations of my work was really a moment of happiness for me.

I would like to say many thanks to my friend dr. Ahmed Hemeida. The very first work I did in my PhD was a complement of the work of Ahmed on the axial flux machines. The result of this start up collaboration was two journal papers for all collaborators.

A word of thanks is also directed to the technicians Vincent Gevaert and Tony Boone for preparation of setups, to Ingrid Dubois and Marilyn Van den Bossche for the administrative work, and Nic Vermeulen for the IT work.

I am also really thankful to my colleagues and staff members in Faculty of Engineering, Cairo University in the Electrical Power and Machines Department. The knowledge and the experience that I gained during my undergraduate and master studies in Faculty of Engineering, Cairo University were the basis for the success of the research I did in the EELAB.

I would like to express my true, sincere and lovely thanks to my wife for everything she does for me and for our daughter. My wife is a brilliant engineer, she offered me a lot of help in my PhD and a lot of technical problems have been solved with a little discussion with her. I would also like to sincerely express my warm and endless love to my pretty daughter for filling my life with happiness and joy.

I would like to express my warm and lovely thanks to my siblings: my sister, the excellent engineer and my brother, the excellent business mind for their continuous support and love. I would also express my sincere love to my lovely niece. I

would also say many thanks for my aunt for her continuous support and love.

I wouldn't say finally but firstly and before everything else, I express my warm, sincere, endless and limitless gratitude and love for my parents for everything they did and still doing for me, for the pure and sincere love they show for me, for the real discipline and ethics they taught to me and for their continuous giving to me. Whatever I say and whatever I do for you, Mama and Baba, it will never fulfill your rights. I hope you a long, healthy and beautiful life.

Abdalla Hussein Rashad Mohamed,
October 2021

Contents

Summary

High power density and efficiency are fundamental requirements in many applications such as electric vehicles (EVs), hybrid electric vehicles (HEVs), and propulsion and aerospace applications.

In the context of increasing the power density and efficiency of electric motor drives, integrated modular motor drives (IMMDs) emerge as a solution to obtain both benefits. IMMDs incorporate physical integration and modularization of the electric machine and the power converter. The physical integration brings the electric machine and the power converter into close proximity so that they can share the same cooling circuit and enclosure. The cables connecting the power converter and the electric machine can be completely eliminated or greatly reduced in length.

The result of this physical integration is a great reduction of the volume, the weight and the power losses of the electric motor drive, which improves its power density and efficiency. Furthermore, the elimination of the cables reduces the electromagnetic interference (EMI) of the drive which means that the EMI filter can be eliminated or reduced in size, and once again this improves the power density and the efficiency of the drive.

Many challenges have to be met in the design of integrated motor drives. A first challenge is to mount the power converter in a small space inside the machine in a mechanically stable way as it is exposed to the motor vibration. A second challenge is the thermal management of this power converter as it resides close to the electric machine windings with its relatively high heat generation.

The design of a modular, small size and low losses power converter facilitates the design of integrated motor drives. The modularity divides the machine into a number of modules with a driving converter for each module. This means that the converter is split into several small low rating units with smaller space and cooling requirements. One more advantage of the drive modularity is the fault-tolerance. If a fault occurs in one module, the drive can continue working with the remaining healthy ones.

Using wide bandgap (WBG) power devices in the converter implementation facilitates the design of a small size and low losses power converter module. The commercially available WBG devices are Gallium Nitride (GaN) and Silicon Carbide (SiC). These WBG devices are existing in small package size and they dissipate lower power compared to Silicon (Si) devices.

The main contribution of this thesis is the design of two novel integrated modular motor drive topologies: a yokeless and segmented armature (YASA) axial flux permanent magnet synchronous machine and a switched reluctance machine (SRM). Both topologies are providing a stable mechanical mounting for the power converter modules and a shared cooling circuit for the electric machine and the power converter.

For the first integration topology - the YASA machine - the physical integration is realized by designing a 3D aluminium part with a polygon-shaped outer surface for mounting the converter modules and an inner surface that well encloses the teeth of the machine. A cooling channel is introduced between the inner and the outer surfaces of the 3D aluminium part to decouple and evacuate the heat from the YASA tooth and the power converter module. This integration topology is named circumscribing polygon (CP) integration topology. This topology is thermally optimized using computational fluid dynamics (CFD) simulations. Each integrated module comprises the machine tooth, the converter module and a shared cooling for both of them. The full motor drive can be easily synthesized from the individual modules. A discrete GaN based half-bridge inverter module is designed for this integration topology.

First, electromagnetic and thermal models of the YASA machine and its driving converter are needed to design the CP integrated YASA drive. In this PhD, analytical electromagnetic models developed by former PhD colleagues for the YASA machine are used. Finite element and lumped parameter thermal network (LPTN) models are built for the YASA machine and the power electronics. These models are used to find optimal geometrical parameters of the YASA machine and an optimal inverter model design. In addition, loss models for the GaN switches are developed as well as an electromagnetic finite element model for the parasitics in the inverter PCB to investigate their influence on the losses and temperature of the switches.

Next, a three teeth CP integrated YASA setup is built to validate the integration concept and the introduced models. The measurements prove the validity of the integration concept and the introduced modelling.

The power density of the designed CP integrated modular motor drive for the YASA machine is extensively investigated in this thesis and some power density enhancement techniques are proposed, simulated and validated by measurements on the setup.

Another contribution of the thesis is the design of a DC-link structure that can be integrated with the CP YASA drive. An analytical design methodology for the DC-link capacitors is provided. Electromagnetic and thermal models are built to study the performance of the designed DC-link structure. The design of this DC-link structure is validated by measurements.

For the second integration topology - the SRM -, the integration is realized by designing a 3D part with a radial cross-sectional area with outer polygon shape and an inner circular shape. The power converter modules are mounted on the

outer surface of this 3D part while the inner surface is retrofitted to tightly enclose the water jacket cooled SRM. By doing so, the water jacket cooling of the non-integrated SRM is used to cool the converter modules as well. This integration concept is named polygon retrofitted (PR) integration concept. This integration topology has the advantage of plug and play of the converter modules without much modifications in the original non-integrated machine. A discrete SiC based asymmetric H-bridge is designed for this integration topology.

Several models are built for the SRM integrated topology. A dynamic model for the closed loop torque controlled SRM is built to compute the exact current waveforms of the SRM windings and the converter power devices. The computed currents from this model are used as inputs for the electromagnetic model of the SRM and the loss model of the converter. Electromagnetic and thermal models of the SRM and its driving converter are developed: an electromagnetic finite element (FE) model, 3D FE thermal models and LPTN models are built for the SRM. Also 3D FE thermal models and thermal network models are built for the asymmetric H-bridge converter. These models are used to design the asymmetric H-bridge converter and to study the performance of the complete PR SRM drive.

Furthermore, a PR integrated SRM setup is built to validate the integration concept and the modelling of the integrated drive. The measurements confirm the effectiveness of the integration concept and the introduced modelling.

A last contribution of the thesis is the design of a novel converter structure for the modular integrated SRM that can be configured to drive the SRM in the conventional mode and the modular mode. Switching from conventional to modular mode is done at high operating speeds and in case of fault in one coil or one inverter modules. The performance of the converter is validated to be good by experimental measurements in conventional mode, modular mode and in case of fault.

Finally, a conclusion of the research conducted in this thesis and some ideas for future research are provided.

Samenvatting

Hoge vermogensdichtheid en hoog rendement zijn fundamentele eisen in vele toepassingen zoals elektrische voertuigen (EVs), hybride elektrische voertuigen (HEVs), en toepassingen in propulsie en luchtvaart.

In de context van het verhogen van de vermogensdichtheid en efficiëntie van elektrische aandrijvingen, komen geïntegreerde modulaire motoraandrijvingen (IMMD's) naar voren als een oplossing om beide voordelen te combineren. IMMD's omvatten fysieke integratie en modularisatie van de elektrische machine en de vermogenselektronische omvormer. De fysieke integratie brengt de elektrische machine en de vermogenselektronische omvormer dicht bij elkaar, zodat ze hetzelfde koelcircuit en dezelfde behuizing kunnen delen. De kabels die de vermogenselektronische omvormer en de elektrische machine verbinden, kunnen volledig worden geëlimineerd of aanzienlijk worden verkort.

Het resultaat van deze fysieke integratie is een grote vermindering van het volume, het gewicht en de vermogensverliezen van de aandrijving, wat de vermogensdichtheid en efficiëntie verbetert. Bovendien vermindert de eliminatie van de kabels de elektromagnetische interferentie (EMI) van de omvormer, wat betekent dat het EMI-filter kan worden geëlimineerd of verkleind, en ook dit verbetert opnieuw de vermogensdichtheid en de efficiëntie van de omvormer.

Bij het ontwerp van geïntegreerde motoraandrijvingen zijn er heel wat uitdagingen. Een eerste uitdaging is om de omvormer in een kleine ruimte in de machine te monteren op een mechanisch stabiele manier, aangezien deze wordt blootgesteld aan motortrillingen. Een tweede uitdaging is het thermische ontwerp van deze omvormer, omdat de omvormer een relatief hoge warmteontwikkeling heeft en zich dicht bij de wikkelingen van de elektrische machine bevindt.

Het ontwerp van een modulaire vermogensomvormer met kleine afmetingen en laag gewicht vergemakkelijkt het ontwerp van geïntegreerde motoraandrijvingen. Het concept van modulariteit verdeelt de machine in een aantal modules met voor elke module een aparte omvormer. Dit betekent dat de vermogenselektronica is opgesplitst in verschillende kleine eenheden die elk een laag vermogen hebben, en dus minder ruimte en koeling nodig hebben. Nog een voordeel van de modulaire aandrijving is de fouttolerantie. Als er een fout optreedt in één module, kan de omvormer blijven werken met de overige gezonde modules.

Het gebruik van wide-bandgap (WBG) halfgeleidertechnologie in de imple-

mentatie van de omvormer vergemakkelijkt het ontwerp van een omvormermodule van klein formaat en met lage verliezen. De in de handel verkrijgbare WBG-halfgeleiders zijn galliumnitride (GaN) en siliciumcarbide (SiC). Ze bestaan in een kleine behuizingen en ze dissiperen een lager vermogen in vergelijking met silicium (Si) halfgeleiders.

De belangrijkste bijdrage van dit proefschrift is het ontwerp van twee nieuwe geïntegreerde modulaire topologieën van elektrische aandrijvingen: een "yoke-less and segmented armature" (YASA) synchrone machine met permanente magneten en axiale flux, en een geschakelde reluctantiemachine (SRM). Beide topologieën bieden een stabiele mechanische montage voor de omvormermodules en een gedeeld koelcircuit voor de elektrische machine en de vermogensomvormer.

Voor de eerste integratietopologie - de YASA-machine - wordt de fysieke integratie gerealiseerd door een 3D aluminium onderdeel te ontwerpen met enerzijds een veelhoekig buitenoppervlak voor het monteren van de convertermodules en anderzijds een binnenoppervlak dat de tanden van de machine goed omsluit. Een koelkanaal tussen de binnen- en buitenoppervlakken van het 3D aluminium onderdeel laat toe de warmte van de tanden en de omvormermodules te ontkoppelen af te voeren. Deze integratietopologie wordt "omschrijvende polygoon" (CP) topologie genoemd. Deze topologie is thermisch geoptimaliseerd met behulp van computational fluid dynamics (CFD) simulaties. Elke geïntegreerde module omvat de machinetand, de convertormodule en een gedeelde koeling voor beide. De volledige motoraandrijving kan eenvoudig worden opgebouwd vanuit de individuele modules. Voor deze integratietopologie is een op GaN gebaseerde module van een halvebrugomvormer ontworpen.

Ten eerste zijn elektromagnetische en thermische modellen van de YASA-machine en de omvormer nodig om de geïntegreerde YASA-topologie met CP te ontwerpen. In dit doctoraat worden analytische elektromagnetische modellen voor de YASA-machine gebruikt die zijn ontwikkeld door voormalige PhD-collega's. Eindige-elementenmodellen en thermische-netwerkmodellen (LPTN) zijn gebouwd voor de YASA-machine en de vermogenselektronica. Deze modellen worden gebruikt om optimale geometrische parameters van de YASA-machine en een optimaal ontwerp van de invertormodule te vinden. Daarnaast zijn er verliesmodellen voor de GaN-schakelaars gemaakt, en ook een elektromagnetisch eindige-elementenmodel voor de parasitaire impedanties in de printplaat van de invertormodule, om hun invloed te bepalen op de verliezen en de temperatuur van de schakelaars.

Vervolgens is er een opstelling gebouwd van een geïntegreerde YASA-setup met drie tanden, volgens de CP topologie. Aan de hand van metingen worden het integratieconcept en de modellen gevalideerd.

De vermogensdichtheid van de ontworpen geïntegreerde modulaire motoraandrijving voor de YASA-machine is uitgebreid onderzocht in dit proefschrift en enkele technieken voor het verbeteren van de vermogensdichtheid worden voorgesteld, gesimuleerd en gevalideerd door metingen op de opstelling.

Een andere bijdrage van het proefschrift is het ontwerp van een DC-busstructuur die kan worden geïntegreerd met de YASA-topologie met CP. Er wordt een analytische ontwerpmethodologie voor de DC-link condensatoren opgebouwd, en er zijn ook elektromagnetische en thermische modellen gebouwd om de prestaties van de ontworpen DC-busstructuur te bestuderen. Ook dit ontwerp is gevalideerd door metingen.

Voor de tweede topologie - de geschakelde reluctantiemotor of SRM - wordt de integratie gerealiseerd door een 3D-onderdeel te ontwerpen met een radiale dwarsdoorsnede met een veelhoekvorm aan de buitenkant en een cirkelvorm aan de binnenkant. Net als bij de eerste topologie worden de omvormermodules op het buitenoppervlak van dit 3D-onderdeel gemonteerd, terwijl het binnenopper-vlak nauwkeurig de watermantelgekoelde SRM omsluit. Zo wordt de waterman-telkoeling van de niet-geïntegreerde SRM ook gebruikt om de convertermodules te koelen. Dit integratieconcept wordt polygon retrofitted (PR) integratieconcept ge-noemd. Deze integratietopologie heeft het voordeel van plug-and-play van de con-vertermodules zonder veel aanpassingen in de oorspronkelijke, niet-geïntegreerde machine. Voor deze integratietopologie is een op SiC gebaseerde asymmetrische H-brug ontworpen.

Er zijn verschillende modellen gebouwd voor de SRM-topologie. Een dy-namisch model voor de koppelgestuurde SRM (in gesloten-lus) is gebouwd om de exacte stroomgolfvormen in de motorwikkelingen en de vermogensomvormer te berekenen. De berekende stromen van dit model worden gebruikt als input voor het elektromagnetische model van de SRM en het verliesmodel van de omzetter. Vervolgens worden elektromagnetische en thermische modellen van de SRM en de omvormer ontwikkeld: een elektromagnetisch eindige-elementenmodel (FE), 3D thermische eindige-elementenmodellen en LPTN-modellen zijn opgesteld voor de SRM; 3D FE thermische modellen en thermische netwerkmodellen zijn gecreëerd voor de asymmetrische H-brugconvertor. Deze modellen worden gebruikt om de asymmetrische H-brugconvertor te ontwerpen en om de prestaties van de volledige aandrijving van de PR SRM te bestuderen.

Een laatste bijdrage van het proefschrift is het ontwerp van een nieuwe conver-torstructuur voor de modulaire geïntegreerde SRM die kan worden geconfigureerd om de SRM zowel in conventionele modus als in modulaire modus aan te sturen. Overschakelen van conventionele naar modulaire modus gebeurt bij hoge of wan-neer er een fout in de spoel of de invertormodule optreedt. De performantie van de omvormer is gevalideerd via metingen op het prototype in conventionele modus, modulaire modus en in geval van storing.

Ten slotte wordt een conclusie gegeven van het onderzoek dat in dit proefschrift is uitgevoerd en enkele ideeën voor toekomstig onderzoekswerk worden opgelijst.

List of Abbreviations

IMMDs	Integrated modular motor drives
EMI	Electromagnetic interference
RHM	Radially housing mounted
AHM	Axially housing mounted
RSM	Radially stator mounted
ASM	Axially stator mounted
PM	Permanent magnet
emf	Electromotive force
Si	Silicon
SiC	Silicon Carbide
GaN	Gallium Nitride
WBG	Wide bandgap
VSI	Voltage source inverter
CSI	Current source inverters
IMDs	Integrated motor drives
YASA	Yokeless and segmented armature
SRM	Switched reluctance machine
CP	Circumscribing polygon
PR	Polygon retrofitted
AFPMSM	Axial flux permanent magnet synchronous machine
CFD	Computational fluid dynamics
PCB	Printed circuit board
FOM	Figure of merit
SPWM	Sinusoidal pulse width modulation
SVPWM	Space vector pulse width modulation
RTD	Resistance temperature detector
PWM	Pulse width modulation
TIM	Thermal interface material
FE	Finite element
LPTN	Lumped parameter thermal network
MEC	Magnetic equivalent circuit
Nd-Fe-B	Neodymium-Iron-Boron
PMSM	Permanent magnet synchronous machine
TSF	Torque sharing function
IC	Integrated circuit
ESL	Equivalent series inductance
UVLO	Under voltage lockout

List of Symbols

Material Properties

ρ_{cu}	mass density of the copper
ρ_{fr4}	mass density of the FR4
ρ_{solder}	mass density of the solder
ρ_e	equivalent mass density
ρ	mass density of the medium
ρ_c	mass density of the core
ρ_w	water mass density
ρ_h	mass density of the heterogeneous material
ρ_m	mass density of the main constituting material
ρ_{im}	mass density of the impregnation material
ρ_{el}	mass density of the element
C_{pcu}	specific heat capacity of the copper
C_{pfr4}	specific heat capacity of the FR4
$C_{psolder}$	specific heat capacity of the solder
C_{pe}	specific heat capacity
ν	kinematic viscosity of the air
k_{air}	air thermal conductivity
k_h	thermal conductivity of the heterogeneous part
k_{im}	thermal conductivity of the impregnation material
k_m	thermal conductivity of the main constituting material
C_p	specific heat capacity of the medium
C_{pm}	specific heat capacity of the main constituting material
$C_{p_{im}}$	specific heat capacity of the impregnation material
C_{p_h}	specific heat capacity of the heterogeneous material
C_{pw}	specific heat capacity of the water
C_{pel}	specific heat capacity of the element
α_t	resistance temperature coefficient
σ_{pm}	electrical conductivity of the PM

Resistance, Capacitance and Inductance

R_{ds}	drain to source resistance
R_{coil}	coil resistance
R_{gint}	internal gate resistance of the switch
R_{pu}	pull up resistance
R_{pd}	pull down resistance
C_{iss}	input capacitance of the switch
C_{rss}	miller capacitance of the switch
C_{oss}	output capacitance of the switch
L_g	gate drive loop inductance
L_{cs}	common source inductance
L_{loop}	commutation loop inductance
L_+, L_-	inductance of the positive and negative DC-link busbar plate
L_{d1}, L_{d2}	drain inductances of the upper and the lower switches
L_{s1}, L_{s2}	source inductances of the upper and the lower switches
L_{dclink}	total DC-link inductance
L_{op}	rate of change of the unsaturated coil inductance with respect to the rotor position
L_a	aligned inductance
L_{un}	unaligned inductance
ESL	equivalent series inductance of the DC-link capacitors

Electromagnetic Quantities

$B(t)$	instantaneous flux density of the core
T	fundamental period of the flux density waveform
S_{pm}	PM area penetrated by the magnetic flux
J_{ns}	current density of the PM induced current
$\mathbf{J}$	current density in the coils
$\mathbf{A}$	magnetic vector potential
f_B	frequency of the flux density waveform
B_m	peak value of the flux density
$\psi(\theta, i)$	flux linkage of the stator coils
$w_c(\theta, i)$	co-energy of the stator coil
n_m	number of local slope reversal of the flux density
ΔB_i	peak-to-peak flux density of the minor loop
K_{Fe3}	classical loss coefficient of the core material
K_{Fe4}, K_{Fe5}	excess loss coefficient of the core material
K_{Fe1}	hysteresis loss coefficient of the core material
K_{Fe2}	hysteresis loss coefficient of the core material
$K(B_m)$	a factor for consideration of the losses of the minor hysteresis loops

Thermal Quantities

T_{am}	modified Taylor number
Nu	Nusselt number
Nu_i	Nusselt number on the surface i
Re	Reynolds number
R_{JC}	junction to case thermal resistance
R_{CP}	case to PCB thermal resistance
R_{PA}	PCB to cooling fluid thermal resistance
R_{conv}	convection resistance
R_{TA}	TIM to ambient thermal resistance
R_{TIM}	TIM thermal resistance
R_{AL}	aluminium shared cooling structure thermal resistance
Z_{th}	junction to case thermal impedance
h_i	average convection coefficient on the surface i
h_{ciw}	average convection coefficient of the inner wall of the channel
h_{PR}	convection coefficient on the 3D polygon retrofitted surface
h_{SRM}	convection coefficient on the SRM surface
h_{airg}	airgap exposed surface convection coefficient
h_c	convection coefficient of the surface
Q_w	water flow rate
A_s	area of the convected surface
T_{case}	case temperature of the switch
T_{wout}	water outlet temperature
T_{ciw}	channel inner wall temperature
T_{wa}	average water temperature
T_j	junction temperature
T_f	fluid temperature
T_{surr}	temperature of the surroundings
T_{win}	inlet water temperature
T_{vec}	temperature vector of the nodes
$T_{ref}\mid_i$	reference temperature on the stator/rotor surface i with $T_{ref} \neq T_a$
T_r	average rotor temperature
T_s	average stator temperature
T_a	ambient temperature
∇T	temperature gradient
q_c	heat flux defined as the rate of heat transfer per unit area
Q_{conv}	rate of heat transfer by convection
Q_{rad}	rate of heat transfer by radiation
Q_{th}	heat generated by the medium per unit volume
ϵ	emissivity of the body
σ	Stefan Boltzmann constant
C_{mat}	diagonal matrix of the thermal capacitance of the nodes
n	vector normal to the boundary surface
s	surface on which the boundary condition is specified
G_{mat}	conductance matrix

Geometrical Parameters

v_c	volume of the core
v_{cu}	volume of the copper
v_{fr4}	volume of the the FR4
v_{solder}	volume of the the solder
v_t	PCB part total volume
R_r	rotor outer radius
R_1	rotor pole arc radius
R_2	stator pole arc radius
R_m	equivalent air gap mean radius
Y_{st}	stator yoke thickness
Y_{rt}	rotor yoke thickness
β_s	stator pole arc angle
β_r	rotor pole arc angle
N_{rp}	number of rotor poles
A_{rlam}	area of the rotor lamination
N_t	number of turns/coil
D_{wj}	water jacket outer diameter
L_{awj}	water jacket axial length
L_{ps}	length of the polygon side
ΔR	maximum tolerable radius increase
D_{so}	stator outer diameter
D_{ro}	rotor outer diameter
D_{out}	housing outer diameter
ΔY_m	thickness of the PM slice
α_m	PM angle span ratio
g	airgap thickness
G	airgap size ratio
L	PM thickness ratio
L_Z	PCB thickness
L_{ax}	housing axial length
N_m	number of PMs in one rotor disk
N_{ph}	number of phases
n_s	number of stator modules
N_s	number of teeth
n_p	number of the polygon sides
A_s	surface area
f_{wors}	winding or stacking factor
f_{ws}	fill factor

Power, Speed and Torque

P_{cons}	switch conduction losses
P_{son}	switch turn on losses
P_{soff}	switch turn off losses
P_{st}	switch total losses
P_{losst}	total losses evacuated by the cooling water
P_{cond}	diode conduction losses
P_{sd}	diode switching losses
P_{dt}	diode total losses
P_{drive}	total drive power
P_{loss}	device loss
P_{hy}	hysteresis loss
P_{cl}	classical loss
P_{ex}	excess loss
P_{wdg}	total winding losses
P_{endup}	power loss in the upper end-winding
P_{endlow}	power loss in the lower end-winding
P_{eff}	power loss in the effective winding
P_{stcore}	stator core losses
P_{PMone}	loss in one PM
P_{PM}	total losses in the rotor PMs
$P'_{f,v}$	windage losses for surface f due to viscous forces
$P'_{f,p}$	windage losses for surface f due to pressure forces
$P'^{*}_{f,v}$	windage losses at the reference point for surface f due to viscous forces
$P'^{*}_{f,p}$	windage losses at the reference point for surface f due to pressure forces
P_{s}	SRM stator power losses
P_{scout}	switch losses due to the output capacitance charging/discharging cycle
ω_{m}	angular speed of the rotor
$T(\theta, i)$	torque of one SRM stator coil
$T_{e}(\theta)$	shaft torque
T_{ref}	desired shaft torque

Voltage, Current and Charges

V_{dc}	DC link voltage
V_{gon}	turn on gate drive voltage
V_{goff}	turn off gate drive voltages
V_{th}	threshold of the switch
V_{plat}	plateau voltage of the switch
V_{DDI}	input bias voltage
V_{DDx}	output voltage
v_d	diode voltage drop
I_{srms}	RMS value of the switch current
I_{rr}	reverse recovery current
I_{DDI}	input bias current
I_{DDx}	output bias current
I_{on}	source current of the driving IC
I_{off}	sink current of the driving IC
$i_{linepeak}$	peak line current
$i_{on}(n)$	switch current at the turn on instants
$i_{off}(n)$	switch current at the turn off instants
i_d	instantaneous diode current
i_x^*	reference current of the coil x
i_x	feedback current of coil x
i_s	instantaneous switch current
Q_g	gate charge
Q_{rr}	reverse recovery charge

Other Symbols

f_o	fundamental frequency of the switch current waveform
f_s	switching frequency
f	fundamental frequency of the flux density
n_{son}	number of turn-on transitions of the switch in one fundamental cycle
n_{soff}	number of turn-off transitions of the switch in one fundamental cycle
n_{doff}	number of turn off transitions of the diode
t_{on}	turn-on time of the switch
t_{off}	turn-off time of the switch
t_{rr}	reverse recovery time
τ_I	integral time constant
D	duty cycle
M	modulation index
$f_{ph}(\theta)$	TSF of the phase as function in the rotor position
k_p	proportional gain of the PI controller
$U(t)$	unit step function

Chapter 1

Integrated Modular Motor Drives: State of the art

1.1 Introduction

Integrated modular motor drives (IMMDs) combine the benefits of the physical integration and the modularity. The physical integration incorporates the integration of the electric machine and the power converter into one unit with the advantages of reduced cable requirements and its associated reduced electromagnetic interference (EMI) [1, 2].

The physical integration could also include a shared cooling structure for both the electric machine and the power converter with elimination of a separate converter heat-sink [3]. Both the electric machine and the power converter can finally be enclosed in the same housing, removing the need of a separate housing for the converter [4]. The elimination of such components leads to more compact, high power density and high efficiency drives [5, 6].

The drive modularity means the segmentation of both the electric machine and the power converter into a number of identical modules. This segmentation enhances the fault tolerance of the whole drive [7, 8], facilitates the physical integration, makes it possible to utilize low rated voltage and/or current semi-conductor devices [9], facilitates the manufacturing of the drive and improves the thermal performance of the power converter modules as the surface area used by the converter modules increases [10].

Although the IMMDs can replace the conventional motor drives in any application, the main targeted applications are those requiring high power density and high efficiency [11]. Traction [12, 13], propulsion [14] and aerospace [6] systems are applications examples where IMMDs can be of great benefit.

In this chapter, an overview is provided for the following:

- the different topologies of IMMDs.

- the segmentation approaches of electric drives.

- the different electric machines for IMMDs.

- the power semiconductor technology for IMMDs.

- the power converters for IMMDs.

- the control architectures for IMMDs.

- the commercial IMMDs.

- the electric machines selected for integration study in the thesis.

Moreover, the contribution of the thesis to the state of the art, the outline of the thesis and the scientific publications are also provided.

1.2   IMMDs Topologies

Depending on the location of the power converter modules with respect to the electric machine housing and/or stator iron, IMMDs are classified into four basic topologies: radially housing mounted (RHM) (see Fig. 1.1(a), axially housing mounted (AHM) (see Fig. 1.1 (b)), radially stator mounted (RSM) (see Fig. 1.2 (a) and axially stator mounted (ASM) (see Fig. 1.2 (b) [11].

The radially mounted integration topologies are more suitable for sausage design type of electric machines where the axial length tends to be longer than the outer diameter of the machine. They are also preferred when the axial direction of the machine is occupied by gear box.

The axially mounted topologies are more suitable for pancake design types of electric machines where the outer diameter tends to be longer than the axial length of the machine.

1.2.1   Housing mounted topologies

The housing mounted topologies (i.e. RHM, AHM) are not considered to be a pronounced aggressive integration solution as the power converter modules are added in a separate enclosure with a separate cooling structure on top of the machine housing as in the RHM topology [15] or on the end plate in the axial direction as in the AHM topology [14, 16]. The main gain of these integration topologies is the close proximity between the machine winding terminals and the power converter which reduces the cable requirements. Fig. 1.1 (a) and (b) illustrate the mechanical construction of RHM and AHM integrated drives.
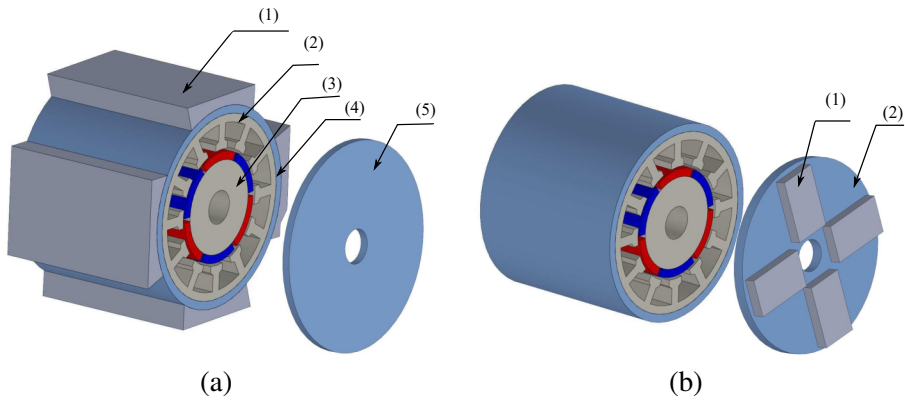
Figure 1.1: Demonstration of housing mounted integration topologies
(a) Radially housing mounted topology: (1) power converter modules,
(2) stator, (3) rotor, (4) housing, (5) end plate. (b) Axially housing
mounted topology: (1) power converter modules, (2) end plate.

1.2.2 Stator mounted topologies

The stator mounted topologies provide more compact integration compared to the
housing mounted topologies, but they have more design challenges to meet [3].
These challenges are emerging from the limited space inside the machine and the
need to design a shared cooling structure for both the machine and the power con-
verter given the high ambient temperature conditions inside the machine [17]. Fig.
1.2 (a) and (b) illustrate the mechanical construction of RSM and ASM integrated
drives.

1.3 Segmentation (Modularity) approaches

In case of distributed winding machines, depending on the number of the stator
coils, the machine windings can be split into groups of three-phase or multi-phase
windings with a driving inverter for each group [18, 19]. Fig. 1.3 shows the con-
ventional three-phase connection of a fifteen stator coils machine with each phase
composed by series connection of five coils.

Fig. 1.4 (a), (b) illustrates the segmentation of the stator coils into five groups
with three-phase windings in each group and the segmentation into three groups
with five-phase windings in each group respectively.

The common advantages of the segmentations in Fig. 1.4 compared to the
conventional connections are as follows:

- Reduced DC input voltage requirement which leads to the following gains:
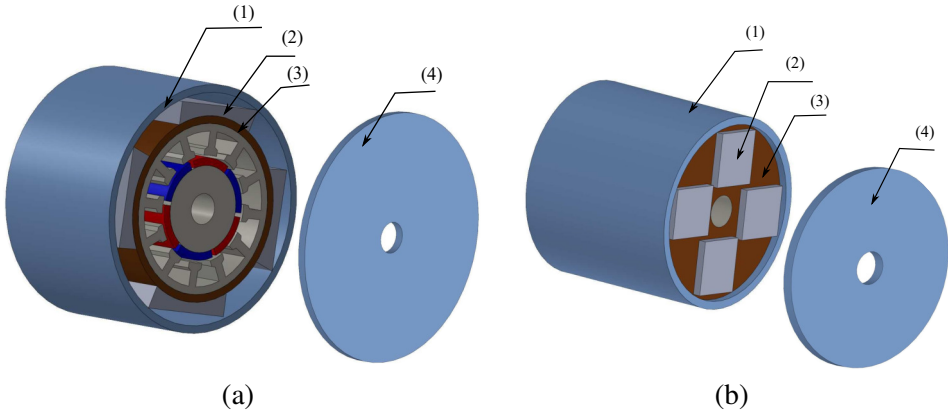
Figure 1.2: Demonstration of stator mounted integration topologies (a) Radially stator mounted topology: (1) housing, (2) power converter modules, (3) shared cooling structure, (4) end plate. (b) Axially stator mounted topology: (1) housing, (2) power converter modules, (3) shared cooling structure, (4) end plate.
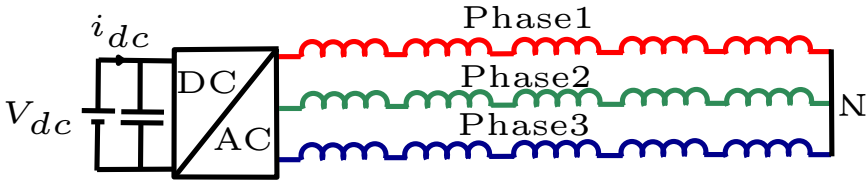
Figure 1.3: Conventional three-phase windings connection of a fifteen stator coils machine.

- – The direct use of the battery voltage with less number of cells in battery powered applications.

- – The possibility to use semi-conductor devices with a lower rated voltage.

- – Lower winding terminal voltage which means less insulation stresses and lower inter-turn capacitive currents, and therefore, longer bearing lifetime and lower electromagnetic noise.

• The breakdown of the driving inverter into several smaller units, making it easier to integrate it with the machine given the smaller size of each unit.

• More effective cooling of the inverter modules as they become distributed over a larger surface area.
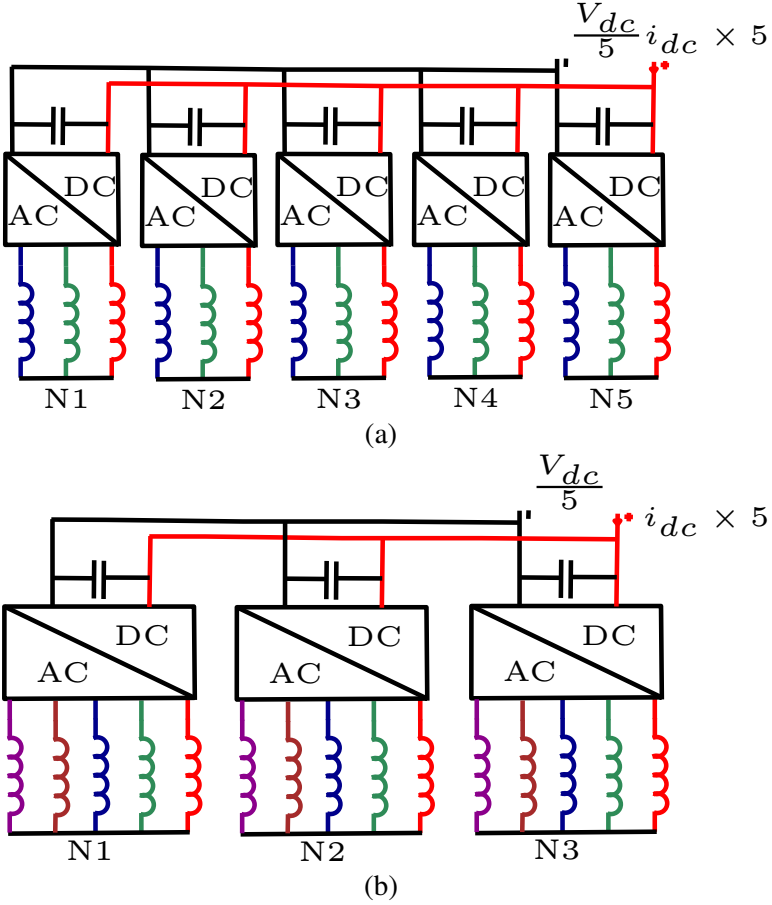
Figure 1.4: Illustration of stator winding segmentation of a fifteen coils stator machine: (a) winding segmentation into five groups with three-phase windings in each group, (b) winding segmentation into three groups with five-phase windings in each group.

- The possibility to implement fault tolerant control algorithms with easier isolation of one inverter module in case of fault.

- The possibility to interleave the pulse width modulation (PWM) carriers of the different groups of modules to reduce the DC-link current ripple [20].

- The distribution of the DC-link capacitance over the modules, making it easier to integrate them in the machine.

The segmentation of Fig. 1.4 (a) provides a more fault tolerant structure compared to the one in Fig. 1.4 (b) due to the higher number of segments. Having

multi-phase winding groups in the segmentation of Fig. 1.4 (b) provides more degrees of freedom in the control of the modules.

The disadvantages of the segmentation in Fig. 1.4 compared to the conventional connections are as follows:

- Higher DC-link current will be drawn for the same drive power which leads to the need of a higher rated current DC source.

- A large number of inverter modules will be needed with the associated higher cost.

- A large number of current sensing devices will be needed which further increases the cost of the system.

- A digital signal controller (DSC) with large number of digital and analogue input/output pins will be needed or multiple-DSC units will be needed.

- The control algorithm will be more complex and high computational burden on the DSC will result..

In case of concentrated winding machines, the same segmentation approach as for the distributed winding machines can be used or alternatively, each stator coil can be driven by a dedicated inverter module [21, 22]. Fig. 1.5 shows the different possibilities of driving each stator coil by one dedicated inverter module.

The segmentation shown in Fig. 1.5 (a) uses less number of devices but is less fault tolerant than the one in Fig. 1.5 (b). Using the segmentation in Fig. 1.5 (b), a separate controller for each phase can be used which further enhances the fault tolerance of the drive [23].

Each winding group with its associated driving inverter can be connected in parallel (as shown in Fig. 1.5 (b)) or in series (as illustrated in Fig. 1.6) with the DC input source [5, 10]. In case of series connection, the required input DC voltage and the drawn input DC current are the same as in the conventional case but the modules' input voltage will need to be equalized by an external circuit or in the control algorithm.

1.4   Electric machines for IMMDs

The most commonly used types of electric machines are the radial flux machines and the axial flux machines. As depicted in Fig. 1.7, the flux is produced in the radial direction in case of radial flux machines. In the axial flux machines, the flux is produced in the axial direction as shown in Fig. 1.8. In principle, both types of machines can be utilized in integrated drives. The radial flux machines tend to have a sausage design while the axial flux machines tend to have a pancake design. The choice of the machine type depends on the space and the power density requirements of the application. For axial flux machines, it would be more challenging to

(a)

(b)
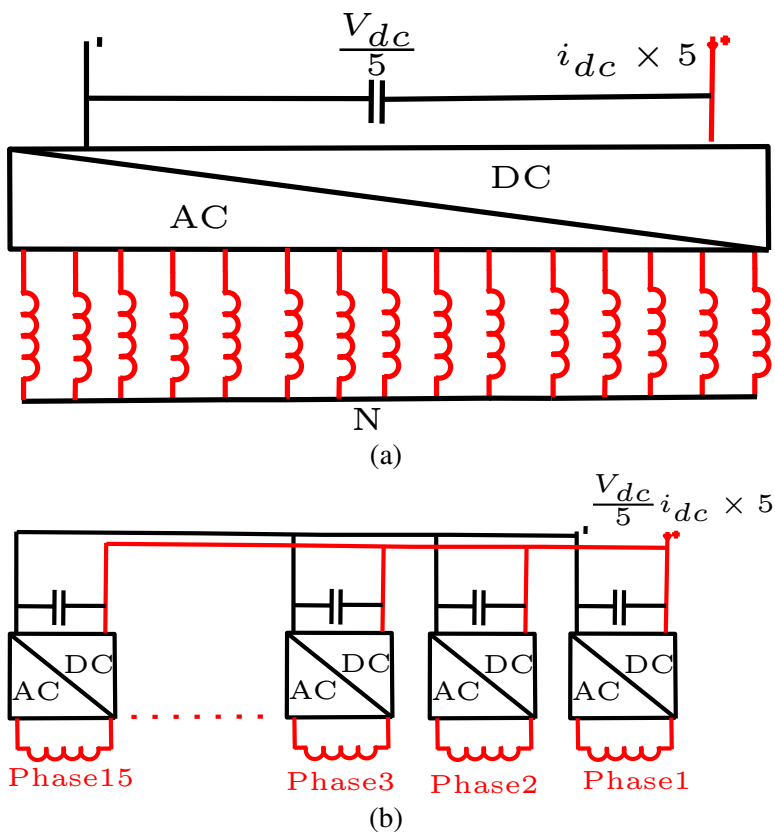
Figure 1.5: Illustration of stator winding connection with each coil driven by one inverter module: (a) one common neutral of all coils, (b) without neutral point.
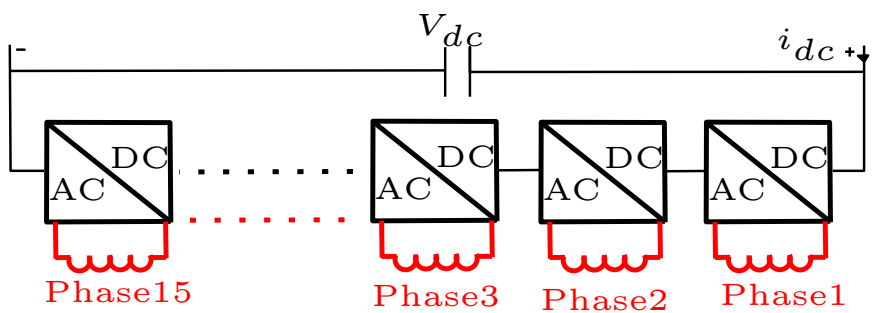
Figure 1.6: Illustration of drive segments connected in series with the DC-source.

design an ASM integration topology as the power converter will be exposed to the high magnetic field generated by the magnets.
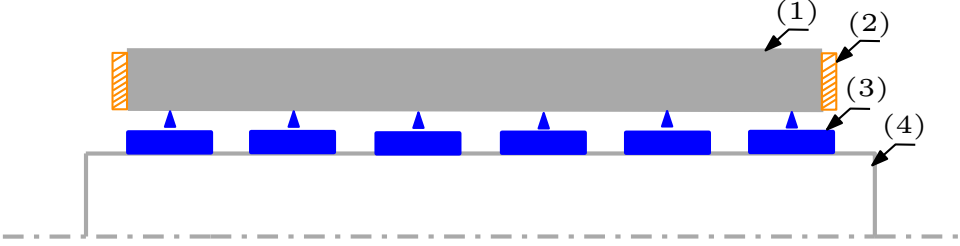
Figure 1.7: Illustration of radial flux machines: (1) stator core, (2) windings, (3) magnets, (4) rotor.
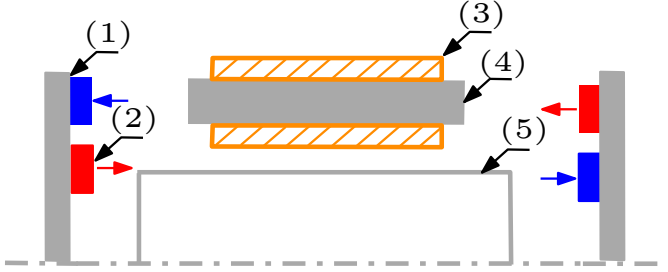
Figure 1.8: Illustration of axial flux machines: (1) rotor, (2) magnets, (3) windings, (4) stator core, (5) shaft.

1.4.1   Electric machines stator construction

The design of the stator of the candidate machine for IMMDs has special importance due to the proximity of the converter modules to the stator windings. The stator can have a distributed winding or concentrated winding as shown in Fig. 1.9. The following advantages of the concentrated winding machines make them more relevant for the IMMDs:

- The relative independence of each stator coil results in a more compact IMMDs.

- The short end-windings and the high slot fill factor [24] enhance the compactness and result in lower copper loss and hence, easier shared thermal management.

- The lower electromagnetic mutual coupling between the phases facilitates the fault tolerant control implementation [17].

- There is no physical contact between the different coils (see Fig. 1.9) which eliminates the possibility of phase to phase short circuit and hence, higher fault tolerant drive results [17].

The general drawback of the concentrated winding machines is the high content of magneto motive force (MMF) space harmonics which cause high rotor losses [25]. So, a special attention should be paid to this point in the design process.

(a)   (b)
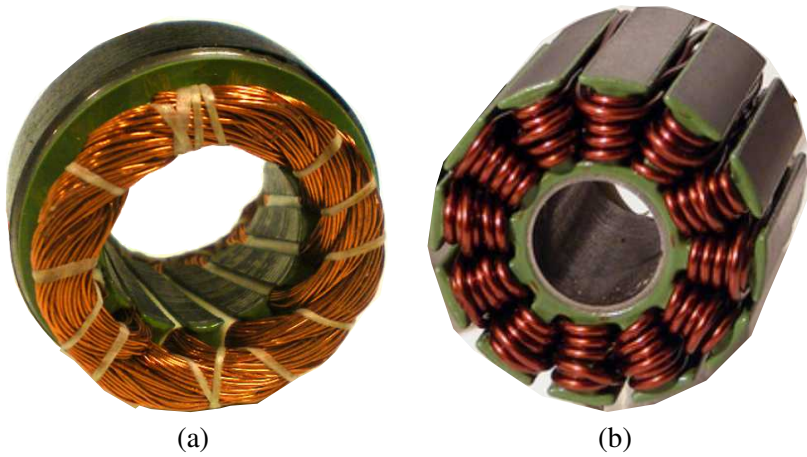
Figure 1.9: Demonstration of the distributed winding machines (a) and concentrated winding machines (b) [26].

1.4.2 Electric machines rotor construction

The rotor of a candidate machine for integration can be a wound rotor structure, a permanent magnet (PM) structure or reluctance type. In the wound rotor structure, the rotor field can be generated by DC excitation as in the wound rotor synchronous machines or by induced electromotive force (emf) as in the wound rotor type and squirrel cage type induction machines. In the permanent magnet rotor type, the rotor field is generated by the PMs. In both wound rotor type and PM rotor type machines, the torque is produced by the interaction of the stator and rotor fields. The reluctance rotor doesn't contain windings or permanent magnets as in the switched reluctance and the synchronous reluctance machines. In this type of machines, the torque is generated by the tendency of the rotor to move to the minimum reluctance position.

Each rotor type provides certain performance in terms of efficiency, torque density, torque ripples and each has its own cost determined by the availability of the driving converter, the usage of rare earth materials and the complexity of manufacturing. The choice of the rotor design depends on the application requirements of

cost and performance. For industrial applications, the induction motor with squir-
rel cage rotor is still the dominant one due to its robustness and lack of high cost
PMs. For electric vehicles, the PM machines are the preferable due to their higher
efficiency and torque density [12, 27–29]. In principle, the rotor design doesn't
have a direct influence on the design of the integration topology.

1.5   Semiconductor technology for IMMDs

The most challenging aspect to meet in the design of the IMMDs is the thermal
management of the power converter modules residing in a small space inside the
machine in close proximity to the major heat source of the machine (i.e. the stator)
[30]. The selection of the semiconductor switch technology influences the size of
the power converter module and the heat dissipation of the switches. Therefore,
the power density of the power converter module and the IMMD is influenced by
the semiconductor switch technology.

The three available power switch technologies available in the market up to
date are the Silicon (Si) devices, the Silicon Carbide (SiC) devices and the Gal-
lium Nitride (GaN) devices. The SiC and the GaN devices are both wide bandgap
(WBG) devices. The material properties of these WBG devices make them ex-
cellent choice for the IMMDs given the stringent environment inside the IMMDs.
Table 1.1 lists the important material characteristics of the Si, SiC and GaN mate-
rials [31].

Table 1.1: Semiconductor material properties

Property	Si	SiC	GaN
Bandgap energy (ev)	1.1	3.26	3.45
Electric field strength (kV/cm)	250	2200	3500
Electron mobility (cm^2/V.s)	1500	1000	2000
Hole mobility (cm^2/V.s)	450	140	30
Electron saturated velocity (cm/s)	1×10^7	2×10^7	2.5×10^7
Thermal conductivity (W/cmK)	1.5	3-3.8	2.3

Both SiC and GaN have higher electric field strength than Si which means that
for the same rated voltage, WBG devices can be thinner than Si counterparts which
is a special benefit for the IMMDs given the space limitations for the converter of
IMMDs [32]. Fig. 1.10 shows the package size of two commercial Si and GaN
Mosfets with the same voltage and current ratings. The GaN device provides a
much smaller size compared to the Si device.
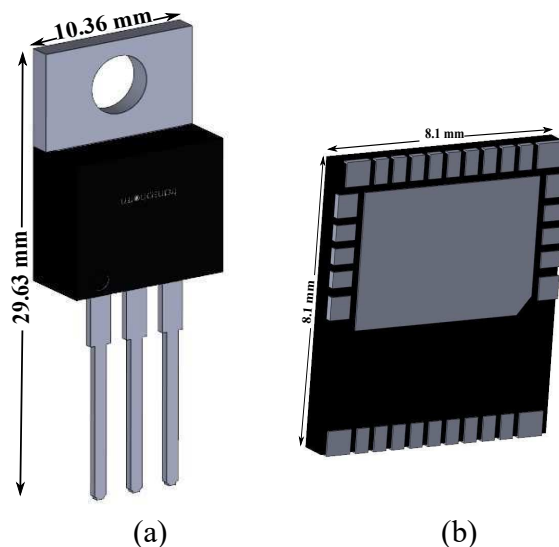
Figure 1.10: package sizes of 600 V, 30 A for (a) Si device (10.36 $\times$ 26.63 mm^2), (b) GaN device (8.1 $\times$ 8.1 mm^2).

The higher bandgap energy of the WBG devices compared to silicon devices means that higher energy is needed to move the electrons from the valence band to the conduction band and hence higher spike energy can be absorbed without breakdown. This means that higher spike energy can be tolerated at higher junction temperature which is an excellent feature for IMMDs due to their high ambient temperature. The higher electric field strength and bangap energy of the WBG devices result in lower leakage currents, and therefore, lower losses and higher converter power density [33].

The high electron saturated velocity of the WBG devices means fast switching speed. This feature enables the operation at high switching frequency with low losses. The operation at high switching frequency results in small size of passive filters and DC-link capacitors [34] which further increases the power density of the IMMD.

SiC has the highest thermal conductivity which means lower junction to case thermal resistance, and hence, the converter can operate at higher ambient temperature for the same switch loss which is an advantage for the IMMDs having high ambient temperatures [35].

The rated junction temperature of the commercially available Si and GaN devices is 150°C while SiC based commercial devices can reach up to 175°C [36]. This higher rated junction temperature of the SiC devices enables the operation at higher ambient temperature for the same junction losses and junction to ambient

thermal resistance which is beneficial for IMMDs.

1.6 Power converters for IMMDs

Power converters for electric machine drives can be classified into two main categories: DC to AC converters and AC to AC converters. The DC to AC converters are classified into two-level and multi-level voltage source converters and current source converters.

1.6.1 Voltage source inverters (VSI)

Both the two-level and the multi-level DC to AC voltage source converters can be constructed using different front-end converter topologies [37]. The front-end converters differ in the number and the rating of the semiconductor devices (i.e. switches and diodes), the number and the size of the magnetic components and the possibility to boost the DC input voltage. Each front-end converter provides certain performance in terms of the EMI generation, the quality of the AC current, the efficiency, the power density and the stability in case of unbalanced input AC voltage [38].

Fig. 1.11 (a), (b) shows the general schematic of the two-level and the multi-level (three-level inverter is shown) voltage source inverter.

The two most important criteria in the selection of the front-end converter for IMMDs are the size of the converter and the efficiency due to the limited space and the high ambient temperature inside the machine. If the quality of the input AC current is not important in the application, the standard diode rectifier with DC-link capacitors would be the smallest and the highest efficiency solution. If the quality of the input AC current is important, the front-end converter with DC-link electronic inductor would be the smallest and the most efficient solution [39].

The two-level voltage source inverter (VSI) is the most commonly used topology due to its relatively simple construction, low number of active devices, the flexibility to apply different control algorithms depending on the application and the availability in the market. The main drawback of this topology compared to the multi-level topologies is the higher output voltage and current distortion.

The multi-level voltage source inverter comprises the following advantages over the two-level topology [40].

- The higher number of output voltage levels results in higher quality output voltage and current waveforms. This results in lower machine losses and a smaller output filter size. This also enables the operation at higher fundamental frequency for a given switching frequency which is an advantage for high speed machines.

- The topology enables the usage of low voltage switches and the operation at lower switching frequency compared to the two-level topology which results

(a)

(b)
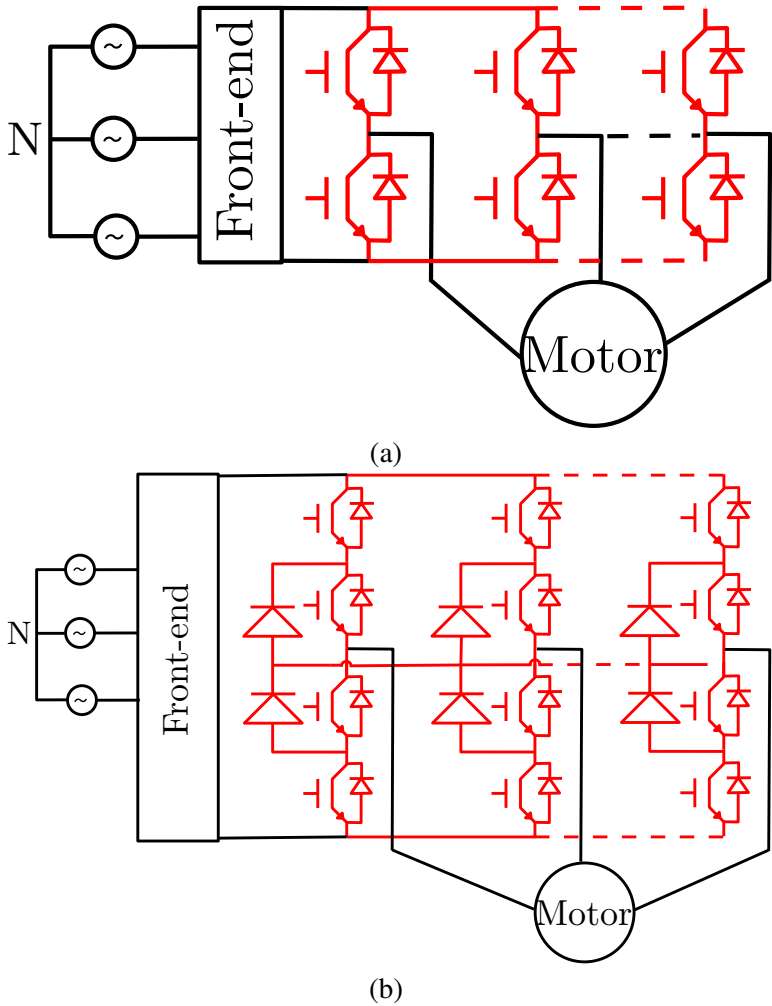
Figure 1.11: Schematic of the DC to AC converters (a) two-level con-
verter, (b) multi-level converter (three level converter).

in lower switching losses and higher efficiency which is a great benefit for
IMMDs.

- The DC-link current stress of multi-level topologies is slightly lower than
  the two-level topology which enables the selection of capacitors with lower
  rated current.

The main drawback of the multi-level voltage source topologies is the increased
number of switches and diodes which leads to higher drive cost and more needed

space.

1.6.2   Current source inverters (CSI)

In the past, the usage of current source inverters (CSI) in electric motor drive applications was avoided due to the higher number of devices (two switches and two diodes per leg), higher losses and the needed bulky DC-link inductor of the current source converters (see Fig. 1.12). But, with the emergence of WBG devices with their small package sizes, lower losses and higher transition speeds, the current source converters can be reconsidered for electric motor drives with the following special benefits for IMMDs [41]:

- With the high switching frequencies of the WBG devices, the size of the DC-link inductor can be significantly reduced replacing the DC-link capacitors of the VSI. The elimination of the DC-link capacitor raises the ambient temperature limit of the IMMD converter module.

- The DC-link inductor limits the shoot-through current in case of fault which enhances the fault tolerance of the drive.

- The output voltage of the CSI is very close to sinusoidal which reduces the motor windings insulation stresses and the windings capacitive currents.
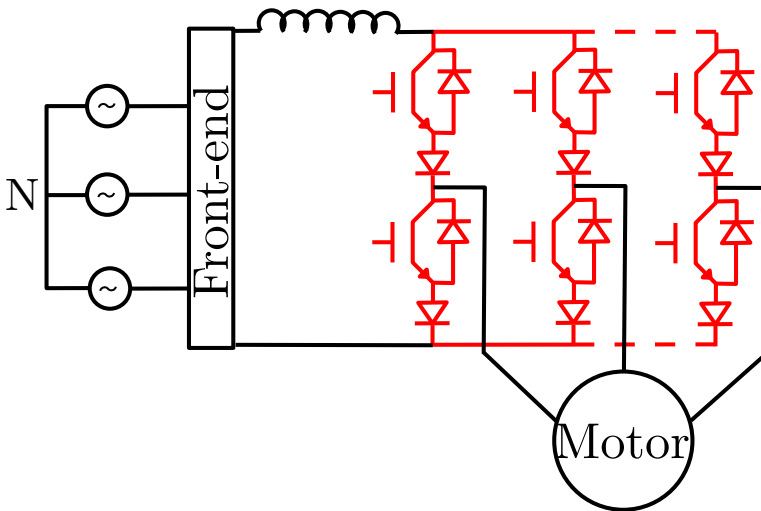
Figure 1.12: Schematic of the current source inverter.

1.6.3 Matrix converters

The most common topology for the AC to AC converters is the matrix converter shown in Fig. 1.13. The matrix converter topology has the following disadvantages compared to the DC to AC topologies:

- The high number of devices (six switches and six diodes per leg) which increases the size of the converter greatly, requires a large space for the converter and the increased cost.

- The limited voltage transfer ratio (0.86).

- The need for custom-made modules due to the uncommon use.
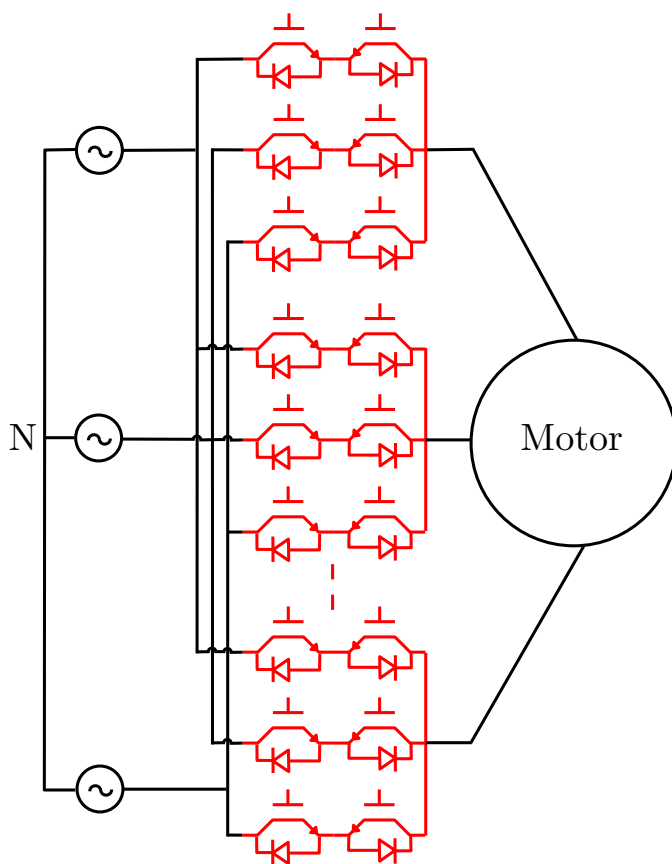
Figure 1.13: Schematic of the matrix converter.

The matrix converters have the following advantages as candidate for the IM-MDs [42]:

- The elimination of the front-end converter with its associated reactive components increases the opportunity of the converter to operate in higher temperature environments as the one inside IMMDs.

- A high quality input current can be obtained which is a great advantage for the power quality.

- The size can be greatly reduced if WBG devices are used with their small package size and low losses resulting in smaller heat-sink requirements.

In case of three-phase or multi-phase stator segmentation (see Fig. 1.4), the most commonly used inverter topology with IMMDs is the two-level voltage source inverter topology either connected in series [43] or in parallel with the input DC source [44]. In case of single inverter per stator coil (see Fig. 1.5), the most commonly used inverter topology is the single phase full bridge inverter [45].

1.7   Control architectures for IMMDs

Two different controller architectures namely hierarchical and heterarchical controllers can be used for IMMDs. The most commonly used architecture is the hierarchical one shown by the block diagram in Fig. 1.14. In this hierarchical controller, only one master controller is carrying out the control of the machine. This centralized controller reads the reference signal for the speed or the torque, the rotor position signal and the phase currents. With this information, it applies the control algorithm and generates the gate signals for the inverter modules. The main drawback of this structure is the system shut down if this centralized controller failed.

In the other heterarchical controller shown in Fig. 1.15, each phase module has a separate controller. If one of these controllers fails, the other controllers continue operating. This controller has a fault tolerant control structure and more suitable for the winding connection in Fig. 1.5.

1.8   Commercially available IMMDs

Many companies are producing integrated motor drives (IMDs) and IMMDs for industrial, traction and wind energy generation [1, 46]. Some of the commercially available integrated drives for different applications are summarized in the following paragraphs.

Integrated drives for industrial applications

ABB is producing a RHM integrated drives in the power range 0.75 to 7.5 kW for driving pumps or fans (see Fig. 1.16). The drive is a combination of an induction motor and a two-level inverter [47].
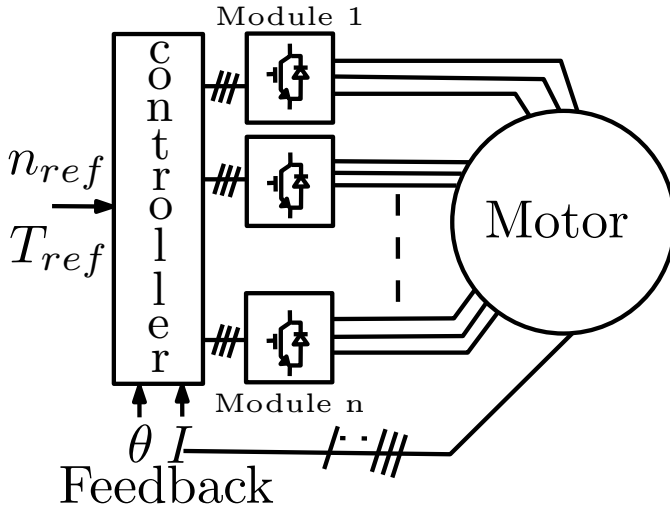
Figure 1.14: Block diagram of the hierarchical control structure.
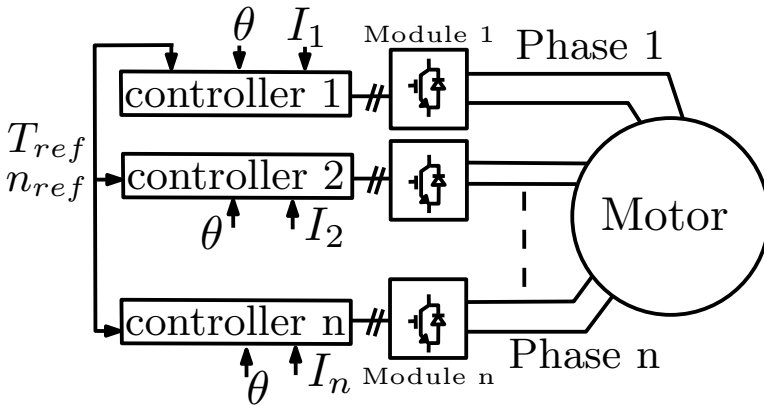
Figure 1.15: Block diagram of the heterarchical control structure.

Siemens (Fig. 1.17 (a)), Danfoss (Fig. 1.17 (b)) and Leroy Somer (Fig. 1.17 (c)) [48, 49] are also producing RHM integrated drives for low-voltage squirrel cage induction motors. In all these drives, the power converter stands in place of the motor terminal box bringing the converter in close proximity to the motor. In these motors, the machine is cooled by a forced ventilator and the converter thermal management is done by a passive heat-sink. The housing acts as a thermal barrier providing thermal isolation between the converter and the machine.

Yaskawa (see Fig. 1.18) is producing a compact 3kW AHM GaN based mo-
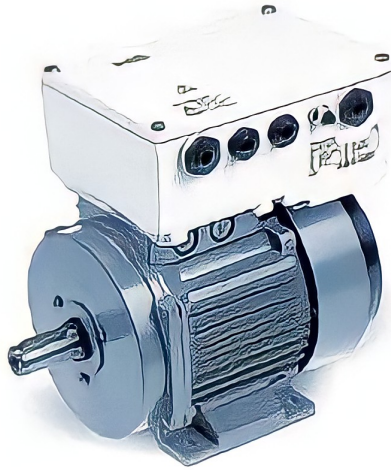
Figure 1.16: ABB RHM integrated drive [47].

| (a) | (b) | (c) |

Figure 1.17: RHM integrated drives of (a) Siemens,(b) Danfoss, (c) Leroy Somer.

tor drive for surface PM machines with smaller losses than the conventional drive system.

Integrated drives for traction applications

Siemens has developed a tightly integrated RHM drive for traction applications (see Fig. 1.19) by inventing a cooling system that creates a water screen between the motor and the inverter for the thermal isolation. Such a strong integration has
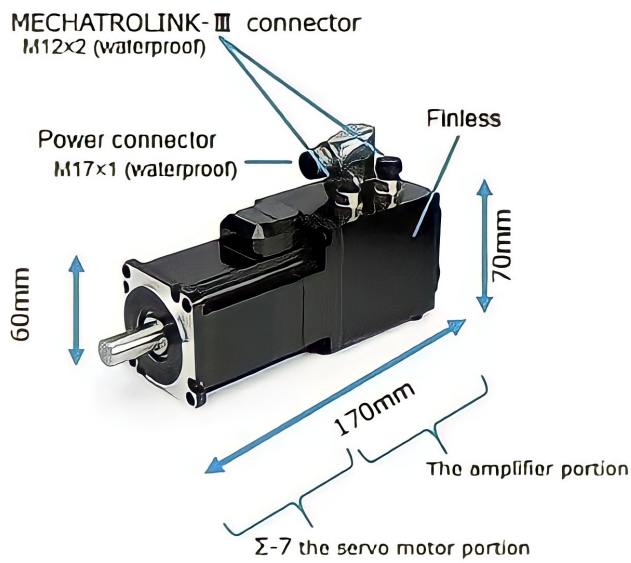
Figure 1.18: Yaskawa AHM integrated drive [50].

resulted in a weight reduction by 10%-15% due to the elimination of the cables and an additional inverter housing [51].
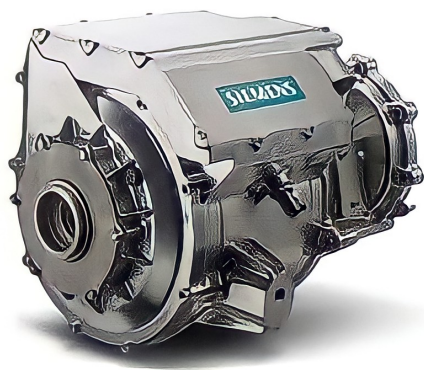
Figure 1.19: Siemens RHM integrated drive for traction applications.

By using SiC devices, Nidec has developed an integrated drive that can operate at a high switching frequency and a high junction temperature with a significantly reduced volume and weight (see Fig. 1.20). The volume and weight of the RHM

integrated drive developed by Nidec are 32% and 69% of the conventional drive system [52].
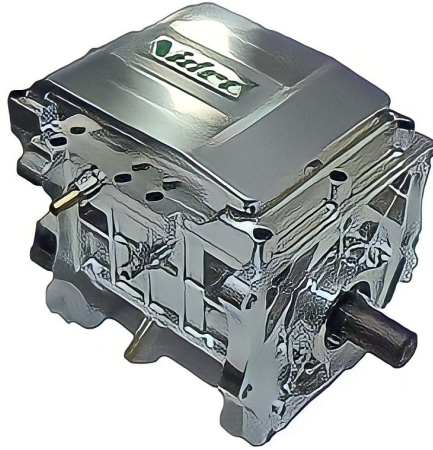
Figure 1.20: Nidec RHM integrated drive for traction applications.

UQM developed an AHM Integrated Electrical Traction System (see Fig. 1.21) [53]. The motor is of the PM type. Both the machine and the inverter are liquid-cooled. This integrated drive has a 30 kW continuous power rating and 75 kW peak power rating with 90 kg weight.
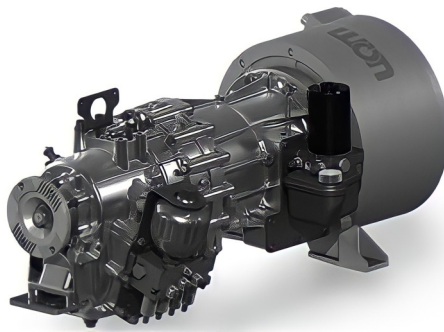
Figure 1.21: UQM AHM integrated drive for traction applications.

Nissan Leaf 2013 has an integrated motor, drive, battery charger and transmission system all together [54]. The motor is a PMSM with peak torque of 254 Nm and peak power of 80 kW. This fully integrated drive has a 30 Kg less weight

compared to the non-fully integrated version.

Protean is producing an integrated electric wheel [55] of 83 kW with modular converter structure. A liquid cooling system is used in the axial and the circumferential path which improves heat evacuation from both the power converter modules and the windings simultaneously. The machine adopted in this in-wheel drive is an outer rotor PMSM with the inverter modules distributed along the machine circumference.

Integrated drives for wind energy generation systems

GE Power Conversion developed an integrated wind energy generation system that consists of a brushless DC PM generator with multiple active rectifier modules distributed around the circumference and integrated with the DC PM generator. The rated power of this system is 450 kW and is suitable for wind energy generation systems [56].

1.9 Selected machines for integration study

Two different integration topologies for two different electric machines are developed and extensively studied in this dissertation. The first machine is the yokeless and segmented armature (YASA) axial flux PM machine. The second is a switched reluctance machine (SRM).

1.9.1 YASA axial flux machine

The construction of the YASA axial flux machine is shown in Fig. 1.22. The stator has a concentrated winding structure with a number of coils. The stator coil shown in Fig. 1.23 (a) consists of a copper winding wound around a laminated core. The stator is sandwiched between two rotor discs. Each rotor disc (see Fig. 1.23 (b)) has surface mounted PMs and ventilation holes distributed around. The torque produced by this machine results from the interaction between the rotating field produced from the stator winding excitation and the PMs field. This torque is called PM torque.

The stator housing of this machine has an outer circular shape with inward radial fins as shown in Fig. 1.24. These fins increase the contact surface area between the stator windings and the housing to increase the rate of heat transfer to the ambient [57, 58].

The YASA axial flux machine has a pancake shape and characterized by its simple construction, high efficiency and power density which gives it a popularity in many applications such as electric vehicles [59–61] and wind energy conversion systems [62].
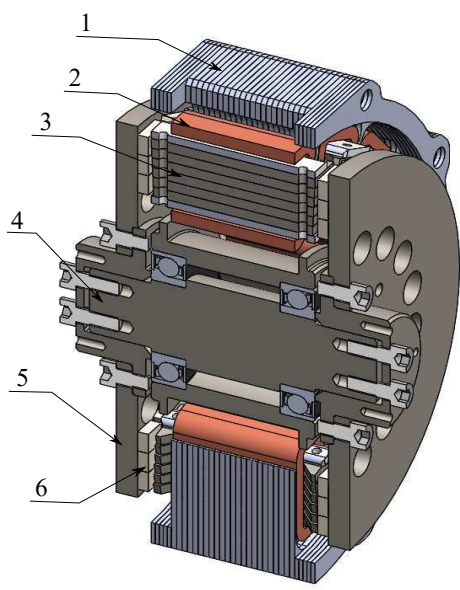
Figure 1.22: Cross-section view of the YASA machine: (1) Housing, (2) Winding, (3) Core, (4) Shaft, (5) Rotor Disc, (6) PMs.

(a)   (b)
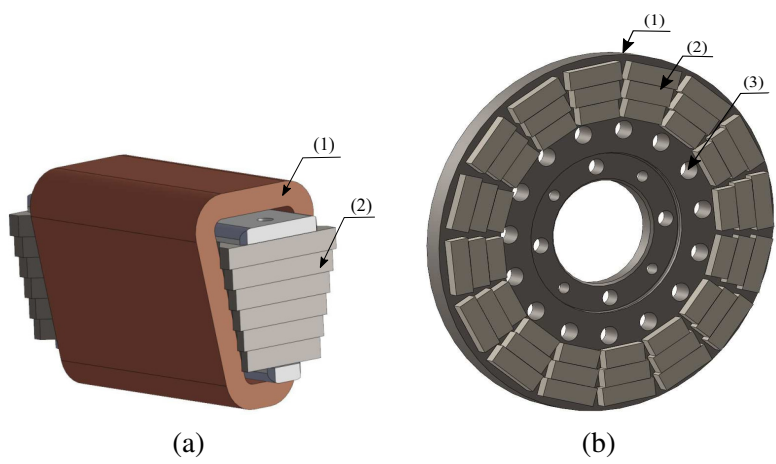
Figure 1.23: The YASA stator and rotor elements (a) stator coil construction: (1) winding, (2) core, (b) rotor construction: (1) rotor back-iron, (2) magnets, (3) ventilation holes.
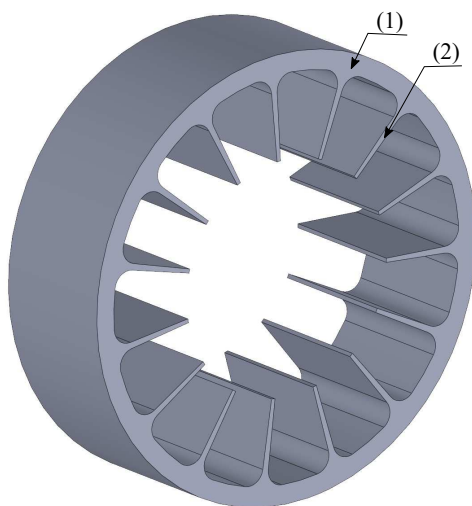
Figure 1.24: The YASA housing construction: (1) outer periphery, (2) fins.

1.9.2 SRM machine

The construction of the SRM machine is shown in Fig. 1.25. The electromagnetic active parts of the stator and the rotor are shown in Fig. 1.26. The stator has a concentrated winding structure. This machine has a double salient structure. The flux is generated in the radial direction by the excitation of the stator coils. The torque is generated by the tendency of the rotor to move to the minimum reluctance position. This torque is called reluctance torque. Due to the absence of the rotor magnets and windings, SRM machines are rugged, have a small construction weight and can operate at high speeds without the high speed problems encountered in PM machines. SRM machines are proposed as competitve candidates in many applications including electric vehicles [63, 64].

1.10 Contribution of the thesis to the state of the art

In the following text, a brief description for the contribution of the thesis to the research area of integrated modular motor drives is given:

- A novel highly modular integration topology with stable mechanical mounting and shared cooling of the electric machine and power converter is designed for a YASA axial flux permanent magnet synchronous machine.

- A novel physical integration topology with flexible retrofitting of the power
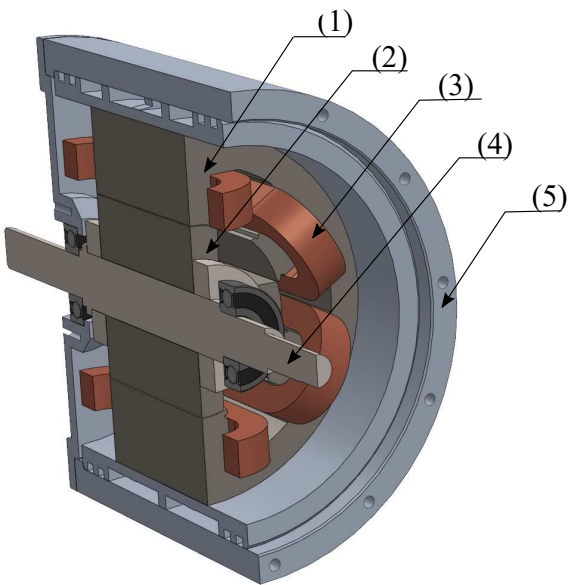
Figure 1.25: SRM construction: (1) stator core, (2) rotor, (3) windings, (4) shaft, (5) housing.
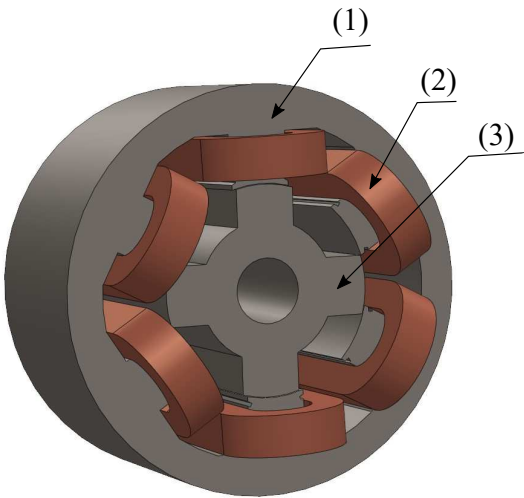
Figure 1.26: SRM machine active parts: (1) stator core, (2) windings, (3) rotor.

converter modules with the electric machine is designed for a switched reluctance machine. In this integration topology, the SRM and the power converter modules are cooled with one cooling circuit.

- A novel DC-link structure that integrates the DC-link busbar and the capacitors with the integrated YASA drive without much increase in the volume of the integrated YASA/converter structure is designed.

- A novel reconfigurable converter topology for the SRM that can configure the SRM machine to operate in the conventional mode and the modular mode is designed. This adds more flexibility in the modular SRM drives and enhances the fault-tolerance of the drive.

- Multiphysics design and optimization methodology for the integrated modular motor drives using finite element method is extensively presented in the thesis. Furthermore, electromagnetic and thermal modelling techniques for the integrated modular motor drives (machine and power converter) using finite element and lumped parameter network methods are elaborated in the thesis.

1.11   Outline of the thesis

The thesis consists of ten chapters. A brief description for each chapter is given in the following:

- **Chapter 1**: In this chapter, a comprehensive review of the integrated modular motor drives (IMMDs) is given. The different types of IMMDs, electric machines for integrated drives, power converters for integrated drives, and power semiconductor technology for integrated drives are discussed in this chapter. Furthermore, different methods of electric drive modularizations and their control structures are discussed in this chapter. The commercial integrated motor drives are also mentioned in this chapter.

- **Chapter 2**: In this chapter, two novel integration topologies designed for a YASA axial flux permanent magnet synchronous machine and a switched reluctance machine (SRM) are introduced. The concepts of mechanical and thermal integration are discussed in this chapter.

- **Chapter 3**: In this chapter, the electromagnetic and thermal models of the YASA machine and the SRM are built. An analytical electromagnetic model for the YASA machine built by former PhD colleagues is described in this chapter. 3D thermal finite element and lumped parameter thermal network (LPTN) models are built and presented in this chapter for the YASA machine. These models are validated by experimental measurements. An electromagnetic finite element model is built and presented in this chapter in

detail for the SRM. Both 3D thermal finite element and lumped parameter thermal network (LPTN) models are built and presented in this chapter for the SRM. Dynamic modelling and torque control of the SRM are also presented in this chapter. This dynamic modelling is needed for the SRM to compute the winding and the power devices currents. These currents are used to excite the windings in the electromagnetic models. They are also used to compute the losses of the power switches and diodes.

- **Chapter 4**: In this chapter, the loss models and the thermal models of the half-bridge inverter module for the YASA machine and the asymmetric H-bridge inverter module are built. Both the instantaneous and the average loss models are presented. The electrical and thermal design of the PCB of the inverter modules are presented in this chapter. An electromagnetic finite element model is built for the PCB to extract its parasitics. The influence of these parasitics on the losses and the temperature of the inverter module is evaluated in this chapter. Steady-state and transient thermal network models are built for the power devices of the inverter modules and presented in this chapter. The parameters of these models are obtained by fitting the thermal impedance curve of the devices and 3D thermal finite element simulations. Both methods are explained in detail in this chapter.

- **Chapter 5**: In this chapter, the design and optimization of the circumscribing polygon and the polygon retrofitted integration topologies introduced in Chapter 2 are provided. The optimization of the inverter module PCB and the cooling structure is discussed in detail in this chapter.

- **Chapter 6**: In this chapter, experimental validations of the modelling and the design of the circumscribing polygon and the polygon retrofitted integration topologies are provided.

- **Chapter 7**: In this chapter, a novel integrated DC-link structure for the YASA machine is designed. This DC-link structure combines the DC-link bus-bar and the capacitors in one structure. An analytical design methodology for the DC-link capacitors is provided in this chapter. Electromagnetic and thermal models are built for the DC-link structure to compute its parasitics, loss density distribution and temperature distribution. This DC-link structure is validated by experimental measurements.

- **Chapter 8**: In this chapter, the power density of the integrated YASA drive is calculated and several design optimization techniques are provided to boost the power density of the initial design. The power density is doubled using the proposed techniques in this chapter.

- **Chapter 9**: In this chapter, a novel reconfigurable converter topology for the SRM is discussed. Using this converter topology, the SRM can be configured to operate in conventional and modular mode. The conventional mode

of operation is preferable in low speed healthy operation as it results in better drive performance. Modular mode of operation is used in high speed operation and in faulty operation. The performance of this converter is validated in conventional mode, modular mode and in case of fault by experimental measurements.

- **Chapter 10**: In this chapter, the conclusions of the research conducted in this thesis are provided with some suggestions for future research in IMMDs.

1.12 Scientific Publications

1.12.1 Journal Papers

In the following, a list of the journal papers published in peer-reviewed international journals is given.

- Abdalla Hussein Mohamed, Hendrik Vansompel and Peter Sergeant,"An Integrated Modular Motor Drive With Shared Cooling for Axial Flux Motor Drives," *IEEE Transactions on Industrial Electronics*, vol. 68, no. 11, pp. $10467-10476$, 2020.

- Abdalla Hussein Mohamed, Hendrik Vansompel and Peter Sergeant,"Electrothermal Design of a Discrete GaN Based Converter for Integrated Modular Motor Drives," *IEEE Journal of Emerging and Selected Topics in Power Electronics*, 2021.

- Abdalla Hussein Mohamed, Hendrik Vansompel and Peter Sergeant,"Design of an Integrated DC-Link Structure for Reconfigurable Integrated Modular Motor Drives," *IEEE Transactions on Industrial Electronics*, 2021.

- Abdalla Hussein Mohamed, Ahmed Hemeida, Alireza Rasekh, Hendrik Vansompel , Antero Arkkio and Peter Sergeant,"A 3D Dynamic Lumped Parameter Thermal Network of Air-Cooled YASA Axial Flux Permanent Magnet Synchronous Machine," *Energies*, vol. 68, no. 11, 2018.

- Abdalla Hussein Mohamed, Ahmed Hemeida, Hendrik Vansompel, and Peter Sergeant,"Parametric Studies for Combined Convective and Conductive Heat Transfer for YASA Axial Flux Permanent Magnet Synchronous Machines," *Energies*, vol. 11, no. 4, 2018.

In the following, a list of the journal papers submitted to peer-reviewed international journals and still under review is given.

- Abdalla Hussein Mohamed, Hendrik Vansompel and Peter Sergeant,"Power Density Boosting Techniques for Reconfigurable Integrated Modular Motor Drives," *IEEE Transactions on Energy Conversion*.

- <u>Abdalla Hussein Mohamed</u>, Hendrik Vansompel and Peter Sergeant, "Reconfigurable Modular Fault-Tolerant Converter Topology for Switched Reluctance Motors," *IEEE Journal of Emerging and Selected Topics in Power Electronics*.

- <u>Abdalla Hussein Mohamed</u>, Hendrik Vansompel and Peter Sergeant,"Polygon Retrofitted Integrated Modular Motor drive for Switched Reluctance Machines," *IEEE Transactions on Industrial Electronics*.

In the following, a list of the co-authored journal papers published in peer-reviewed international journals is given.

- Bishal Silwal, <u>Abdalla Hussein Mohamed</u>, Jasper Nonneman, Michel De Paepe and Peter Sergeant,"Assessment of Different Cooling Techniques for Reduced Mechanical Stress in the Windings of Electrical Machines," *Energies*, vol. 12, no. 10, 2019.

- Haitao Sun, Ali Farzan Moghaddam, <u>Abdalla Hussein Mohamed</u>, Mohamed Nabil Ibrahim, Peter Sergeant, Alex Van den Bossche,"Controlling a Switched Reluctance Motor with a Conventional Three-Phase Bridge Instead of Asymmetric H-Bridges," *Energies*, vol. 11, no. 12, 2018.

1.12.2   Conference Papers

In the following, a list of the papers published in Proceedings of international conferences is given.

- <u>Abdalla Hussein Mohamed</u>, Hendrik Vansompel and Peter Sergeant,"Design of a circumscribing polygon wide bandgap based integrated modular motor drive topology with thermally decoupled windings and power converters," *2020 22nd European Conference on Power Electronics and Applications (EPE'20 ECCE Europe)*, Lyon, France, 2020, pp. 1−9.

- <u>Abdalla Hussein Mohamed</u>, Hendrik Vansompel and Peter Sergeant,"A Generic DC link Capacitor Sizing Methodology for Multi-phase Wide Bandgap Based Integrated Modular Motor Drives," *2020 IEEE International Conference on Environment and Electrical Engineering and 2020 IEEE Industrial and Commercial Power Systems Europe (EEEIC / ICPS Europe)*, Madrid, Spain, 2020, pp. 1−6.

- <u>Abdalla Hussein Mohamed</u>, Hendrik Vansompel, Ahmed Hemeida and Peter Sergeant,"Wide Bandgap Based Modular Driving Techniques for Switched Reluctance Motor Drives," *IECON 2020 The 46th Annual Conference of the IEEE Industrial Electronics Society*, Singapore, 2020, pp. 1−6.

- <u>Abdalla Hussein Mohamed</u>, Hendrik Vansompel and Peter Sergeant,"An Integrated Motor Drive with Enhanced Power Density Using Modular Converter Structure," *2021 IEEE International Electric Machines Drives Conference (IEMDC)*, Hartford, CT, USA, 2021, pp. 1−6.

- <u>Abdalla Hussein Mohamed</u>, Hendrik Vansompel, Ahmed Hemeida and Peter Sergeant,"Transient lumped parameter thermal model based loadability studies for the YASA axial flux permanent magnet synchronous machines," *Young Researchers Symposium 2018 (YRS)*, Brussels, Belgium, 2018, pp. 1−6.

In the following, a list of the co-authored papers published in Proceedings of international conferences is given.

- Mohamed N Ibrahim, Jasper Nonneman, <u>Abdalla Hussein Mohamed</u>, Andries Daem, Ahmed AE Abdallh, Stephan Schlimpert, Michel De Paepe and Peter Sergeant,"Directly Cooled Windings in Switched Reluctance Machines ," *2020 International Conference on Electrical Machines (ICEM)*, Gothenburg, Sweden, 2020, pp. 1−7.

- Haitao Sun, Ali Farzan Moghaddam, Mohannad Jabbar Mnati, <u>Abdalla Hussein Mohamed</u>, Mohamed Nabil Ibrahim, Peter Sergeant, Alex Van den Bossche,"A Control Method with Ring Structure for Switched Reluctance Motor ," *2018 IEEE International Conference on Electrical Systems for Aircraft, Railway, Ship Propulsion and Road Vehicles International Transportation Electrification Conference (ESARS-ITEC)*, Nottingham, UK, 2018, pp. 1−5.

Chapter 2

Circumscribing Polygon and Polygon Retrofitted Integration Concepts

2.1 Introduction

In this chapter, two novel integrated modular motor drive topologies are introduced. The first one is called the circumscribing polygon (CP) integration topology. This CP integration topology is applied on a YASA axial flux permanent magnet synchronous machine. The second one is called polygon retrofitted (PR) integration topology. This PR integration topology is applied on a switched reluctance machine. In both topologies a flat surface for mounting the inverter modules is created (mechanical integration) and a technique for decoupling the heat dissipated by the inverter modules and the electrical machine is designed (thermal integration).

2.2 Mechanical Design of the CP Integration Topology for the YASA machine

Fig. 2.1 shows the construction of the non-integrated YASA machine. The stator consists of a number of coils of the concentrated winding type, where each coil consists of a concentrated copper winding wound around a silicon steel core. All the coils are arranged circumferentially, impregnated with epoxy resin and casted to form the active part of the stator. An aluminum housing is enclosing the stator to evacuate the heat generated by the stator to the ambient [58]. The rotor has two discs with surface mounted permanent magnets (PMs). The key parameters of the non-integrated YASA machine are listed in Table 2.1.

Fig. 2.2 shows the geometry of the housing lamination of the non-integrated YASA machine. It has a circular outer periphery with inward fins in contact with
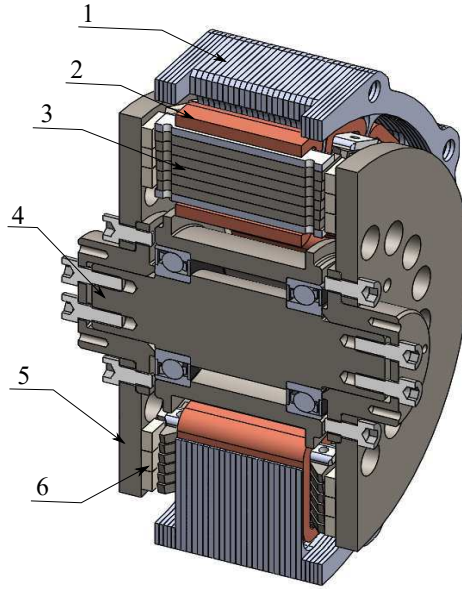
Figure 2.1: Cross-section view of the non-integrated YASA machine: (1) Housing, (2) Winding, (3) Core, (4) Shaft, (5) Rotor Disc, (6) PMs.

Table 2.1: The key parameters of the non-integrated YASA machine

Quantity	Symbol	Value
# Pole pairs	p_r	8
# Slots	n_s	15
Axial length (housing) (mm)	L_{ax}	60
Outer diameter (housing) (mm)	D_{out}	190

the stator windings for more effective heat transfer to the ambient.

In order to utilize the same housing for cooling both the stator modules and the power converter modules, two main modifications should be done to the housing. The first one is to introduce a flat surface on the housing to mechanically mount the power converter modules (mechanical reason) and to have a good contact between the switch thermal pad and the housing (thermal reason). The second one is to thermally decouple the stator modules and the power converter modules.
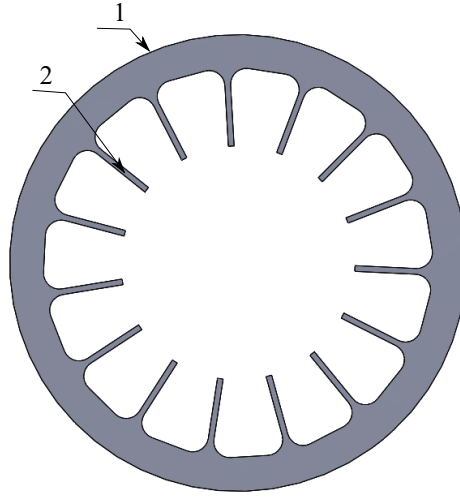
Figure 2.2: The geometry of the housing lamination of the non-integrated YASA machine: (1) Outer circular periphery, (2) Stator heat extraction fins.

A flat surface can be created for mounting the power converter modules by replacing the outer circular cross section of the non-integrated housing by its circumscribing polygon as shown in Fig. 2.3. The new housing geometry becomes as shown in Fig. 2.4. For the decoupling of the heat generated by the stator of the YASA machine and the power converter modules, an axial channel is introduced between the power converter flat mounting surface and the YASA machine stator module. A cooling fluid can be pumped in this channel to decouple and evacuate the heat of the power converter modules and the stator of the YASA machine. The final new shared cooling structure lamination with flat surface for mounting the power converter modules and the heat decoupling cooling channel is shown in Fig. 2.5.

The 3D geometry of the non-integrated housing and the shared cooling structure for integrating the power converter and the YASA machine is shown in Fig. 2.6 (a) and (b) respectively. The flat surface for mounting the power converter module has in the axial direction the same length as the non-integrated housing L_{ax} and the other dimension in the circumferential direction with the length (L_{cir}). The length L_{cir} depends on the number of the stator modules (n_s) and the diameter of the inscribed circle which is the outer diameter of the non-integrated housing (D_{out}). L_{cir} can be calculated from (2.1). For the 15 stator modules, 190 mm outer housing diameter non-integrated YASA machine, the dimensions of the flat surface per module are 60×40 mm^2.

$$L_{cir} = D_{out} \tan(\frac{180°}{n_s}) \tag{2.1}$$
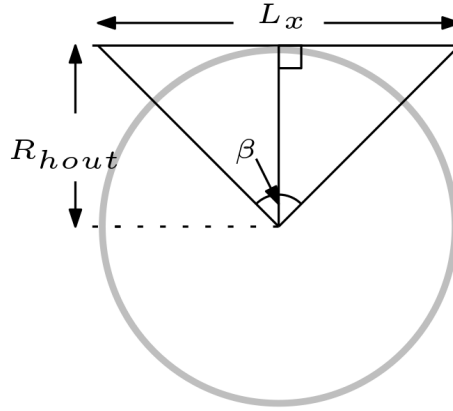
Figure 2.3: Illustration of the replacement of the outer circular cross section of the non-integrated housing by its circumscribing polygon.
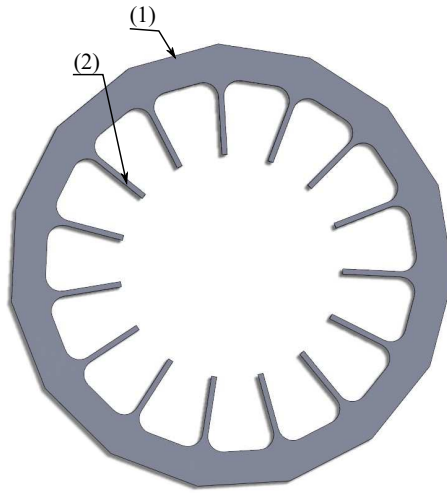
Figure 2.4: Illustration of the resulted flat surface for mounting the power converter modules: (1) Flat surface , (2) Stator heat extraction fins.

The final integrated YASA machine is shown in Fig 2.7 with the printed circuit boards (PCBs) of the converter modules indicated. This circumscribing polygon integration topology has the following advantages:

- The full integrated drive can be synthesized from several identical pole drive units combining the machine stator parts, their associated driving converter and a shared cooling for both of them. In that way, the manufacturing process can be greatly simplified and a fully modular drive approach can be achieved.
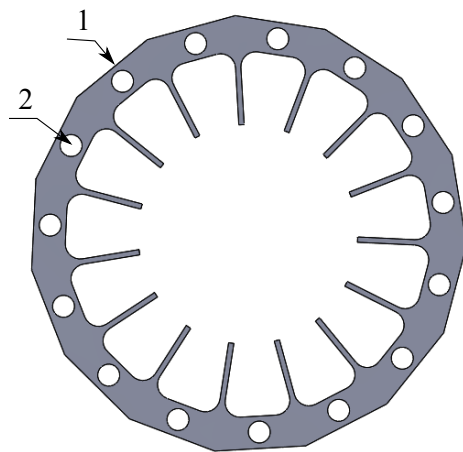
Figure 2.5: The new shared cooling structure lamination with flat surface for power converter module mounting and a decoupling cooling channel: (1) Flat surface for mounting the half-bridge modules, (2) Cooling channel.
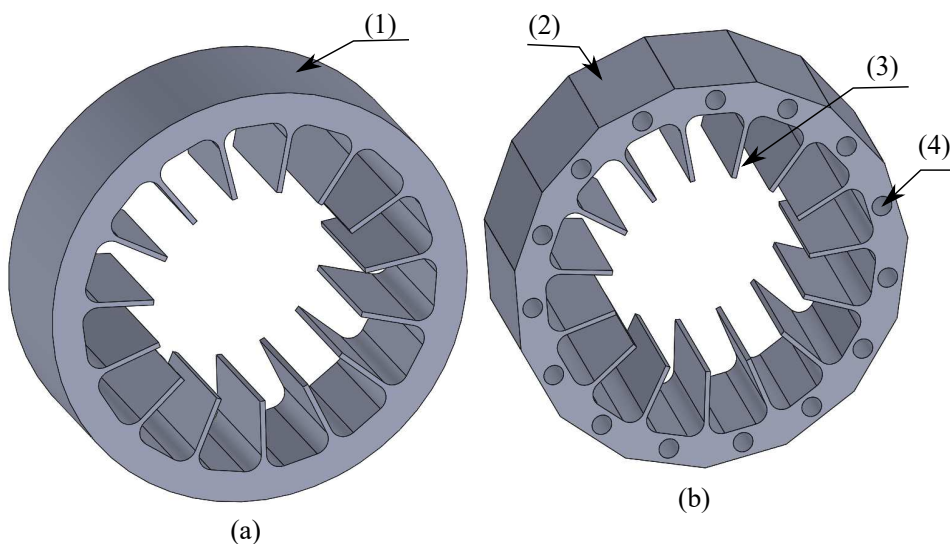
Figure 2.6: The 3D geometry of the non-integrated housing and the integrated shared cooling structure: (a) housing of the non-integrated machine, (b) integrated shared cooling structure, (1) cylindrical housing, (2) converter mounting surface, (3) radially inward stator heat extraction fins, (4) cooling channel.

- Only one cooling circuit is used to evacuate the heat generated by the power

converter modules and the stator modules which simplifies the structure of the cooling system and reduces the weight of the integrated drive.

- Small increase in the outer diameter of the integrated drive compared to the non-integrated one resulting from the thickness of the power converter module PCB and the components.

- Flexibility in the stator phase configuration. Each stator coil can be driven by one inverter module or alternatively a number of stator coils can be connected together to form one phase to be driven by one inverter module.
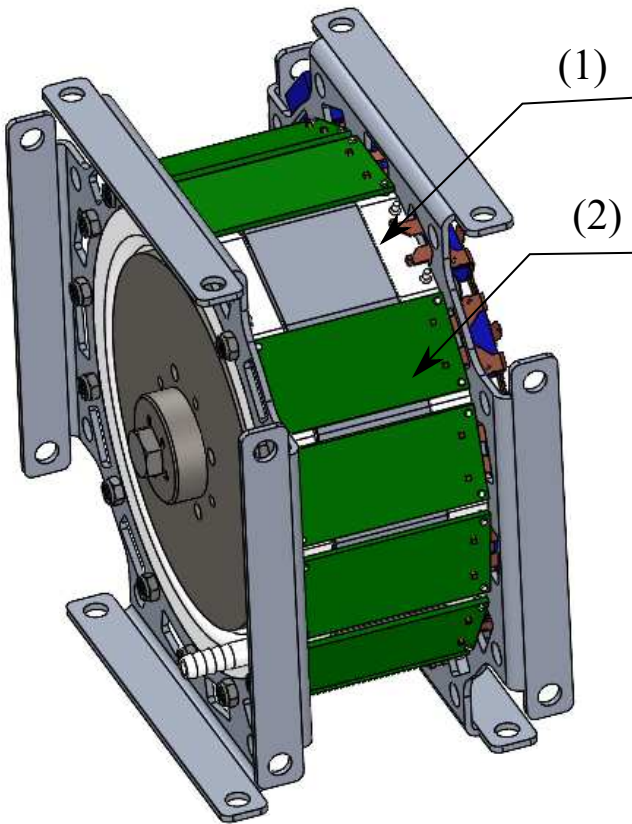
Figure 2.7: The CP integrated YASA machine with the converter PCB on top: (1) The polygon shared cooling structure, (2) Converter module PCB.

2.3 Mechanical Design of the PR Integration Topology for the SRM

Fig. 2.8 shows the construction of the non-integrated 6/4 SRM considered for the study. This machine has a doubly salient construction. The stator consists of six coils of concentrated winding type. The stator core has a pole-yoke construction with the coils wound around the poles. Axially extended end-winding inserts are added to the stator to increase the contact surface area between the end-windings and the ambient [65]. The rotor has a pole-yoke construction without windings or permanent magnets. The key geometrical parameters of the case study SRM are given in Table 2.2.
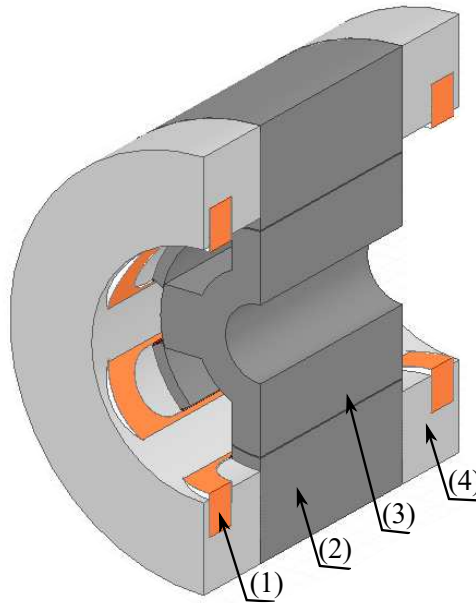
Figure 2.8: The construction of the 6/4 SRM case study: (1) stator coil, (2) stator core, (3) rotor core, (4) end-winding cooling insert.

For the integration of the power converter modules with the SRM, a mounting surface for the power converter modules and a shared cooling circuit for the power switches and the SRM should be created. To do so, the 3D part shown in Fig. 2.9 is proposed to be retrofitted around the stator outer surface. This part has an inner circular cross section and an outer hexagon cross section in the radial direction. The outer cross section can be a polygon with any number of sides depending on the number of the power converter modules. For the 6/4 SRM case study, a hexagon is considered for a fully modular driving of the stator windings with one converter module driving one stator coil [13].

The power converter modules are mounted on the flat outer surface of the 3D

Table 2.2: The key parameters of the 6/4 SRM case study

Parameter	Symbol	Value
stator outer diameter (mm)	D_{so}	100
stator yoke thickness (mm)	Y_{st}	9
rotor outer diameter (mm)	D_{ro}	51.5
rotor yoke thickness (mm)	Y_{rt}	7.75
airgap length (mm)	g	0.25
axial length (active) (mm)	L_{ax}	50
water jacket axial length (mm)	L_{awj}	90
water jacket outer diameter (mm)	D_{wj}	130
number of turns/coil	N_t	168
coil resistance $\vert_{25°C}$ (Ω)	R_{coil}	1.8
steel grade	-	NO20

part and the inner surface is press fitted with the SRM stator. By doing so, the stator heat flux flows radially outward and the power switches heat flux flows radially inward. These two heat fluxes should be decoupled. For doing so, a water jacket is fitted between the SRM stator and the 3D part. Fig. 2.10 shows the proposed polygon retrofitted integration topology for the SRM.

The axial length of the 3D part is equal to the axial length of the water jacket (L_{awj}). The length of the polygon side (L_{ps}) depends on the maximum tolerable increase (ΔR) in the outer radius above the water jacket outer radius ($\frac{D_{wj}}{2}$), the water jacket outer radius and the number of the polygon sides (n_p). L_{ps} can be calculated from (2.2). ΔR is considered to be 4 mm. Since the SRM converter modules will be mounted on the outer surface of the 3D part, the size of the PCB of each converter module should be 100×75 mm^2.

$$L_{ps} = 2 \times \left(\frac{D_{wj}}{2} + \Delta R \right) \times \tan \frac{180°}{n_p} \qquad (2.2)$$

The polygon retrofitted integration topology has the following advantages:

- Easy fitting of the power converter modules with the SRM and easy installation and maintenance.
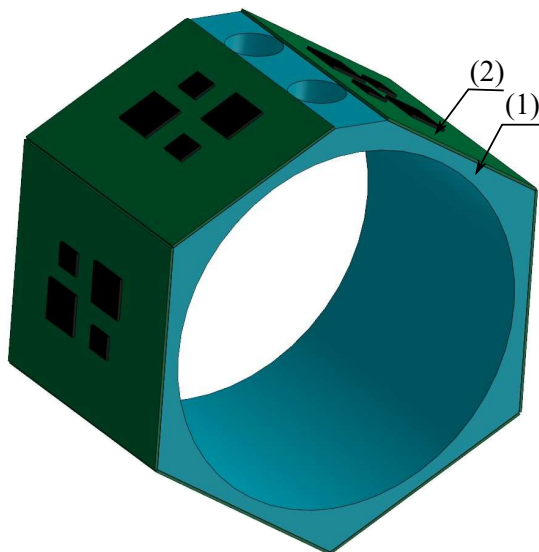
Figure 2.9: The proposed 3D part to be retrofitted with the SRM: (1) 3D part, (2) power converter module.
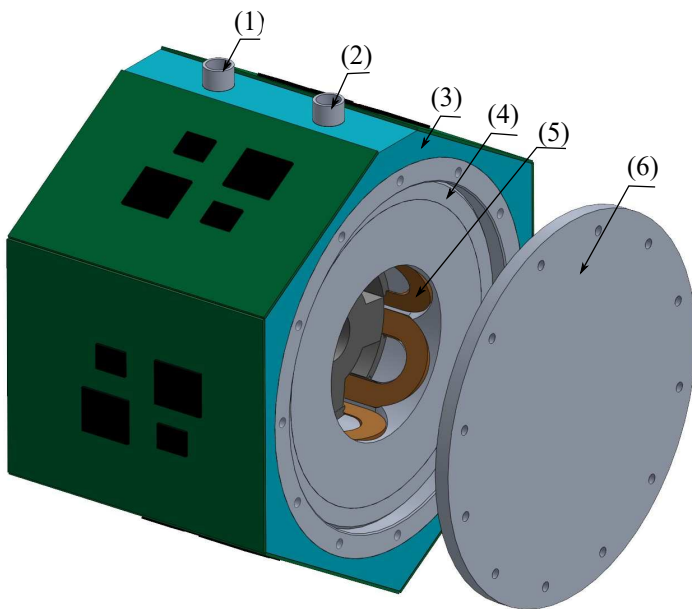

Figure 2.10: The proposed polygon retrofitted integrated SRM drive: (1) water inlet, (2) water outlet, (3) proposed 3D part, (4) water jacket, (5) the SRM, (6) end-plate.

- Only one cooling system is utilized for both the SRM and the power converter modules.

- No increase in the axial length of the non-integrated machine. Only small increase in the outer diameter of the machine.

2.4   Conclusion

Two novel physical integration topologies are introduced in this chapter. The first one is called circumscribing polygon integration topology in which the radial circular cross section of the normal cylindrical housing is replaced by its circumscribing polygon. The result is a new housing with an inner cylindrical surface in contact with the stator of the machine and an outer flat surface for mounting the power converter modules. The heat generated by the machine flows radially outward and the heat generated with the converter module flows radially inward. To decouple and evacuate the heat generated by the machine and the power converter, a cooling channel is introduced in the redesigned housing between both of them. This circumscribing polygon integration concept is applied on a yokeless and segmented armature axial flux permanent magnet synchronous machine.

The introduced circumscribing polygon integration topology is highly modular in the sense that the full drive can be synthesized from the separate modules comprising the stator coil, the driving power converter module and the cooling system for both the machine and the converter module.

The second introduced integration topology is called polygon retrofitted integration topology. In this topology, a 3D part with an outer flat surface and an inner circular section is designed. The inverter modules are mounted on the outer flat surface and the electrical machine is fitted in the inner cylinder. A cooling water jacket is fitted between the electrical machine and the 3D part to decouple the heat dissipated by the inverter modules and the electrical machine. The polygon retrofitted integration concept is applied on a switched reluctance machine.

The polygon retrofitted integration topology eliminates the need for a separate cooling for the inverter modules which reduces its size and weight. It also reduces the distance between the inverter terminals and the electrical machine terminals which reduces the length of the connecting cables. It is easy to assemble and disassemble the 3D part with the inverter modules for replacement or maintenance.

Chapter 3

Modelling of Modular Electric Machines

3.1 Introduction

Due to the close proximity of the power converter and the electric machine in integrated modular motor drives, conducting thermal studies is crucial to ensure proper operation of the power converter and the electric machine [15]. So, thermal modelling of the electric machine and the power converter is required to compute the temperature field in the machine and the power switches.

Two methods of thermal modelling can be applied to find the temperature distribution of the machine and the power converter. These methods are the finite element (FE) method and the lumped parameter thermal network (LPTN) [66]-[67]- [68]- [69]- [70]. In both modelling methods, the geometry is divided into small elements and an approximate solution of the heat conduction equation is found. The number of elements in the FE modelling is much more than the number of elements considered by the LPTN. The computational burden of the FE model is much higher than the LPTN but the solution accuracy of the FE model is better than the LPTN one.

The temperature rise of the machine components and the power switches is caused by the power losses in the machine and power switches. These power losses are the heat source input in the thermal model. In the electric machine, these losses take place in the windings and the core. The computation of the power losses in the windings can be calculated from the current waveform, the winding resistance and the material of the windings. The core loss computation requires the knowledge of the magnetic flux density waveform in the different parts of the machine. The core loss depends on the magnetic characteristics of the core material, the peak flux density, the rate of change of the flux density and the local slope reversal of the flux density waveform [71]. The core flux density waveform is computed from electromagnetic models. So, electromagnetic models are required for the

computation of the heat sources in the machine.

In this chapter, the electromagnetic and the thermal modelling of the two machines studied for integration namely the YASA axial flux machine and the SRM are discussed.

3.2 Electromagnetic modelling of the YASA AFPMSM

The objective of the electromagnetic modelling of the YASA AFPMSM is to compute the flux density distribution in the airgap, the stator core and the rotor permanent magnets (PMs). From the flux density distribution, all electromagnetic quantities which include the developed torque, the induced voltage of the windings, the core losses and the PM losses can be calculated [72]. Two types of electromagnetic models are developed for this machine: a FE model and a combined magnetic equivalent circuit (MEC)-analytical model.

The electromagnetic FE models of the YASA machine can be 3D or multi-layer 2D [73]. The 3D FE models are the most accurate and the most time consuming models. The analytical models are less accurate but less time consuming models. The combined MEC and analytical model presented in [72] is used for the electromagnetic computations of the YASA AFPMSM in this thesis. This model solves Maxwell's equations in the airgap of the YASA AFPMSM to obtain the flux density distribution in the airgap and then it applies the computed airgap flux to a MEC model of the stator core to compute the flux density distribution in the stator core. More details about this model can be found in [74].

From the stator flux density distribution, the stator core losses are computed using the loss separation method introduced in [75]. This method classifies the core loss into a hysteresis loss (P_{hy}), a classical loss (P_{cl}) and excess loss (P_{ex}). The total core loss is the summation of the three loss components. The hysteresis loss depends on the peak flux density of the core, the fundamental frequency of the flux density and the core material hysteresis loss coefficients. The hysteresis loss can be computed from (3.1).

$$P_{hy} = K_{Fe1}B_p{}^{K_{Fe2}}f \times \rho_c V_c \qquad (3.1)$$

where K_{Fe1}, K_{Fe2} are the hysteresis loss coefficients of the core material, B_p is the peak flux density, f is the fundamental frequency of the flux density, ρ_c is the mass density of the core and V_c is the volume of the core.

The classical loss component depends on the rate of change of the flux density and the core material classical loss coefficient. The classical loss component is computed from (3.2).

$$P_{cl} = \frac{1}{T} \int_0^T K_{Fe3} \left(\frac{dB(t)}{dt} \right)^2 dt \times \rho_c V_c \qquad (3.2)$$

where K_{Fe3} is the classical loss coefficient of the core material, $B(t)$ is the instantaneous flux density of the core, T is the fundamental period of the flux density waveform.

The excess loss component depends on the rate of change of the flux density and the core material excess loss coefficient. The excess loss component is computed from (3.3).

$$P_{ex} = \frac{1}{T} \int_0^T K_{Fe4} \left(\sqrt{1 + K_{Fe5} \left| \frac{dB(t)}{dt} \right|} - 1 \right) \left| \frac{dB}{dt} \right| dt \times \rho_c V_c \qquad (3.3)$$

where K_{Fe4}, K_{Fe5} are the excess loss coefficients of the core material

The stator core material used with the YASA AFPMSM is the M100-23P with the B-H curve shown in Fig. 3.1 and the core loss parameters in Table 3.1.
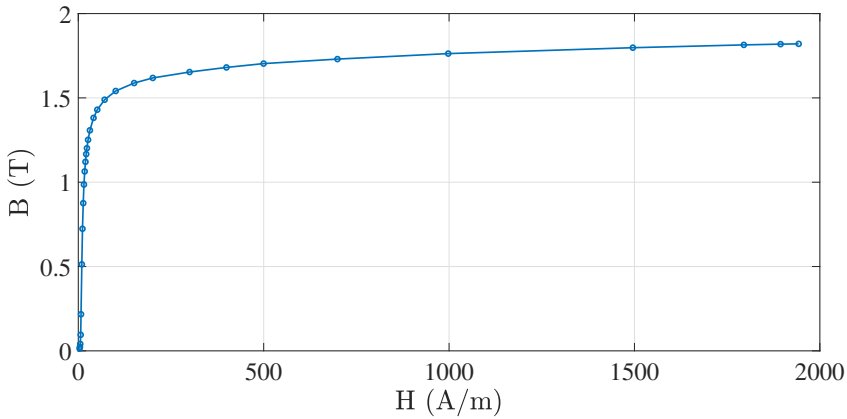
Figure 3.1: The B-H curve of the M100-23P used for the core of the YASA AFPMSM.

The losses in the rotor PMs are calculated using the analytical method presented in [76]. In this method, each PM is segmented to a number of slices in the axial direction. Each slice is modelled by a network of resistances and inductances. Maxwell's equations are solved to obtain the flux enclosing the PMs. From this flux, the PM induced voltage is computed. From the induced voltage and the electric network of each PM, the induced magnet current is calculated. The PM loss in each slice is computed from (3.4). The total PM loss is computed by summing the losses of the slices. Neodymium-Iron-Boron (Nd-Fe-B) magnets are used with the YASA machine for its excellent magnetic properties.

$$P_{pms} = \frac{\Delta Y_m}{\sigma_{pm}} \int_{S_{pm}} J_{ns}^2 dS_{pm} \qquad (3.4)$$

Table 3.1: The loss parameters of the M100-23P used in the core of
the YASA AFPMSM

Parameter	Value
K_{Fe1}	0.0074
K_{Fe2}	2.0000
K_{Fe3}	1.026860×10^{-6}
K_{Fe4}	1.407179×10^{-2}
K_{Fe5}	8.358120×10^{-5}
ρ_c (kg/m^3)	7650

where ΔY_m is the thickness of the PM slice, σ_{pm} is the electrical conductivity of
the PM, S_{pm} is the PM area penetrated by the magnetic flux and J_{ns} is the current
density of the PM induced current.

3.3   Fundamentals of thermal modelling of electric machines

Thermal modelling of electric machines is performed to compute the temperature
of the stator and the rotor components to ensure safe thermal operation of these
components in the full torque-speed range of the machine [77]. The temperature
of the windings should be limited to the rated winding insulation temperature.
The rated winding insulation temperature is specified by the winding insulation
class [69]. The insulation class of the windings can be A, B, F or H with the rated
temperature values listed in Table 3.2 [69]. If the temperature of the windings ex-
ceeded the rated insulation class value, an insulation breakdown will occur causing
an inter-turn short circuit.

Table 3.2: The rated temperature of the windings insulation classes

Insulation class	Rated temperature (°C)
A	105
B	130
F	155
H	180

The performance of the rotor PMs is influenced by the temperature. Both the remanent induction and the coercivity of the PM decreases with the temperature. Depending on the temperature level of the PM, three mechanisms of magnetization loss can occur. These magnetization loss mechanisms are [78]:

- A reversible loss of magnetization where the PM loses part of its magnetization at temperatures higher than its normal working temperature and returns back again when it cools down.

- An irreversible but recoverable loss of magnetization which happens when the temperature rise takes the operating point beyond the knee. This loss of magnetization would be recovered by re-magnetizing the magnets. This would cause stop of operation of the electric machine and removal of PMs for re-magnetization.

- An irreversible irrecoverable loss of magnetization which happens at highly elevated temperatures above the maximum working temperature of the PM. This high temperatures causes structural change in the PM. Re-magnetizing the magnet again doesn't bring the PM performance back again.

Depending on the grade of the NdFeB magnet, the maximum working temperature ranges from 80°C to 230°C [79]. The reversible temperature coefficient of the remanent induction of the NdFeB ranges from -0.11%/°C to -0.13%/°C. The reversible temperature coefficient of the coercivity of the NdFeB ranges from -0.55%/°C to -0.65%/°C.

The temperature of the impregnation material that is used to bond the stator components together should stay within an allowable limit. Above this rated temperature, the impregnation material starts to lose its compressive strength and deformation occurs. Depending on the type of the impregnation material, the maximum working temperature ranges from 110°C to 180°C [80]. The impregnation material used with the studied YASA AFPMSM and the SRM in this chapter is Stycast 3050+Catalyst 9. The maximum working temperature of this impregnation material is 130°C [81].

3.3.1 Heat transfer mechanisms

The heat transfer can take place by three different mechanisms, heat transfer by conduction, heat transfer by convection and heat transfer by radiation [82].

Heat transfer by conduction

The rate of heat transfer between two points in the space with different temperature is proportional to the temperature gradient between both of them and the thermal conductivity of the medium through which the heat transfer takes place.

The local heat flux within the medium through which the heat transfer takes place can be described by Fourier's law of heat conduction (3.5) [82].

$$q_c = -k_{th}\nabla T \tag{3.5}$$

where q_c (W/m^2) is the heat flux defined as the rate of heat transfer per unit area, k_{th} (W/mK) is the thermal conductivity of the medium and ∇T (K/m) is the temperature gradient.

Heat transfer by convection

The heat transfer by convection takes place between a surface and a moving fluid in contact with that surface [82]. The heat transfer by convection can be natural or forced. In the natural convection, the fluid layers with high temperature move up and the colder layers replace them. This natural fluid motion results from the difference in the fluid mass density between the different fluid layers with different temperatures. The force that results between the fluid layers is called buoyancy force. In the forced convection, the fluid motion results from an external force exerted on the fluid by means of a fan or a pump.

The rate of heat transfer by convection between the surface and the fluid is proportional to the surface area, the temperature difference between the surface and the fluid and the convection coefficient of the surface. The relation between the rate of heat transfer by convection, the temperature difference between the surface and the fluid, the surface area and the convection coefficient is described by Newton's law (3.6).

$$Q_{conv} = h_c A_s (T_s - T_f) \tag{3.6}$$

where Q_{conv} (W) is the rate of heat transfer by convection, h_c (W/m^{2}K) is the convection coefficient of the surface, T_s is the surface temperature and T_f is the fluid temperature.

The convection coefficient depends on the fluid properties (the dynamic viscosity, the thermal conductivity, the mass density and the specific heat capacity) as well as the fluid velocity [83]. It also depends on the geometry and the roughness of the surface, in addition to the type of fluid flow (laminar or turbulent). The convection coefficient is determined by computational fluid dynamics (CFD) simulations [84].

Heat transfer by radiation

Heat transfer by radiation takes place in a form of electromagnetic waves. As the object heats up, the molecules gain energy and vibrate more resulting in electric charge acceleration and electromagnetic radiation. All bodies at a temperature above absolute zero emit thermal energy. The rate of heat transfer by radiation between a surface and the surrounding depends on the absolute temperature of

the surface, the absolute temperature of the surrounding, the surface area and the surface emissivity. The rate of heat transfer by radiation can be calculated from (3.7).

$$Q_{rad} = \epsilon \sigma A_s \left(T_s^4 - T_{surr}^4 \right) \tag{3.7}$$

where Q_{rad} (W) is the rate of heat transfer by radiation, ϵ is the emissivity of the body which ranges from 0 to 1, σ is the Stefan Boltzmann constant which equals 5.67×10^{-8} (W/m^{2}K^4), A_s is the surface area, T_s is the surface temperature in K, T_{surr} is the temperature of the surroundings in K.

Due to the small value of the Stefan Boltzmann constant, for the encountered temperature differences between the surface of the electric machine and the surroundings, the heat transfer by radiation can be neglected.

3.3.2 Heat conduction equation

The temperature distribution over the stator and the rotor parts of the machine can be evaluated by solving the general heat conduction equation (3.8). Due to the complicated geometry of the electric machines and the 3D heat transfer, the heat conduction equation is usually solved numerically.

$$\nabla \cdot (k_{th} \nabla T) + Q_{th} = \rho C_p \frac{\partial T}{\partial t} \tag{3.8}$$

where k_{th} (W/mK) is the thermal conductivity of the medium, Q_{th} (W/m^3) is the heat generated by the medium per unit volume, ρ is the mass density of the medium and C_p is the specific heat capacity of the medium.

3.3.3 Thermal boundary conditions

As the heat conduction equation is second order in space and first order in time, a unique solution for the temperature distribution in space can be obtained if an initial value of the temperature is defined as well as two boundary conditions in each direction. Thermal boundary conditions can be specified as heat flux, convection or specified temperature.

Heat flux boundary condition

If the heat flux on the boundary surface is known, this means that the temperature gradient on this boundary can be calculated from (3.5). The heat flux boundary condition is a Neumann boundary condition as the derivative of the independent variable (i.e. the temperature) is known on the boundary surface.

Two special cases of the specified heat flux boundary condition are the thermally insulated surfaces and the thermal symmetry planes. In both cases the heat flux in the direction normal to the insulated surface and the thermal symmetry plane

is equal to zero. The thermally insulated surfaces are also called adiabatic surfaces in thermal analysis. These two boundary conditions can be described mathematically by (3.9).

Consideration of thermal symmetry boundary condition is crucial in the thermal modelling of electric machines because it makes it possible to model only a part of the full machine which reduces the numerical solution time of the heat conduction equation.

$$\mathbf{n} \cdot (\nabla T \mid_s) = 0 \tag{3.9}$$

where $\mathbf{n}$ is the vector normal to the boundary surface, s stands for the surface on which the boundary condition is specified.

Convection boundary condition

The boundary condition on the surfaces exposed to a fluid in motion is called convection boundary condition. In electric machines this boundary condition exists on the surfaces facing the airgap between the stator and the rotor [85], the surfaces exposed to the air flow of the fan in fan cooled machines, the surfaces in contact with a water jacket in water jacket cooled machines, and the surfaces exposed to the surrounding environment.

This boundary condition is expressed mathematically by (3.10). This boundary condition is a Robin boundary condition as a first order differential equation is defined on the boundary surface.

$$\mathbf{n} \cdot (-k_{th} \nabla T) = h_c (T_s - T_f) \tag{3.10}$$

where $\mathbf{n}$ is the vector normal to the boundary surface, k_{th} is the thermal conductivity of the exposed surface, h_c is the convection coefficient on the exposed surface, T_s is the surface temperature, T_f is the fluid temperature.

Specified temperature boundary condition

If the temperature on the boundary surface is known, this condition can be expressed as (3.11). A simple modelling approach for the water jacket cooled machines is to impose a constant temperature on the surface in contact with the water jacket [86]. The surfaces with constant temperature are called isothermal surfaces and this boundary condition is Dirichlet boundary condition as the value of the independent variable is known on the surface.

$$T(x, y, z, t) \mid_s = T_o \tag{3.11}$$

where T_o is the specified surface temperature.

3.3.4 Thermal properties of heterogeneous parts

Some parts of the electric machine have a homogeneous structure and the other parts have a heterogeneous structure. The windings, the core and the housing parts have heterogeneous structure. The windings consist of copper, insulation coating and the impregnation material. The core consists of thin laminations of silicon steel, insulation coating and the impregnation material. The housing consists of aluminium laminations, insulation coating and the impregnation material.

Two different approaches can be followed to model the heterogeneous parts of the electric machines. The first one is to model each strand of the windings or each lamination of the core and the housing [83]. The second approach is to homogenize the heterogeneous parts by calculating the equivalent thermal properties of these parts [87]. The first approach is more accurate than the second one but much more time consuming as well.

Three different approaches can be used for the homogenization of the heterogeneous parts. The first one is to measure the equivalent thermal properties using specific setups [88]. The second one is to homogenize using finite element simulations [89]. The third one is the Hashin-Shtrikman approximations [90]. The finite element method considers the geometry and the insulation coating of the windings and the core while the Hashin-Shtrikman approximations don't consider the geometry and the insulation coating. So, the finite element based homogenization calculates a more accurate equivalent thermal conductivity than the Hashin-Shtrikman approximations.

The Hashin-Shtrikman homogenization method approximates the thermal conductivity by two expressions. One expression (3.12) gives the thermal conductivity in the good heat conduction direction(s) and the other expression (3.12) gives the thermal conductivity in the less heat conduction direction(s). The good heat conduction direction(s) is (are) the direction(s) at which the constituting materials of the heterogeneous part are in parallel with respect to the heat flow. The less heat conduction direction(s) is (are) the direction(s) at which the constituting materials of the heterogeneous part are in series with respect to the heat flow.

$$
K_h = \begin{cases} f_{ws}k_m + (1 - f_{ws})k_{im} & \text{good heat conduction direction} \\[2ex] k_{im}\dfrac{(1+f_{ws})k_m + f_{ws}k_{im}}{(1-f_{ws})k_m + (1+(1-f_{ws}))k_{im}} & \text{less heat conduction direction} \end{cases} \tag{3.12}
$$

where K_h is the thermal conductivity of the heterogeneous part, k_{im} is the thermal conductivity of the impregnation material, k_m is the thermal conductivity of the main constituting material, and f_{ws} is the fill factor.

The mass density and the specific heat capacity of the heterogeneous part are calculated from (3.13).

$$C_{p_h} = f_{ws}C_{p_m} + (1 - f_{ws})C_{p_{im}}$$
$$\rho_h = f_{ws}\rho_m + (1 - f_{ws})\rho_{im} \tag{3.13}$$

where C_{p_h} is the specific heat capacity of the heterogeneous material, f_{ws} is the winding or stacking factor, C_{p_m} is the specific heat capacity of the main constituting material , $C_{p_{im}}$ is the specific heat capacity of the impregnation material, ρ_h is the mass density of the heterogeneous material, ρ_m is the mass density of the main constituting material and ρ_{im} is the mass density of the impregnation material.

3.4   Thermal modelling approaches of electric machines

The two thermal modelling approaches of electric machines are the finite element modelling and the lumped parameter thermal modelling.

3.4.1   Finite element thermal modelling

The following steps are conducted in the thermal finite element (FE) modelling of electric machines:

- The geometry of the stator and the rotor part is defined by considering the thermal symmetry of the stator and the rotor.

- The thermal boundary conditions and the volumetric heat sources are specified.

- The considered stator and rotor geometry are meshed. The accuracy of the solution and the CPU time increase with the number of mesh elements.

- The heat conduction equation (3.8) is solved numerically inside each element considering the defined boundary conditions and heat sources.

- The mesh is refined until a negligible difference in the temperature distribution is noticed.

- Due to the dependence of the heat sources of the electric machines on the temperature, the solution is iterated until the temperature stabilization.

The thermal FE modelling method provides accurate results and good coloured visualization of the temperature distribution but it requires high computational time. The bigger and the more complex the geometry, the higher the computational time.

3.4.2 Lumped parameter thermal modelling

In the lumped parameter thermal modelling, the electric machine is divided into several elements. Each element is modelled with a network of thermal resistances and thermal capacitances [91]. The thermal resistances represent the heat conduction across the boundaries of the element while the thermal capacitances represent the heat storage in the element.

Two modelling networks can be used to model each element, the classical two-resistor network shown in Fig. 3.2 and the T-equivalent network [92] shown in Fig. 3.3. The classical two-resistor network is derived from the 1-D steady state solution of the heat conduction equation assuming zero heat generation in the element and independent heat flow in each direction [93]. The temperature of the mid-point of the two-resistor gives the average temperature of the element. In case of internal heat generation which is the case of electric machines windings and core, if the spatial resolution of the thermal network along the heat transfer path is not high enough, the two-resistor network method leads to overestimated temperatures [93].
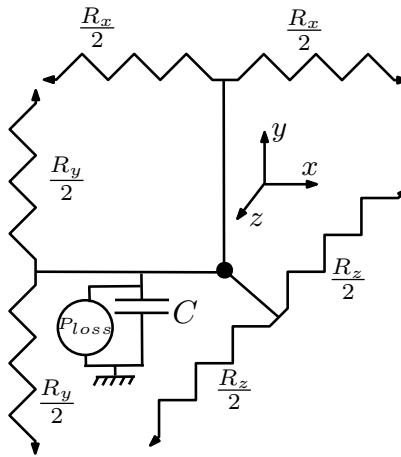

Figure 3.2: The classical two-resistor network.

In the T-equivalent network, a negative resistor is introduced between the mid-point of the two resistors and the node at which the average temperature of the element is calculated. This negative resistor compensates for the overestimated temperature of the two-resistor network in case of internal heat generation of the element [92]. The T-equivalent network is derived from the 1-D solution of the heat conduction equation twice. The first solution assumes no internal heat generation which means heat flow between the two positive resistors only. The second solution considers the internal heat generation and assumes zero temperature on the sides of the two positive resistors. From the first solution, a formula is derived for the calculation of the two positive resistors in each direction of the heat flow (3.14). From the second solution, a formula is derived for the calculation of the negative
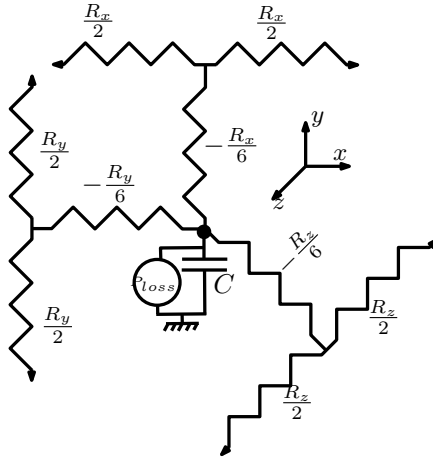
Figure 3.3: The T-equivalent network.

resistor. The absolute value of the negative resistor in each direction equals one third of the value of the two resistors.

$$R_x = \frac{L_x}{k_x A_x}, R_y = \frac{L_y}{k_y A_y}, R_z = \frac{L_z}{k_z A_z} \tag{3.14}$$

where R_x, R_y and R_z are the thermal resistances in the x, y, z directions respectively, L_x, L_y, L_z are the lengths of the heat conduction paths in the x, y, z directions respectively, k_x, k_y , k_z are the thermal conductivities of the element in the x, y, z directions respectively, A_x, A_y, A_z are the areas perpendicular to the heat flow.

The thermal capacitance is the amount of the thermal energy stored by the element per one degree Celsius increase in its temperature. The thermal capacitance of the element can be calculated from (3.15).

$$C = \rho_{el} V_{el} C_{pel} \tag{3.15}$$

where ρ_{el} (kg/m^3) is the mass density of the element, V_{el} (m^3) is the volume of the element and C_{pel} (J/kgK) is the specific heat capacity of the element.

The heat transfer by convection is modelled by a thermal resistance and reference temperature in the lumped parameter thermal model. This lumped parameter convection model is shown in Fig. 3.4. The reference temperature is the temperature of the fluid. The convective thermal resistance is inversely proportional to the convection coefficient and the surface area. The convective thermal resistance can be calculated from (3.16). Since the mass of the exposed surface is zero, it cannot store energy. Thus no thermal capacitance is presented.

$$R_{conv} = \frac{1}{h_c A_s} \tag{3.16}$$

where R_{conv} (°C/W) is the convection resistance, h_c (W/m²K) is the convection coefficient and A_s (m²) is the convected surface area.

$$T_s \qquad\qquad T_{ref}$$

Figure 3.4: The lumped parameter convection model.

The equation relating the different quantities in the lumped parameter thermal network can be derived by applying the power balance rule on the thermal network. The power balance states that the rate of heat generation (the power losses) equals the rate of heat storage in the thermal capacitance plus the rate of heat transferred across the element boundaries in the thermal resistances. This power balance can be expressed mathematically by (3.17).

$$C_{mat}\frac{dT_{vec}}{dt} + G_{mat}T_{vec} = P_{lossvec} \tag{3.17}$$

where C_{mat} is a diagonal matrix of the thermal capacitance of the nodes, T_{vec} is the temperature vector of the nodes, G_{mat} is the conductance matrix and $P_{lossvec}$ is the power losses vector.

Equation (3.17) is a first order differential equation. It is discretized and solved in a time stepping manner. The result of the discretization is presented in (3.18).

$$T_{vec}(n) = \left(\frac{C_{mat}}{\Delta t} + G_{mat}\right)^{-1}\left[P_{lossvec} + P_{ref} + \frac{C_{mat}}{\Delta t}T_{vec}(n-1)\right] \tag{3.18}$$

where

- C_{mat} is a diagonal matrix of the thermal capacitances of the nodes. C_{mat} is constructed as presented in (3.19).

$$C_{mat} = \begin{bmatrix} C_1 & 0 & \cdots & 0 \\ 0 & C_2 & \cdots & 0 \\ \vdots & \vdots & \ddots & \vdots \\ 0 & 0 & \cdots & C_m \end{bmatrix} \tag{3.19}$$

where m is the number of the nodes in the lumped parameter thermal network model.

- Δt is the time step.

- G_{mat} is the conductance matrix constructed as given in (3.20).

$$
G_{mat} = \begin{bmatrix} \sum_{i=1,..}^{m} \frac{1}{R_{1,i}} & -\frac{1}{R_{1,2}} & \cdots & -\frac{1}{R_{1,m}} \\ -\frac{1}{R_{2,1}} & \sum_{i=1,..}^{m} \frac{1}{R_{2,i}} & \cdots & -\frac{1}{R_{2,m}} \\ \vdots & \vdots & \ddots & \vdots \\ -\frac{1}{R_{m,1}} & -\frac{1}{R_{m,2}} & \cdots & \sum_{i=1,..}^{m} \frac{1}{R_{m,i}} \end{bmatrix} \tag{3.20}
$$

where $R_{i,i}$ is the resistance between the node i and the convection reference temperature.

- $P_{lossvec}$ is the power losses vector constructed as presented in (3.21).

$$
P_{lossvec} = \begin{bmatrix} P_1 \\ P_2 \\ \vdots \\ P_m \end{bmatrix} \tag{3.21}
$$

- P_{ref} is a vector with each element computed as the ratio of the reference temperature connected to the node i to the resistance between the node i and the reference temperature. P_{ref} is constructed as given in (3.22).

$$
P_{ref} = \begin{bmatrix} \frac{T_{ref1}}{R_{1,1}} \\ \frac{T_{ref2}}{R_{2,2}} \\ \vdots \\ \frac{T_{refm}}{R_{m,m}} \end{bmatrix} \tag{3.22}
$$

- $T_{vec}(n)$ is the temperature vector at the time step n, $T_{vec}(n-1)$ is the temperature vector at the time step $(n-1)$.

3.5   Thermal modelling of the air cooled YASA AFPMSM

The 3D finite element and the lumped parameter thermal network modelling (LPTN) of the YASA axial flux machine are discussed in this part.

3.5.1   YASA geometry and thermal boundary conditions

The construction of the air cooled yokeless and segmented armature (YASA) axial flux permanent magnet synchronous machine (PMSM) is presented in Chapter 1

Fig. 1.22. The stator has fifteen modules. Each module (see Fig. 1.23 (a) in Chapter 1) consists of a coil with a number of turns wound around a silicon steel core. The fifteen coils are arranged circumferentially and bonded together with the housing to form the concentrated winding structure of the machine. The machine has two rotor disks with surface mounted permanent magnets (PMs) as shown in Fig. 1.23 (b) in Chapter 1.

The major part of the heat dissipated by the stator transfers to the ambient through the heat extraction system shown in Fig. 1.24 in Chapter 1. The rest of the stator heat transfers partly to the air-gap by the ventilation action of the rotor discs and partly to the ambient through the shaft. The heat generated by the rotor PMs gets evacuated in the air-gap.

Thanks to the thermal symmetry, only a quarter stator tooth and one rotor pole are modelled. The geometry and the thermal boundary conditions of the stator and the rotor modelled parts are shown in Fig. 3.5 and Fig. 3.6 respectively.
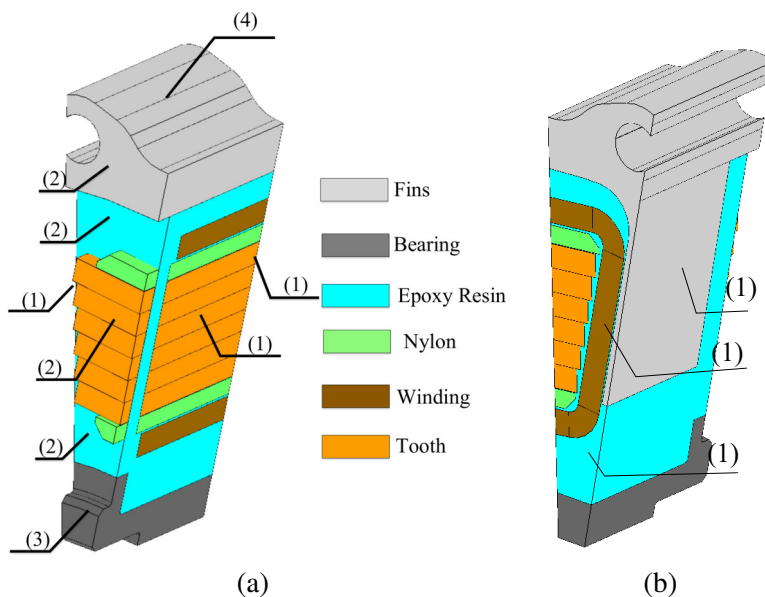

Figure 3.5: One quarter of the stator tooth. The boundary conditions are: 1) thermal insulation, 2) convected stator surface facing rotor upper part, 3) convected stator surface facing rotor lower part, 4) convected stator side wall.

The thermal boundary conditions of the air cooled YASA are the thermal symmetry which is modelled by (3.9) and convection boundary condition which is modelled by (3.10). The surfaces labelled by (1) in Fig. 3.5 and Fig. 3.6 for the stator and the rotor represent the symmetry planes. The other surfaces from 2 to 13
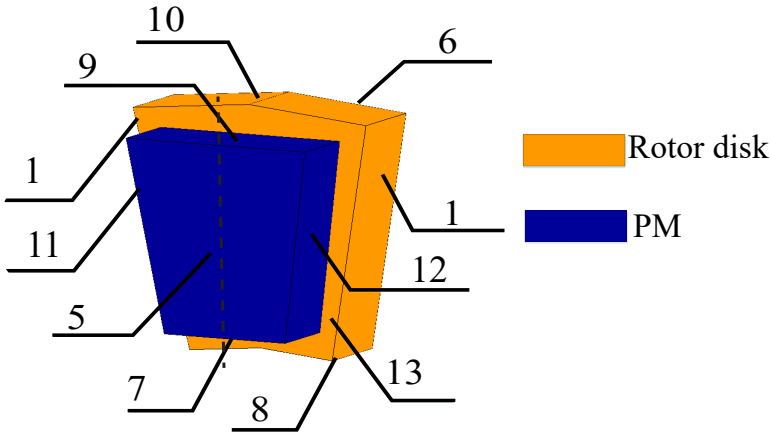
Figure 3.6: One rotor pole. The boundary conditions are: 1) Thermal insulation (symmetry), 5) Rotor facing stator upper, 6) Rotor left side, 7) PM lower 8) Rotor lower 9) PM upper, 10) Rotor upper, 11) PM left, 12) PM right, (13) Rotor facing stator.

are exposed to convection.

For the calculation of the convection coefficients and the reference temperatures on the stator and the rotor exposed surfaces, the correlations developed in [94] for the YASA machine are used. These correlations are derived from CFD simulations with the following assumptions:

- The air is considered an incompressible gas with temperature independent properties except the mass density.

- Heat transfer by radiation is negligible.

- Isothermal surfaces

In the convection model developed in [94], the convection coefficient on the different surfaces is considered to be temperature independent while the reference temperature is considered to be a function of the average stator temperature, the average rotor temperature, and the ambient temperature. Both the convection coefficient and the reference temperature are dependent on the geometrical parameters of the YASA machine, the rotor speed and the fluid properties of the air.

It is shown in [94] that the reference temperature of the stator surface 4 (see Fig. 3.5) and the rotor surfaces (6,7,8,9,10,11,13) (see Fig. 3.6) equals the ambient temperature (T_a). For the other surfaces, the reference temperature is expressed as given in (3.23) [94].

$$T_{ref} \mid_i = a_i T_r + b_i T_s + (1 - (a_i + b_i)) T_a \tag{3.23}$$

where $T_{ref} \mid_i$ is the reference temperature on the stator/rotor surface i with $T_{ref} \neq T_a$, T_r is the average rotor temperature, T_s is the average stator temperature.

The variables a_i and b_i are functions of the airgap size ratio G, Reynolds number Re, the permanent magnet span ratio α_m and the axial length of the PM Y_m. The airgap size ratio and the Reynolds number are calculated from (3.24).

$$G = \frac{2g}{D_o}, \; Re = \frac{\omega_m D_o^2}{4\nu} \tag{3.24}$$

where g is the airgap thickness, D_o is the stator outer diameter, ω_m is the angular speed of the rotor, ν is the kinematic viscosity of the air.

The expressions of a_i and b_i are given in (3.25). At each convected surface with $T_{ref} \neq T_a$, the variables a_i and b_i are calculated from four independent functions. The expressions of the four functions for the calculation of a_i and b_i at each surface are given in Table 3.3.

$$\begin{aligned} a_i &= a_i^* f_i(G) \times f_i(Re) \times f_i(\alpha_m) \times f_i(Y_m) \\ b_i &= b_i^* g_i(G) \times g_i(Re) \times g_i(\alpha_m) \times g_i(Y_m) \end{aligned} \tag{3.25}$$

Table 3.3: Correlations to calculate the reference temperature for the surfaces with $T_{ref} \neq T_a$ [94]

Surface	Stator facing rotor upper, $i = 2$	Stator facing rotor lower, $i = 3$	Rotor facing stator upper, $i = 5$	PM right, $i = 12$
a_i^*	0.4153	0.2317	0.00100	0.00100
b_i^*	0.0010	0.0010	0.1744	0.1739
$f_i(G)$	$0.2824G^{-0.3381} - 0.2002$	$0.2033G^{-0.373}$	$1.71 \times 10^{-10} G^{5.386}$	$-0.01155G + 1$
$f_i(Re)$	$74.78Re^{-0.3734}$	$2.096 \times 10^6 \, Re^{-1.422} + 0.9092$	1	$-1.967 \times 10^{-9} \, Re + 1$
$f_i(\alpha_m)$	$2.803 \, \alpha_m^{1.518} - 0.9881$	$26.323 \, \alpha_m^2 - 40.02\alpha_m + 16.23$	$9.892 \times 10^{-6} \, \alpha_m + 0.9997$	$1.46 \times 10^{-4} \alpha_m^{-102.4} + 0.9929$
$f_i(Y_m)$	$0.4205Y_m^{-0.2972}$	$0.1982Y_m^{-0.5497}$	$-3.205 \times 10^{-10} \, Y_m + 0.9996$	$5.96 \times 10^{-11} \, Y_m + 0.9999$
$g_i(G)$	$13.386 \times 10\text{-}16G^{-7.289} + 0.9843$	$0.009G + 1$	$0.005875G^{-1.206}$	$-15.73G + 1.135$
$g_i(Re)$	$7.556 \times 10^{13} \, Re^{-3.218} + 0.9953$	$1.824 \times 10^{-9} \, Re + 1$	$1.638 \times 10^4 \, Re^{-0.8264} - 0.1472$	$31.79Re^{-0.1803} - 2.969$
$g_i(\alpha_m)$	$1.731 \times 10^{-15} \, \alpha_m + 1$	$1.731 \times 10^{-15} \, \alpha_m + 1$	$3.416 \, \alpha_m^{6.722} + 0.2816$	$-0.09794\alpha_m^{-7.204} + 1.452$
$g_i(Y_m)$	$-7.017 \times 10^{-11} \, Y_m + 0.9999$	$2.506 \times 10^{-10} \, Y_m + 1$	$0.03617Y_m^{-0.9332} + 0.4602$	$-4.089 \times 10^5 \, Y_m^{5.46} + 1.021$

The convection coefficient of each surface i is calculated from (3.26) [94].

$$h_i = \frac{Nu_i k_{air}}{l_i} \tag{3.26}$$

where h_i is the average convection coefficient on the surface i, k_{air} is the air thermal conductivity, l_i is the characteristic length.

The Nusselt number on the surface i is function of the airgap size ratio, Reynolds number, the permanent magnet span ratio and the axial length of the

PM. The expression of the Nusselt number is given in (3.27). At each convected surface, the Nusselt number is calculated from four independent functions. The expressions of these functions are given in Table 3.4 and Table 3.5 for the surfaces with $T_{ref}=T_a$ and Table 3.6 for the surfaces with $T_{ref} \neq T_a$ [94].

$$Nu_i = Nu_i^* y_i(G) \times y_i(Re) \times y_i(\alpha_m) \times y_i(Y_m) \tag{3.27}$$

Table 3.4: Correlations to calculate the Nusselt number for the surfaces with $T_{ref} = T_a$ [94]

Surface	Stator side wall, $i = 4$	Rotor left side, $i = 6$	PM lower, $i = 7$	Rotor upper, $i = 8$
Nu_i^*	105.76	216.52	492.10	239.56
$y_i(G)$	$-4.476G^{-0.03846}$ - $6.795G$ + 6.373	$1.785G + 0.9766$	$-3.29G + 1.024$	$1.645G + 0.976$
$y_i(Re)$	$2\,3.91 \times 10^{-5}\,Re^{0.8773}$	$6.501 \times 10^{-6}\,Re + 0.3041$	$5.755 \times 10^{-6}\,Re$ - 0.3702	$5.238 \times 10^{-6}\,Re + 0.425$
$y_i(\alpha)$	$0.8805\alpha_m^{6.245} + 1.218$	$0.1325\alpha_m + 0.8983$	$-1.20163\alpha_m^{7.461} + 1.226$	$-0.7163\alpha_m + 1.567$
$y_i(Y_m)$	$-1.246Y_m^{-0.1443} + 2.899$	$1.751Y_m + 0.9061$	$-0.03425Y_m^{-0.5286} + 1.159$	$1.478Y_m + 0.9211$

Table 3.5: Correlations to calculate the Nusselt number for the surfaces with $T_{ref} = T_a$ [94]

Surface	PM upper, $i = 9$	Rotor upper, $i = 10$	PM left, $i = 11$	Rotor facing stator, $i = 13$
Nu_i^*	202.28	181.40	285.20	235.85
$y_i(G)$	$1.62G^{0.11}$	$2.322G + 0.9728$	$-0.002076G^{-1.193} + 1.345$	$1.647G^{0.1117}$
$y_i(Re)$	$8.669 \times 10^{-6}\,Re + 0.06863$	$4.737 \times 10^{-6}\,Re^{1.038} + 0.2024$	$9.1 \times 10^{-6}\,Re + 0.02189$	$7.975 \times 10^{-6}\,Re + 0.1496$
$y_i(\alpha_m)$	$-0.9382\alpha_m^{8.902} + 1.132$	$-1.005\alpha_m + 1.803$	$-7.126\alpha_m^{29.8} + 0.9939$	$-2.903\alpha_m + 3.29$
$y_i(Y_m)$	$-0.007892Y_m^{-1.107} + 1.189$	$1.806Y_m^{0.2031}$	$6.707Y_m^{0.04971} - 4.8$	$3.917Y_m + 0.7895$

Table 3.6: Correlations to calculate the Nusselt number for the surfaces with $T_{ref} \neq T_a$ [94]

Surface	Stator facing rotor upper, $i = 2$	Stator facing rotor lower, $i = 3$	Rotor facing stator upper, $i = 5$	PM right, $i = 12$
Nu_i^*	374.53	243.90	304.84	606.37
$y_i(G)$	$-2.967G^{0.6937} + 1.142$	$-0.6211G + 1.005$	$-0.0167G^{-0.6493} + 1.277$	$4.723G^{0.3274} - 14.47G$
$y_i(Re)$	$0.0001122Re^{0.7824} + 0.04018$	$0.0003289Re^{0.679} + 0.1569$	$3.552 \times 10^{-5}\,Re^{0.886}$	$0.001593Re^{0.5825} - 0.3542$
$y_i(\alpha)$	$-0.7732\alpha_m^{5.583} + 1.224$	$-0.8183\alpha_m^{6.34} + 1.21$	$-0.905\alpha_m^{4.158} + 1.35$	$-15.86\alpha_m^{35.42} + 0.998$
$y_i(Y_m)$	$13.86Y_m^{1.709} + 0.9064$	$7.906Y_m^{1.575} + 0.9243$	$3.607Y_m + 0.8067$	$-113.7Y_m^2 + 12.51Y_m + 0.6539$

3.5.2   YASA material thermal properties

The heterogeneous structure of the windings, the stator core and the housing of the YASA machine is modelled with (3.12) and (3.13). The good heat conduction direction of the windings is the lapping direction while the perpendicular directions

are the less heat conduction directions. For the core laminations, the stacking direction which is the radial direction is the less heat conduction direction while the perpendicular directions are the good heat conduction directions. For the housing laminations, the stacking direction which is the axial direction is the less heat conduction direction while the perpendicular directions are the good heat conduction directions. The thermal properties of the stator and the rotor constituting materials of the YASA machine are given in Table 3.7.

Table 3.7: Thermal properties of the materials of the YASA machine

Material	k(W/mK)	C_p(J/kgK)	ρ(kg/m^3)
copper	385	392	8890
aluminium	167	896	2712
impregnation material (epoxy)	0.4	600	1540
nylon	0.25	1600	1140
steel	40	490	7650
Nd-Fe-B	9	500	7500

3.5.3 YASA heat sources

Power losses in the YASA machine take place in the windings, the stator core and the PMs. These power losses represent the heat source Q_{th} in the heat conduction equation (3.8) solved by the FE model and the lumped heat source in the lumped parameter thermal modelling explained in section 3.4.2.

YASA winding losses

The winding losses P_{wdg} are calculated using (3.28). They are temperature dependent due to the dependence of the coil resistance on the temperature. As the lapping direction of the end-windings and the effective windings is different, the winding is divided into three parts: effective winding, upper end-winding and lower end-winding. The total copper losses are divided on these parts according to their respective volumes assuming uniform loss distribution. Equation (3.29) governs the sum of the three-loss parts in the quarter tooth shown in Fig. 3.5.

$$P_{wdg} = N_s I^2 R_{coil}(T_{wdg})$$

$$R_{coil}(T_{wdg}) = R_o(1 + \alpha_t (T_{wdg} - T_o))$$

(3.28)

where P_{wdg} is the total winding loss, N_s is the number of teeth, I is the rms value of the coil current, $R_{coil}(T_{wdg})$ is the coil resistance at the average winding temperature T_{wdg}, R_o is the coil resistance at 25°C and α_t is the resistance temperature coefficient which equals 0.393%/°C for the copper.

$$P_{endup} + P_{endlow} + P_{eff} = \frac{P_{wdg}}{4N_s} \tag{3.29}$$

where P_{endup} is the power loss in the upper end-winding, P_{endlow} is the power loss in the lower end-winding, P_{eff} is the effective winding power loss and P_{wdg} is the power loss in the effective winding.

YASA stator core losses

The stator core losses P_{stcore} are calculated using the method explained in section 3.2 [72]. The tooth is divided into two parts: the part in contact with the windings and the tooth tip. The tooth losses are divided in these parts according to their respective volumes assuming uniform loss distribution. Equation (3.30) governs the sum of the two-loss parts in the quarter tooth shown in Fig. 3.5.

$$P_{tin} + P_{ttip} = \frac{P_{stcore}}{4N_s} \tag{3.30}$$

where P_{tin} is the loss in the tooth part in contact with the windings and P_{ttip} is the loss in the tooth tip.

YASA PM losses

The total rotor PM losses are calculated using the method explained in section 3.2 [76]. The loss in one magnet for the rotor thermal model in Fig. 3.6 is calculated from 3.31.

$$P_{PMone} = \frac{P_{PM}}{2N_m} \tag{3.31}$$

where P_{PMone} is the loss in one PM, P_{PM} is the total loss in the rotor PMs and N_m is the number of PMs in one rotor disk.

YASA mechanical losses

The aerodynamic forces acting on the rotary parts of the machine cause mechanical losses in the surfaces exposed to them. The surfaces exposed to aerodynamic forces are illustrated in Fig. 3.7. These losses are called windage losses and according to [95], they are caused by viscous forces and pressure forces.

    The windage losses caused by the viscous forces and the pressure forces are both functions of the air gap size ratio, the Reynolds number, the PM angle span
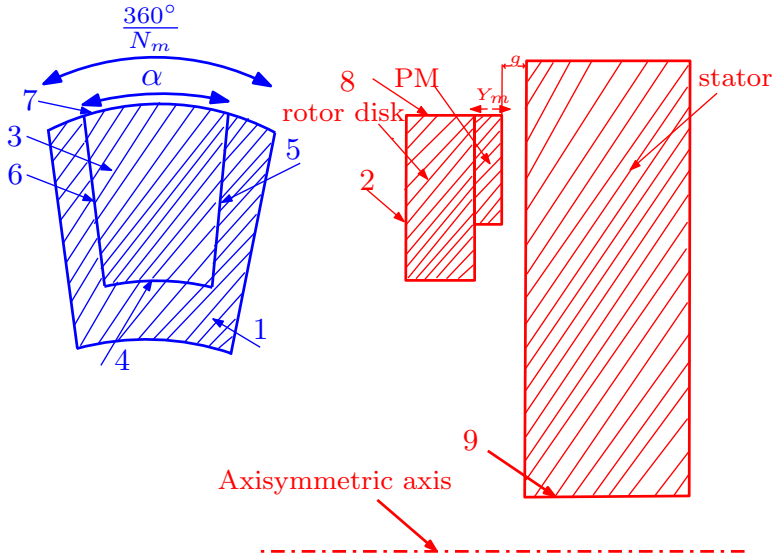
Figure 3.7: The surfaces exposed to the aerodynamic forces: (1) rotor facing stator, (2) rotor left side, (3) PM front, (4) PM lower, (5) PM left, (6) PM right, (7) PM upper, (8) rotor sidewall, (9) shaft.

ratio and the PM thickness ratio. Each loss component is expressed as a function of four single variable functions of the air gap size ratio, the Reynolds number, the PM angle span ratio and the PM thickness ratio [95]. The expressions of the windage loss components are given in (3.32) [95].

$$P'_{f,v} = P'^{*}_{f,v} \times Z_{f,1}(G) \times Z_{f,2}(Re) \times Z_{f,3}(\alpha_m) \times Z_{f,4}(L)$$
$$P'_{f,p} = P'^{*}_{f,p} \times X_{f,1}(G) \times X_{f,2}(Re) \times X_{f,3}(\alpha_m) \times X_{f,4}(L)$$

(3.32)

where $P'_{f,v}$ and $P'_{f,p}$ are the windage losses for surface f due to viscous forces and pressure forces respectively. $P'^{*}_{f,v}, P'^{*}_{f,p}$ are the windage losses at the reference point, α_m and L are the PM angle span ratio and the PM thickness ratio. α_m and L are calculated from (3.33).

$$\alpha_m = \frac{\alpha \times N_m}{360}$$
$$L = \frac{Y_m}{R_r}$$

(3.33)

where α is the PM angle illustrated in Fig. 3.7 and R_r is the rotor outer radius.

It is shown in [95] that the surfaces magnet left and magnet right exhibit windage losses due to the pressure forces only and the rest of the surfaces contribute to the windage losses because of the viscous forces. The correlations for

the calculation of the windage losses due to the viscous forces are given in Table 3.8 and Table 3.9. The correlations for the calculation of the windage losses due to the pressure forces are given in Table 3.10. The mechanical losses are considered to be part of the PM losses.

Table 3.8: Correlations to calculate the windage losses due to viscous forces [95]

Surface	Rotor Facing Stator, $f = 1$	Rotor Left Side, $f = 2$	PM Front, $f = 3$	PM Lower, $f = 4$
$P'^*_{f,v}$	-20.796	420.403	251.028	62.156
$Z_{f,1}(G)$	$-4.389 \times 10^{-7} G^{-2.942} + 1.112$	1	$0.8593G + 0.9902$	$-1.9016G^{0.4745} + 1.231$
$Z_{f,2}(Re)$	$-17.19Re^{-0.07896} + 7.895$	$6.423 \times 10^{-6} Re + 0.3119$	$6.324 \times 10^{-6}Re + 0.3254$	$0.0007882Re^{0.6173}$
$Z_{f,3}(\alpha_m)$	$-8.61\alpha_m^{4.393} + 4.212$	$0.2052\alpha_m + 0.8358$	$3.551\alpha_m^{23.38} + 0.9882$	$3.551\alpha_m^{23.38} + 0.9882$
$Z_{f,4}(L)$	$-7311L^{3.265} + 1.518$	$0.4958L + 0.9742$	$2.715L + 0.8581$	$20.74L - 0.1176$

Table 3.9: Correlations to calculate the windage losses due to viscous forces [95]

Surface	PM Upper, $f = 7$	Rotor Sidewall, $f = 8$	Shaft, $f = 9$
$P'^*_{f,v}$	27.902	150.382	2.868
$Z_{f,1}(G)$	$0.6994G^{-0.09581}$	$1.894G + 0.9848$	$11.76G + 0.8452$
$Z_{f,2}(Re)$	$1.023 \times 10^{-5} Re^{-0.08718}$	$7.285 \times 10^{-6} Re + 0.2174$	$4.432 \times 10^{-6} Re + 0.5308$
$Z_{f,3}(\alpha_m)$	$1.854\alpha_m^{9.287} + 0.7816$	$-0.7086\alpha_m + 1.579$	$-0.144\alpha_m + 1.114$
$Z_{f,4}(L)$	$13.88L + 0.2696$	$2.688L + 0.8593$	$9.633L + 0.4791$

Table 3.10: Correlations to calculate the windage losses due to pressure forces [95]

Surface	PM Left, f = 5	PM Right, f = 6
$P'^*_{f,p}$	0.02218	0.00527
$X_{f,1}(G)$	$0.688G^{-0.2192} - 0.7961$	$-0.01947G - 1.104 + 3.299$
$X_{f,2}(Re)$	$0.1116Re^{0.1866}$	$-1.633 \times 10^8 Re^{-1.806} + 1.121$
$X_{f,3}(\alpha_m)$	$-3.876\alpha_m + 4.101$	$-7.127\alpha_m^{10.56} + 1.645$
$X_{f,4}(L)$	$142.4L^{1.703}$	$-1.708 \times 10^4 L^{3.453} + 1.733$

3.5.4 YASA lumped parameter thermal network

The stator segment model shown in Fig. 3.5 is divided into two parts in the axial direction. One part is in contact with the winding and the other part is the tooth tip. These parts are shown in Fig. 3.8 (a) and (b) respectively. The stator is divided into twenty regions (nodes) based on the contacted layers in each direction. The model of each region is constructed using the method described in section (3.4.2) and Fig. 3.3 for the T-equivalent network. The regions are labelled and shown in Fig. 3.8. The resulted LPTN model of the stator is shown in Fig. 3.9.
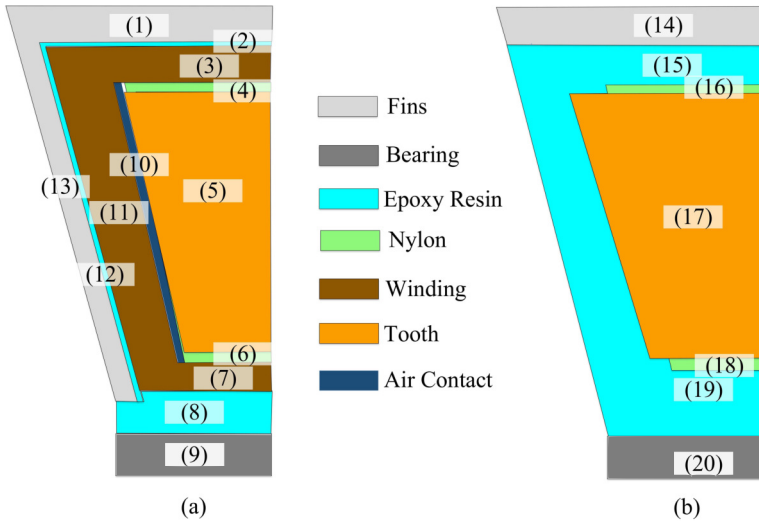
Figure 3.8: The two parts of the quarter tooth considered for the construction of the LPTN of the YASA stator. (a) the part in contact with the winding, (b) the tooth tip.

The YASA rotor is divided into four regions (nodes). The PM is one region and the rotor back iron is three regions, one in contact with the PM and two other regions. The YASA rotor lumped parameter thermal network is shown in Fig. 3.10.

3.6 Dynamic modelling of switched reluctance machines

Unlike the conventional machines operating with sinusoidal currents with superimposed high frequency harmonics, the SRMs are operating with non-sinusoidal unidirectional currents [96]. The performance of the SRM (i.e. the torque ripple and the losses) depends on the winding current waveform. The current waveform depends on the control strategy of the SRM. The purpose of the dynamic modelling is to compute the winding current waveform at the control strategy used.

The torque of the SRM is produced by the tendency of the rotor to align with
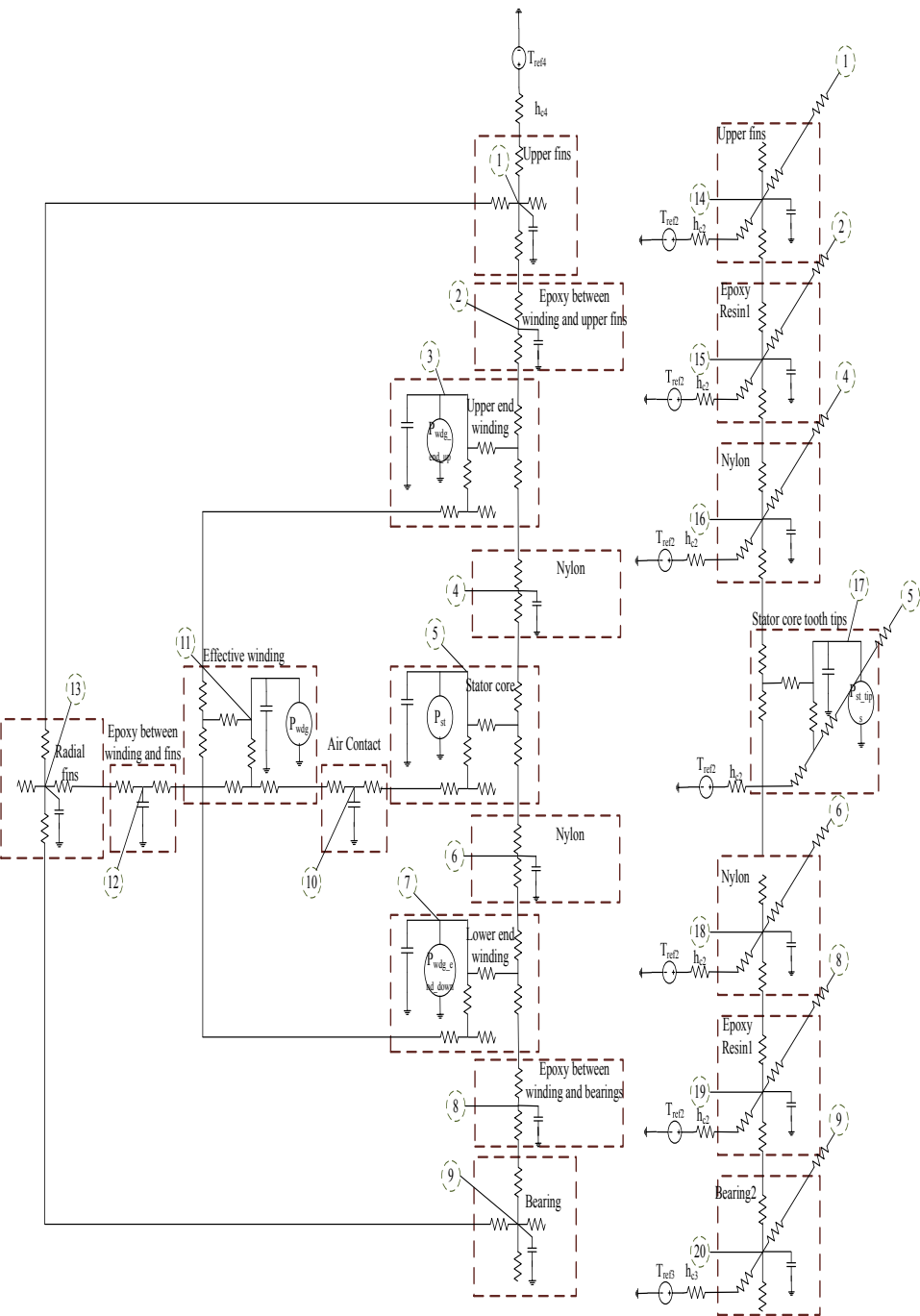
Figure 3.9: The lumped parameter thermal network of the YASA stator.

Figure 3.10: The lumped parameter thermal network of the rotor of the YASA machine.

the excited phase of the stator which is the minimum reluctance position. Fig. 3.11 (a) shows the stator and the rotor poles of a 6/4 SRM with the rotor in a completely unaligned position with coil 1 and coil 4. In Fig. 3.11 (b), the rotor starts to align with coil 1 and coil 4. In Fig. 3.11 (c), the rotor is in complete alignment with coil 1 and coil 4.
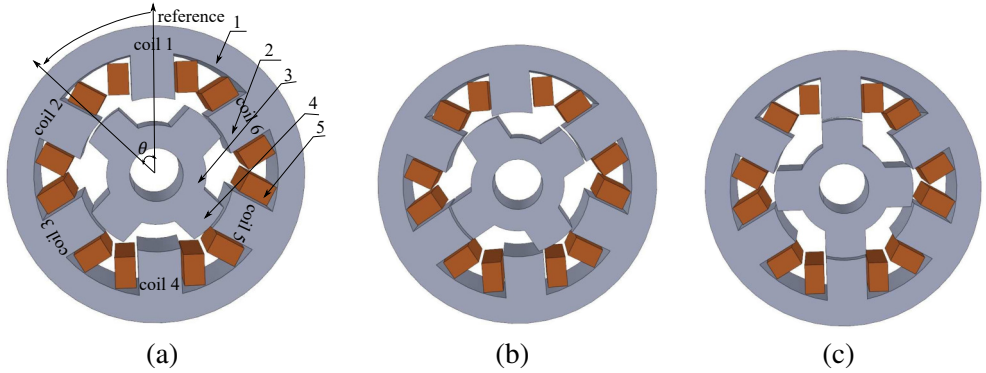

Figure 3.11: Illustration of the stator and the rotor poles of a 6/4 SRM with (a) the rotor in a completely unaligned position with the stator coil 1 and coil 4: (1) stator yoke, (2) stator pole, (3) rotor yoke, (4) rotor pole, (5) stator coil side (b) the rotor starts to align with coil 1 and coil 4 and (c) the rotor is in complete alignment with coil 1 and coil 4.

The torque production in the SRM is illustrated in Fig. 3.12 assuming a linear magnetic circuit. In the unaligned position, the phase inductance remains constant at L_u. Once the rotor starts to align with the stator phase, the phase inductance increases linearly, and a positive torque production can be obtained by injecting current in the phase winding. Once the rotor pole and the stator pole come to a complete alignment, the phase inductance plateaus at L_a and the torque becomes zero. Once the rotor starts to leave the completely aligned position, the phase inductance falls down and if the phase current is still there, the torque produced by this phase becomes negative.

The angles $(\alpha_1, \alpha_2, \alpha_3, \alpha_4, \alpha_5)$ shown in Fig. 3.12 can be calculated from (3.34).

$$\begin{aligned}
\alpha_1 = \alpha_5 &= \tfrac{180}{N_{rp}} - (\beta_s + \beta_r) \\
\alpha_2 = \alpha_4 &= \beta_s \\
\alpha_3 &= \beta_r - \beta_s
\end{aligned} \tag{3.34}$$

where N_{rp} is the number of rotor poles, β_s is the stator pole arc angle and β_r is the rotor pole arc angle.
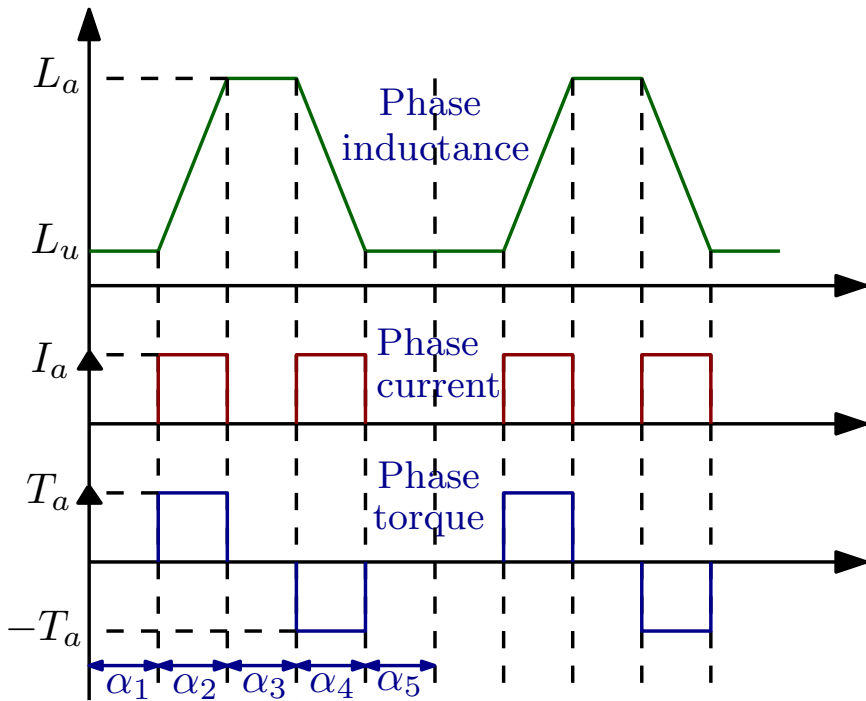
Figure 3.12: Illustration of the torque production in the SRM. The upper figure represents the phase inductance, the middle figure represents the phase current and the lower figure represents the phase torque. These figures are ideal, non realistic figures.

Due to the phase inductance, the phase current cannot rise or fall instantaneously. Therefore, to build the phase current to the reference value at the beginning of the rotor alignment with the stator phase, the phase winding should be excited before the beginning of the alignment with an advance angle. Similarly, to avoid negative torque production, the phase current should be pulled to zero before the complete alignment. So, the phase winding should be de-energized before the complete alignment position by an advance angle. Fig. 3.13 illustrates the turn-on and the turn-off advance angles with a realistic phase current waveform.

The turn-on and the turn-off angles are called the firing angles. The values of the firing angles determine the performance of the SRM at each torque/speed operating point [97]. Thus, the turn-on and the turn-off angles should be set to the optimal values at each operating point. The optimal turn-on and turn-off angles can be obtained by optimizing an objective function. The optimization problem can be minimization of the torque ripple, minimization of the copper losses or maximization of the torque per ampere [98].

Average torque control and instantaneous torque control can be employed with
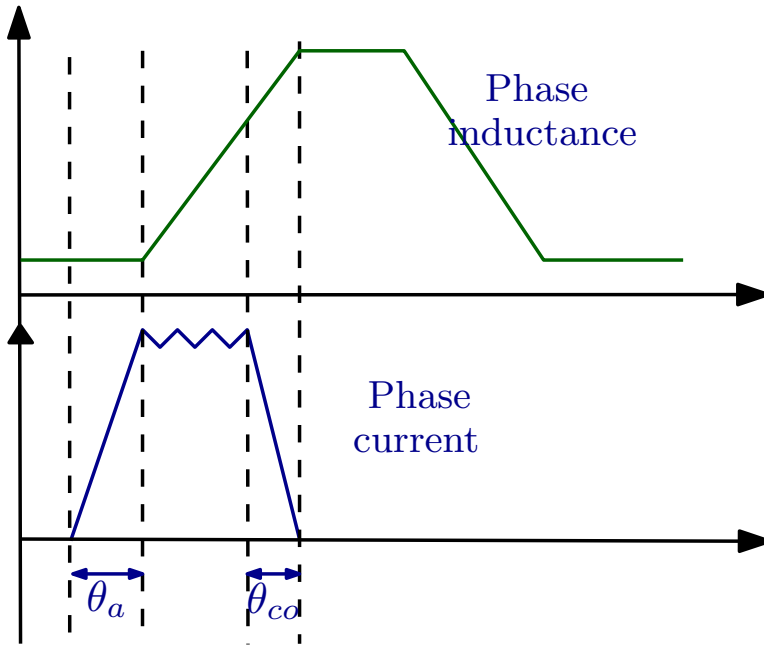
Figure 3.13: Illustration of the turn-on and turn-off advance angles.

the SRMs [99]- [100]. Average torque control is employed in low performance applications while instantaneous torque control is used for high performance applications such as actuators and electric vehicles. The general torque control block diagram is shown in Fig. 3.14. The reference torque and the speed are applied to a look up table with the optimal values of the turn-on angle (θ_{on}) and the turn-off angle (θ_{off}). The turn-on, the turn-off and the rotor position are applied to a commutation algorithm that decides which stator phase to energize for how long. The reference torque is applied to a torque controller which generates the reference current that is compared to the feedback current and applied to a current controller. The output of the current controller and the commutation algorithm are applied to a pulse generator that controls the converter switches.

Due to the non-linear characteristics of the silicon steel cores and the doubly salient construction of the SRM, the flux linkage of the SRM stator phases depends on the phase current and the rotor position [96]. The torque ripples in the SRMs are the commutation ripple due to the uncontrolled free wheeling current in the outgoing phase, the ripples resulting from the dependence of the torque in the rotor position and the high frequency ripples resulting from the switching of the inverter devices [101].

In average torque control, only the current in the incoming phase is controlled while the current in the outgoing phase is free wheeling in an uncontrolled way and the dependence of the torque on the rotor position is not taken into account.
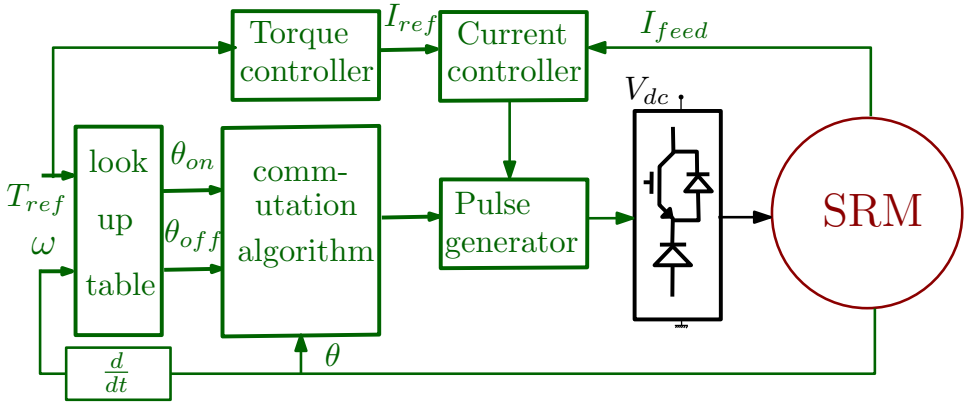
Figure 3.14: The general torque control block diagram of the switched reluctance machines: T_{ref} is the reference torque, ω is the angular speed of the SRM, θ_{on} is the turn-on angle, θ_{off} is the turn-off angle, I_{ref} is the reference phase current, I_{feed} is the feedback current and θ is the rotor position.

Therefore, the torque ripples in case of average torque control are high.

In instantaneous torque control, the required shaft torque is distributed instantaneously over two phases using a position dependent torque sharing function (TSF) [102]. Using the TSF, the current rise in the incoming phase and the current fall in the outgoing phase are controlled so that the summation of the torque produced by the two phases equals the desired shaft torque. In this way, the torque ripples due to the phase commutation and the dependence of the torque on the rotor position are eliminated. The TSF can be sinusoidal [103], cubic [104], exponential [105] or other functions. Each TSF has its own rate of rise and rate of fall which sets the required speed of the current controller.

The instantaneous torque control using sinusoidal torque sharing function is employed in this thesis. The block diagram of the torque controlled SRM using the TSF is shown in Fig. 3.15. The key specifications of the 6/4 SRM studied in this thesis are given in Table 3.11. To compute the current and the torque waveforms of the SRM, each subsystem of the SRM drive in Fig. 3.15 should be modelled in a dynamic simulation environment.

3.6.1 The SRM dynamic model

The SRM winding current can be computed at a given rotor speed, stator voltage and finger prints by numerically solving (3.35).

$$[v]^\top = [R_{coil}] [i]^\top + \omega \frac{\partial [\psi(\theta, i)]^\top}{\partial \theta} + \frac{\partial \mathbf{diag}([\psi(\theta, i)]) }{\partial i} \frac{d [i]^\top}{dt} \qquad (3.35)$$
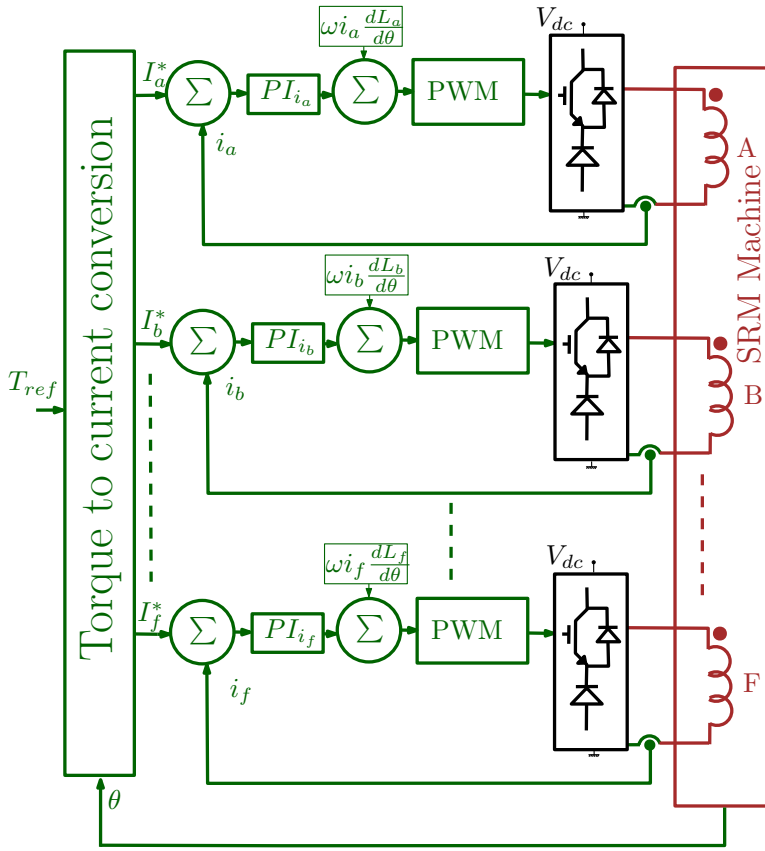
Figure 3.15: Block diagram for the torque controlled PR SRM drive system.

where $[v]^\top \in \mathbb{R}^n$ is the voltage vector applied on the n stator coils, $[R_{coil}] \in \mathbb{R}^{n \times n}$ is a diagonal matrix of the resistances of the stator coils, $[i]^\top \in \mathbb{R}^n$ is the vector of the current flowing in the stator coils, ω is the angular speed of the rotor, $[\psi(\theta, i)]^\top \in \mathbb{R}^n$ is the vector of the flux linkage of the stator coils as function of the rotor position θ and the coil current i.

The finger prints (i.e. $\psi(\theta, i)$) of the case study SRM are computed using the 2D electromagnetic FE model explained in section (3.7.1) and the result is shown in Fig. 3.16 for a single stator coil.

The torque generated by each stator coil and the total shaft torque can be calculated from (3.36)-(3.38).

Table 3.11: The key parameters of the 6/4 SRM case study

Parameter	Symbol	Value
stator outer diameter (mm)	D_{so}	100
stator yoke thickness (mm)	Y_{st}	9
rotor outer diameter (mm)	D_{ro}	51.5
rotor yoke thickness (mm)	Y_{rt}	7.75
airgap length (mm)	g	0.25
stator pole arc angle (°)		32.4
rotor pole arc angle (°)		32.7
axial length (active) (mm)	L_{ax}	50
water jacket axial length (mm)	L_{awj}	90
water jacket outer diameter (mm)	D_{wj}	130
number of turns/coil	N_t	168
coil resistance $\vert_{25°C}$ (Ω)	R_{coil}	1.8
steel grade	-	NO20
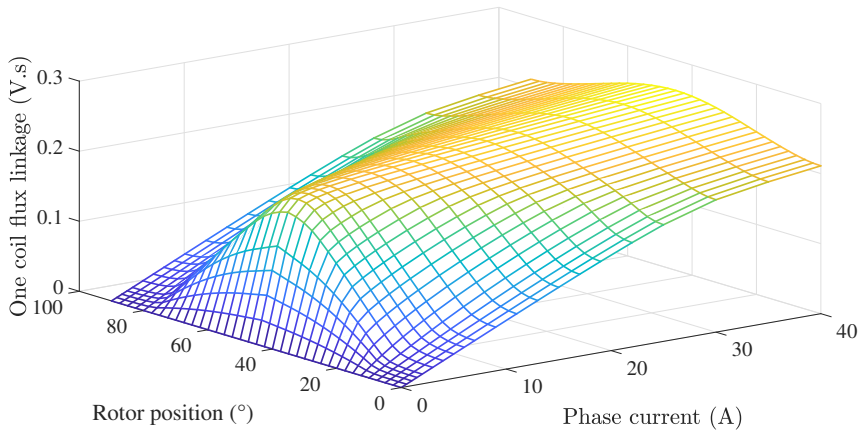
Figure 3.16: The finger prints of the case study SRM for one stator coil.

$$[w_c(\theta, i)]^\top = \int_0^i [\psi_x(\theta, i)]^\top \, di \tag{3.36}$$

$$[T(\theta, i)]^\top = \frac{\partial [w_c(\theta, i)]^\top}{\partial \theta} \tag{3.37}$$

$$T_e(\theta) = \sum [T(\theta, i)]^\top \tag{3.38}$$

where $[w_c(\theta, i)]^\top \in \mathbb{R}^n$ is the co-energy vector of the stator coils, $[T(\theta, i)]^\top \in \mathbb{R}^n$ is the torque vector of the stator coils and $T_e(\theta)$ is the shaft torque.

3.6.2 The SRM power converter model

Fig. 3.17 shows the modular asymmetric H-bridge converter that drives the 6/4 case study SRM. Each converter module drives one stator coil. The converter module consists of two power switches and two power diodes. Due to their low losses, small junction to case thermal resistance and small form factor, the SiC devices C3M0075120J from Wolfspeed and LSIC2SD120C10 from Littlefuse are chosen for the power switches and the power diodes respectively. The power converter is simulated using the static characteristics of the chosen devices.
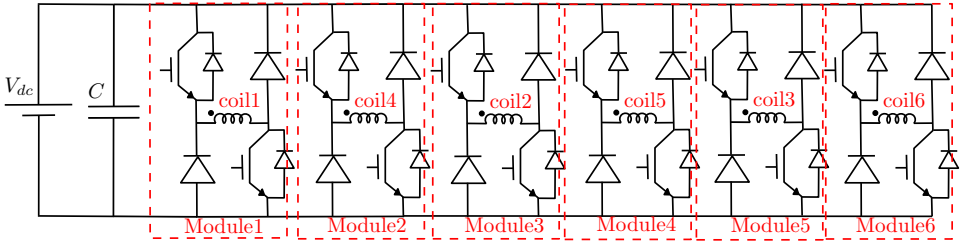
Figure 3.17: The asymmetric H-bridge topology for the modular 6/4 SRM.

During the energization time of the stator coil, the two power switches are turned on and the DC-link voltage is applied on the coil terminals. Therefore, the current starts to build up. De-energization of the coils can be done by hard switching or soft switching [106]. In hard switching, the two power switches are switched off simultaneously, and hence, the two power diodes turn-on to return the coil energy to the DC-link capacitors. In hard switching, the full DC-link voltage is applied on the coil terminals with reverse polarity. The hard switching has the advantage of fast decaying the coil current which is beneficial in the instantaneous torque control. Nevertheless, the slew rate of the coil voltage will be double the DC-link voltage divided by the turn-on/off transition time of the switches. This causes high common mode current in the coils.

In soft switching, only one power switch is turned off. In this case, the winding current freewheels in one power switch and one power diode. The voltage drop across the stator coil in this case is the summation of the voltage drops across the power switch and the power diode. The coil current decays slowly but the common mode current of the coils will be smaller than the hard switching case.

3.6.3 The torque to current conversion block

The torque to current conversion block has two parts. The first part is the TSF which distributes the desired shaft torque on the stator phases. The second part calculates the phase current required at each rotor position to obtain the required phase torque. The sinusoidal TSF presented in [103] is adopted in this thesis. The sinusoidal TSF of each phase can be calculated from (3.39).

$$
f_{ph}(\theta) = \begin{cases} 0.5\left(1 - cos\left(k_f(\theta - \theta_{on})\right)\right) & \to \theta_{on} \leq \theta < \theta_1 \\ 1 & \to \theta_1 \leq \theta < \theta_2 \\ 0.5\left(1 + cos\left(k_f(\theta - \theta_{on})\right)\right) & \to \theta_2 \leq \theta < \theta_{off} \\ 0 & \to \theta_{off} < \theta < \theta_{on} \end{cases} \tag{3.39}
$$

where $f_{ph}(\theta)$ is the TSF of the phase as function in the rotor position, θ is the rotor position, θ_{on} is the turn-on angle, θ_{off} is the turn-off angle. k_f, θ_1, θ_2 can be calculated from (3.40).

$$
k_f = \frac{\pi}{\theta_1 - \theta_{on}}
$$

$$
\theta_1 = \theta_{off} - \frac{2\pi}{P_r \times N_{ph}} \tag{3.40}
$$

$$
\theta_2 = \theta_{on} + \frac{2\pi}{P_r \times N_{ph}}
$$

where P_r is the number of rotor poles, N_{ph} is the number of phases.

Fig. 3.18 shows the torque sharing function of the six stator coils of the 6/4 case study SRM at 2 Nm and 1000 rpm. The TSF of each two diagonally opposite coils is the same. The instantaneous summation of the torque sharing functions equals one.

The reference phase torque $T_{xref}(\theta)$ can be calculated from (3.41).

$$
T_{xref}(\theta) = f_{ph}(\theta) \times T_{ref} \tag{3.41}
$$

where T_{ref} is the desired shaft torque.

The reference phase current is calculated from the invertible torque function introduced in [107]. The reference phase current is expressed as a function of the reference phase torque and two position dependent functions f and L_{op}. Equation
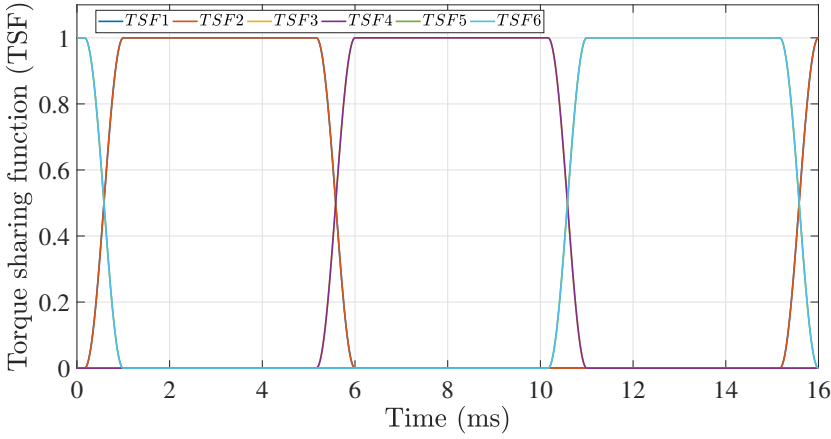
Figure 3.18: The torque sharing functions of the six coils of the 6/4 SRM case study at 2 Nm and 1000 rpm.

(3.42) gives the reference phase current expression as function of the reference phase torque T_{xref}.

$$i_{xref}(\theta, T_{xref}) = \frac{2T_{xref}}{L_{op}} \left[\frac{f}{2} + \sqrt{\frac{f^2}{4} + \left(\frac{L_{op}}{2T}\right)^p} \right]^{\frac{1}{p}} \tag{3.42}$$

where

- p is a constant. The value of p depends on the ratio of the aligned unsaturated inductance to the unaligned unsaturated inductance ($\frac{L_a}{L_{un}}$). if $\frac{L_a}{L_{un}}$ is < 13.4, the optimal value of p would be 3. For SRMs with $\frac{L_a}{L_{un}} > 13.4$, the optimal value of p would be < 3. The unsaturated inductance of the 6/4 SRM case study is shown in Fig. 3.19. The aligned unsaturated inductance value is 67.2 mH. The unaligned unsaturated inductance value is 7.2 mH. The $\frac{L_a}{L_{un}} = 9.3$ which is less than 13.4. Therefore, p is chosen to be 3.

- L_{op} is the rate of change of the unsaturated coil inductance with respect to the rotor position ($\frac{dL}{d\theta}$). The L_{op} of the case study 6/4 SRM is shown in Fig. 3.20.

- f is calculated from (3.43).

$$f = \left(\frac{L_{op}I_2}{2T_2}\right)^p - \frac{1}{I_2^p} \tag{3.43}$$

where I_2 is a current at which the magnetic circuit is saturated. T_2 is the phase torque at I_2 versus rotor position. T_2 for the 6/4 SRM case study is shown in Fig. 3.21. The function f of the case study 6/4 SRM is shown in Fig. 3.22.

3.6.4 The current controller

The current controller used is a PI controller plus a feedforward compensation. To design the PI controller using linear control design techniques, the SRM equations should be linearized [96]. The form of the PI controller used is given in (3.44).

$$c(t) = k_p \left(i_x^* - i_x \right) + \frac{k_p}{\tau_I} \int_0^t \left(i_x^* - i_x \right) d\tau \tag{3.44}$$

where $c(t)$ is the controller output, k_p is the proportional gain of the PI controller, i_x^* is the reference current of the coil x, i_x is the feedback current of coil x and τ_I is the integral time constant of the integral controller.

The state-space form of the equations of one coil of the SRM is given in (3.45).

$$\frac{di_x}{dt} = \frac{-R_x}{L_x} i_x + \frac{1}{L_x} \left(v_x - i_x \omega \frac{\partial L_x}{\partial \theta} \right) \tag{3.45}$$

where R_x is the coil resistance, L_x is the coil inductance, i_x is the coil current, v_x is the coil voltage and ω is the angular speed of the motor.

Due to the term $i_x \omega$ which is the multiplication of two states of the SRM (i.e. the rotor speed and the coil current), the system is non-linear. To decouple the non-linear term, the auxiliary input $\hat{v}_x$ given in (3.46) is defined.
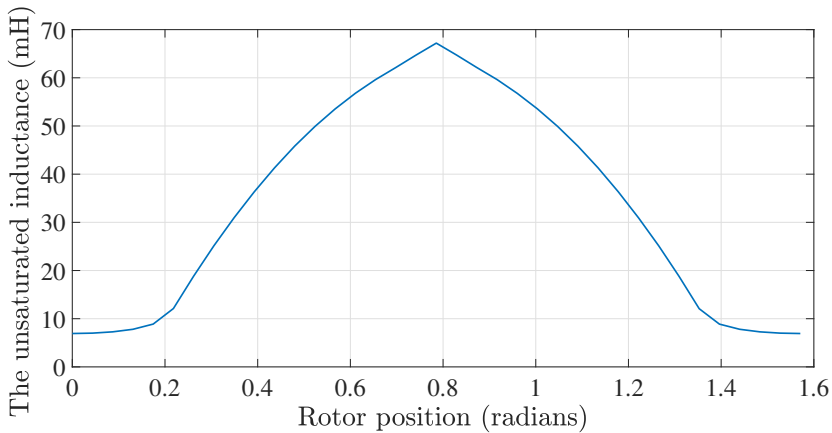
Figure 3.19: The unsaturated inductance of the 6/4 SRM case study.
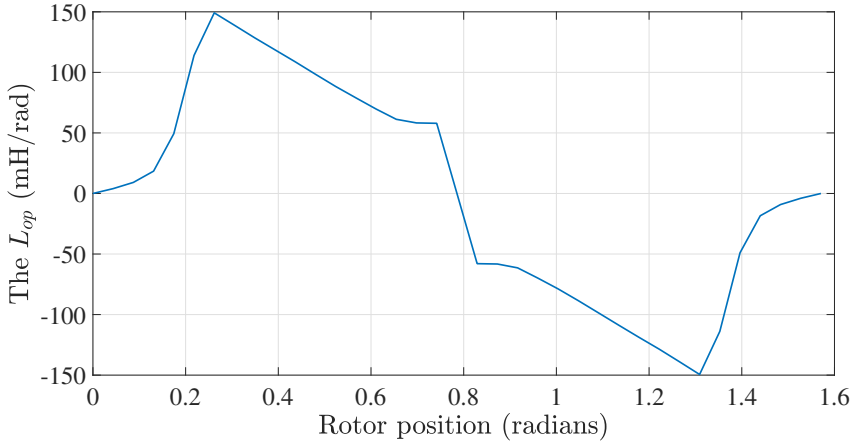
Figure 3.20: The L_{op} of the 6/4 SRM case study.
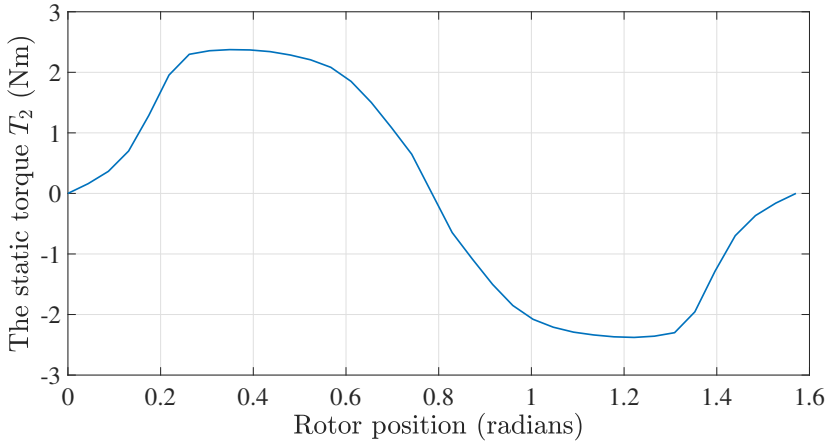
Figure 3.21: The static torque T_2 of the 6/4 SRM case study.

$$\hat{v}_x = v_x - i_x\omega\frac{\partial L_x}{\partial \theta} \tag{3.46}$$

The new state-space equation of one SRM coil takes the form in (3.47).

$$\frac{di_x}{dt} = \frac{-R_x}{L_x}i_x + \frac{\hat{v}_x}{L_x} \tag{3.47}$$

The auxiliary input $\hat{v}_x$ is the output of the PI controller.
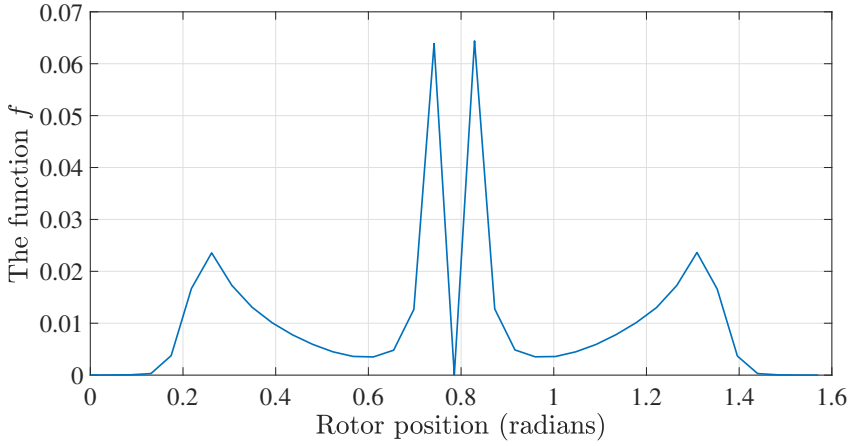Substitution of (3.46) in the PI controller equation in (3.44) results in (3.48).

Figure 3.22: The function f of the 6/4 SRM case study.

$$v_x = k_p \left(i_x^* - i_x \right) + \frac{k_p}{\tau_I} \int_0^t \left(i_x^* - i_x \right) d\tau + i_x \omega \frac{\partial L_x}{\partial \theta} \qquad (3.48)$$

Equation (3.48) has two decoupled terms, the scaled PI controller term and the term $(i_x \omega \frac{\partial L_x}{\partial \theta})$. The latter term is the feedforwad compensation term. This term depends on $\frac{\partial L_x}{\partial \theta}$ which is a function in the rotor position and the coil current. $\frac{\partial L_x}{\partial \theta}$ is implemented as a look up table in the controller.

A block diagram for the equation (3.48) is shown in Fig. 3.23.
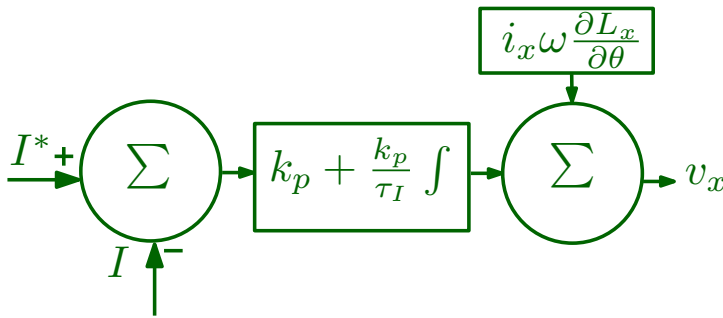
Figure 3.23: A block diagram for the non-linear feedforward controller in (3.48).

The closed loop block diagram of the current control loop of the SRM is shown in Fig. 3.24 with the open loop transfer function of the SRM with the auxiliary input given in (3.49).

$$\frac{I_x(s)}{\hat{V}_x(s)} = \frac{\frac{1}{L_x}}{\left(s + \frac{R_x}{L_x}\right)} \tag{3.49}$$
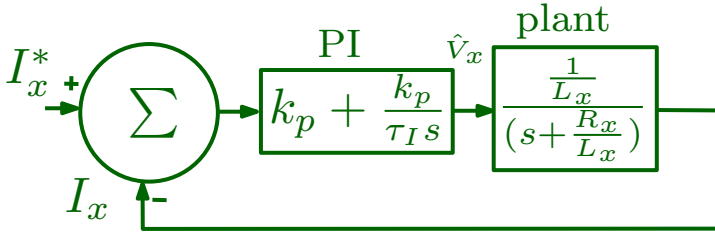
Figure 3.24: The closed loop block diagram of the current control loop of the SRM.

The closed loop transfer function of the SRM current control loop is given in (3.50). The gains of the PI controller can be obtained by comparing the characteristic polynomial of the closed loop transfer function with the standard characteristic polynomial (3.51). The proportional gain and the integral time constant of the PI controller are given in (3.52).

$$\frac{I_x(s)}{I_x^*(s)} = \frac{k_p}{L_x} \frac{s + \frac{1}{\tau_I}}{s^2 + \left(\frac{R_x}{L_x} + \frac{k_p}{L_x}\right) s + \frac{k_p}{\tau_I L_x}} \tag{3.50}$$

$$s^2 + 2\zeta\omega_n s + \omega_n^2 \tag{3.51}$$

$$k_p = 2\zeta\omega_n L_x - R_x$$

$$\tau_I = \frac{2\zeta\omega_n L_x - R_x}{L_x \omega_n^2} \tag{3.52}$$

Due to the dependence of the controller gains on L_x which is function of the coil current and the rotor position, gain scheduling should be used to adjust the controller gains with the rotor position [96]. If a fixed controller gain is required for less computational burden, L_x can be used as the mean value of the aligned and the unaligned inductance at rated current [96]. The selection of $\zeta = 0.707$ results in natural frequency ω_n equals the bandwidth of the closed loop. So, ζ is selected equal to 0.707. The bandwidth of the closed loop current control loop is selected equal to 10 times the bandwidth of the plant which is equal to $\frac{R_x}{L_x}$.

The duty cycle input to the PWM generator is calculated from the output of the PI controller depending on the switching method used (hard or soft switching). Fig. 3.25 illustrates the PWM signal generation. The duty cycle is calculated from the controller output and the DC-link voltage as given in (3.53).
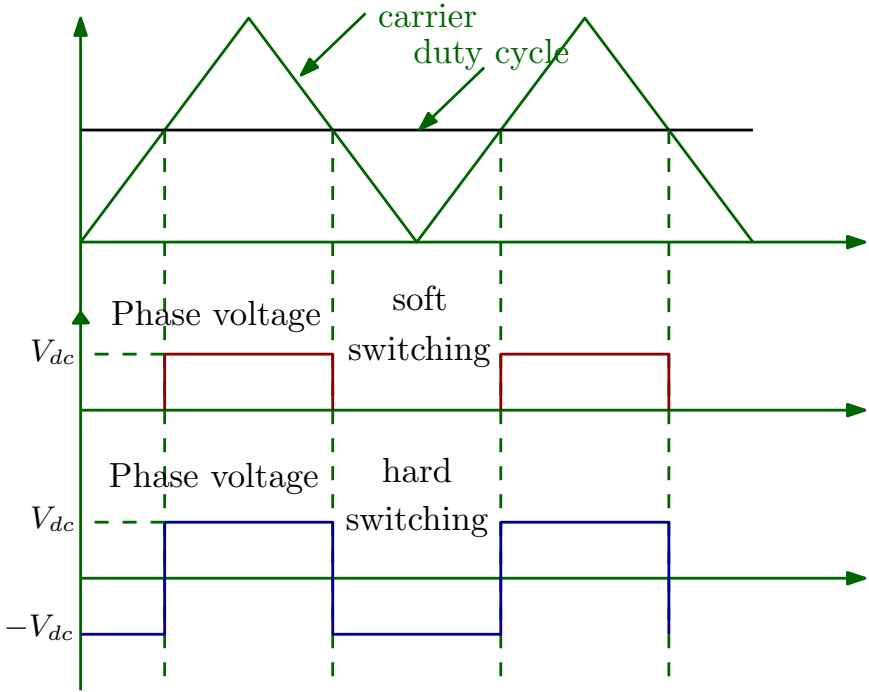
Figure 3.25: The PWM signal generation in case of soft switching and hard switching.

$$D = \frac{v_x}{V_{dc}} \rightarrow \text{in case of soft switching}$$

$$D = \frac{v_x}{2V_{dc}} + 0.5 \rightarrow \text{in case of hard switching}$$

(3.53)

where D is the duty cycle.

3.6.5 Waveforms of the case study 6/4 SRM

The block diagram shown in Fig. 3.15 is simulated for the case study 6/4 SRM at 800 V DC-link voltage and 20 kHz switching frequency. The turn-on and the turn-off angles used are the values that minimize the torque ripple. The phase currents and torques at 2 Nm and 1000 rpm are shown in Fig. 3.26. A high current is required at the beginning of the phase conduction because the rotor is still in an unaligned position with the stator which means that the change in the $\psi - i$ curve of the stator coil with the rotor position is small. Therefore, the change in the area under the $\psi - i$ curve which is the co-energy of the coil with the rotor position at the same current is small. As the coil current increases the change in the co-energy with the rotor position increases which means higher torque. So, a high current is

required at the beginning of the phase conduction.

A small torque ripple can be noticed at the commutation moments due to the small deviation between the actual coil current required for obtaining constant torque and the current calculated by (3.42). High frequency torque ripples can be noticed due to the converter switching. These high frequency ripples are easily filtered by the inertia of the SRM.

(a)

(b)
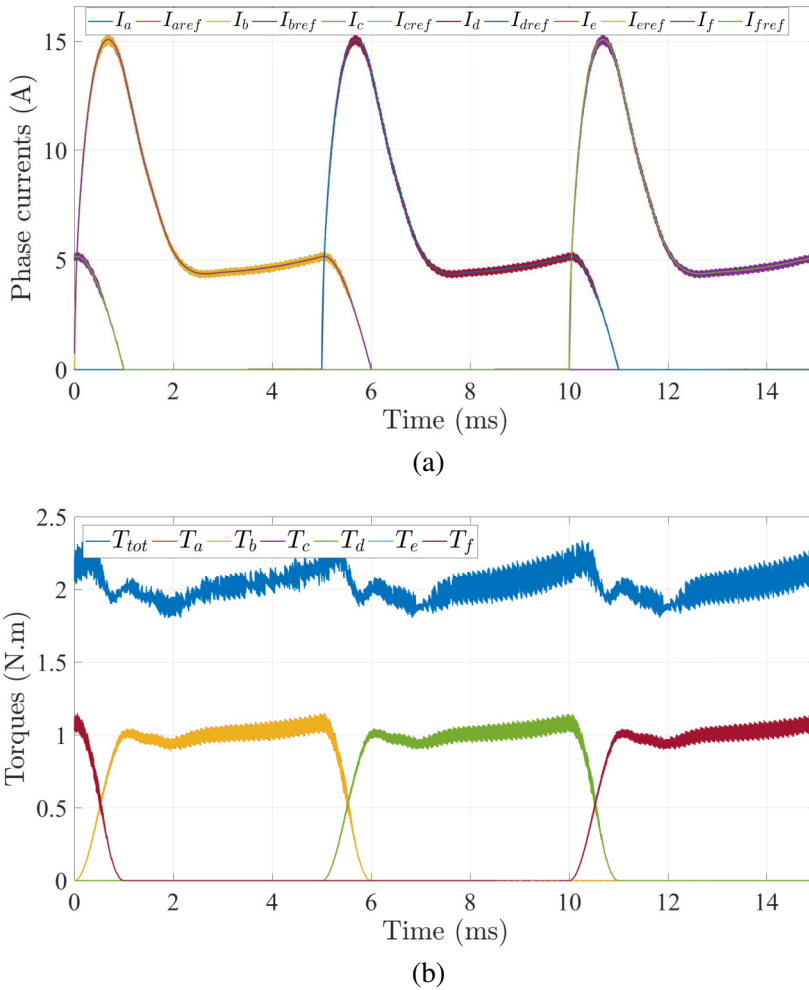
Figure 3.26: The phase currents (a) and torques (b) at 2 Nm and 1000 rpm.

3.7 Electromagnetic modelling of switched reluctance machines

Electromagnetic modelling of the SRMs is mandatory for two purposes. The first one is computing the finger prints (i.e. ψ-i-θ) necessary for the dynamic modelling and control of the SRMs. The second one is computing the flux density distribution in the stator and the rotor cores to compute the core losses. Finite element (FE) electromagnetic modelling is usually used for both purposes [108].

The electromagnetic FE model solves (3.54) for obtaining the magnetic vector potential $\mathbf{A}$ and then the flux density distribution is obtained from the curl of the magnetic vector potential. Equation (3.54) considers the non-linear characteristics of the silicon steel core [73] which is crucial for the modelling of the SRM to obtain accurate finger prints and flux density distribution.

$$\nabla \times \left(\frac{1}{\mu_o \mu_r(B)} \nabla \times \mathbf{A} \right) = \mathbf{J} \tag{3.54}$$

where $\mathbf{J}$ is the current density in the coils.

3.7.1 2D FE modelling of switched reluctance machines

A 2D electromagnetic FE model is built for the 6/4 case study SRM using the geometrical parameters given in Table 3.11. The used core material is NO20 with the B-H curve shown in Fig. 3.27. The model is built using FEMM software. The Mesh of the 2D FE model is shown in Fig. 3.28 along with the flux lines at 5 A current in coil 3 and coil 6.
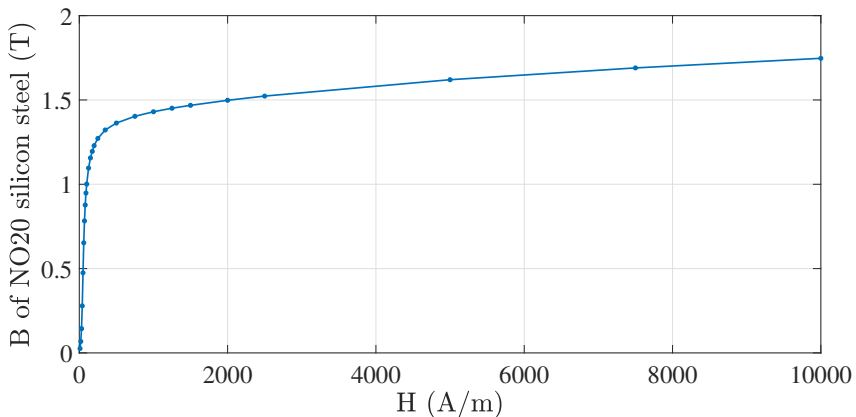
Figure 3.27: The B-H curve of the NO20 silicon steel used for the core of the case study SRM.

The current waveforms shown in Fig. 3.26 (a) are injected in the respective coils of the case study 6/4 SRM and the electromagnetic FE model is solved for two complete power cycles. The flux density distribution at the phase commutation moment is shown in Fig. 3.29. At this moment, the current in all the coils is zero except coils 3 and 6. The current in coils 3 and 6 is 5 A at this moment. It can be noticed that the edges of the rotor poles and stator poles have the highest local flux density (local saturation). This makes sense because the total flux generated by the stator coils splits into two parts in the stator yoke. One part flows clock-wise and the other counter clock-wise. These two parts sum up in the overlapping areas of the stator and the rotor poles (the area with the smallest reluctance) causing local saturation in these parts.
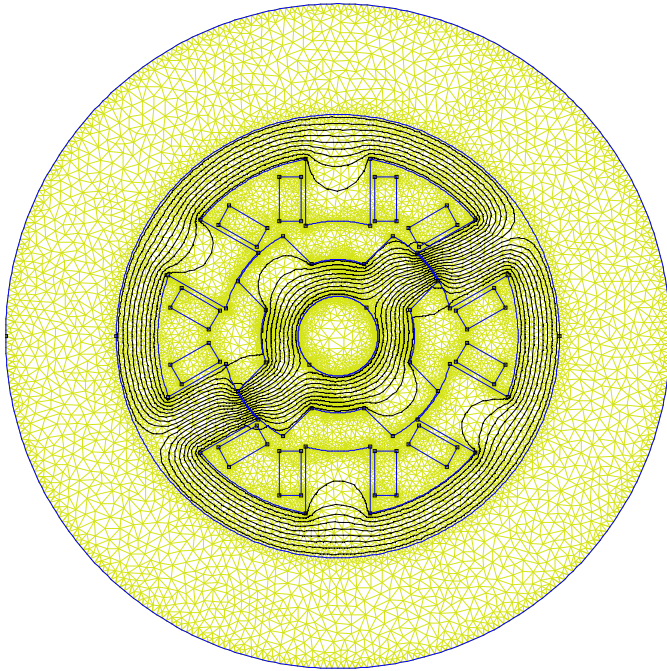
Figure 3.28: The mesh of the 2D electromagnetic model of the SRM along with the flux lines resulting from 5 A current in coils 3 and 6.

3.7.2   Core losses of switched reluctance machines

The computation of the core losses in the SRMs is crucial for evaluation of the SRM efficiency and the computation of the temperature field in thermal analysis.

Different types of flux density waveforms exist in the different parts of the SRM stator and rotor core. The flux density waveform can be unipolar or DC-biased bipolar with multiple times of local flux slope reversal [109]. The frequency
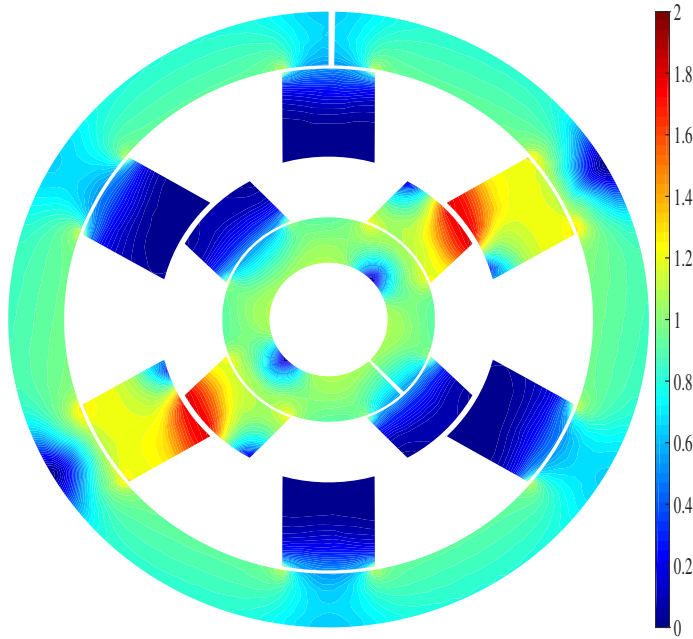
Figure 3.29: The SRM flux density (T) distribution at the end moment of the current cycle.

of these waveforms is also different from part to part of the stator and the rotor core [110].

To take into account the variation of the flux density waveform from part to part in the core, the stator and the rotor core are divided into small volumes in which the flux density waveform is computed and recorded by the FE model and the core losses in these small volumes are calculated. The total core losses are computed by summing the loss components in the small core volumes and multiplying by the mass of the core.

The core losses have three components, the hysteresis loss, the eddy current loss and the excess loss. These three loss components are computed using the formulas provided in [111]. The hysteresis loss per kg is calculated from (3.55).

$$P_h = K_{f5} f_B B_m^\alpha K(B_m) \tag{3.55}$$

where

- K_{f5}, α are material dependent constants obtained by curve fitting for the loss measurements of the core laminations at different frequencies and peak

flux density of the core [71] .

- f_B is the frequency of the flux density waveform, B_m is the peak value of the flux density.

- $K(B_m)$ is a factor for consideration of the losses of the minor hysteresis loops. $K(B_m)$ is calculated from (3.56) for unipolar flux density waveforms and DC-biased bipolar flux density waveforms [111].

$$K(B_m) = \begin{cases} 0.4 + \frac{0.65}{B_m} \sum_{i=1}^{n_m} \Delta B_i \rightarrow \text{unipolar flux density} \\ \frac{0.65}{B_m} \sum_{i=1}^{n_m} \Delta B_i \rightarrow \text{DC biased bipolar flux density} \end{cases} \tag{3.56}$$

where n_m is the number of local slope reversal of the flux density (i.e. the minor loops) and ΔB_i is the peak to peak flux density of the minor loop.

The eddy current losses and the excess losses are computed from (3.2) and (3.3) taking into account the frequency of the flux density waveform in each small volume of the stator and the rotor core.

The flux density waveforms at the middle of the poles and the yokes of the stator and the rotor cores are recorded versus time at 2 Nm and 1000 rpm for two current cycles (half mechanical revolution). The flux density at the middle of the stator poles and yokes is shown in Fig. 3.30.

The following can be noticed from Fig. 3.30 (a):

- It can be noticed that the flux density of the stator pole is unipolar with a frequency equivalent to the frequency of the current waveform. Since the stator coil current is unidirectional, the stator pole flux density is expected to be unipolar.

- It is also noticed that the flux density follows the current waveform until the beginning of the current plateau which indicates that the magnetic circuit is still linear (no overlapping between the stator and the rotor poles).

- Then, although the coil current plateaus, the flux density keeps increasing which indicates that the overlapping area between the stator and the rotor poles is increasing (the reluctance is decreasing).

- The peak flux density at the middle of the stator pole occurs at the end of the current plateau region which indicates that the coil current starts to decrease while the overlapping area between the stator and the rotor poles is still increasing.

- It also can be noticed that the flux density of the stator pole of the incoming phase equals the flux density of the stator pole of the outgoing phase at the
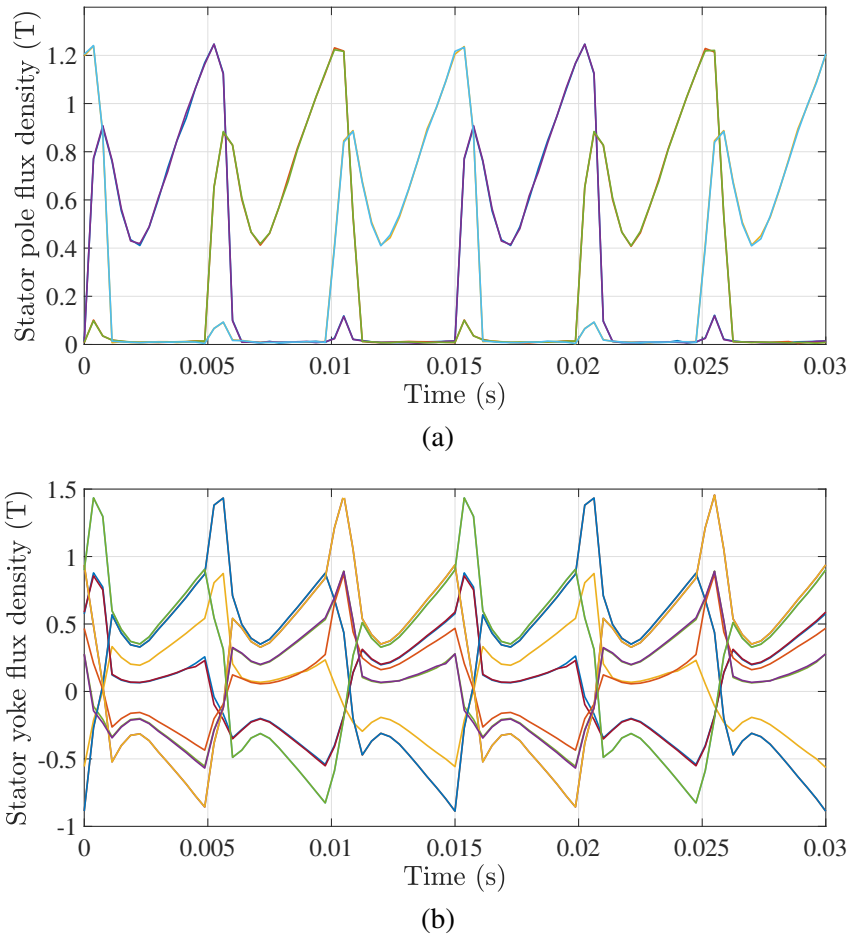
(a)

(b)

Figure 3.30: The flux density waveforms of the stator of the 6/4 SRM case study (a) at the middle of the stator poles and (b) at the middle of the stator yokes.

moment of peak current of the incoming phase. This means that the torque of the incoming phase equals the torque of the outgoing phase at the moment of peak current of the incoming phase. A current of 15 A is required in the incoming phase to produce 1 Nm while only 2.65 A is required in the outgoing phase to produce the same torque. The reason is the high reluctance seen by the incoming phase compared to the one seen by the outgoing phase.

- The small peaks in the stator pole flux density waveforms indicate small mutual flux between the two excited phases and the unexcited one. This can be seen from Fig. 3.31.
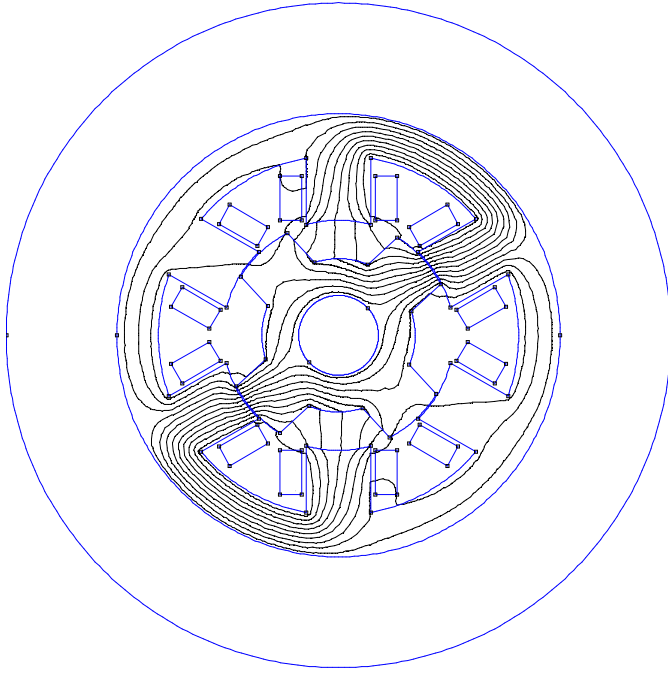
Figure 3.31: Illustration of the mutual flux between the two excited phases and the unexcited one. The additive flux in the stator yokes between adjacent excited poles is also shown. The subtractive flux in the other stator yokes is also shown.

It can be noticed from Fig. 3.30 (b) that the stator yoke flux density is DC-biased bipolar with a frequency equivalent to the excitation current frequency. This makes sense because during the commutation of the phases, the total flux in the stator yoke can be either the summation of the flux of the two phases or the subtraction of both of them. This can be seen from Fig. 3.31. The flux is additive in the stator yokes between two adjacent excited stator poles and subtractive in the other yokes.

The flux density at the middle of the rotor poles and yokes is shown in Fig. 3.32.

As the rotor pole flux reverses every half rotor revolution, the frequency of the rotor pole flux equals the frequency of the excitation current divided by the number of the rotor poles. For the 6/4 case study machine, the frequency of the rotor flux density is one fourth of the current frequency. Fig. 3.32 shows the rotor flux density for half rotor revolution. It can be noticed from Fig. 3.32 that the rotor flux density is DC-biased bipolar. The construction of the rotor pole flux is highly dependent on the rotor position and the state of excitation of the stator phases. If only one phase is excited and no overlap area between the stator pole and the rotor pole, the rotor pole flux is almost zero. If only one phase is excited and there is an
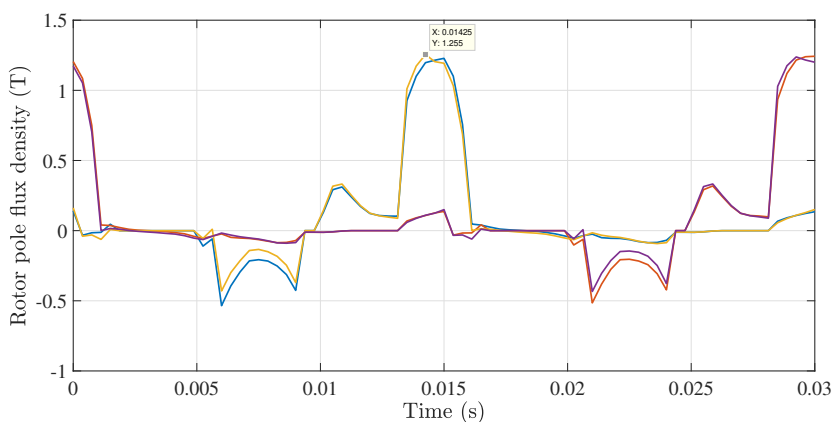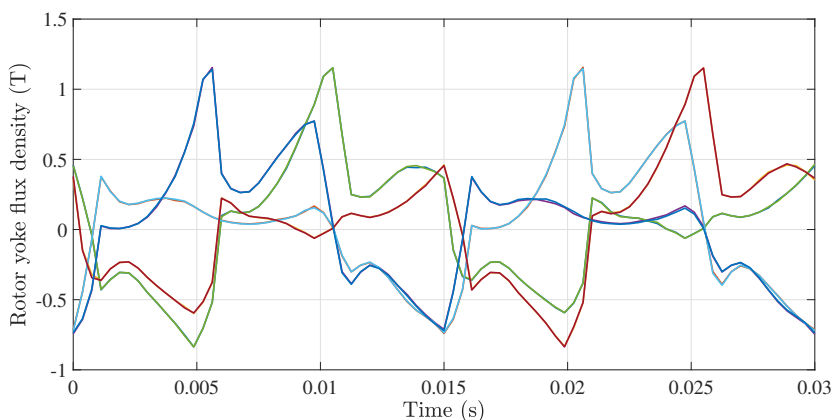
Figure 3.32: The flux density waveforms of the rotor of the 6/4 SRM case study (a) at the middle of the rotor poles and (b) at the middle of the rotor yokes.

overlap area between the stator pole and the rotor pole, the rotor pole flux is the same as the stator pole flux. If the rotor pole is between an incoming and outgoing phase in the cross conduction period, the rotor pole flux is the summation of the flux of the two commutating phases. In other positions, the rotor pole flux is zero. The negative flux in the rotor pole flux density waveform results from the fringing flux lines.

The rotor yoke flux density has the same frequency as the rotor pole and DC-biased bipolar waveform. If only one phase is excited, the rotor yoke flux is the same as the stator pole flux. If two phases are commutating, the rotor yoke flux

can be either the subtraction or the summation of their respective stator pole fluxes depending on the location of the rotor yoke with respect to the commutating phases. The direction of the rotor yoke flux depends on the rotor position with respect to the excited phase.

The small divisions of the core area at which the stator and the rotor core losses are computed is shown in Fig. 3.33.
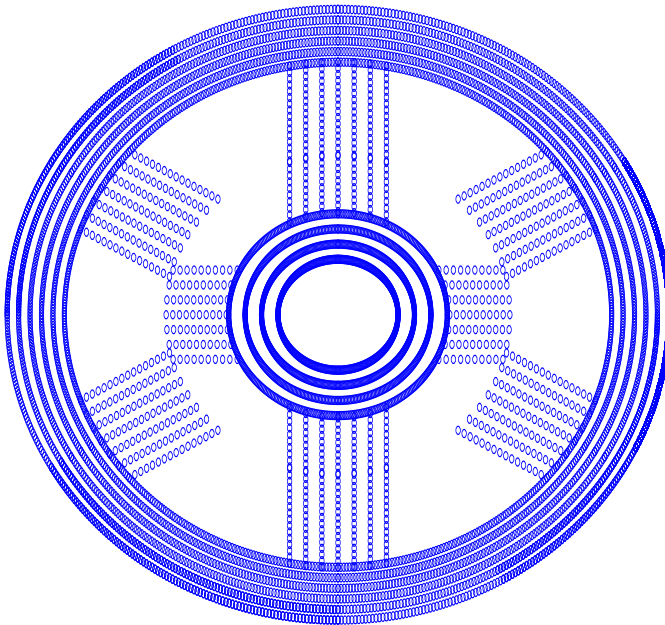
Figure 3.33: The SRM core divisions at which the core loss is computed.

The loss density distribution in the stator and the rotor cores of the 6/4 case study SRM at 2 Nm and 1000 rpm is shown in Fig. 3.34. The rotor has higher loss density than the stator. This depends on the nature of the flux density waveform (the number of local flux slope reversals and the rate of change of the flux density). The flux density in the rotor is bipolar everywhere which increases the chance of having higher hysteresis loss component in the rotor. A local high loss density can be observed on the rotor pole parts that overlap with the stator poles during the phase excitation. This makes sense as these parts have the highest flux density as the whole flux generated by the excited phase passes through these parts causing saturation. This high local flux density causes high hysteresis losses. The stator

pole has high local loss density in the part that overlap with the rotor pole for the same reason. The stator yoke area overlapping with the stator poles has smaller loss density compared to the rest of the stator yoke because the flux generated by the stator coils splits in the stator yoke before reaching this area causing small local flux density in these parts (see Fig. 3.31).
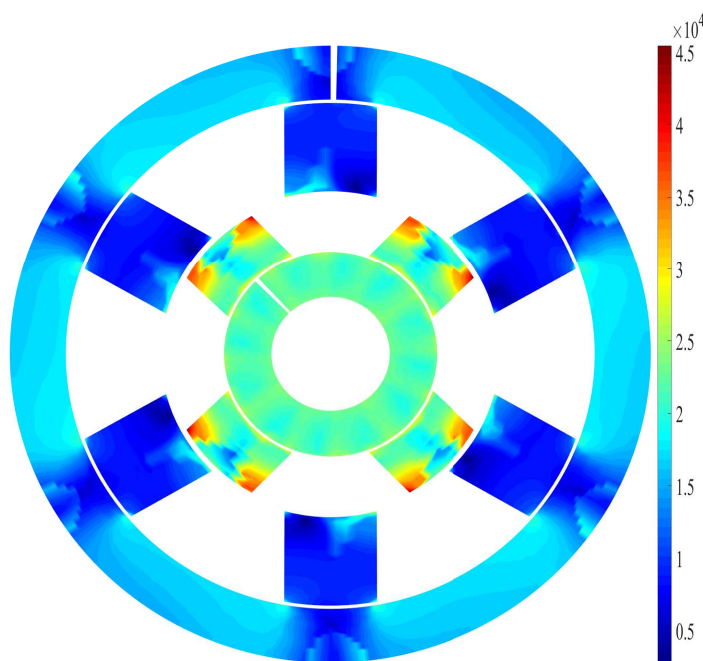
Figure 3.34: The SRM core loss density (W/m^3) distribution at 2 Nm and 1000 rpm.

The stator and the rotor core loss maps of the 6/4 SRM case study are computed up to 5500 rpm and 3 Nm and reported in Fig. 3.35 (a) and (b) respectively. The total stator core loss is higher than the total rotor core loss because of the bigger mass of the stator.

As the speed increases, the frequency of the flux density increases which would tend to increase the core loss. At the same time, the higher speed means higher back-emf. This higher back-emf limits the rate of rise of the phase current which in turn limits the rate of rise of the flux density and tends to decrease the core loss (the dynamic part). The high back-emf tends to increase the rate of fall of the phase current which in turn increases the rate of fall of the flux density and tends to increase the core loss. Therefore, as a synthesis of these effects, the core loss

would be expected to increase with the speed. This core loss increase with the speed is not monotonic as can be seen from Fig. 3.35 because the minor hysteresis loops and the value of the peak flux density are also influencing the core losses and both of them depend on the specific current waveform at each speed. This current waveform depends not only on the torque value but also on the turn-on and the turn-off angles.
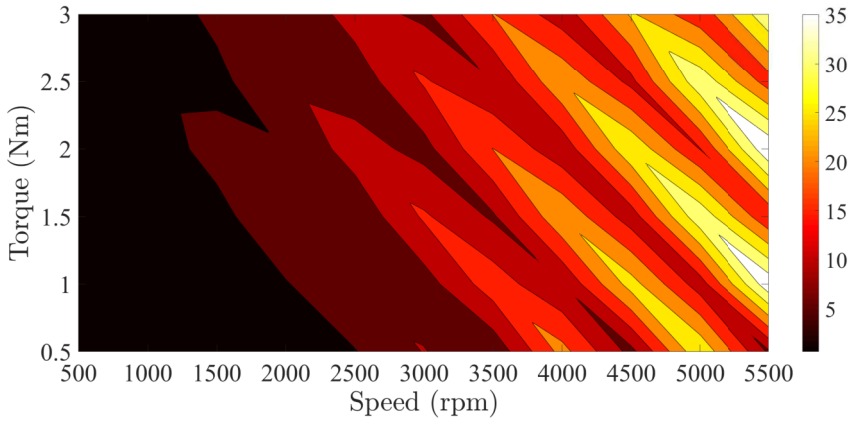
(a)
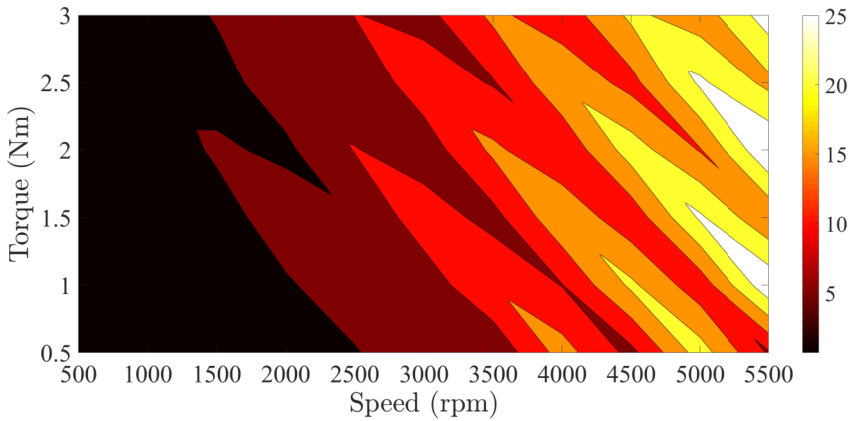
(b)

Figure 3.35: The SRM core loss (W) map for (a) the stator core and the rotor core (b) up to 5500 rpm and 3 Nm.

3.8 Thermal modelling of the water cooled SRM

The 3D finite element and the lumped parameter thermal network modelling (LPTN) of the switched reluctance machines are discussed in this part.

3.8.1 SRM geometry and thermal boundary conditions

A cross-section of the 6/4 SRM case study is shown in Fig. 3.36. This machine has a doubly salient construction. The stator consists of six coils with concentrated windings. The stator core has a pole-yoke construction with the coils wound around the poles. Axially extended end-winding inserts are added to the stator to increase the contact surface area between the end-windings and the ambient [65]. The rotor has a pole-yoke construction without windings or permanent magnets.
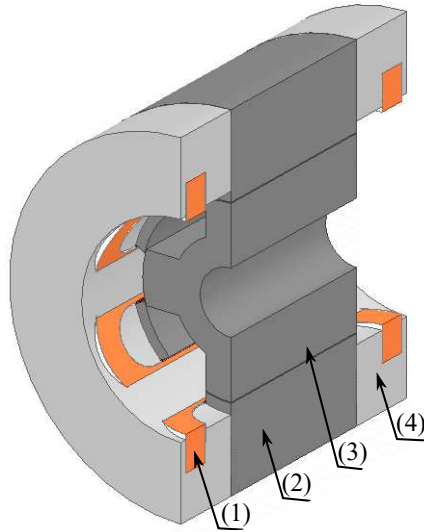
Figure 3.36: The construction of the 6/4 SRM case study: (1) stator coil, (2) stator core, (3) rotor core, (4) end-winding insert.

The SRM is cooled with a water jacket having the construction and the water trajectory shown in Fig. 3.37. The full SRM geometry with the water jacket cooling is shown in Fig. 3.38.

Due to the symmetry of the stator and the rotor construction, only a quarter stator pole and a quarter rotor pole are modelled. The modelled stator and rotor geometry of the SRM are shown in Fig. 3.39.

The stator and the rotor of the SRM have two types of thermal boundary conditions. Thermal symmetry which is described by (3.9) and convection which is described by (3.10). The exposed surfaces of the stator are the surfaces in contact

(a)   (b)
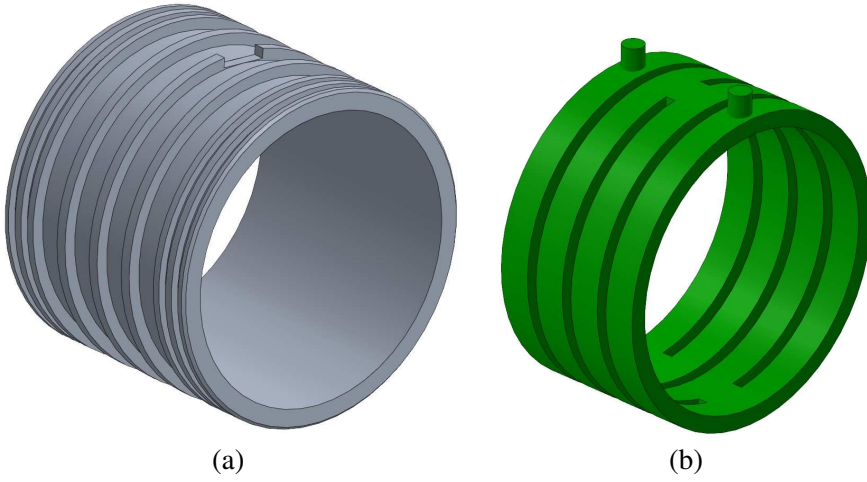
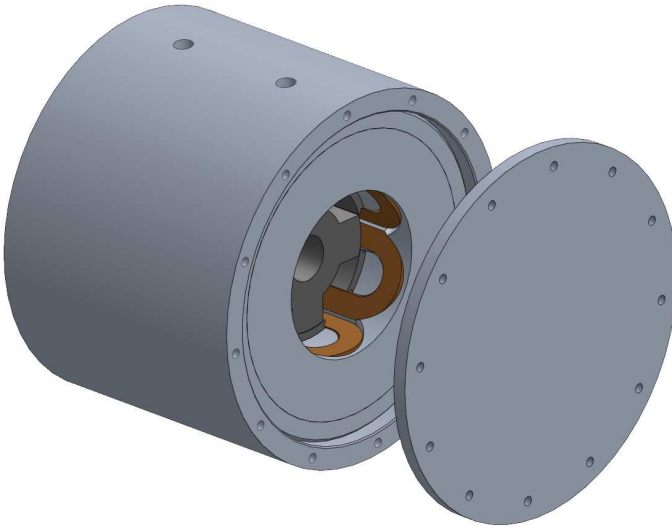Figure 3.37: The internal structure (a) and the water trajectory (b) of the SRM water jacket.

Figure 3.38: The full construction of the water cooled SRM.

with the water jacket and the surfaces exposed to the air gap. The exposed surfaces of the rotor are the surfaces exposed to the air gap.

The convection coefficient of the surfaces in contact with the water jacket is calculated using a CFD model of the water jacket shown in Fig. 3.37.

The convection coefficient of the surfaces in contact with the water jacket is
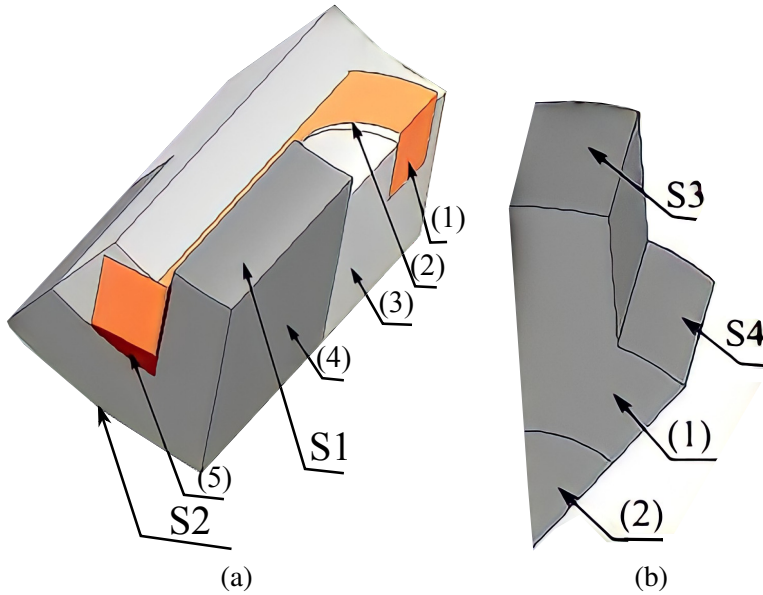
Figure 3.39: The geometry of the 3D parts considered for the SRM thermal modelling: (a) the stator model: (1) the winding, (2) the slot liner (thermal insulation paper), (3) end-winding insert, (4) the stator core, (5) epoxy. S1 is the airgap exposed surface with h_{airgap}. S2 is the surface in contact with the water jacket with h_{SRM}. (b) the rotor model: (1) the rotor, (2) the shaft. S3 and S4 are the airgap exposed surfaces with h_{airgap}.

calculated at different flow rates considering an inlet water temperature of 25°. At each flow rate, the average temperature of the surface in contact with the water jacket is calculated at different imposed power losses on this surface. After that, the difference between the average temperature of the surface and the average temperature of the water is plotted versus the power loss imposed on the surface. The slope of the resulting figure gives the reciprocal of the convection coefficient multiplied by the surface area. An example for the resulting figure at 10 Litre/min flow rate is given in Fig. 3.40. As can be seen, the temperature difference varies linearly with the imposed surface power loss. The resulted average convection coefficient versus the water flow rate is shown in Fig. 3.41.

The convection coefficient of the air gap exposed surfaces can be determined from the Nusselt number which expresses the enhancement in the heat transfer
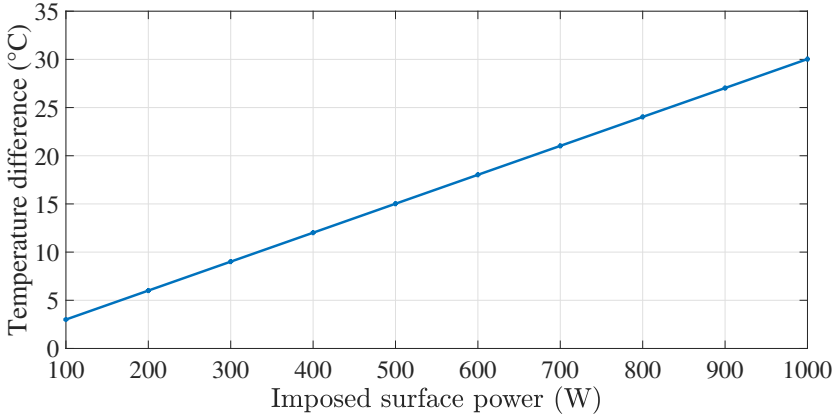
Figure 3.40: The temperature difference between the surface in contact with the water jacket and the water at 10 Litre/min water flow rate.
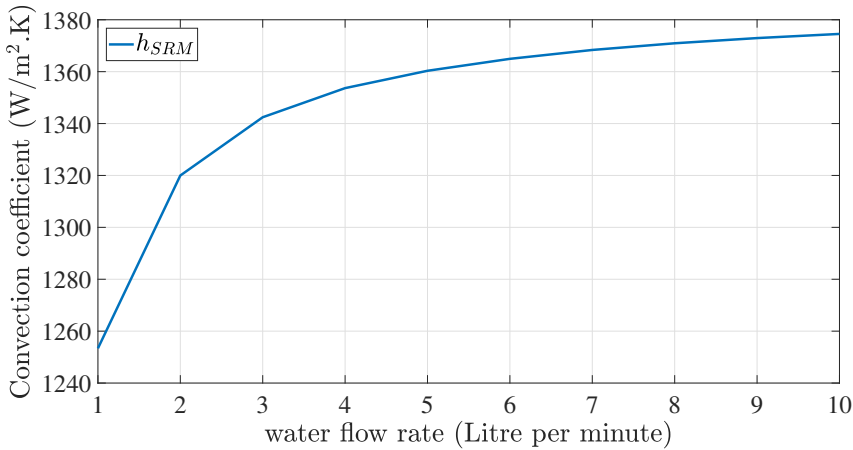

Figure 3.41: The average convection coefficient of the SRM surface in contact with the water jacket.

caused by the movement of the fluid near the convected surface compared to the stationary state of the fluid, the characteristic length of the fluid which is the air gap length in case of air gap convection and the thermal conductivity of the air [112]. The convection coefficient can be calculated from (3.57).

$$h_{airgap} = \frac{k_{airavg}Nu}{g} \qquad (3.57)$$

where h_{airgap} is the airgap convection coefficient, k_{airavg} is the average thermal conductivity of the air and g is the air gap length.

Different CFD based correlations are developed in the literature for the calculation of Nusselt number [113]- [114]- [85]. The Nusselt number depends on the geometry of the SRM, the air properties, the rotational speed and the flow regime. The flow regime is determined from the modified Taylor number [85]. Taylor studied the air flow between two concentric cylinders with smooth air gap in between with outer stationary cylinder and inner rotating cylinder (which is the case of the SRM except of having non-uniform air gap). The modified Taylor number can be calculated from (3.58) [85].

$$
\begin{aligned}
p1 &= 0.0571 \left(1 - 0.652 \frac{g}{R_1} \right) + 0.00056 \left(1 - 0.652 \frac{g}{R_1} \right)^{-1} \\
F_g &= \frac{\pi^4}{1697 p1} \frac{2R_1 + g}{2R_1 + 2g} \\
T_{am} &= \frac{\omega^2 R_m g^3}{F_g \nu^2}
\end{aligned}
\tag{3.58}
$$

where

- R_1 is the rotor pole arc radius, ω is the angular speed of the rotor, ν is the kinematic viscosity of the air and T_{am} is the modified Taylor number.

- R_m is the equivalent air gap mean radius. An expression for calcualting R_m is given in (3.59) [85].

$$
\begin{aligned}
R_m &= \frac{b}{\ln \left(\frac{R_1 + b}{R_1} \right)} \\
b &= \frac{2\pi R_2^2 - A_{rlam}}{2\pi R_1}
\end{aligned}
\tag{3.59}
$$

where R_1 is the rotor pole arc radius, R_2 is the stator pole arc radius and A_{rlam} is the area of the rotor lamination.

The air flow regime is determined from the value of the modified Taylor number. The flow regime can be laminar, laminar with vortices or turbulent [85]. In the laminar flow regime, the air layers flow in a steady organized way. In laminar flow with vortices, the air flows in a steady way with local rotational velocity field (vortices). In the turbulent flow, the air flows in a chaotic unsteady way. As the speed of the motor increases, the flow type transitions from laminar to turbulent and the convection coefficient increases. The correlations for calculating the Nusselt number for each flow type are given in (3.60) [85].

$$Nu = \begin{cases} 1 \rightarrow T_{am} < 1740 \rightarrow \text{laminar} \\ 0.064T_{am}^{0.367} \rightarrow 10^4 > T_{am} > 1740 \rightarrow \text{laminar with vortices} \\ 0.205T_{am}^{0.241} \rightarrow T_{am} > 10^4 \rightarrow \text{turbulent} \end{cases} \quad (3.60)$$

Taylor correlations are derived for smooth cylindrical surfaces. In [85] it is shown that the convection coefficient can increase or decrease by about 20% depending on the flow type due to the slotting effect. So, for the SRM in case of laminar flow, the convection coefficient estimated by (3.57) is decreased by 20% while in case of turbulent flow, it is increased by 20%.

To completely describe the boundary condition on a convective surface, both the convection coefficient and the temperature of the fluid should be specified. For the surfaces in contact with the water jacket the average water temperature is considered. The average water temperature is calculated from (3.61).

$$\Delta T_w = \frac{P_s}{\rho_w C_{pw} Q_w}$$
$$T_{wavg} = T_{win} + \frac{\Delta T_w}{2} \quad (3.61)$$

where ΔT_w is the water temperature rise, P_s is the SRM stator power loss, ρ_w is the water mass density, C_{pw} is the specific heat capacity of the water, Q_w is the water flow rate, T_{win} is the inlet water temperature and T_{wavg} is the average water temperature.

For the air gap exposed surfaces, the air temperature cannot be considered equal to the ambient temperature because the part of the heat that transfers from the stator and the rotor to the air gap raises the air temperature. The air temperature can be determined from the experimental measurements or the LPTN model [112]. In this thesis, the air temperature is determined from the LPTN model developed for the SRM and presented in section (3.8.2).

The material parts of the heterogeneous parts of the SRM are modelled with the same way presented in section (3.3.4). The heterogeneous parts of the SRM are the windings, the cores and the end-winding insert. Table 3.12 lists the thermal properties of the materials of the SRM.

The heat sources of the SRM are the power losses in the windings, the stator core and the rotor core. The winding losses are calculated with the same way discussed in (3.5.3). The core losses are calculated as presented in (3.7.2). The losses distribution of the different parts of the SRM is assumed to be uniform over the volume.

3.8.2   The SRM lumped parameter thermal network

A 3D lumped parameter thermal network model is developed for the SRM geometry shown in Fig. 3.39. The thermal resistances and capacitances of the different

Table 3.12: Thermal properties of the SRM materials

Material	k(W/mK)	C_p(J/kgK)	ρ(kg/m^3)
copper	385	392	8890
End-winding insert	167	896	2712
impregnation material (epoxy)	0.4	600	1540
slot liner	0.2	1600	1140
steel	28	480	7850

nodes are derived as presented in section (3.4.2). The air gap node connects the lumped parameter network of the stator and the lumped parameter network of the rotor.

The lumped parameter thermal model of the SRM rotor is shown in Fig. 3.42. The lumped parameter thermal network of the SRM stator is shown in Fig. 3.43. The full LPTN model of the SRM has 40 nodes. Due to the surface roughness of the core laminations, contact air gaps exist between the stator core and the water jacket. This contact resistance depends on the surface roughness, the materials in contact and the contact pressure [83]. This contact gap is represented by an interface air gap. The typical range of this gap for iron-aluminium contact surfaces is from 0.006 mm to 0.06 mm [83]. This contact resistance is taken into account as a series resistance with the convection resistance.
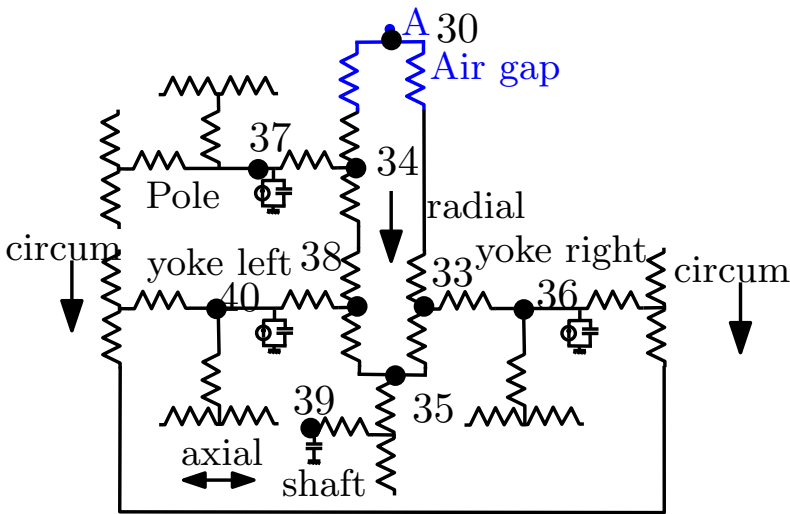
Figure 3.42: The lumped parameter thermal network of the rotor of the SRM.

radial

axial

Pole Middle

5

11

29

Air gap

A

30

Pole Lower

21

26

17

1

Eff. Wind

2

Yoke Middle 3

8

7

Pole Upper

32

15

Yoke Left

25

16

23

13

6

Yoke Right

Insert Effective

Rconv+Rcont

Circumferential

10

20

End. Windtwo

Axial

Insert End heart

12

Eff. Wind

1

9

4

18

End. Windone

insert INCC effe

14

Rconv+Rcont

6

Insert Effective

24

insert right

Yoke Right

27

19

insert Middle1

Yoke Middle

31

22

insert Left

Yoke Left

32

28

insert Middle2

Winding nodes
Core nodes
End-insert nodes
slot liner nodes
Epoxy nodes
Stator to water jacket node
End-insert to water jacket node
Stator to airgap node

Figure 3.43: The lumped parameter thermal network of the stator of the SRM.

3.9   Conclusion

Due to the close proximity of the power converter and the electric machine in the integrated modular motor drives, studying the thermal performance of both the power converter and the electric machine is crucial to ensure that the heat generated by the electric machine is not destructive to the power converter. Electromagnetic and thermal models are both needed to perform such a study. Using the electromagnetic model, the core losses can be computed. Subsequently they can be used as heat sources in the thermal model. The electromagnetic and thermal modelling of the YASA axial flux permanent magnet synchronous machine and the switched reluctance machines are studied in this chapter.

An analytical electromagnetic model developed by former colleagues for the YASA axial flux machine is used. A brief explanation of this model is provided in this chapter. This model finds the flux density distribution in the YASA machine using combined solution of Maxwell's equations and magnetic equivalent circuit. This model has the advantage of being much faster than the FE models. Using this model, the heat sources of the core and the permanent magnets are calculated.

Lumped parameter thermal models and finite element thermal models are both developed for the YASA machine to study its thermal performance. The lumped parameter thermal model is a kind of coarse discretization of the geometry to compute the average temperature of the different components of the machine. Each discrete element in the modelled geometry is represented by a thermal network of resistances, capacitances and heat sources. The LPTN solves the thermal problem in a faster way than the finite element model. This has a particular advantage in the design optimization of the machines.

Due to the unipolar current excitation and the non-linear behaviour of the SRMs, the study of their electromagnetic and thermal performance requires accurate computation of the winding current waveform. The winding current waveform is highly dependent on the finger prints and the control strategy of this machine. Therefore, the torque control of the SRM is studied in this chapter through dynamic simulations of the whole drive (i.e. the SRM, the converter and the controller).

Different flux density waveforms with different frequencies are existing in the core of the SRM. Using the current waveform computed by the dynamic simulation model and a developed 2D electromagnetic finite element model of the SRM, the flux density waveforms in the different parts of the SRM are computed. Using the loss separation method and a modified hysteresis loss computation method, the core loss at different parts of the SRM is computed.

It is found that the flux density in the core of the SRM can be either unipolar or DC-biased bipolar with the same frequency of the excitation current which is the case of the stator flux density or with lower frequency as in the case of the rotor flux density. High local saturation in the rotor and the stator poles that depend on the turn-on and the turn-off angles are noticed. Due to the bipolar nature of the rotor pole flux density and the small area of flux density saturation, the rotor pole

shows the highest local loss density. The total losses in the rotor core are found to be smaller than those of the stator core due to the smaller volume of the rotor.

Both LPTN and finite element thermal models are developed in this chapter for the SRM. In case of SRM machines, LPTN models are crucial for the computation of the air temperature rise in the air gap to use it as part of the convection boundary condition of the air gap exposed surfaces.

Chapter 4

Modelling of Modular Power Converters

4.1 Introduction

Thermal modelling of the power converter modules is required to compute the temperature of the different components of the module PCB to ensure reliable operation of the integrated modular motor drive. These components are the power switches, the power diodes, the gate drive integrated circuit (IC) and the PCB. The temperature of these components should be kept below the rated value for the entire operating region of the integrated drive. The rated junction temperature of most of the commercial power switches and power diodes is 150°C for the Silicon (Si), the Gallium Nitride (GaN) and the Silicon Carbide (SiC) technologies. Some SiC devices have a rated junction temperature of 175°C [35]. The rated temperature of most of the commercial gate drive ICs is 125°C. The rated temperature of the PCB laminate which is FR4 in most of the PCBs is 130°C.

Temperature rise of the power converter modules occurs due to the power dissipation of the components and the heat conduction through the PCB. The main power dissipation components of the converter module are the power devices and the gate drive IC. These losses are used as inputs to the FE model and the thermal networks. Therefore, the computation of the power losses of these components is crucial for computing the temperature of the power converter components.

Thermal modelling of power converter modules can be conducted using the finite element (FE) method or thermal networks [66]. FE modelling gives more accurate results but it requires a high computational time compared to the thermal networks and it also requires the detailed internal geometry and material properties of the power devices. The detailed geometry and materials of the power devices can only be known in case of custom designed devices. Therefore, the power devices are modelled with thermal networks. The PCB and the cooling structure are modelled using FEM and thermal networks.

In this chapter, the average and instantaneous loss models of the power switches and diodes are explained to obtain the input heat sources of the steady-state and the transient thermal models of the modular power converters.

The finite element and the thermal network modelling of the modular GaN based half-bridge inverter module for the CP integrated YASA is discussed in this chapter.

Since the converter parasitics influence the losses in the power devices, an electromagnetic finite element model is developed for the GaN half-bridge inverter module to extract its parasitics. After that, the influence of these parasitics on the losses of the power converter is evaluated.

Also, the finite element and the thermal network modelling of the modular SiC based asymmetric H-bridge inverter module for the PR integrated SRM is discussed in this chapter.

4.2 Fundamentals of thermal modelling of the power converters

The loss models and the thermal network models of the power devices are explained in this section.

4.2.1 Average losses of the power devices

The average power losses of the power switches and diodes are needed for the calculation of the steady state temperature of these devices. The losses in the power devices are divided into conduction losses and switching losses. Both depend on the junction temperature [115].

Average conduction losses of the switches

At steady state, the power MOSFETs can be modelled by a temperature dependent resistor between the drain and the source terminals. The losses in this resistor are called conduction losses. They can be calculated from (4.1). Due to the dependence of the drain to source resistance on the temperature, these losses depend on the junction temperature of the switch.

$$P_{consa} = I_{srms}^2 R_{ds}(T_{sj}) \tag{4.1}$$

where I_{srms} is the RMS value of the switch current and $R_{ds}(T_{sj})$ is the drain to source resistance of the switch as function of the switch junction temperature (T_{sj}).

Average switching losses of the switches

The switching losses of the switches have two components: the overlap losses and the losses due to the output capacitance charging and discharging in each switching cycle [116].

The switch doesn't transition from on to off state and vice versa instantaneously due to the charging and the discharging of the parasitic capacitances. At each transition moment, both the drain to source voltage and the drain current show non-zero values. This overlap between the voltage and the current causes losses. These losses are called the overlap losses and they represent the highest portion of the switching losses. These losses depend on the gate drive parameters, the parasitic capacitances of the switch and the instantaneous voltage and current of the switch.

Fig. 4.1 illustrates the switching losses at the on and off transition moments of the switch.
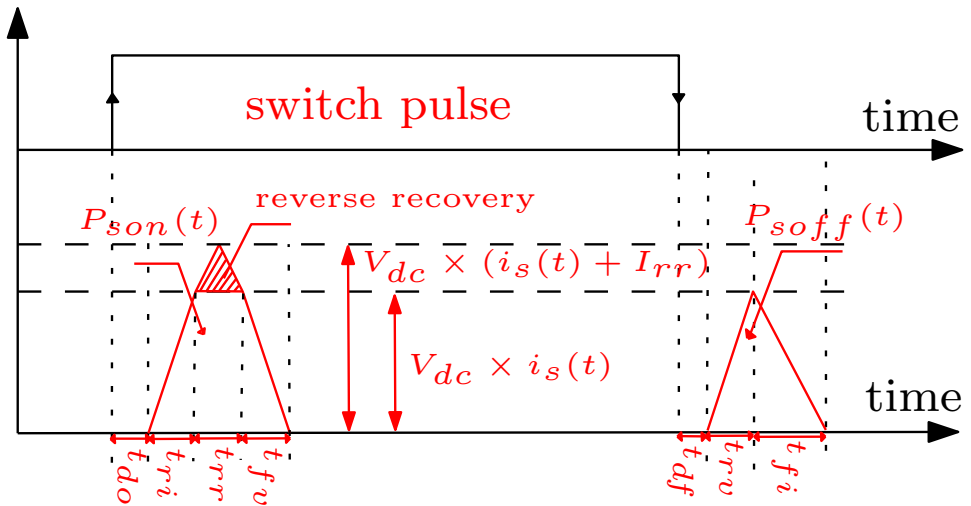
Figure 4.1: The instantaneous turn on and turn off losses in the switches.

Four distinct durations in the turn on transition of the switch can be noticed. The first one is the turn on delay period (t_{do}). During this period, the gate voltage rises to the threshold voltage while the drain current and voltage remain unchanged. The second one is the current rise period (t_{ri}). During this period, the current commutates from the diode to the switch while the voltage on the switch is fixed at the DC-link value. The third one is the diode reverse recovery period (t_{rr}). During this time, the switch current rises above the load current by the reverse recovery current of the diode while the switch voltage is fixed at the DC-link value. The fourth period is the voltage fall period (t_{fv}). During this period the current of the

switch remains constant at the load current while the voltage across it decreases from the DC-link value to the fully on value. These durations can be calculated from (4.2) [117].

$$
\begin{aligned}
t_{ri} &= R_{gon} C_{iss} \ln \frac{V_{gon} - V_{th}}{V_{gon} - V_{plat}} \\
t_{fv} &= \frac{(V_{dc} - R_{ds} i_s(t)) R_{gon} C_{rss}}{V_{gon} - V_{plat}}
\end{aligned}
\tag{4.2}
$$

where R_{gon} is the turn on external gate resistance, V_{gon} is the turn on gate drive voltage, C_{iss}, C_{rss} are the input capacitance and the miller capacitance of the switch respectively, V_{th}, V_{plat} are the threshold and the plateau voltage of the switch respectively.

The average turn on switching loss of the switches is obtained from the summation of the area under the instantaneous turn on power curve shown in Fig. 4.1 at each turn on switching moment for one cycle of the current waveform and then multiplying by the fundamental frequency of the current waveform. Equation (4.3) gives the average turn on switching loss of the switch.

$$
P_{son} = V_{dc} f_o \sum_{n=1}^{n_{son}} (0.5 t_{on}(n, T) i_{on}(n) + Q_{rr}(n))
\tag{4.3}
$$

where P_{son} is the switch turn on loss, V_{dc} is the DC link voltage, f_o is the fundamental frequency of the switch current waveform, n_{son} is the number of turn-on transitions of the switch in one fundamental cycle, $t_{on}(n, T)$ is the turn-on time of the switch at the transition number n and temperature T_{sj}, $i_{on}(n)$ is the switch current at the turn on transition moment and $Q_{rr}(n)$ is the reverse recovery charge of the diode.

Three distinct durations in the turn off transition of the switch can be noticed. The first one is the turn off delay period (t_{df}). During this period, the gate voltage decreases to the plateau voltage while the drain current and voltage remain unchanged. The second period is voltage rise period (t_{rv}). During this period, the reverse transfer capacitance of the switch charges to the DC-link value while the drain current remains constant. The third duration is the current fall duration (t_{fi}). During this duration, the current commutates from the switch to the diode while the voltage across the switch remains constant at the DC-link value. These durations can be calculated from (4.4) [117].

$$
\begin{aligned}
t_{rv} &= \frac{(V_{dc} - R_{ds} i_s(t)) R_{goff} C_{rss}}{V_{plat} - V_{goff}} \\
t_{fi} &= R_{goff} C_{iss} \ln \frac{V_{plat} - V_{goff}}{V_{th} - V_{goff}}
\end{aligned}
\tag{4.4}
$$

where R_{goff} is the turn off external gate resistance, V_{goff} is the turn off gate drive voltage, C_{iss}, C_{rss} are the input capacitance and the miller capacitance of the switch respectively, V_{th}, V_{plat} are the threshold and the plateau voltage of the switch respectively.

The average turn off switching loss of the switches is obtained from the summation of the area under the instantaneous turn off power curve shown in Fig. 4.1 at each turn off switching moment for one cycle of the current waveform and then multiplying by the fundamental frequency of the current waveform. Equation (4.5) gives the average turn off switching loss of the switch.

$$P_{soff} = 0.5 V_{dc} f_o \sum_{n=1}^{n_{soff}} (t_{off}(n,T) i_{off}(n)) \qquad (4.5)$$

where P_{soff} is the switch turn off loss, V_{dc} is the DC link voltage, f_o is the fundamental frequency of the switch current waveform, n_{soff} is the number of turn-off transitions of the switch in one fundamental cycle, $t_{off}(n,T)$ is the turn-off time of the switch at the transition number n and temperature T, and $i_{off}(n)$ is the switch current at the turn off instant.

As the output capacitance of the switch charges to the full DC-link voltage during the off time of the switch and then discharges in the switch itself during the on time, power losses occur in the switch due to this. These losses can be calculated from (4.6).

$$P_{scout} = 0.5 n_{soff} C_{oss} V_{dc}^2 f_o \qquad (4.6)$$

where P_{scout} is the switch loss due to the output capacitance charging/discharging cycle, n_{soff} is the number of turn-off transitions of the switch in one fundamental cycle and C_{oss} is the output capacitance of the switch.

Due to the dependence of R_{ds}, V_{th} and V_{plat} on the junction temperature, the duration of the instantaneous switching loss pulses changes with the junction temperature. Therefore, the switching losses depend on the junction temperature as well.

The total average switching loss of the switches is obtained by summing the overlap losses and the losses due to the output capacitance charging/discharging cycle.

Average conduction losses of the diodes

The power diode dissipates power at steady state due to the voltage drop across its terminals. This voltage drop depends on the current flowing in the diode and the junction temperature of the diode. The variation of the voltage drop across the diode with the flowing current is usually given in the datasheet at two different

junction temperatures. From the instantaneous current of the diode, the instantaneous voltage drop can be obtained at each junction temperature and the average power losses can be calculated from (4.7).

$$P_{cond} = f_o \int_t^{t+T_o} i_d(t) v_d(t, T_{dj}) dt \qquad (4.7)$$

where P_{cond} is the average conduction loss of the diode, $T_o = \frac{1}{f_o}$, $v_d(t, T_{dj})$ is the voltage drop across the diode terminals at the diode junction temperature T_{dj}.

Average switching losses of the diodes

After the complete commutation of the current from the diode to the switch during the turn on transition of the switch, a reverse current flows in the diode from the cathode to the anode to charge the diode body capacitance with the reverse voltage. This process is called diode reverse recovery. As shown in Fig. 4.2, the reverse recovery losses in the diode are approximated by a triangular power loss with duration equal to the reverse recovery time and a peak value equal to $0.5 V_{dc} I_{rr}$ [118].
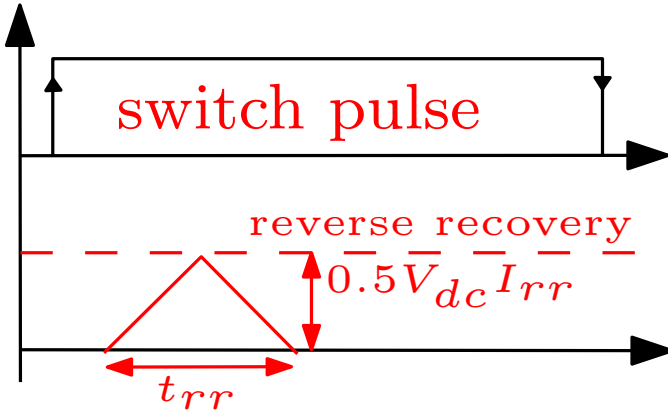
Figure 4.2: The reverse recovery losses of the diode.

The average reverse recovery switching loss of the diode is obtained from the summation of the area under the instantaneous reverse recovery loss power curve shown in Fig. 4.2 at each diode turn off moment for one cycle of the current waveform and then multiplying by the fundamental frequency of the current waveform. Equation (4.8) gives the average reverse recovery switching loss of the diode.

$$P_{sd} = 0.25 V_{dc} f_o \sum_{n=1}^{n_{doff}} Q_{rr}(n) \qquad (4.8)$$

where P_{sd} is the average diode switching loss and $Q_{rr}(n)$ is the reverse recovery charge of the diode at the transition number n and n_{doff} is the number of turn off transitions of the diode.

4.2.2 Instantaneous losses of the power devices

The instantaneous power losses of the power switches and diodes are needed for the calculation of the transient temperature of these devices. The calculations of the instantaneous conduction and switching losses of the switches and the diodes are explained in this part.

Instantaneous conduction losses of the switches

The instantaneous conduction losses of the switches are calculated from the instantaneous switch current and the drain to source resistance of the switch. Equation (4.9) is used for the calculation of the instantaneous conduction loss in the switch.

$$P_{cons}(t) = i_s^2(t) R_{ds}(T_{sj}) \tag{4.9}$$

where i_s is the instantaneous switch current, $R_{ds}(T_{sj})$ is the drain to source resistance of the switch as function of the temperature.

The temperature dependence of the drain to source resistance is taken into account by fitting a polynomial of degree n with the form given in (4.10).

$$R_{ds}(T_{sj}) = [K_1 K_2 \cdots K_{n+1}] \begin{bmatrix} T_{sj}^n \\ T_{sj}^{n-1} \\ \vdots \\ 1 \end{bmatrix} \tag{4.10}$$

where $K_1 \cdots K_n$ are the polynomial coefficients.

Instantaneous switching losses of the switches

The instantaneous turn on and turn off losses are approximated with the linear variations shown in Fig. 4.1. The instantaneous turn off losses are computed from (4.11) at each falling edge of the switch pulses. Similarly, the instantaneous turn on switching loss is computed at each rising edge of the switch pulse.

$$P_{soff}(t) = V_{dc} i_s(t) \int_0^{t_{soff}} [U(t - t_{df}) - U(t - (t_{df} + t_{rv}))] - \\ [U(t - (t_{df} + t_{rv})) - U(t - (t_{df} + t_{rv} + t_{fi}))] \, dt \tag{4.11}$$

where $t_{soff} = t_{df} + t_{rv} + t_{fi}$ and $U(t)$ is the unit step function.

Instantaneous conduction losses of the diodes

The instantaneous conduction losses of the diodes are calculated from the diode output characteristics by multiplying the anode current by the corresponding anode to cathode voltage drop to obtain the instantaneous diode losses versus the diode current. Then, the resulting diode power loss is fitted with the polynomial given in (4.12).

$$P_{cond}(t) = [K_1 K_2 \cdots K_{n+1}] \begin{bmatrix} i_d^n \\ i_d^{n-1} \\ \vdots \\ 1 \end{bmatrix} \tag{4.12}$$

where i_d is the instantaneous diode current and $K_1 \cdots K_n$ are the polynomial coefficients.

Usually the diode characteristics are given at two junction temperatures in the datasheet. To consider the temperature dependence of the diode losses, the constant coefficients of the polynomial (4.12) are replaced by a linear temperature dependent coefficients. For example, K_1 is replaced by $(a_1 T_{dj} + b_1)$. The coefficients a_1 and b_1 are calculated from (4.13).

$$\begin{bmatrix} a_1 \\ b_1 \end{bmatrix} = \begin{bmatrix} T_{dj1} & 1 \\ T_{dj2} & 1 \end{bmatrix}^{-1} \begin{bmatrix} K_1 \mid_{T_{dj1}} \\ K_1 \mid_{T_{dj2}} \end{bmatrix} \tag{4.13}$$

where T_{dj1} and T_{dj2} are the given diode junction temperatures, $K_1 \mid_{T_{dj1}}$ is the polynomial coefficient at temperature T_{dj1}.

Instantaneous switching losses of the diodes

The instantaneous diode switching losses are approximated with the linear variations shown in Fig. 4.2. These losses are calculated from (4.14).

$$P_{sd}(t) = 0.5 V_{dc} I_{rr} \int_0^{t_{rr}} \left[U(t - (t_{do} + t_{ri})) - U(t - (t_{do} + t_{ri} + \frac{t_{rr}}{2})) \right] -$$
$$\left[U(t - (t_{do} + t_{ri} + \frac{t_{rr}}{2})) - U(t - (t_{do} + t_{ri} + t_{rr})) \right] dt$$
$$\tag{4.14}$$

where I_{rr} is the reverse recovery current and $U(t)$ is the unit step function.

4.2.3 Average losses of the gate drive ICs

To compute the temperature of the driving IC to make sure that it stays below the rated value, the power loss of the IC P_{Dic} should be calculated. Equations (4.15)

are used to calculate the losses of the driving IC [119]. The driving IC power losses consist of three terms: the bias loss P_{D1}, the parasitic switching loss P_{D2} and the pull up/down resistance loss P_{D3}.

$$
\begin{aligned}
P_{D1} &= V_{DDI}I_{DDI} + 2V_{DDx}I_{DDx} \\
P_{D2} &= 2f_sC_{int}V_{DDx}^2 \\
P_{D3} &= f_sQ_gV_{DDx}\Big[\frac{R_{pu}}{R_{pu}+R_{gon}} + \frac{R_{pd}}{R_{pd}+R_{goff}}\Big] \\
P_{Dic} &= P_{D1} + P_{D2} + P_{D3}
\end{aligned}
\tag{4.15}
$$

where, V_{DDI}, I_{DDI}, V_{DDx}, I_{DDx} are the input bias voltage, input bias current, the output voltage and the output bias current, Q_g is the gate charge.

4.2.4   Thermal networks of the power devices

The junction to case thermal model of the switches and the diodes can be represented by a Foster or a Cauer network [67]. The Foster network is a behavioural thermal model that consists of four series connected RC blocks. The R and C are connected in parallel in each RC block. Fig. 4.3 shows the Foster network. The Foster network assumes that the heat generated in the die reaches immediately the subsequent layers (insulation layer, solder layer and the case) without any delay. This doesn't reflect the actual physical behaviour of the power device. Due to the thermal capacitance of each layer, the heat generated in the die takes time to heat the die itself and to transfer to the subsequent layers.
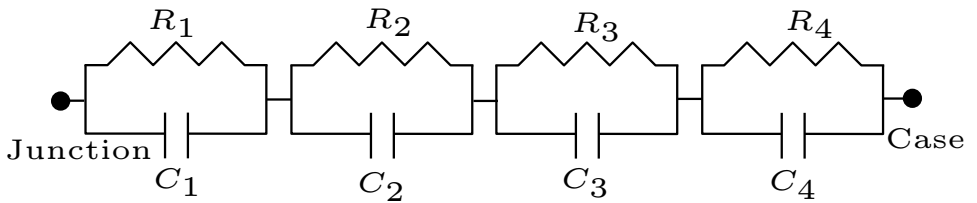
Figure 4.3: Foster network.

The junction to case thermal impedance from a Foster network can be described in the time domain by (4.16).

$$
Z_{th}(t) = \sum_{i=1}^{m} R_i\left(1 - e^{\frac{-t}{\tau_i}}\right)
\tag{4.16}
$$

where m is the number of layers, R_i is the layer thermal resistance, $\tau_i = R_iC_i$ is the layer thermal time constant.

The RC parameters of the Foster network can be obtained by least squares fitting of the thermal impedance curve of the power device given in the datasheet.

Due to the non-true physical behaviour of the Foster network, it cannot be extended by the thermal networks of the rest of the components from the case of the power device to the ambient. So, a network that describes the true physical behaviour of the switch is needed. This network is a Cauer network [120]. Such a Cauer network is shown in Fig. 4.4.
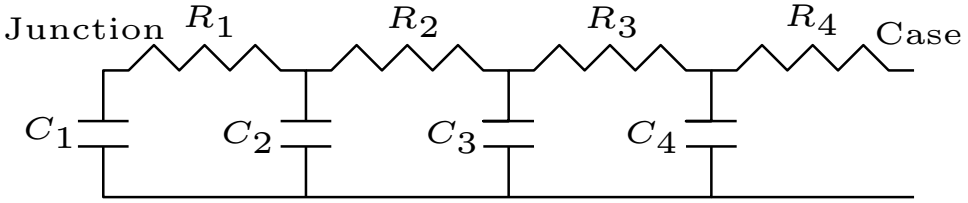
Figure 4.4: Cauer network.

The Cauer network takes into account the time taken by the die to heat up and the heat up delay between the layers by the capacitor located at each layer. The parameters of a Cauer network can be obtained by a Foster to a Cauer network transformation [121].

4.3 Modelling of the half-bridge inverter module of the CP integrated YASA drive

A schematic diagram for the cooling structure of the CP integrated drive introduced in Chapter 2 Fig. 2.7 for the YASA machine is shown in Fig. 4.5. The heat transfer path from the junction to the cooling ambient includes the switch, the PCB, the TIM and the shared cooling structure. The steady-state and transient thermal modelling of these components are discussed in this section.

4.3.1 Steady-state thermal model of the half-bridge module

The steady-state thermal model of the half-bridge inverter module incorporates the derivation of the thermal resistance from the junction of the switch to the cooling ambient. These thermal resistances are the junction to case thermal resistance R_{JC}, the case to PCB thermal resistance R_{CP} and the PCB to ambient thermal resistance R_{PA}. R_{JC} is extracted from the datasheet of the switch.

Case to PCB thermal resistance

The case to PCB thermal resistance depends on the geometry of the switch case, the layer stack design, and the thermal vias pattern beneath the case. The thermal

Figure 4.5: The shared cooling concept with the arrows indicating the heat dissipation path: (1) the switch junction, (2) the thermal pad, (3) the PCB, (4) the thermal interface material, (5) the shared cooling structure, (6) the cooling channel.

vias reduce the thermal resistance from the switch case to the bottom layer of the PCB extensively.

Thermal vias have a heterogeneous structure. Each via consists of a via barrel plated with copper and filled with a solder. This barrel is drilled through the layer stack structure. So, each via is composed of the following materials: copper, PCB laminate (FR4) and the filling solder (SnAgCu). For faster thermal simulations and easier thermal resistance calculations, the PCB part with thermal vias beneath the case of the switch is homogenized using 3-D thermal FEM simulations.

The homogenization process involves the calculation of an equivalent thermal conductivity in each direction (k_{xe}, k_{ye}, k_{ze}), an equivalent mass density (ρ_e) and specific heat capacity (C_{pe}) for the PCB. Fig. 4.6 illustrates the homogenization method for the calculation of k_{ze}. A general rectangular piece of the PCB with populated thermal vias is considered to illustrate the method.

A finite element thermal simulation is performed considering a 1 W loss on the top surface, a constant temperature of 20°C on the bottom surface of the PCB and all other surfaces are considered adiabatic. The maximum temperature of the top surface is calculated from the model. The thermal resistance and the equivalent thermal conductivity in the Z direction can be calculated from (4.17). The calculated thermal resistance in the Z direction is the case to PCB thermal resistance R_{CP}.

$$R_z = \frac{T_t - T_b}{P_{loss}}$$
$$k_{ze} = \frac{L_z}{R_z A_z}$$

(4.17)

where R_z is the thermal resistance in the Z direction, T_t is the calculated maximum
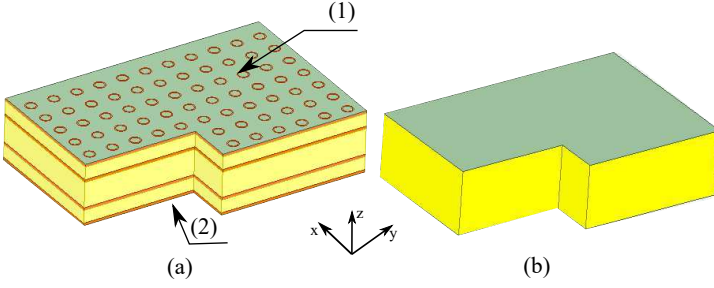
Figure 4.6: Illustration of the PCB homogenization (a) non-homogeneous PCB: (1) PCB top surface, (2) PCB bottom surface (b) homogenized PCB.

temperature of the top surface of the PCB, T_b is the imposed temperature on the bottom surface, P_{loss} is the power loss imposed on the top surface of the PCB, k_{ze} is the thermal conductivity of the PCB in Z direction, L_Z is the PCB thickness and A_z is the area of the top or the bottom surface.

The homogenization is done in a similar way for the x and y directions. The equivalent mass density (ρ_e) and specific heat capacity (C_{pe}) are calculated using the volumetric ratio of each material with respect to the total volume of the PCB part under homogenization. C_{pe} and ρ_e can be calculated from (4.18) and (4.19) respectively.

$$C_{pe} = C_{pcu}\frac{v_{cu}}{v_t} + C_{pfr4}\frac{v_{fr4}}{v_t} + C_{psolder}\frac{v_{solder}}{v_t} \qquad (4.18)$$

$$\rho_e = \rho_{cu}\frac{v_{cu}}{v_t} + \rho_{fr4}\frac{v_{fr4}}{v_t} + \rho_{solder}\frac{v_{solder}}{v_t} \qquad (4.19)$$

where C_{pcu}, C_{pfr4}, $C_{psolder}$ and ρ_{cu}, ρ_{fr4}, ρ_{solder} are the specific heat capacities and mass densities of the copper, FR4 and the solder respectively. v_{cu}, v_{fr4}, v_{solder} are the volumes of the copper, FR4 and the solder respectively and v_t is the PCB part total volume.

PCB to ambient thermal resistance

From Fig. 4.5, the R_{PA} has three components: two conduction components through the thermal interface material (TIM) and the aluminium shared cooling structure, and one convection component through the cooling fluid. Although the calculation of the R_{PA} is sufficient for the steady state cooling performance analysis, the breakdown of this resistance into its components gives an insight into the heat transfer from the bottom of the PCB to the cooling fluid and makes it possible to model the transient temperature accurately.

For calculation of the R_{PA} and its three constituting components, the three curves are generated using the CFD model of one integrated module of the CP

YASA machine. These curves are the temperature difference between the PCB bottom surface and the ambient, the TIM bottom surface and the ambient, the inner wall of the cooling channel and the ambient versus the switch losses. The slopes of these curves give the R_{PA}, the TIM to ambient thermal resistance R_{TA} and the convection resistance of the channel inner wall R_{conv}. From these thermal resistances, the TIM thermal resistance R_{TIM} and the aluminium shared cooling structure thermal resistance R_{AL} can be calculated from (4.20).

$$R_{TIM} = R_{PA} - R_{TA}$$
$$R_{AL} = R_{TA} - R_{conv}$$

(4.20)

Steady-state thermal network

Fig. 4.7 shows the detailed steady-state thermal model from the junction of the switch to the ambient. The junction temperature can be obtained by solving the simple equation (4.21).
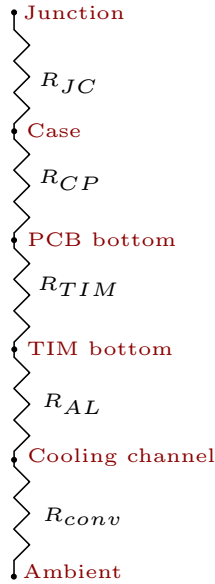
Figure 4.7: The steady state thermal model from the inverter switch junction to the ambient (cooling fluid).

$$T_{sj} = T_A + P_{sw}R_{JA}$$

(4.21)

where T_{sj} is the switch junction temperature, T_A is the ambient temperature, P_{sw} is the switch loss and R_{JA} is the junction to ambient thermal resistance of the switch.

4.3.2   Transient thermal model of the half-bridge module

The transient thermal model is required for calculation of the peak temperature of the switches. Calculation of the peak junction temperature is crucial to ensure reliable operation of the switches. The fast switching speed of the WBG switches can cause a high voltage spike over the switch due to the parasitic inductance of the circuit. This voltage spike can cause avalanche breakdown of the switch. This avalanche breakdown can only be avoided if the energy content of the voltage spike is below the avalanche energy and the peak instantaneous junction temperature is below the rated value.

The transient thermal network modelling from junction to ambient of the half-bridge module of the CP integrated YASA machine is explained in this part. The junction to case thermal model of the switch is represented by a Cauer network discussed in section (4.2.4).

The case to ambient model includes the PCB, the TIM, the aluminium shared cooling structure and the convection in the cooling fluid. Each of these components is represented by a first order RC network. The R part is the same as the ones discussed in section(4.3.1). Due to the localised heat generated by the switches, the thermal capacitance of each part is calculated from the equivalent heat transfer volume V_{eq} of the part which is calculated from the distance travelled by the heat through the part L_{eq}, the thermal conductivity of the part K_{eq} and the thermal resistance of the part R_{eq}. The thermal capacitance of each part C_{eq} is calculated from (4.22). The resulting transient thermal model from the junction to the ambient is shown in Fig. 4.8.

$$C_{eq} = \rho_{eq} V_{eq} C_p$$
$$V_{eq} = \frac{L_{eq}^2}{R_{eq} K_{eq}} \tag{4.22}$$

where C_{eq} is the equivalent thermal capacitance of the part, ρ_{eq} and C_p are the equivalent mass density and specific heat capacity of the part, V_{eq} is the equivalent thermal volume of the part, L_{eq} is the distance travelled by the heat through the part, R_{eq} is the equivalent thermal resistance of the part and K_{eq} is the equivalent thermal conductivity of the part.
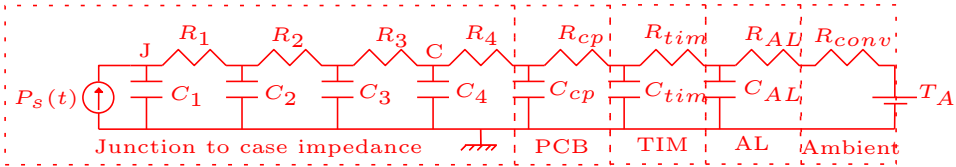
Figure 4.8: The transient thermal model of one half-bridge module of the CP integrated YASA machine.

4.4   Modelling of the asymmetric H-bridge module of the PR integrated SRM drive

A schematic diagram for the cooling structure of the PR integrated drive introduced
in Chapter 2 Fig. 2.10 for the SRM is shown in Fig. 4.9. The schematic of the
asymmetric H-bridge is given in Chapter 3 section (3.6.2). The heat transfer path
from the junction to the cooling ambient includes the junction to case structure of
the device, the PCB, the TIM and the 3D polygon retrofitted part. The thermal
impedance modelling of each of these components is explained in this part.
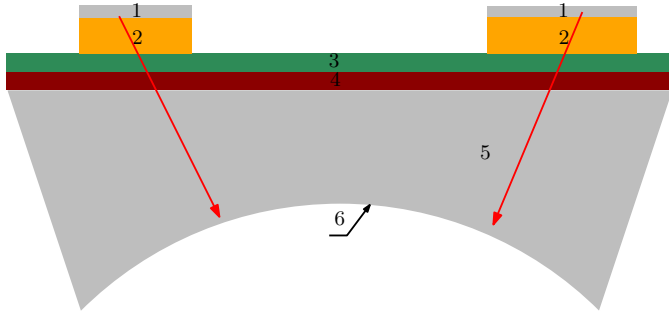
Figure 4.9: The cooling of the asymmetric H-bridge of the PR inte-
grated drive of the SRM with the arrows indicating the heat dissipa-
tion path: (1) the switch/diode junction, (2) the thermal pad, (3) the
PCB, (4) the thermal interface material, (5) the 3D polygon retrofitted
part, (6) the convected surface.

4.4.1   Steady-state thermal model of the asymmetric H-bridge module

From Fig. 4.9, the thermal resistances that need to be modelled in the heat transfer
path from the switch and the diode to the cooling ambient are: the junction to
case thermal resistance of the switch R_{JCs} and the diode R_{JCd}, the case to PCB
thermal resistance of the switch R_{CPs} and the diode R_{CPd} and the PCB to ambient
thermal resistance of the switch R_{PAs} and the diode R_{PAd}. R_{JCs} and R_{JCd} are
extracted from the datasheet of the device.

Case to PCB thermal resistance

The PCB homogenization and the PCB thermal resistance calculation of the switch
and the diode of the asymmetric H-bridge are done in the same way explained in
section (4.3.1) considering the footprint of the selected devices and the thermal
vias pattern designed for them.

PCB to ambient thermal resistance

The three components of the PCB to ambient thermal resistance of the switch R_{PAs} and the diode R_{PAd} are calculated in the same way explained in section (4.3.1) using a 3D thermal finite element model of one integrated asymmetric H-bridge module.

The geometry of one integrated asymmetric H-bridge module is shown in Fig. 4.10. The convection coefficient of the surface in contact with the water jacket h_{PR} is calculated from the CFD model of the water jacket explained in Chapter 3 section (3.8.1). The heat flux generated by the switches and the diodes is imposed on the top surfaces of the PCB parts labelled (1,2,3,4). All other surfaces are considered adiabatic.
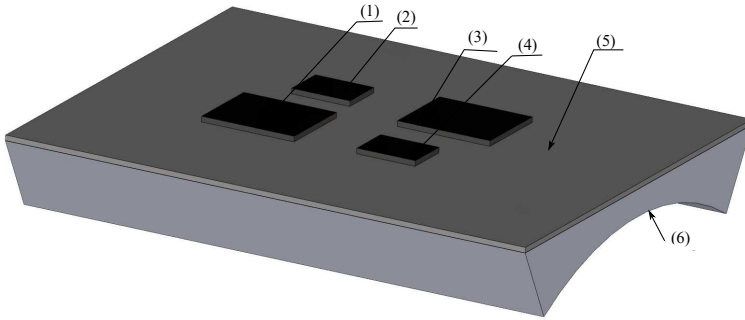
Figure 4.10: The geometry of a single asymmetric H-bridge module considered for the finite element thermal modelling: (1) switch 1, (2) diode 1, (3) switch 2, (4) diode 2, (5) TIM, (6) The surface in contact with the water jacket with the convection coefficient h_{PR}.

The resulted average convection coefficient versus the water flow rate is shown in Fig. 4.11.

Steady-state thermal network

A similar steady state thermal network to the one shown in Fig. 4.7 results for the switch and the diode with the corresponding derived switch and diode thermal resistances.

4.4.2   Transient thermal model of the asymmetric H-bridge module

The junction to case thermal models of the switch and the diode are represented by a Cauer network discussed in section (4.2.4). The case to ambient thermal models of the switch and the diode are derived in the same way explained in section (4.3.2).
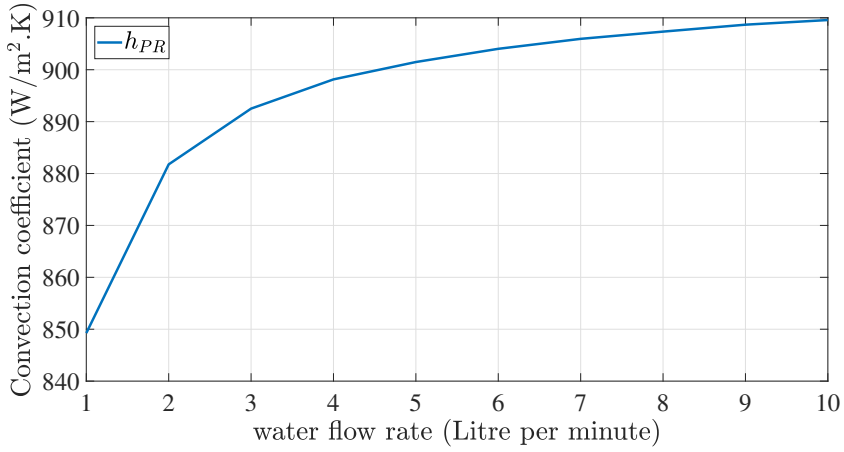
Figure 4.11: The average convection coefficient h_{PR} of the 3D polygon surface in contact with the water jacket.

4.5 Conclusion

The thermal network modelling of the modular half-bridge converter for the CP integrated YASA machine and the asymmetric H-bridge inverter for the PR integrated SRM drive is discussed in detail in this chapter. These models are crucial for the design and optimization of integrated drives.

The average and instantaneous loss modelling of the power switches and power diodes is explained as a mandatory step for the calculation of the heat sources of the inverter for thermal modelling.

A Cauer network is used to model the transient thermal behaviour of the switches and the diodes from junction to case. CFD and 3D finite element thermal modelling are used to compute the thermal impedance of the components from the case of the power device to the ambient. A full steady state and transient thermal models are derived for the switches and the diodes from junction to case.

Chapter 5

Design of the Circumscribing Polygon and Polygon Retrofitted Integration Topologies

5.1 Introduction

The circumscribing polygon and polygon retrofitted integration concepts are introduced in Chapter 2. These integration concepts are applied on a YASA axial flux machine and a switched reluctance machine. The electromagnetic and thermal models of the YASA machine and the SRM are built and explained in detail in Chapter 3. The loss and thermal models of the half-bridge inverter module for the YASA machine and the asymmetric H-bridge module for the SRM are built in Chapter 4. These machine and inverter models are applied in this chapter to design the CP integration topology for the YASA machine and the PR integration topology for the SRM.

The structure of the chapter is as follows:

- The optimal geometrical parameters of the air cooled YASA machine are selected based on several parametric studies performed using the electromagnetic and the thermal models of the YASA machine introduced in Chapter 3.

- The design and optimization of the CP integrated YASA drive is presented. The half-bridge inverter topology is selected for the YASA machine for its small number of switches. The switches are implemented using GaN technology.

- The losses and the thermal model parameters of the CP integrated YASA are evaluated and the results of the finite element and the thermal network models are computed and compared to each other.

- The design and optimization of the PR integrated SRM drive is presented. The asymmetric H-bridge inverter topology is selected for the SRM for its small number of passive components. The power devices are implemented using SiC technology.

- The losses and the thermal model parameters of the PR integrated SRM are evaluated and the results of the finite element and the thermal network models are computed and compared to each other.

- Finally, a conclusion of the chapter is given.

5.2 Selection of the geometrical parameters of the air cooled YASA machine

Three geometrical parameters that influence the losses and the cooling of the air cooled YASA machine presented in Chapter 3 section (3.5.1) are studied in this part for optimal selection of these parameters. These parameters are the thickness of the inward heat extraction fins, the PM thickness and the air gap length. These studies are done using the electromagnetic and the thermal models introduced in Chapter 3 for the YASA machine.

5.2.1 Influence of the thickness of the inward heat extraction fins

This study is performed for the fin thickness range from 0 to 6 mm at rated power and speed. As the thickness of the inward heat extraction fins increases, its axial cross sectional area increases which enhances the heat transfer from the windings to the ambient. But, at the same time, the slot area available for the windings decreases causing higher winding resistance and losses. Thus, the fins thickness should be selected carefully. Fig. 5.1 shows the variation of the different losses with the fin thickness. The minimum winding losses occur at a fin thickness of 0.6 mm.

Fig. 5.2 shows the variation of the temperature of the winding, the stator core and the PM with the fin thickness. The winding and the stator core temperatures decrease for the fin thickness range from 0 to 1.4 mm and then the temperature increases again. The winding and the core temperatures decrease by 8°C at 1.4 mm fins thickness compared to the case without fins.

Fig. 5.3 shows the efficiency variation with the fins thickness. It reduces from 96.1% in the case without fins to 95% at 6 mm thickness. The efficiency doesn't decrease too much at the optimal fin thickness of 1.4 mm.

It can be concluded that the coolest machine is obtained at 1.4 mm fin thickness while the most efficient machine is obtained at 0.6 mm fin thickness.
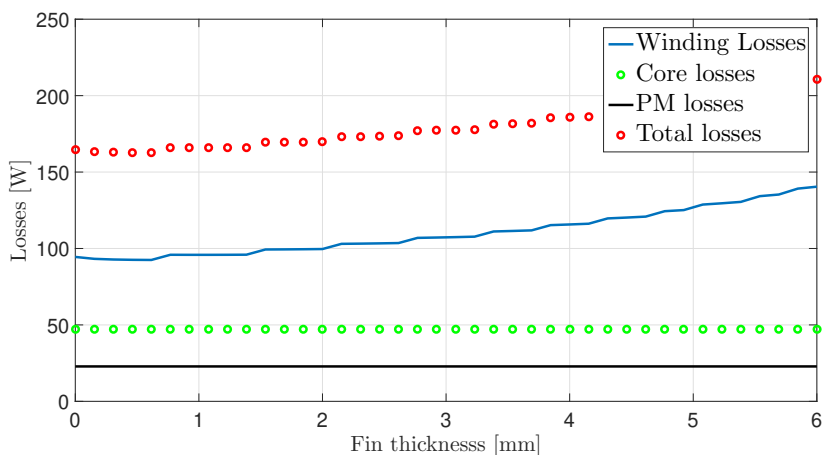
Figure 5.1: The variation of the YASA losses with the fin thickness.
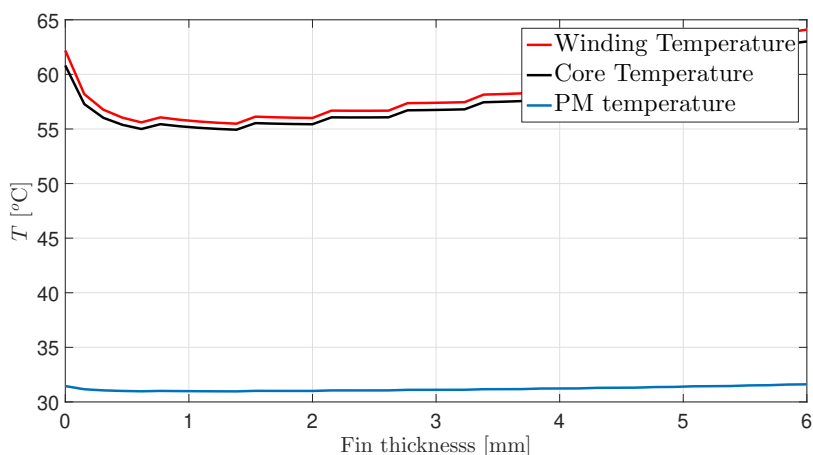
Figure 5.2: The winding, the stator core and the PM temperature variation with the fin thickness.

5.2.2   Influence of the PM thickness

This study is done for a magnet thickness range from 1 mm to 6 mm at rated operating point. The PM thickness affects the flux density, and hence, the losses in the machine. It also affects the air gap convection coefficient.

Fig. 5.4 shows the variation of the losses with the PM thickness. The copper losses keep decreasing with the magnet thickness. This can be explained as follows: as the PM thickness increases, the PM flux density component in the air gap
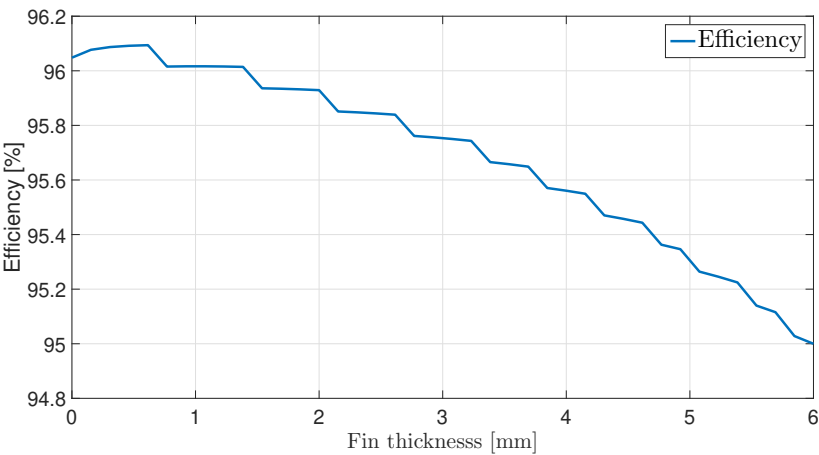
Figure 5.3: The YASA efficiency variation with the fins thickness.

increases and the required stator flux density component to produce certain torque decreases, and hence, the stator current decreases leading to a decreased winding losses.

The PM losses are also decreasing with the magnet thickness. This is due to the smaller stator flux causing smaller induced voltage in the PM and smaller eddy currents.

The core losses don't show a significant discernible variation with the PM thickness indicating no significant variation in the peak flux density of the core.
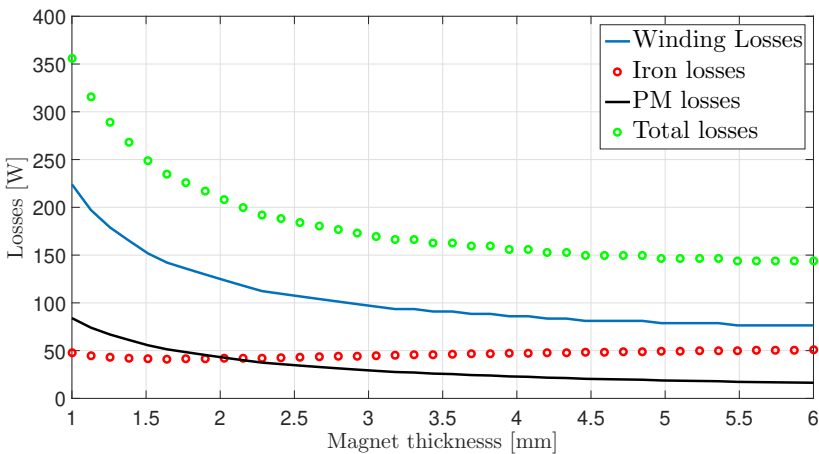
Figure 5.4: The YASA losses variation with the permanent magnet thickness.

The temperatures of the winding, the stator core and the PM are shown in Fig. 5.5. The temperature decreases with the PM thickness due to the reduction in the losses.
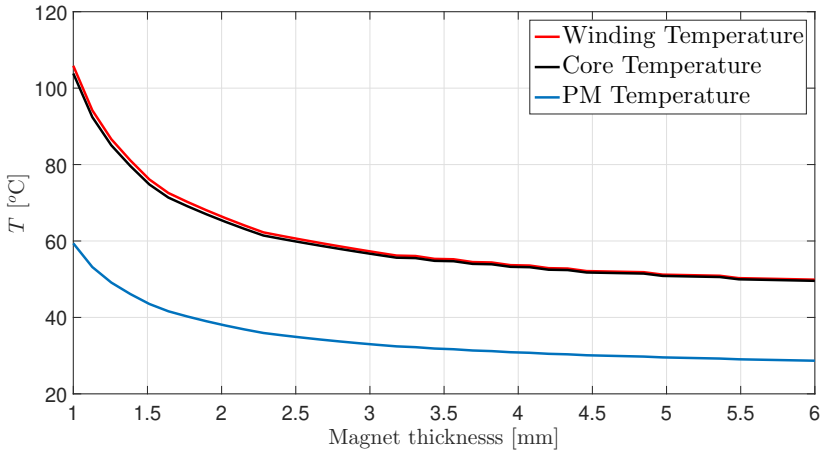
Figure 5.5: The temperature variation with the permanent magnet thickness.

The efficiency is shown in Fig. 5.6. It can be noticed that the efficiency increases with the PM thickness due to the reduction of the losses of the machine.
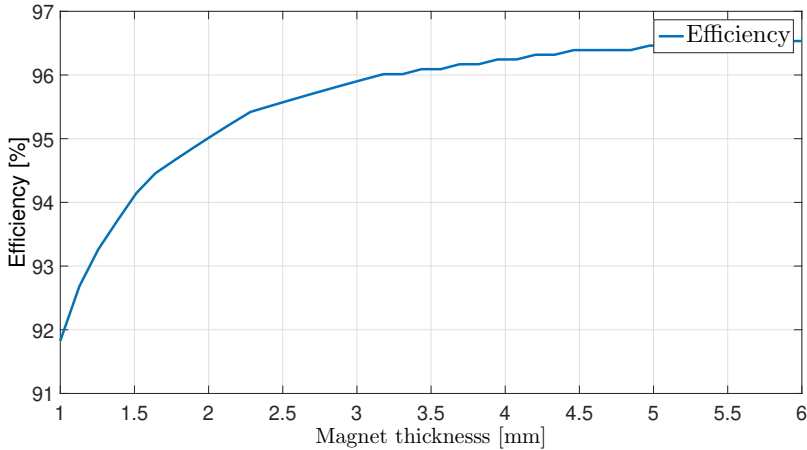
Figure 5.6: The YASA efficiency variation with the permanent magnet thickness.

5.2.3 Influence of the air gap length

The study is done for air gap lengths ranging from 0.6 mm to 5 mm at rated operating point. As the air gap length increases, the current needed to provide the same output torque increases leading to winding losses increase.

Fig. 5.7 shows the losses variation with the air gap length. The winding losses keep increasing with the air gap length as a result of the increasing stator current.

From Fig. 5.8, the iron losses don't show a fixed trend. They decrease until an air gap length of 3.5 mm indicating that the peak flux density decreases until this air gap length. For the air gap lengths higher than 3.5 mm, the core losses increase indicating that the peak flux density increases.

The PM losses keep decreasing with the air gap length as shown in Fig. 5.8 which indicates that the magnetic flux penetrating the PM radially decreases with the air gap length causing lower PM induced voltage and eddy currents.
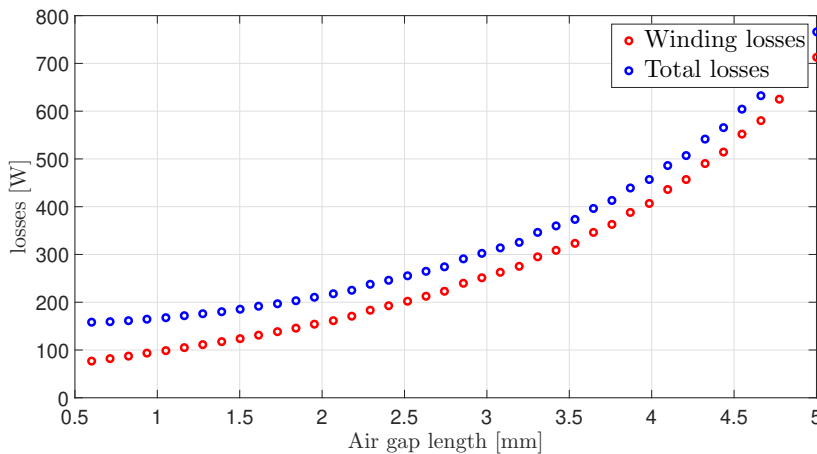
Figure 5.7: The winding and the total losses variation with the air gap length.

Whether the steady-state temperature will increase or decrease with the air gap length depends not only on the losses but also on the change of the air gap convection coefficient. From Fig. 5.9, it can be seen that the air gap convection coefficient reduces with the air gap length. This explains the monotonic increase in the winding and the core temperature with the air gap length as shown in Fig. 5.10.

The PM temperature variation with the air gap length is shown in Fig. 5.11. The minimum PM temperature occurs at the air gap length of 2.7 mm. As the PM losses and the air gap convection coefficient are both decreasing from 0.6 mm to 2.7 mm, a decrease in the PM temperature means that the amount of PM loss reduction with the air gap length is bigger than the amount by which the air gap
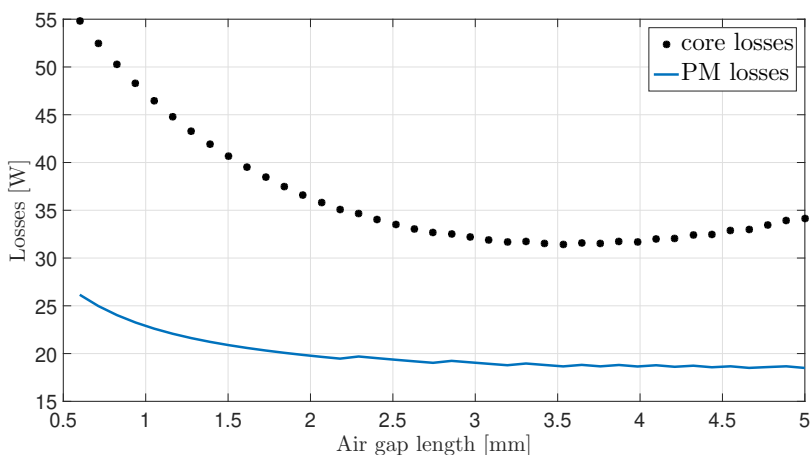
Figure 5.8: The core and the PM losses variation with the air gap length.
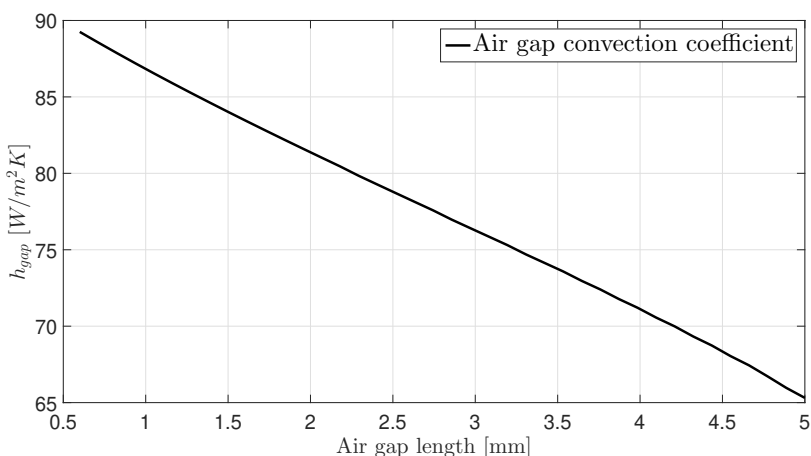
Figure 5.9: The air gap convection coefficient variation with the air gap length.

convection coefficient decreases. The opposite occurs for the air gap lengths bigger than 2.7 mm.

Since the total losses keep increasing with the air gap length, the efficiency shown in Fig. 5.12 keeps decreasing with the air gap length.

Based on the above presented air gap variation effects on the losses and the temperature, it is recommended to keep the air gap length as small as possible to get high operating efficiency and low temperature.
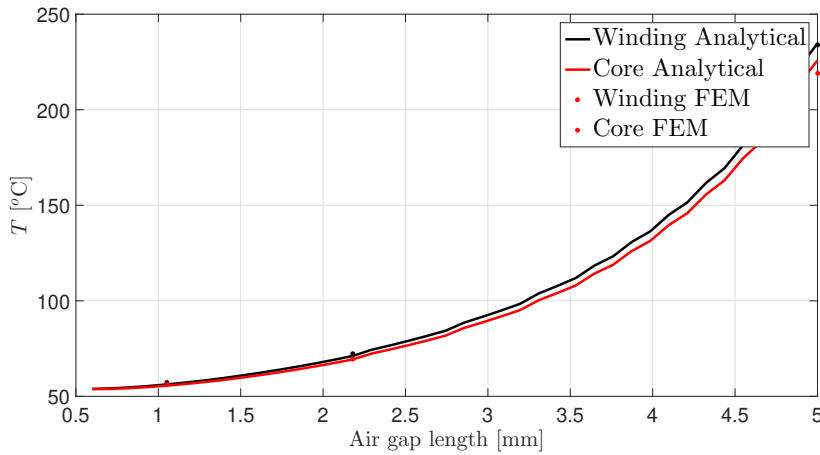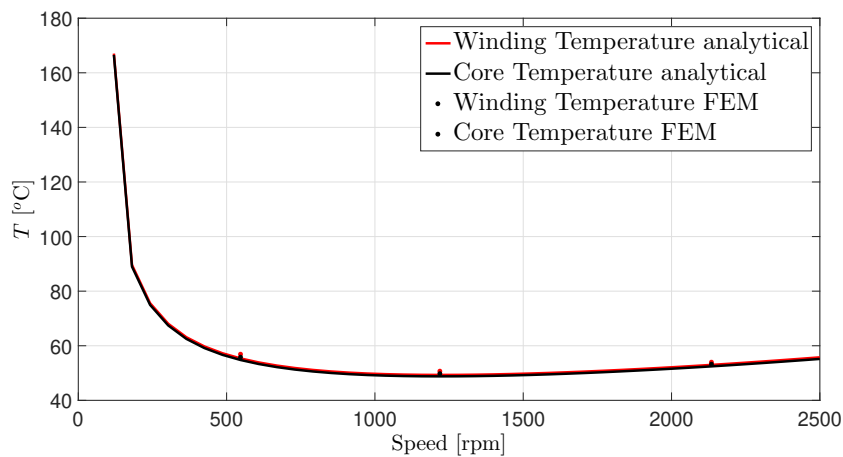
Figure 5.10: The winding and the core temperature variation with the air gap length.
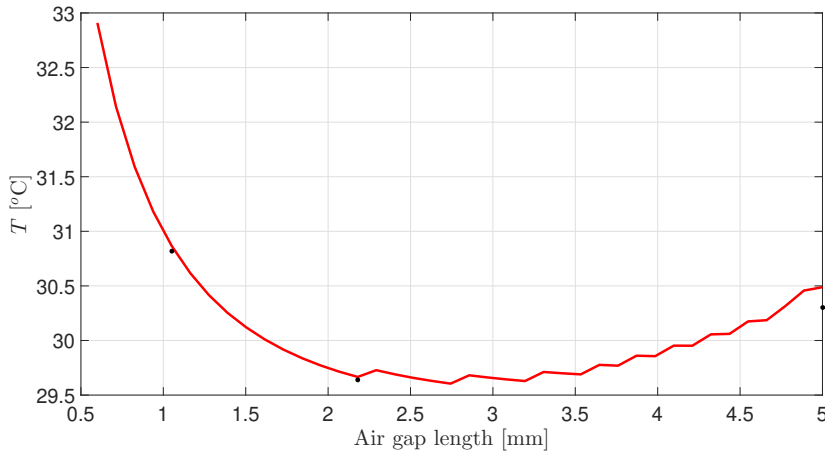
Figure 5.11: The PM temperature variation with the air gap length.

5.2.4 Influence of the rotational speed on the performance of the air cooled YASA machine

The influence of the rotor speed on the losses, the efficiency and the temperature of the different components of the YASA machine is studied in this part. This study is performed for the speed range from 120 rpm to 2500 rpm at a fixed torque of 15 Nm which is the rated torque of the machine. As the speed increases, the supply frequency increases as well. This increase in the frequency and the speed of the
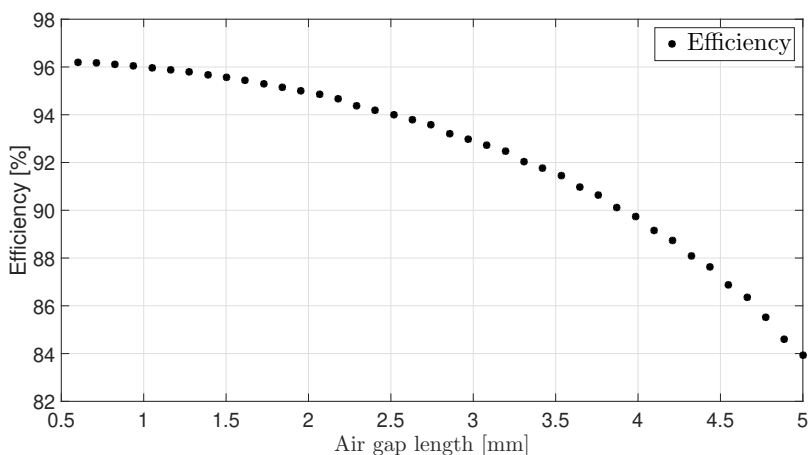
Figure 5.12: The efficiency variation with the air gap length.

machine would result in an increase in the losses of the machine and the airgap convection coefficient. The losses increase would tend to increase the machine temperature while the increase in the airgap convection coefficient would tend to decrease the temperature of the machine. Therefore, the influence of the speed on the losses and the temperature of the machine is studied.

The losses of the different components of the machine and the total losses are given in Fig. 5.13. It can be noticed from Fig. 5.13 that the core and the PM losses increase monotonically with the speed because of the higher hysteresis and eddy current losses in the core and the higher eddy current losses in the PM at the higher excitation frequency. The variation of the air gap convection coefficient with the speed is given in Fig. 5.14. It can be noticed that the convection coefficient increases monotonically with the speed. The temperatures of the winding, the core and the PM are given in Fig. 5.15 and Fig. 5.16 respectively.

The investigation of Fig. 5.13 and Fig. 5.15 reveals that there are three regions for the winding losses. The first one up to speed of 486.2 rpm, the winding losses decrease with the speed. This can be explained as follows: at such low speeds, the skin and the proximity effects have little influence on the resistance of the windings. The temperature of the windings keeps decreasing in this speed range which results in decreasing winding resistance and losses.

The second winding loss region is from 486.2 rpm to 1218 rpm. In this region, the winding temperature is still decreasing but the winding losses increase, which means that the skin and proximity effects became significant and resulted in an increase in the winding resistance rather than decreasing with the decreasing temperature. In the third region, the skin and the proximity effects are significant and the temperature is increasing which results in an increase in the winding resistance and hence the winding losses.
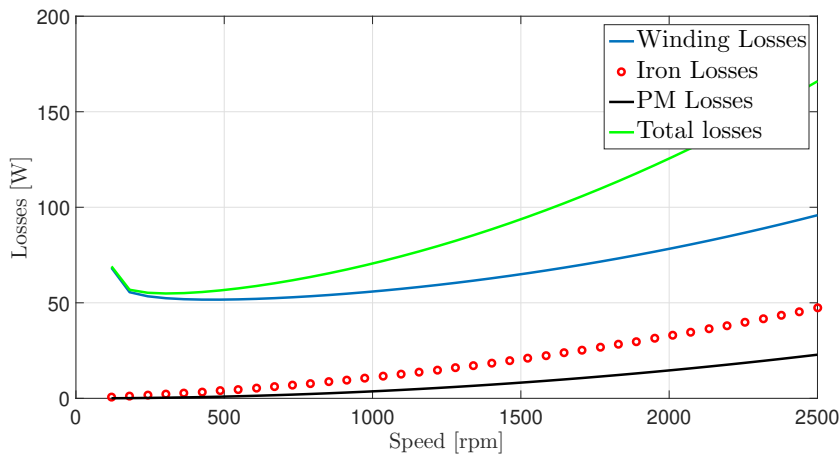
Figure 5.13: The variation of the YASA losses with the rotor speed
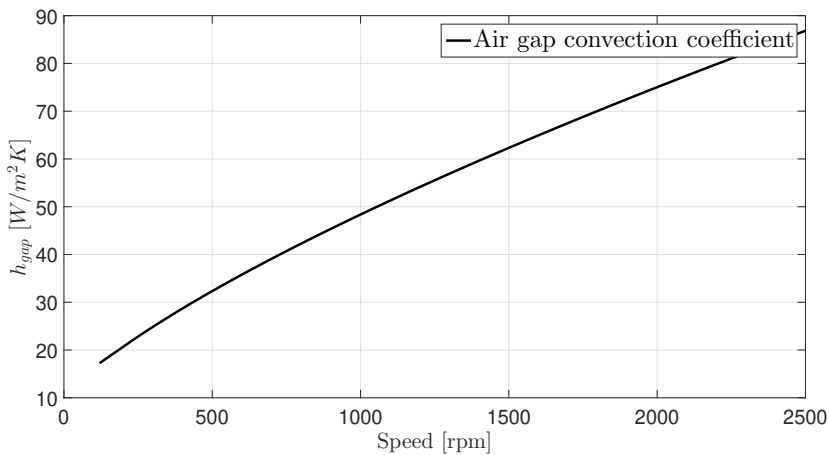
Figure 5.14: The YASA air gap convection coefficient variation with
the speed

The investigation of Fig. 5.16 reveals that the PM temperature has a minimum
at the speed 1035 rpm. Below this speed, the increase in the PM loss with respect
to the speed is lower than the increase in the air gap convection coefficient. Above
this speed, the increase in the PM loss with respect to the speed is higher than the
increase in the air gap convection coefficient

The variation of the efficiency with the speed is shown in Fig. 5.17. It is
observed that the efficiency increases up to the speed 1500 rpm and then it plateaus.
The efficiency increase indicates that the increase of the output power with the

Figure 5.15: The winding and the core temperature variation with the speed
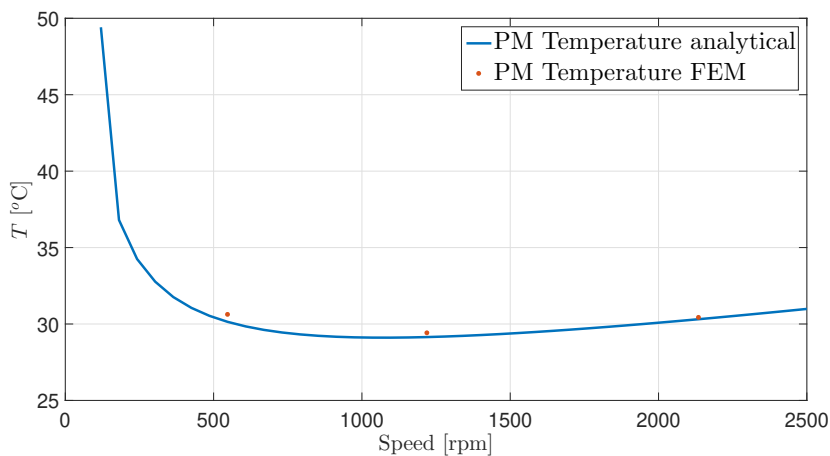
Figure 5.16: The PM temperature variation with the speed

speed is higher than the increase of the total loss with the speed.

5.3 Design of the power converter module for the CP integrated YASA machine

The selection of the inverter switches and the PCB design of the inverter module for the CP integrated YASA machine are explained in this section.
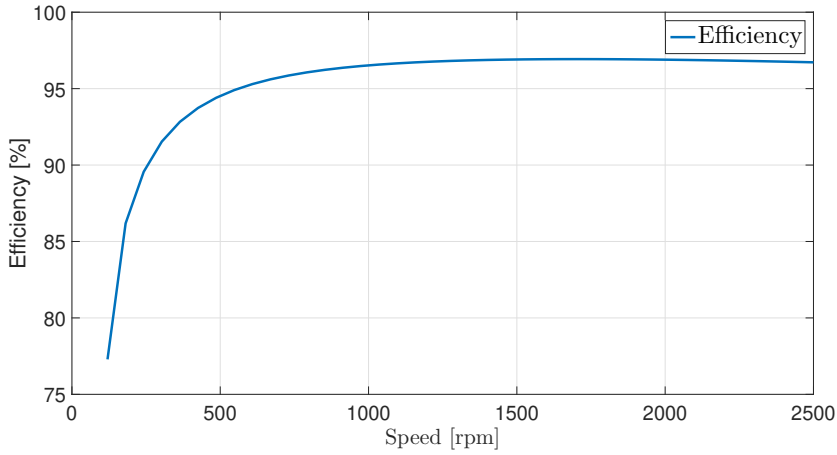
Figure 5.17: The YASA efficiency variation with the speed

5.3.1 Selection of the inverter switches for the CP integrated YASA machine

As explained in Chapter 2 section (2.2), the size of each converter module is limited to 60×40 mm^2, the topology of the converter module should have a small number of power switches, and the power switches should have small power losses and small package size. For these reasons, the half bridge inverter topology shown in Fig. 5.18 is chosen for the converter module design.
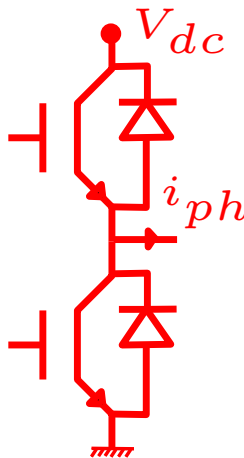
Figure 5.18: The half-bridge inverter topology selected for the converter module design for the YASA AFPMSM.

For the selection of the power switches, four candidate devices with the same voltage and current rating suitable for the application are compared for selection of the switches. Each switch belongs to a different power semiconductor technology in the market (Si, GaN, SiC). Table 5.1 contains the key specifications of the four switches.

Table 5.1: The key specifications of candidate inverter switches

Device	STW38N65M5	GS66508B	SCT3080ALHR	LMG341xR070
technology	Si	GaN	SiC	GaN
rated voltage (V)	650	650	650	600
rated current (A)	30	30	30	30
drain to source resistance $\vert_{25°C}$ R_{ds} (mΩ)	95	50	80	70
gate charge Q_g (nC)	71	5.8	48	-
reverse recovery charge Q_{rr} (nC)	6.6	0	53	0
reverse recovery time (t_{rr})	382	0	15	0
Figure of merit (FOM)	6745	290	3840	-
package size (mm^2)	306.7	60.4	327.6	64
case size (mm^2)	275.6	28.66	275.6	23.25

For selection of one of the power switches from Table5.1, the package size and the power losses of these devices are compared. From Table 5.1, the two GaN devices have the smallest package sizes among the four devices. The figure of merit (FOM) which can be calculated from (5.1) is used as an indication of the total losses in the forward conduction path. The smaller the FOM, the smaller the losses in the forward conduction path. It can be seen from Table 5.1 that the two GaN devices have the smallest R_{ds}. The GaN device GS66508B has the smallest gate charge compared to the SiC and the Si devices. Although Q_g is not defined for the GaN device LMG341xR070, it is expected to be smaller than the Q_g of the SiC and the Si devices due to the higher switching speed of the GaN devices. Therefore, the two GaN devices are expected to have the smallest losses in the forward conduction path. The value of the reverse recovery charge (Q_{rr}) is an indication of the switching losses in the reverse conduction path of the switch. From Table 5.1, the two GaN switches achieve the lowest losses among the three technologies. Thus, one of the GaN switches should be selected for the converter implementation.

$$FOM = R_{ds} \times Q_g \qquad (5.1)$$

For the choice of one of the GaN devices for the converter implementation, the heat flux density of the two GaN devices GS66508B and LMG341xR070 is evaluated at different modulation indices (M). The heat flux density is defined to be the total power losses dissipated by the switch during one fundamental power

cycle divided by the case (thermal pad) area of the device. The heat flux density is considered for the calculation to take into account the influence of the thermal pad area on the heat transfer from the switches. The losses are calculated as explained in Chapter 4 section (4.2.1).

The heat flux density of the two GaN devices is calculated in case of sinusoidal pulse width modulation (SPWM) and space vector pulse width modulation (SVPWM) and the results are shown in Fig. 5.19 and Fig. 5.20 respectively. Both figures are generated at V_{dc} = 400 V, I_{phase} = 9 A, switching frequency of 50 kHz and 150°C junction temperature.
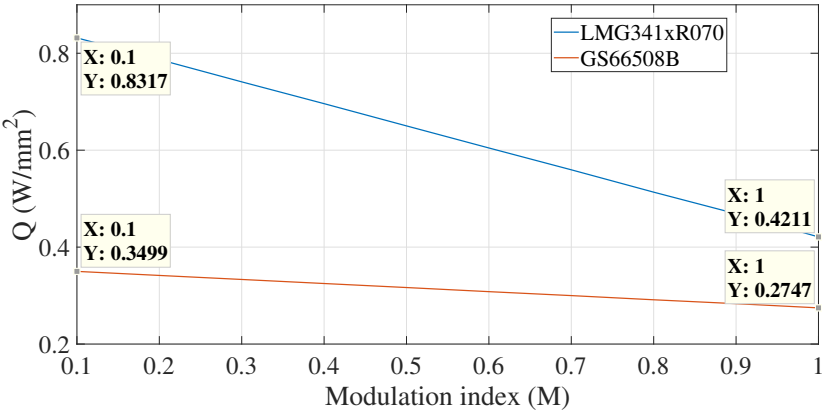
Figure 5.19: The heat flux density for both GaN devices at unity PF versus the modulation index in case of SPWM.
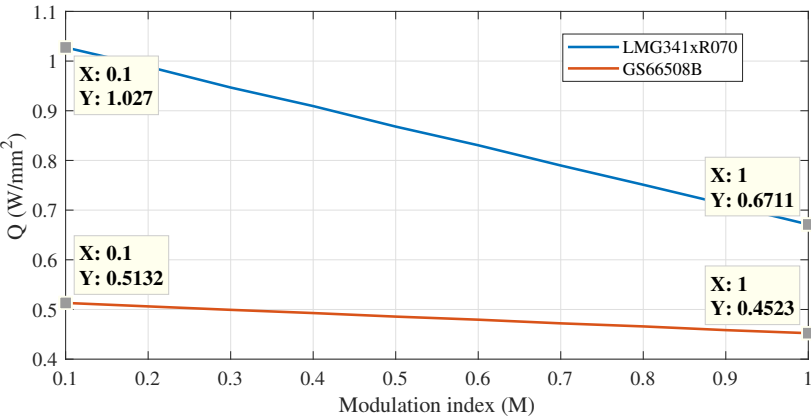
Figure 5.20: The heat flux for both GaN devices at unity PF versus the modulation index in case of SVPWM.

By inspecting Fig. 5.19 and Fig. 5.20, the heat flux density of GS66508B is globally smaller than the other device and this makes it the best choice for the implementation of the integrated inverter module. Also, the power losses generated at SPWM are lower than the SVPWM, which makes the SPWM a better choice for controlling the converter.

From Fig. 5.19 and Fig. 5.20, it can be observed that the power losses decrease with the modulation index. This can be explained by the significance of the conduction losses in the reverse conduction path compared to the forward path due to the high voltage drop on the reverse path compared to the forward path. As the modulation index increases, the forward conduction duration prevails over the reverse one which means lower reverse losses, and hence, total losses reduction with the modulation index.

5.3.2 PCB design of the inverter module for the CP integrated YASA machine

The design of the inverter PCB influences the thermal and the electromagnetic behaviour of the converter [122]. The PCB is designed as a four layer board with the layer stack design shown in Fig. 5.21. The copper layers serve as heat spreaders for better heat transfer [123]. They are also used in effective magnetic field cancellation routing to reduce the parasitics of the converter.
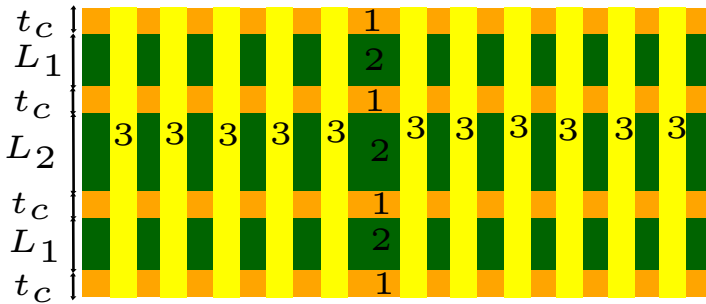
Figure 5.21: The layer stack design of the inverter module PCB: (1) copper layers, (2) PCB laminate, (3) thermal vias. L_1= 0.36mm, L_2= 0.71mm, t_c= 0.07mm.

Two main loops should be carefully routed for proper operation of the inverter module: the power commutation loop and the gate drive loop [124]. The area of both loops should be minimized for reduction of the commutation loop inductance and the gate loop inductance. Ceramic decoupling capacitors of 0.01 μF each are used in parallel with the main DC-link capacitors and routed in a top and a bottom layer as shown in Fig. 5.22.

Thanks to the small equivalent series inductance (ESL) of the decoupling capacitors compared to the main capacitor, the current flows through them rather
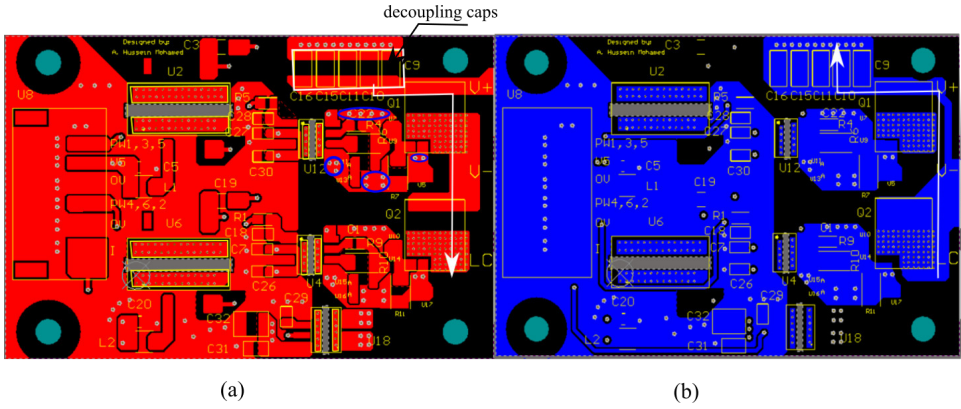
Figure 5.22: PCB copper plot on the top layer (a) and the bottom layer
(b) of the GaN based half-bridge inverter module.

than the main capacitor during the commutation period. The commutation loop is
routed in such away the current during the commutation period flows as indicated
by the white arrows in Fig. 5.22. In this way, the current flows from the decoupling
capacitors through the upper and the lower switches on the top layer and then re-
turns back as a mirror on the bottom layer to cancel the magnetic field, and hence,
reduces the parasitic inductance.

The isolated gate drive IC SI8271GB-IS with the main specifications in Table
5.2 from SILICON LABS is used for driving the switches. It has a small prop-
agation delay, an under voltage lockout (UVLO) of 3 V suitable for the driving
voltage (V_{gon}) of the switch of 6 V and a suitable source/sink current of 4 A. The
external turn on gate resistance (R_{gon}) and turn off resistance (R_{goff}) should be
selected to satisfy the inequalities in (5.2) and (5.3), otherwise the turn on/off speed
of the switch will be limited by the current limit of the driving IC. For this design
case, any value greater than or equal to zero for R_{gon} and R_{goff} would satisfy the
inequalities.

$$R_{gon} \geq \frac{V_{gon}}{I_{on}} - (R_{gint} + R_{pu}) \tag{5.2}$$

$$R_{goff} \geq \frac{V_{gon}}{I_{off}} - (R_{gint} + R_{pd}) \tag{5.3}$$

where I_{on}, I_{off} and R_{gint} are the sink current, the source current of the driving IC
and the internal gate resistance of the switch.

One more inequality that should be satisfied by the selected gate resistances
(R_{gon}) and (R_{goff}) is given in (5.4). The satisfaction of this inequality makes
sure that the switches don't turn on spuriously by the miller current during the
commutation of the switches.

Table 5.2: SI8271GB-IS gate drive IC main specifications

property	value
source/sink current (A)	4
$\frac{dv}{dt}$ immunity	200 kV/μs
maximum propagation delay (ns)	60
under voltage lockout (UVLO) (V)	3
pull up resistance (R_{pu}) (Ω)	2.7
pull down resistance (R_{pd}) (Ω)	1
rated junction temperature (°C)	125
junction to ambient thermal resistance (°C/W)	115

$$(\frac{V_{gon} - V_{plat}}{R_{gon} + R_{gint} + R_{pu}}) \times (R_{goff} + R_{gint} + R_{pd}) < V_{th} \qquad (5.4)$$

where V_{plat} is the plateau voltage of the switch, V_{th} is the threshold voltage of the switch.

The values selected for the R_{gon} and R_{goff} are 10 Ω and 1 Ω respectively.

For extra protection of the switch against spurious turn on, a gate pull down resistor (R_{gpd}) of 10 kΩ and two back to back zener diodes (BZT52C6V8S-7-F) of 6.8V zener voltage are connected between the gate and the source of the switch as shown in Fig. 5.23. R_{gpd} shunts the miller current and makes sure that the switch voltage doesn't reach the threshold voltage during turn off period. The zener diodes clamp the gate voltage to its rated value.

The gate drive components are located as close as possible to the gate of the switch and the same routing method used with the power commutation loop is used. The gate current leaves the gate drive IC to the gate of the switch on the top layer and mirrors back on the below layers in order to minimize the loop area and the gate parasitic inductance.

To make sure that the temperature of the gate drive IC stays below its rated value (125°C), a thermal model from the case of the IC to the cooling ambient is built. Fig. 5.24 (a) shows the thermal model of the IC. To calculate the case to ambient thermal resistance of the IC, a 1 W loss is imposed on the top surface of Fig. 5.24 (a), the bottom surface is considered isothermal at 25°C and all other surfaces are considered adiabatic. The temperature distribution is shown in Fig. 5.24 (b). The peak temperature of the top surface is 172.6°C.
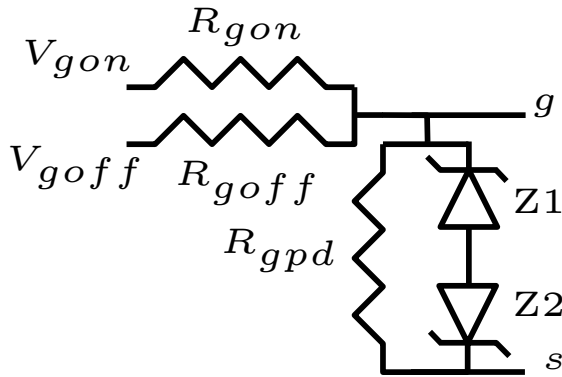
Figure 5.23: Gate protection circuit.

(a)   (b)
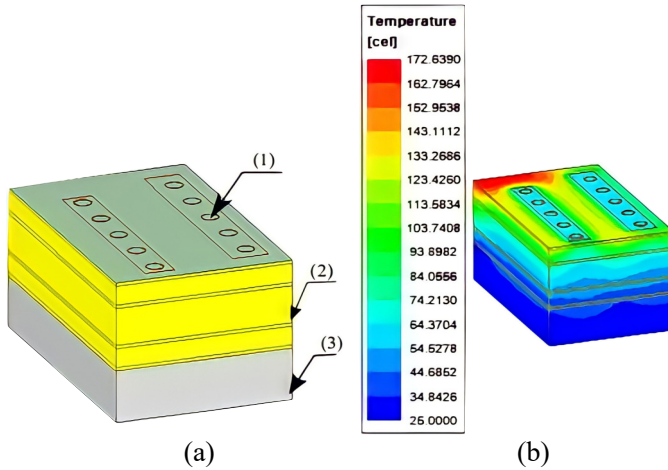
Figure 5.24: Driving IC thermal model (a) geometry: (1) thermal vias,
(2) PCB, (3) TIM, (b) temperature distribution at 1W loss top surface
and 25°C bottom temperature.

From Fig. 5.24 (b), the case to ambient thermal resistance of the IC is
147.6°C/W. The junction to case thermal resistance of the IC is 115°C/W [119].
This means that the junction to ambient thermal resistance of the IC is 262.6°C/W.
The power losses of the gate drive IC are calculated as explained in Chapter 4
section (4.2.3) and the operating conditions in Table 5.3. The value of the losses
is 100.57 mW and the value of the junction temperature is 51.5°C which is lower
than the rated value of the IC.

Fig. 5.25 shows the implemented GaN based half-bridge inverter module for
the CP integrated YASA machine.

Table 5.3: Gate drive loss calculation parameters

parameter	value
V_{DDI} (V)	5
I_{DDI} (mA)	10
V_{DDx} (V)	6
I_{DDx} (mA)	4
Q_g (nC)	5.8
f_s (kHz)	50
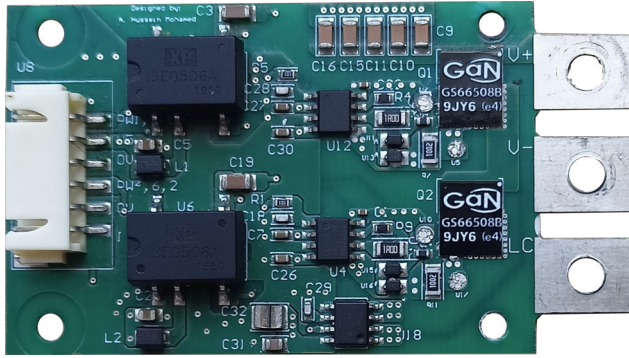
Figure 5.25: The implemented GaN based half-bridge inverter module.

5.4 Optimization of the thermal performance of the CP Integrated YASA AFPMSM

From Fig. 4.5 in Chapter 4, two main heat transfer paths exist: one path from the switches to the cooling fluid and the other path from the YASA AFPMSM stator to the cooling fluid. The thermal path from the switches to the cooling fluid includes the junction to case thermal resistance (R_{JC}), the case to PCB thermal resistance (R_{CP}) and the PCB to cooling fluid thermal resistance (R_{PA}). So, R_{JC}, R_{CP} and R_{PA} should be minimized for optimal heat evacuation from the switches. The only geometrical parameter that can be optimized in the path of the heat transfer from the YASA AFPMSM stator to the cooling fluid is the radius of the cooling channel.

The $R_{JC}= 0.5$ °C/W is defined by the internal structure of the switch and can be extracted from its datasheet. R_{CP} can be minimized by distributing thermal vias beneath the thermal pad of the switch. The selected GaN switch package and the thermal vias pattern populated beneath the switch case and beyond are shown

in Fig. 5.26.

(a)   (b)
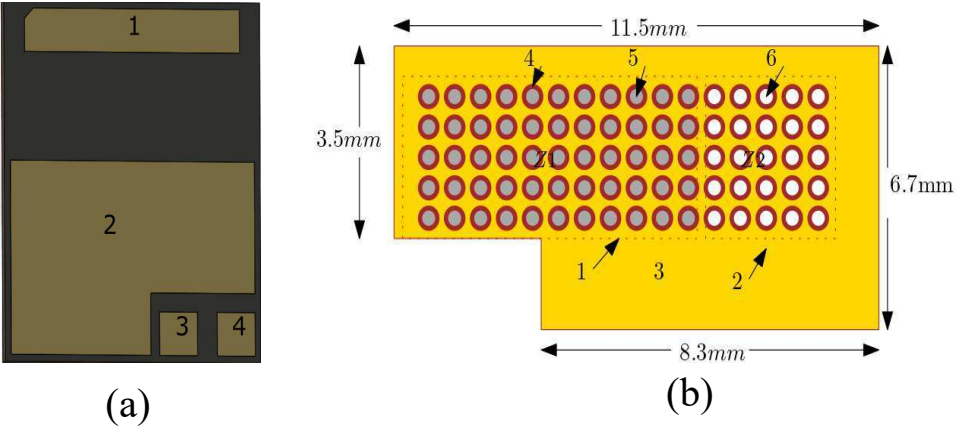
Figure 5.26: Selected switch package and thermal vias pattern (a) switch package: (1) drain, (2) case (source), (3) gate, (4) source sense (b) thermal vias pattern: (1) inner thermal vias beneath the switch, (2) outer zone vias, (3) copper plot, (4) via plating copper, (5) via filling solder, (6) air.

To evaluate the reduction in the thermal resistance resulting from the via pattern in Fig. 5.26 (b), two thermal finite element models are built. One without the thermal vias and the other with them included. The dimensions of the thermal via barrel are given in Table 5.4. The material properties of the different PCB parts are given in Table5.5. The 3D models of the PCB with and without thermal vias are shown in Fig. 5.27 (a) and (b) respectively.

Table 5.4: The dimensions of the thermal via

Quantity	Value
Via outer diameter (mm)	0.35
Thickness of via plating (μm)	25
Via spacing (mm)	0.65

Table 5.5: The thermal properties of the PCB materials

Property	copper (CU)	FR4	air	solder (SnAgCu)
mass density (kg/m^3)	8890	1250	1.1614	7500
specific heat capacity (J/kg.K)	392	1300	1005	250
thermal conductivity(W/m.K)	385	0.35	0.0261	57.3
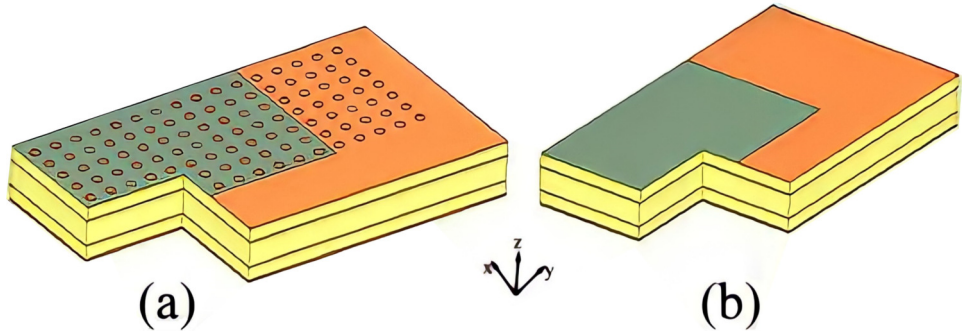
Figure 5.27: The 3D thermal models of the PCB (a) with thermal vias,
(b) without thermal vias.

The boundary conditions are 1W of heat losses imposed on the top part of the
PCB (P_{sw}) while the whole bottom surface is isothermal at a temperature (T_{bottom})
of 20°C, the other surfaces are adiabatic. The temperature distribution over the
PCB part beneath the switch is shown in Fig. 5.28 (a) and (b) for the case without
and with vias respectively. The thermal resistance R_{CP} is calculated from (5.5).
The maximum thermal resistance R_{CP} in the case with and without thermal vias is
2.2 °C/W and 66.9 °C/W respectively. A reduction of about 98.7% in the thermal
resistance R_{CP} results in the case with thermal vias. This significant reduction in
R_{CP} will extremely increase the upper bound of the current that can be supplied
to the motor before reaching the junction temperature limit of the switch.

$$R_{th} = \frac{T_{case} - T_{bottom}}{P_{sw}} \tag{5.5}$$

where T_{case} is the case temperature of the switch.

For the optimization of the heat transfer from the bottom of the converter PCB
to the ambient and the from the stator of the YASA machine to the ambient, the
radius of the cooling channel should be optimized. As the cooling radius increases
the area through which the heat transfer takes place increases which enhances the

(a)   (b)
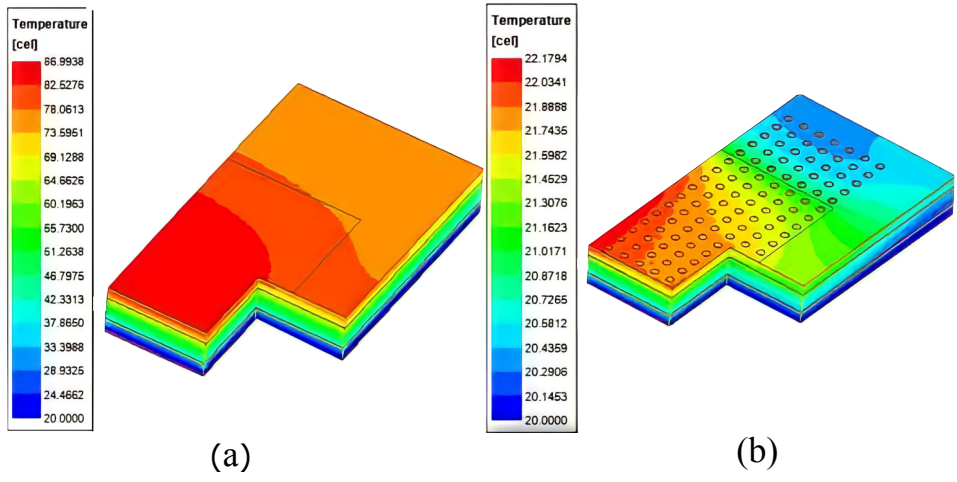
Figure 5.28: The temperature distribution on the PCB part without
thermal vias (a) and with thermal vias (b). These figures are generated
at 1 W loss over the top surface and 20°C over the bottom surface and
all other surfaces are considered adiabatic.

Table 5.6: The thermal properties of the materials of one integrated
CP module for YASA AFPMSM

Module part	Material	ρ (kg/m^3)	C_p (J/kg.k)	K (W/m.K)
Winding	copper	8890	392	385
Core	silicon steel	7650	490	40
Housing	aluminum	2712	896	167
Impregnation	epoxy	1540	600	0.4
Winding insulation	Nomex	1140	1600	0.2
TIM	silicon compound	2750	710	4.4

heat transfer rate but at the same time the speed of the coolant at a given flow
rate will reduce. A computational fluid dynamics (CFD) model is built for one
integrated YASA AFPMSM module for the optimization of the cooling channel
radius. The model of one module of the CP integrated YASA AFPMSM is shown
in Fig. 5.29. The materials and the thermal properties of this module are listed in
Table 5.6.
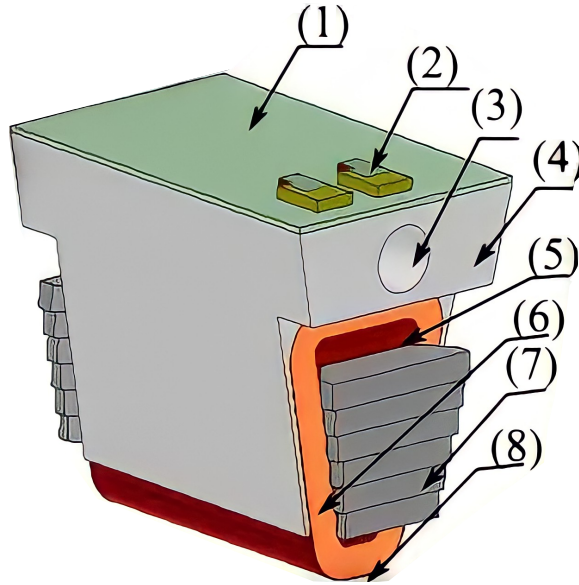
Figure 5.29: The 3D CFD model of one module of the CP integrated
YASA AFPMSM: (1) The thermal interface material (TIM), (2) The
inverter PCB, (3) The cooling channel, (4) The shared cooling struc-
ture, (5) The impregnation epoxy resin, (6) The windings, (7) The
core, (8) The winding insulation Nomex paper.

The CFD simulations are run for the channel radii from 2 mm to 6 mm and
the water flow rates from 1 litre/min to 10 litre/min considering 5W losses in each
transistor of the half-bridge, 25 W per module winding loss, 25 W per module core
loss and 25°C water inlet temperature. Both the average convection coefficient of
the inner wall of the channel and the temperature of the switch thermal pad are
calculated and reported in Fig. 5.30. The water outlet temperature (T_{wout}) and
the channel inner wall temperature (T_{ciw}) are calculated from the CFD model and
then the average convection coefficient of the inner wall of the channel h_{ciw} is
calculated from (5.6).

$$\begin{cases} T_{wa} & = \frac{T_{win}+T_{wout}}{2} \\ h_{ciw} & = \frac{T_{ciw}-T_{wa}}{P_{losst}\times A_{ciw}} \end{cases} \tag{5.6}$$

where P_{losst} is the total loss evacuated by the cooling water. These losses are the
per module winding loss, the per module core loss and the inverter module loss.
T_{wa} is the average water temperature and A_{ciw} is the channel inner wall area.

It can be noticed from Fig. 5.30 that the highest convection coefficient and the
lowest switch thermal pad temperature occur at the smallest channel radius which
is 2 mm. Therefore, the optimal channel radius is 2 mm. It is also noticed that the

switch thermal pad temperature decreases by 16% at the flow rate of 10 litre/min compared to the flow rate 1 litre/min at the channel radius 2 mm.
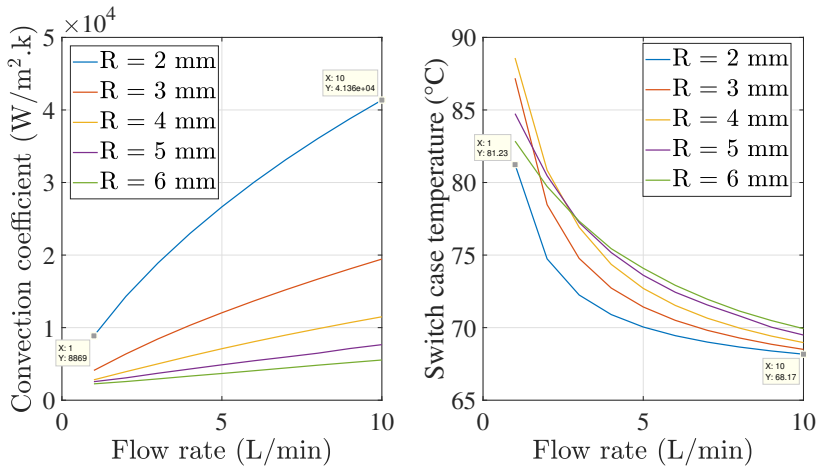
Figure 5.30: The average convection coefficient of the inner wall of the cooling channel (left) and the temperature of the switch case computed for the cooling channel radii 2 mm to 7 mm and the water flow rates 1 Litre/min to 10 litre/min. These figures are generated considering 5 W per switch loss, 25 W per module winding loss, 25 W per module core loss and 25°C water inlet temperature.

5.5   Losses of the YASA half-bridge module

The average and instantaneous losses of the designed half-bridge inverter module for the CP integrated YASA machine are presented in this section. These losses are calculated as explained in Chapter 4 section (4.2).

5.5.1   Average losses of the YASA half-bridge module

Fig. 5.31 shows the total losses of the switch GS66508B versus the junction temperature rise at 10 kHz and 50 kHz switching frequencies. These losses are calculated at the conditions listed in Table 5.7. Thanks to the low switching losses of the GaN devices, not much increase is noticed in the switch losses at 50 kHz compared to 10 kHz switching frequency.

5.5.2   Instantaneous losses of the YASA half-bridge module

The instantaneous conduction and switching losses of the switch GS66508B in the forward and reverse conduction paths are presented in this part.
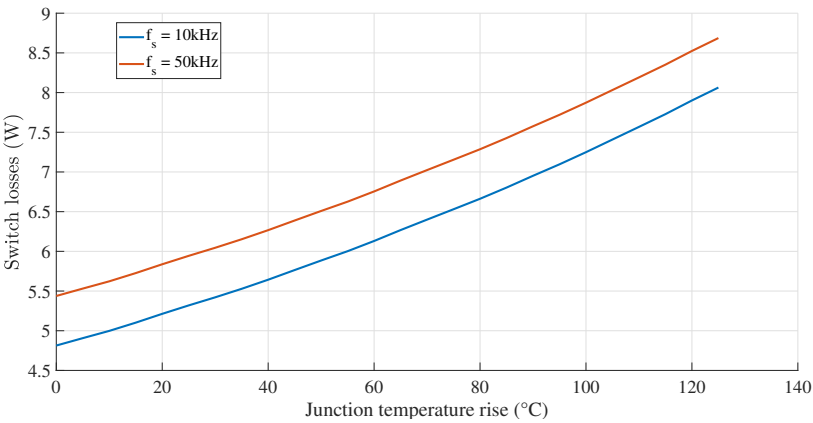
Figure 5.31: Switch losses versus junction temperature rise for 10 kHz and 50 kHz switching frequencies.

Table 5.7: The conditions at which the average losses of the CP integrated YASA are calculated

parameter	value
DC-link voltage (V)	400
Peak line current (A)	14
Modulation index	0.9
Fundamental frequency (Hz)	333.3
Power factor	0.85
Ambient temperature(°C)	25

Instantaneous conduction losses of the half-bridge module

The drain to source resistance R_{ds} versus junction temperature of the switch GS66508B is extracted from the datasheet and fitted with the polynomial in (5.7). The fitting result is plotted in Fig. 5.32 (left).

$$R_{ds}(T) = K_1 T^2 + K_2 T + K_3 \tag{5.7}$$

where $K_1 = 1.5 \times 10^{-6}$, $K_2 = 3.67 \times 10^{-4}$, $K_3 = 0.04$.

The instantaneous conduction loss in the forward path is shown in Fig. 5.33. This figure is generated at the operating conditions in Table 5.7. The peak value
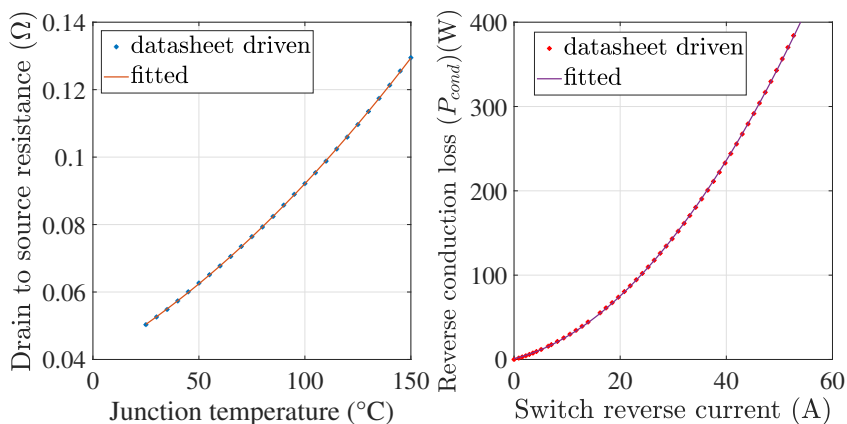
Figure 5.32: The datasheet driven and the fitted drain to source resistance (R_{ds}) (left) and conduction loss in the reverse direction (right) of the switch GS66508B.

of these losses corresponds to the peak value of the instantaneous switch current in the forward conduction path.
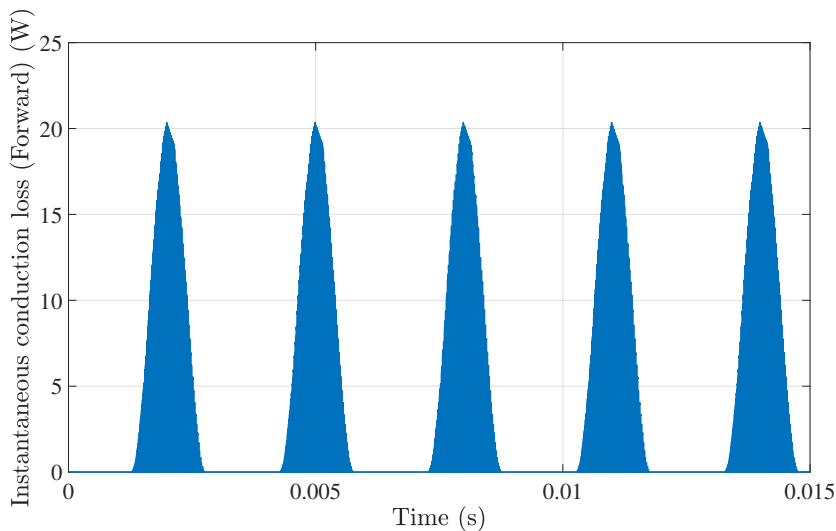
Figure 5.33: The instantaneous conduction losses in the forward path of the switch GS66508B.

The instantaneous conduction losses of the switch GS66508B in the reverse conduction path are derived from the datasheet and fitted with the polynomial in (5.8). The fitting result is shown in Fig. 5.32 (right).

$$P_{cond}(t) = K_4 i_d^2(t) + K_5 i_d(t) + K_6 \tag{5.8}$$

where $K_4 = 0.1$, $K_5 = 1.6$, $K_6 = 1$.

The instantaneous conduction loss in the reverse path is shown in Fig. 5.34. This figure is generated at the operating conditions in Table 5.7.
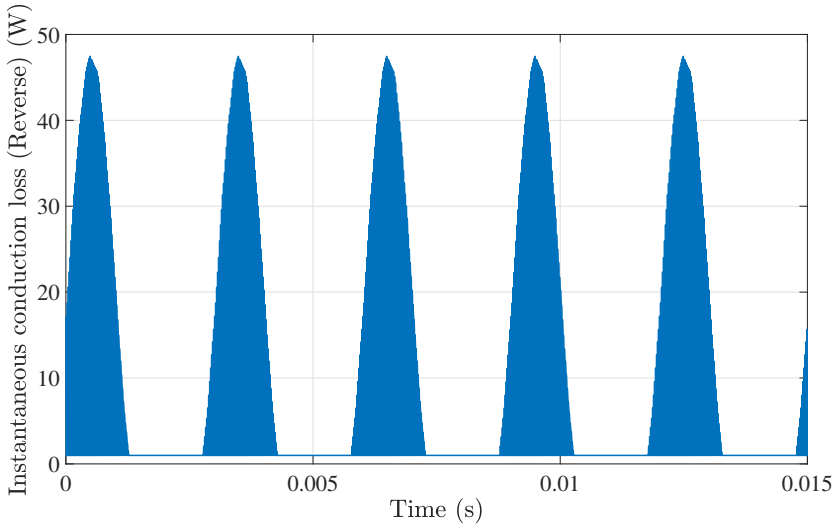
Figure 5.34: The instantaneous conduction losses in the reverse path of the switch GS66508B.

It can be noticed that the peak conduction losses in the reverse conduction path are higher than the peak conduction losses in the forward path due to the higher drop in the reverse path.

Instantaneous switching losses of the half-bridge module

The instantaneous switching losses of the switch GS66508B are computed at the operating conditions in Table 5.7. The result is shown in Fig. 5.35. The peak value of these losses correspond to the multiplication of the DC-link voltage and the peak line current. These large loss needles cause deviations between the time average and peak junction temperature.

5.6 Thermal model parameters and results of the YASA half-bridge inverter module

The parameters and results of the steady-state and the transient thermal models of the YASA half-bridge inverter module are computed in this section. A generic
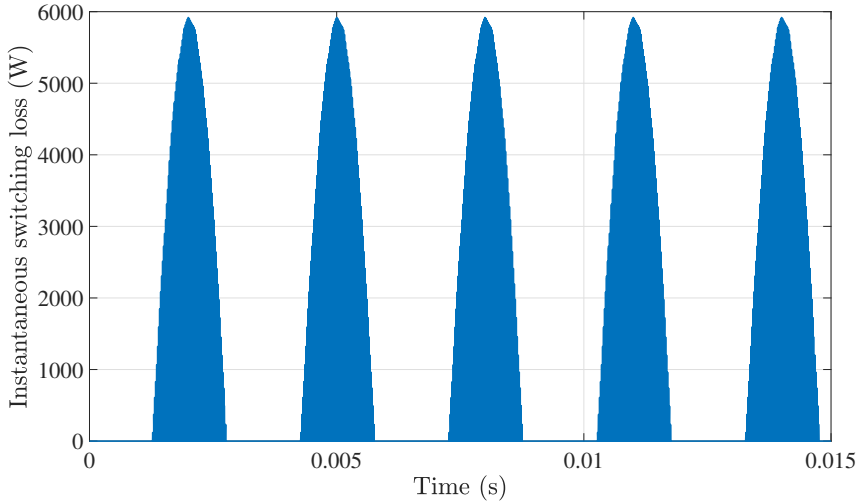
Figure 5.35: The instantaneous switching losses of the switch GS66508B.

description of these models is given in Chapter 4 section (4.3.1).

5.6.1 Calculation of the steady-state thermal model Parameters of the YASA half-bridge inverter module

The steady-state thermal model of the YASA half-bridge inverter module consists of five thermal resistances from the junction to the ambient. These thermal resistances are the junction to case thermal resistance R_{JC}, the PCB thermal resistance R_{CP}, the TIM thermal resistance R_{TIM}, the aluminium shared cooling structure thermal resistance R_{AL} and the convection thermal resistance R_{conv}. The summation of R_{TIM}, R_{AL} and R_{conv} gives the PCB to ambient thermal resistance R_{PA}. R_{JC} for the selected switch GS66508B is 0.5°C/W.

Calculation of R_{CP} of the half-bridge module

From Fig. 5.28 (b), the value of R_{CP} resulting from the thermal vias pattern in Fig. 5.26 (b) is 2.2°C/W.

The inner and the outer zone of the PCB shown in Fig. 5.26 are homogenized using the method explained in Chapter 4 section (4.3.1). The result of the homogenization of the inner zone in the z direction is shown in Fig. 5.36. This result is obtained at 1 W loss imposed on the top surface and constant temperature of 20°C on the bottom surface. The maximum temperature of the top surface is 21.9984°C which means a thermal resistance of 1.9984°C/W in the z direction.
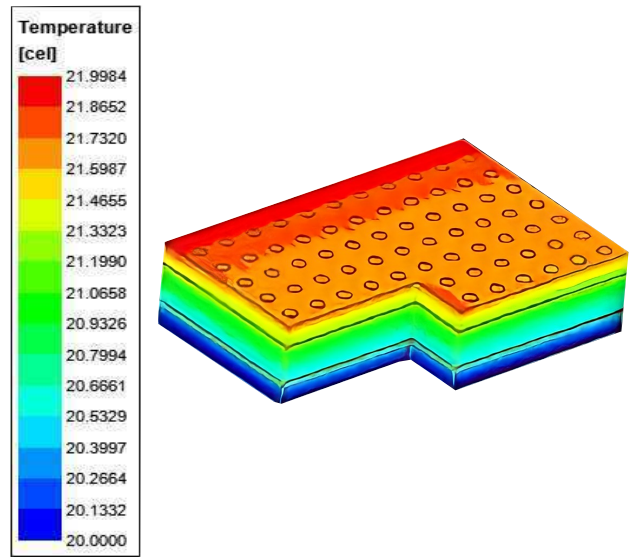
Figure 5.36: PCB temperature distribution for 1W top surface loss,
20°C bottom surface temperature and all other surfaces are adiabatic.

The equivalent thermal properties of the homogenized PCB are given in Table
5.8.

Table 5.8: Equivalent thermal properties of the homogenized PCB

Zone	Property	Value
inner	k_{xe} (W/m.K)	5.8767
	k_{ye} (W/m.K)	7.7
	k_{ze} (W/m.K)	25.3476
	C_{pe} (J/kg.K)	1017.7
	ρ_{pe} (kg/m^3)	3345
outer	k_{xe} (W/m.K)	5.4
	k_{ye} (W/m.K)	6.4
	k_{ze} (W/m.K)	1.3638
	C_{pe} (J/kg.K)	1127
	ρ_{pe} (kg/m^3)	2523.3

Fig. 5.37 shows the PCB temperature distribution using the non-homogeneous and the homogenized models. The simulations are done using 1W loss over the inner zone top surface (the switch case) and 20°C constant temperature on the bottom surface. The non-homogeneous model takes 22 minutes to solve while the homogenized one takes only 2 minutes.

(a)   (b)
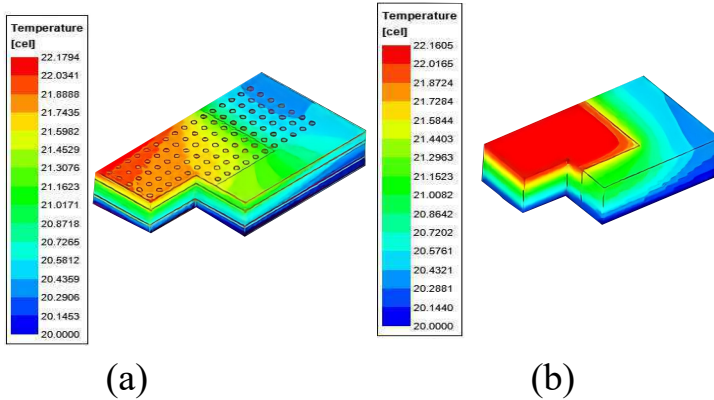
Figure 5.37: PCB temperature distribution for 1W switch loss, 20°C bottom surface temperature, other surfaces are adiabatic (a) non-homogeneous model (b) homogenized model.

Fig. 5.38 shows the error in temperature estimation due to homogenization versus the switch power loss. As the switch loss is not expected to be higher than 10W, the error in the temperature estimation using the fast homogenized model will not exceed 3.7%.

Calculation of R_{PA} of the half-bridge module

For calculation of the R_{PA} and its three constituting components, the three curves in Fig. 5.39 are generated using CFD simulations at 1 litre/min flow rate, 22.5°C water inlet temperature and 2 mm channel radius. The machine loss is swept from 10 W to 100 W and the switch loss is swept from 1 W to 10 W. The slopes of these curves give the R_{PA}, the TIM to ambient thermal resistance R_{TA} and the convection resistance of the channel inner wall R_{conv}. From these resistances, R_{TIM} and R_{AL} are calculated as explained in Chapter 4 section (4.3.1).

The R_{TIM} constitutes 73.1% of R_{PA} due to its relatively big thickness of 1 mm.

Full thermal model parameters of the half-bridge module

The values of the parameters of the steady-state thermal model of the YASA half-bridge inverter module are given in Table 5.9. The total resistance from junction to
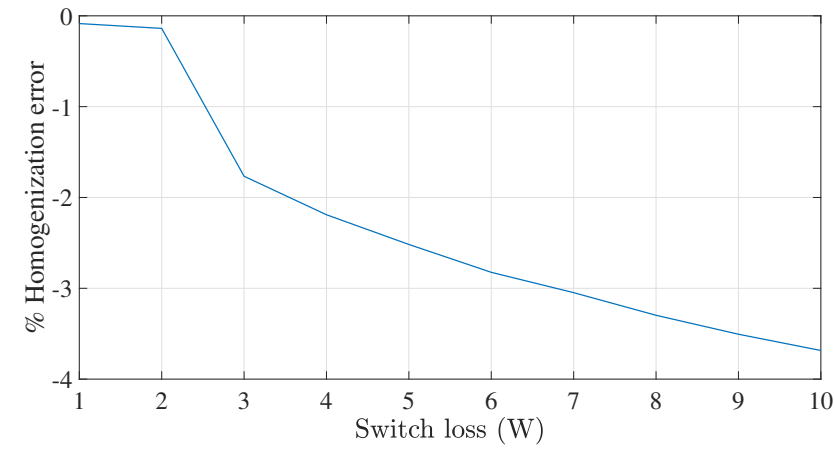
Figure 5.38: PCB temperature estimation error due to homogeniza-
tion.
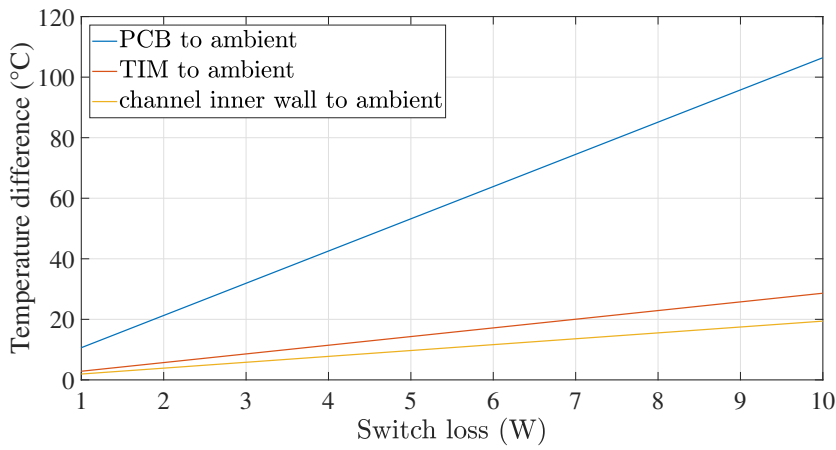
Figure 5.39: The variation of the temperature difference from the PCB
bottom surface to ambient, the TIM to ambient, the channel inner wall
to ambient considering both switch and machine losses.

ambient R_{JA} is 13.3396 °C/W.

The accuracy of the steady state thermal model is assessed by running CFD
simulations at two different operating conditions. The first one is 25°C water inlet
temperature, 1 litre/min flow rate, 2 W switch loss and 20 W machine module loss.
The second one is 25°C water inlet temperature, 1 litre/min flow rate, 10 W switch
loss and 100 W machine module loss. Fig. 5.40 (a) and (b) show the temperature

Table 5.9: Steady-state thermal model parameters of the half-bridge
inverter module

Thermal resistance (°C/W)	Value
R_{JC}	0.5
R_{CP}	2.2
R_{TIM}	7.7783
R_{AL}	0.9226
R_{conv}	1.9387

distribution of one integrated module for the first and the second operating con-
ditions respectively. For the first case, the simulated and the steady state model
calculated junction temperature is 39.3°C and 38.8°C respectively. For the second
case, the temperature is 94.1°C from the simulations and 91.7°C from the lumped
parameter model. A good correspondence between the model and the CFD simula-
tions can be noticed. It worth mentioning that the CFD model takes 15 min to solve
for the temperature of the switch case while the lumped parameter model requires
the solution of a simple network of resistances.

(a)   (b)
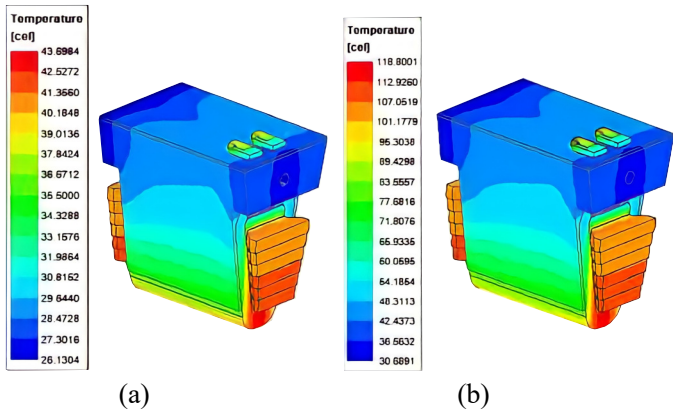
Figure 5.40: The CFD simulation results at (a) 1 litre/min flow rate,
25°C water temperature, 2W switch loss and 20W machine loss (b)1
litre/min flow rate, 25°C water temperature, 10W switch loss and
100W machine loss.

5.6.2   Calculation of the transient thermal model parameters of the YASA half-bridge inverter module

As explained in Chapter 4 section (4.3.2), the junction to case transient thermal model of the switch is represented by a Cauer network. The parameters of this network for the switch GS66508B are given in the datasheet. Each of the components from case to ambient is represented by a first order RC network. The R value of these components is computed in section (5.6.1). The C value is computed as explained in Chapter 4 section (4.3.2) . The calculated parameters of the transient thermal model are listed in Table 5.10.

Table 5.10: Transient thermal model parameters of the CP integrated YASA converter module

Parameter	Value
R_1 (°C/W)	0.015
R_2 (°C/W)	0.23
R_3 (°C/W)	0.24
R_4 (°C/W)	0.015
C_1 (J/°C)	8×10^{-5}
C_2 (J/°C)	7.4×10^{-4}
C_3 (J/°C)	6.5×10^{-3}
C_4 (J/°C)	2×10^{-3}
The PCB (C_{cp}) (J/°C)	0.3095
The TIM (C_{TIM}) (J/°C)	0.0761
The Aluminium (C_{AL}) (J/°C)	0.8871

Fig. 5.41 shows the step response of the transient thermal model from the junction to the case with and without consideration of the capacitance of the case to the ambient components. The step amplitude is 8.5 W and the ambient temperature is 25°C. The thermal time constant is 5.03 s and 0.12 s with and without the case to ambient capacitance. The influence of the capacitance from the case to the ambient would be a smoother junction temperature and a smaller difference between the peak and the average junction temperature.

Fig. 5.42 (left) shows the instantaneous switch loss resulting at the operating conditions in Table 5.7. The large height needles correspond to the turn on and the turn off switching loss. The average value of the loss waveform is 8.5 W. The instantaneous loss in the reverse conduction path is zoomed on the figure for com-
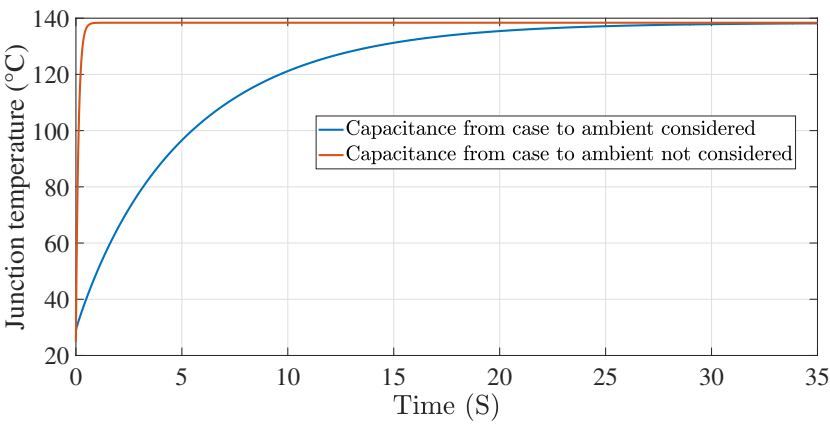
Figure 5.41: The step response of the junction to ambient transient thermal model with and without the capacitance from the case to the ambient.

parison of instantaneous loss amplitudes. The instantaneous junction temperature is shown in Fig. 5.42 (right). The average temperature is 138.3°C and the peak value is 142.5°C. A difference of 4.5°C between the peak and the average value results mainly due to the large switching loss needles at the transition moments of the switch.
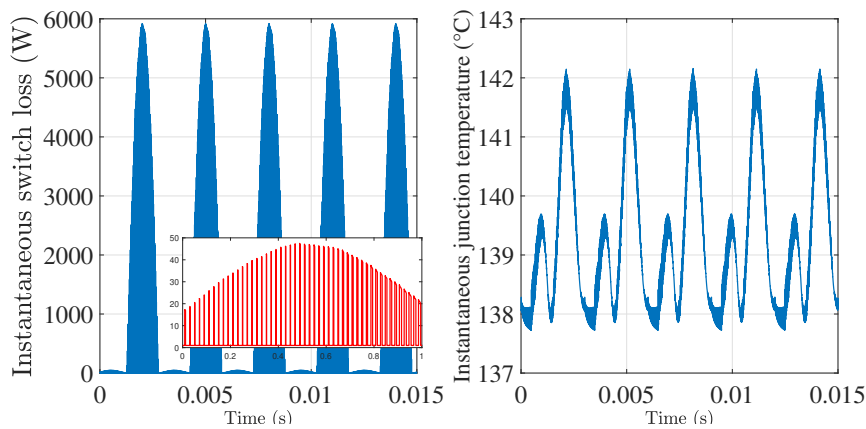

Figure 5.42: The instantaneous switch loss (left) and junction temperature (right) at rated operating conditions with the loss in the reverse conduction path zoomed.

5.7 Influence of the parasitics of the half-bridge inverter module

The influence of the inverter module parasitics on the losses and the temperature of the switches is assessed in this section.

Fig. 5.43 shows the half-bridge inverter module with the different parasitics that influence the switching loss of the switches namely the gate drive loop inductance L_g, the common source inductance L_{cs} and the commutation loop inductance L_{loop}. The L_{loop} can be calculated from (5.9).

$$
\begin{aligned}
L_{dclink} &= ESL + L_+ + L_- \\
L_{comm} &= L_{d1} + L_{cs1} + L_{s1} + L_{d2} + L_{cs2} + L_{s2} \\
L_{loop} &= L_{dclink} + L_{comm}
\end{aligned} \tag{5.9}
$$

where ESL, L_+, L_-, L_{d1}, L_{s1}, L_{d2}, L_{s2} are the equivalent series inductance of the DC-link capacitors, the inductance of the DC-link busbar positive plate, the inductance of the DC-link busbar negative plate, the drain and the source inductances of the upper and the lower switches respectively, L_{dclink} is the total DC-link inductance.

The L_g reduces the rate of rise/fall of the gate current during the turn on/off transition of the switch. This rate reduction results in a longer turn on/off transition duration, and hence, a higher switching loss. Thanks to the additional source sense pin in the selected switch (pin 4 in Fig. 5.26 (a)), the L_{cs} is negligible. The L_{loop} has two components: L_{dclink} which represents the parasitic inductance of the DC-link capacitors and busbar, L_{comm} which represents the parasitic inductance of the switches and the inverter module PCB. The decoupling capacitors C_{d1}, C_{d2}, C_{d3} in Fig. 5.43 compensate the effect of the L_{dclink}. The L_{comm} causes a voltage dip/spike in V_{ds} during the turn on/off transition of the switch causing a decrease/increase in the turn on/off switching loss. V_{ds} during turn on/off transition of the switch can be calculated from (5.10).

$$
V_{ds} = V_{dc} \mp L_{comm} \frac{di_{a1}}{dt} \tag{5.10}
$$

where V_{dc} is the DC-link voltage, i_{a1} is the upper switch current during transition.

The L_g and the L_{comm} are computed at different frequencies using electromagnetic finite element (FE) simulation for the inverter module PCB model shown in Fig. 5.44.

Fig. 5.45 shows the variation of L_g and L_{comm} with the frequency. It can be seen that the inductance decreases with frequency until 50 MHz and then it plateaus. The maximum turn on time of the switch occurs at the rated current and amounts to 15.5 ns, the corresponding frequency is 64.5 MHz. The maximum turn
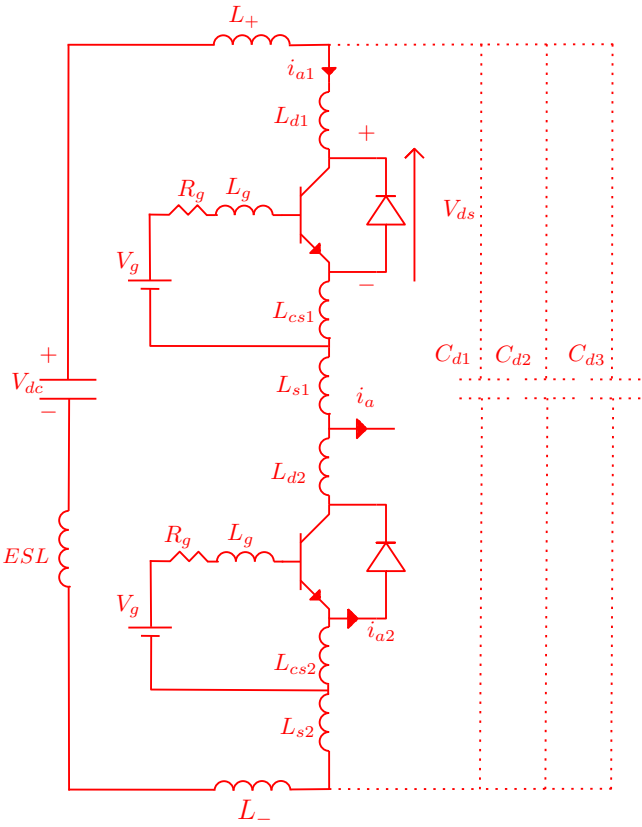
Figure 5.43: The half-bridge inverter module with the parasitics that influence the switching loss of the switches.
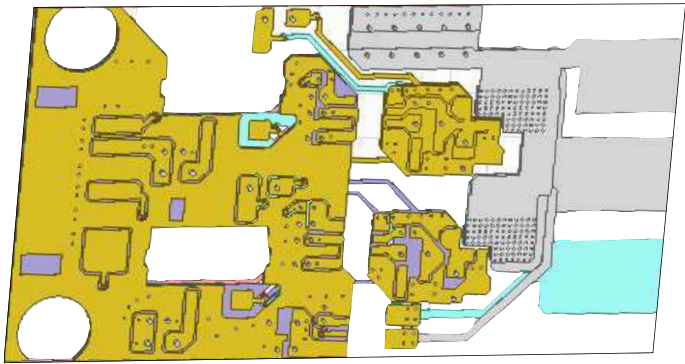

Figure 5.44: FE model of the half-bridge inverter module PCB.

off time is 4.2 ns and the corresponding frequency is 0.23 GHz. The frequency corresponding to the turn on/off moments is beyond the plateau frequency. Therefore, from Fig. 5.45, the values of L_{comm} and L_g are 9.22 nH and 3.08 nH respectively.
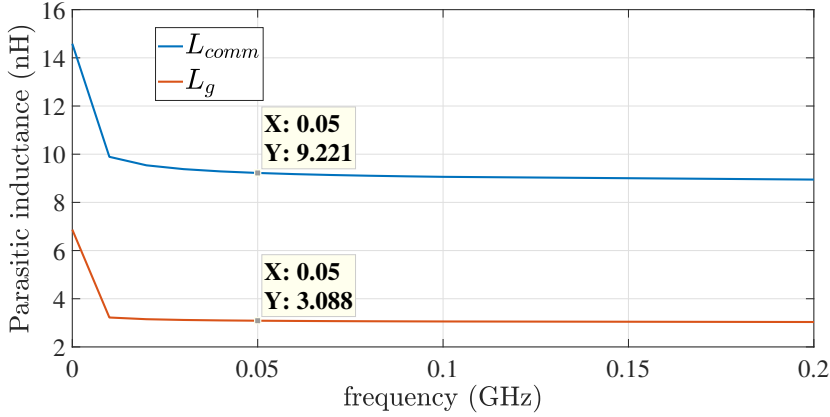

Figure 5.45: The variation of L_{loop} and L_g with frequency for the GaN based half-bridge inverter module designed for the CP YASA machine.

The turn on/off transition time delay resulting from the L_g is calculated by simulating the circuit in Fig. 5.46 (a)/(b) with the switch s off/on. The resulting turn on/off delay from L_g is 0.055 ns.
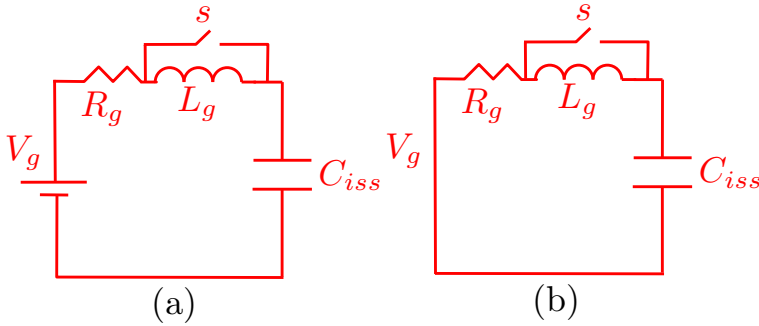
Figure 5.46: The L_g turn on/off delay calculation circuits (a) turn on transition delay, (b) turn off delay.

The voltage spike resulting from the L_{comm} during the turn off transition at the rated current is $L_{comm} \frac{di_{a1}}{dt}$ and amounts to 37.5V. The voltage dip at the turn on time is 8.5V. The peak value of the turn on energy pulse and the turn off energy pulse is modified to $(V_{dc} - 8.5)\, i_s(t)$ and $(V_{dc} + 37.5)\, i_s(t)$ respectively. The resulting peak temperature is the same as the one without consideration of the

parasitics as the increase in the turn off energy loss compensated the decrease in the turn on energy loss and the delay in the turn on/off transition time due to the L_g is small.

5.8 Power calculations of the CP integrated YASA AF-PMSM

The maximum power that can be injected by one inverter module in the windings of the CP integrated YASA machine limited by the rated temperature of the windings and the rated junction temperature of the inverter switches. Due to the much smaller thermal time constant of the switches compared to the windings, the following power calculation procedure is applied:

- The switch loss that results in 115°C thermal pad temperature is computed using the CFD model. 35°C is left as a safety margin to account for heat coupling and high instantaneous switch loss that results in a difference between peak and average junction temperature.

- From the switch loss versus temperature model, the peak winding current that results in the switch loss in step 1 is calculated.

Applying the above steps at the operating conditions in Table 5.11 results in 115°C thermal pad temperature at 8.5 W switch loss. The corresponding junction temperature is 119.25°C. The switch losses versus the junction temperature are calculated at different peak line currents to search for the current at which the switch loss is 8.5 W at a junction temperature of 119.25°C. The result is shown in Fig. 5.47. From this figure, the peak line current that can be injected by one inverter module in case of three-phase is 14 A which corresponds to 9.8 A rms.

At 9.8 A rms line current, the per module winding loss is 14.6 W and the per module core loss is 3 W [72]. Fig. 5.48 (a) shows the temperature distribution over one integrated module at these power losses. The maximum winding temperature is 51.5°C. The total drive power P_{drive} calculated from (5.11) is 4.2 kW. Since the winding temperature is only 51.5°C, higher current can still be tolerated by the windings. So, several methods for increasing the windings current, and hence, the drive power without exceeding the rated junction temperature of the switches are discussed in Chapter 8.

$$P_{drive} = n_{phase} \times \frac{M V_{dc} i_{linepeak} pf}{4} \tag{5.11}$$

where $i_{linepeak}$ is the peak line current and $n_{phase}= 3$ is the number of phases.

Table 5.11: The operating conditions at which the maximum current injected by one inverter module is computed

Parameter	Value
Modulation index (M)	1
Switching frequency (f_s) (kHz)	50
Fundamental frequency (f_o) (Hz)	333.3
Power factor (pf)	0.85
$V_{dc}|_{3-phase}$ (V)	400
$R_{coil}|\ |_{25°C}$ (mΩ)	138.9
T_{win} (°C)	25
Water flow rate (litre/min)	1
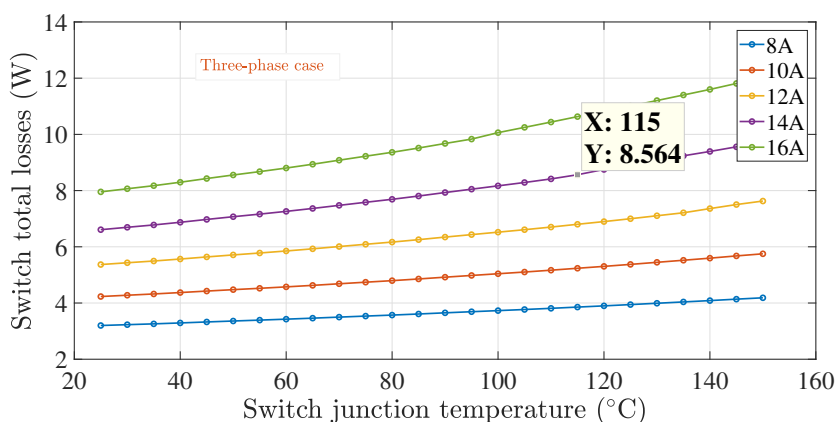
Figure 5.47: The switch loss versus the junction temperature at different peak line currents at the operating conditions in Table 5.11 in case of three-phase operation.

5.9   Design of the power converter module for the PR integrated SRM

The asymmetric H-bridge is the commonly used converter topology for driving the SRM [125, 126] due to its small number of passive components and the possibility to apply a unipolar or a bipolar voltage across the SRM windings. Fig. 5.49 shows the schematic of the asymmetric H-bridge driving the six stator coils of the 6/4
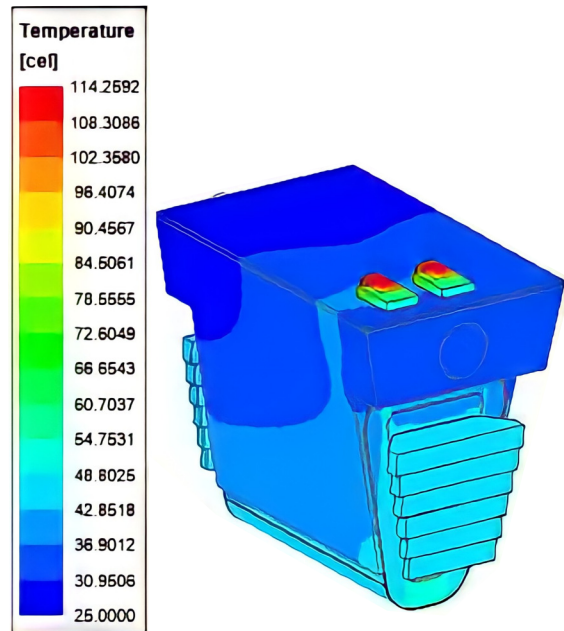
Figure 5.48: Temperature distribution over one integrated module at 14.6 W per module winding loss, 3.0 W per module core loss and 8.5 W per switch loss.

SRM presented in Chapter 2 section (2.3). Each asymmetric H-bridge converter module consists of two power switches and two power diodes.
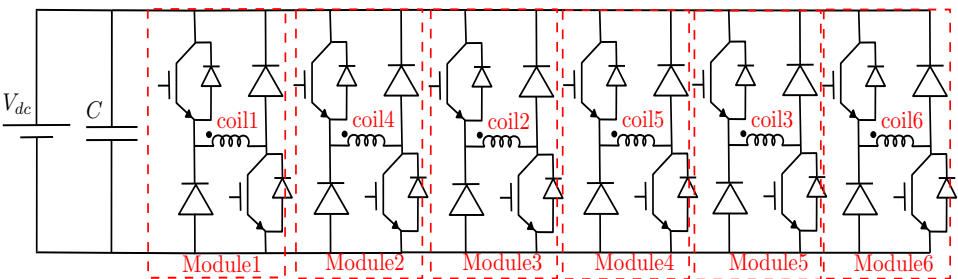
Figure 5.49: The schematic of the asymmetric H-bridge driving the six stator coils of the PR integrated SRM.

Due to their low losses and small package size, the SiC devices C3M0075120J from Wolfspeed and LSIC2SD120C10 from Littlefuse are chosen for the power switches and the power diodes respectively. The key parameters of these devices are listed in Table 5.12.

Table 5.12: The key parameters of the switch and the diode of the PR SRM converter

Property	Value	
	Switch	Diode
Rated voltage (V)	1200	1200
Continuous current rating (A)	30	33
Peak current rating (A)	80	80
Rated junction temperature (°C)	150	175
Junction to case thermal resistance (°C/W)	1.1	0.85
Drain to source resistance $\mid_{25°C}$ (mΩ)	75	-
Gate charge (nC)	51	-
FOM (mΩ.nC)	3825	-
The current rise time (ns)	9	-
The current fall time (ns)	10	-
Anode to cathode voltage drop (V)	-	1.5
Reverse recovery charge (nC)	-	57
Package size (mm^2)	164.7	56.2
Case size (mm^2)	34.7	34.4

The power loss maps of the switch and the diode are calculated for the torque range from 0.5 Nm to 3 Nm and the speed range from 500 rpm to 5500 rpm using the average losses calculation method explained in Chapter 4 section (4.2). These loss maps are calculated at 800 V DC-link voltage, a switching frequency of 20 kHz and the current waveforms calculated by the torque controlled closed loop dynamic simulation model discussed in detail in Chapter 3 section (3.6). For example, the current waveforms of the stator windings, the current of the upper switch and the lower diode of the asymmetric H-bridge module driving coil 1 of the SRM stator are shown in Fig. 5.50 (a), (b) and (c) respectively. The phase current is the summation of the switch and diode current.

The switch and the diode loss maps are shown in Fig. 5.51 (a) and (b) respectively. It can be observed that the higher the torque, the higher the switch loss due to the higher switched current with the torque. The switch and the diode losses are not showing a fixed trend with the operating speed (see Fig. 5.52). This is because the exact switched current waveform at each torque and speed point depends on
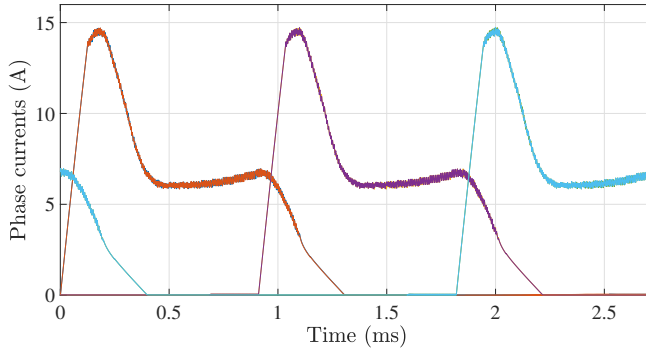
(a)
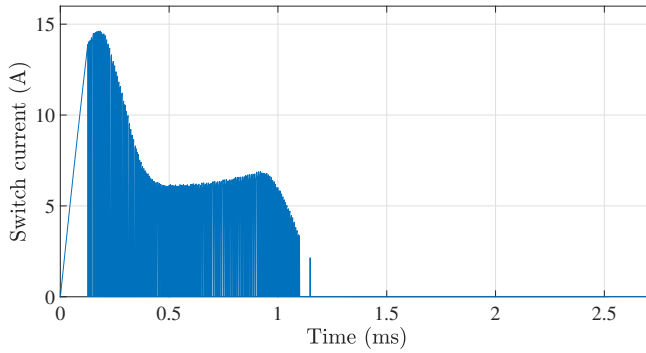
(b)
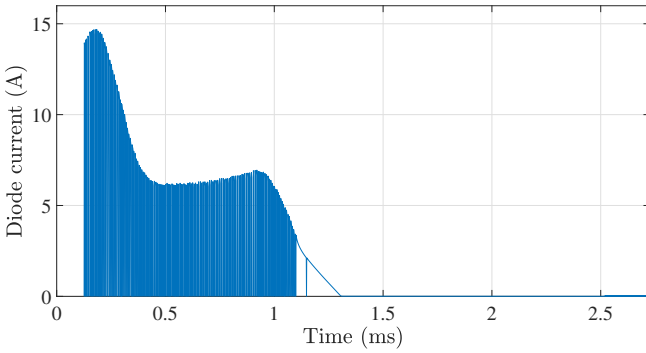
(c)

Figure 5.50: The current waveforms of the torque controlled SRM:
(a) Winding currents, (b) Switch current, (c) Diode current. These
current waveforms are generated at 3 Nm shaft torque and 5500 rpm
at DC-link voltage of 800 V.

the turn on and the turn off angles which change from one point to the other. Also, as the speed increases, the current rises slower and decays faster which reshapes the current waveform with the speed.
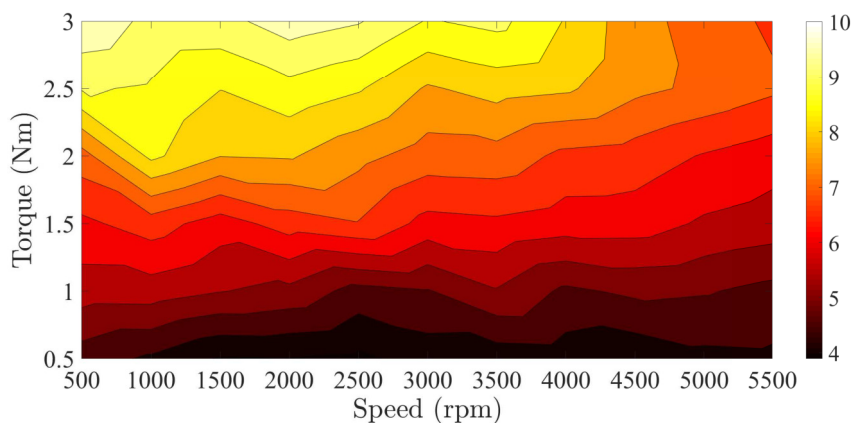
(a)
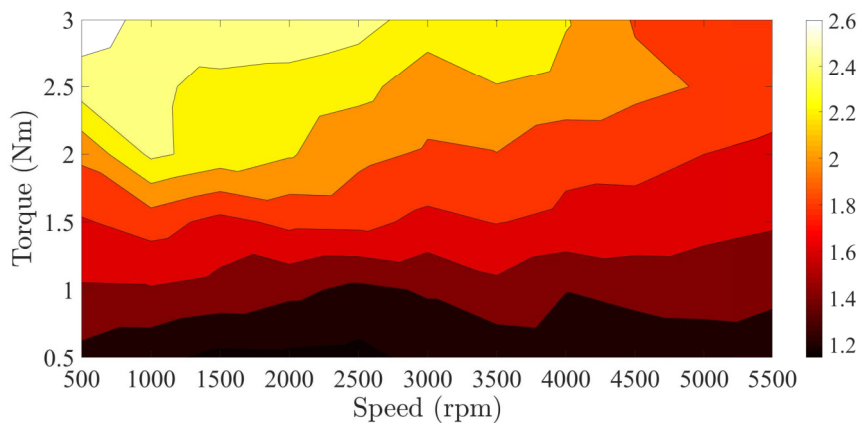
(b)

Figure 5.51: The switch loss (W) map (a) and the diode loss (W) map (b) up to the speed of 5500 rpm and the torque of 3 Nm assuming a junction temperature of 125°C for both the switch and the diode and DC-link voltage of 800 V.

The PCB of the asymmetric H-bridge is designed with the same method discussed in section (5.3.2). A picture for the implemented asymmetric H-bridge module is shown in Fig. 5.53. The size of the converter is 100×75 mm^2.
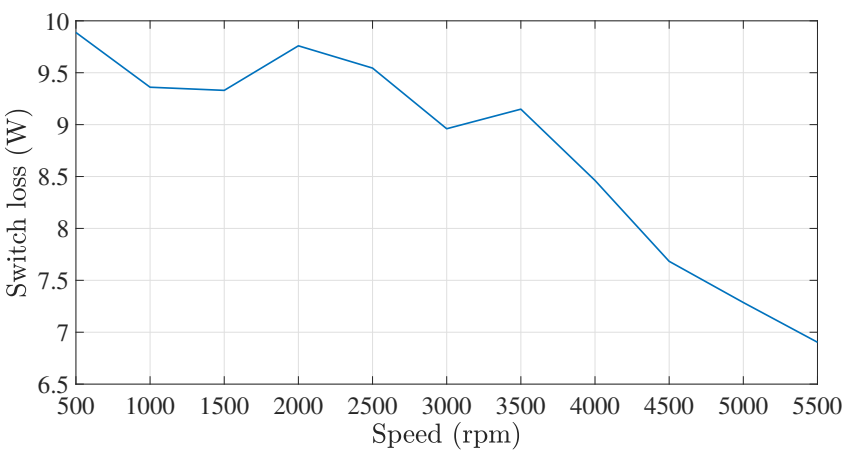
Figure 5.52: The switch loss at 3 Nm up to the speed 5500 rpm at DC-link voltage of 800 V.
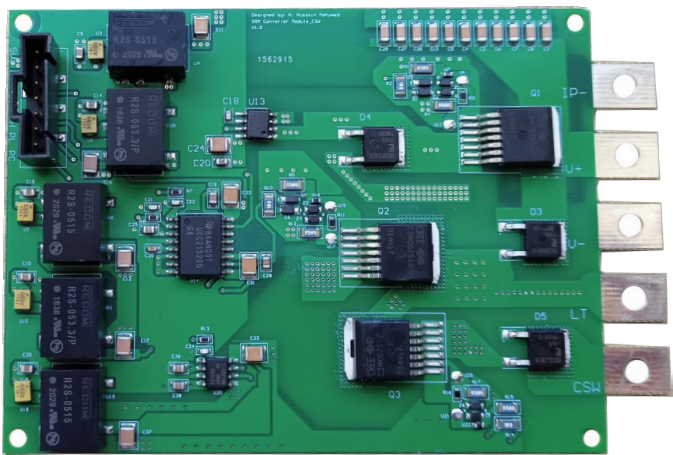
Figure 5.53: The implemented SiC based asymmetric H-bridge inverter module.

5.10 Optimization of the thermal performance of the PR integrated SRM

The thermal performance of the PCB is optimized by populating thermal vias beneath the case of the switch and the diode in a similar way as discussed in section (5.4) considering the different footprint of these devices. A picture that illustrate the thermal vias beneath the switch and the diode is shown in Fig. 5.54.
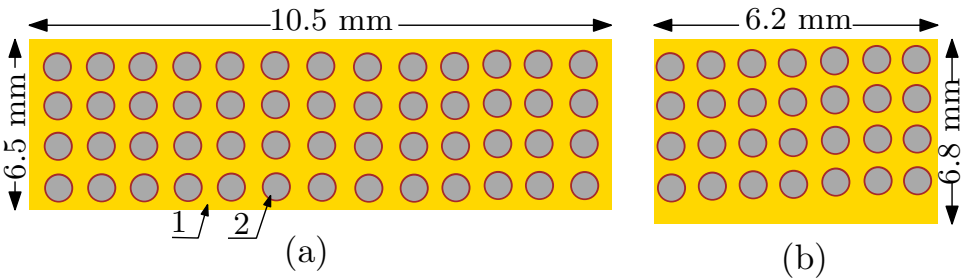
Figure 5.54: The thermal via pattern underneath the switch C3M0075120J (a) and the diode LSIC2SD120C10 (b) of the asymmetric H-bridge module of the PR integrated drive: (1) copper plot, (2) thermal vias.

5.11 Losses of the SRM asymmetric H-bridge module

The average and instantaneous losses of the designed asymmetric H-bridge inverter module for the PR integrated SRM are presented in this section. These losses are calculated as explained in Chapter 4 section (4.2).

5.11.1 Average losses of the SRM asymmetric H-bridge module

Fig. 5.55 shows the total average losses of the switch C3M0075120J versus the junction temperature. Fig. 5.56 shows the total average losses of the diode LSIC2SD120C10 versus the junction temperature. These losses are calculated at the conditions listed in Table 5.13.

Table 5.13: The conditions at which the average losses of the PR integrated SRM are calculated

parameter	value
DC-link voltage (V)	200
Switching frequency (kHz)	20
Speed (rpm)	1000
Torque (Nm)	2

5.11.2 Instantaneous losses of the SRM asymmetric H-bridge module

The instantaneous losses of the switch C3M0075120J and the diode LSIC2SD120C10 are calculated in this part.
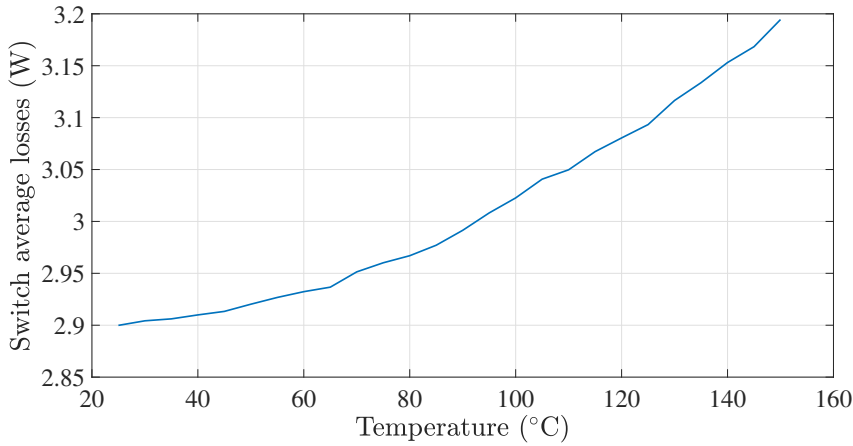
Figure 5.55: C3M0075120J switch losses versus junction temperature rise computed at the operating conditions in Table 5.13.
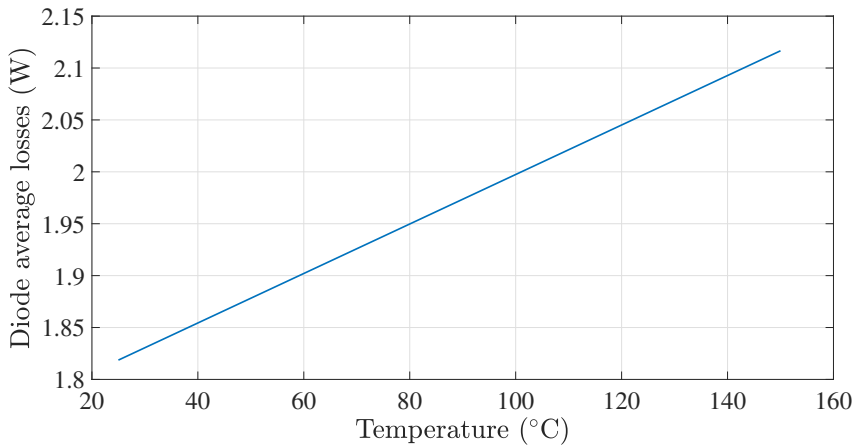

Figure 5.56: LSIC2SD120C10 diode losses versus junction temperature rise computed at the operating conditions in Table 5.13.

Instantaneous conduction losses of the SRM asymmetric H-bridge module

The drain to source resistance R_{ds} versus junction temperature of the switch C3M0075120J is extracted from the datasheet and fitted with a polynomial similar to the one given in (5.7). The polynomial coefficients are K_1 =1.6×10^{-6}, K_2 = -4.3× 10^{-5}, K_3 = 0.083.

The instantaneous conduction loss in the switch is shown in Fig. 5.57. This figure is generated at the operating conditions in Table 5.13.
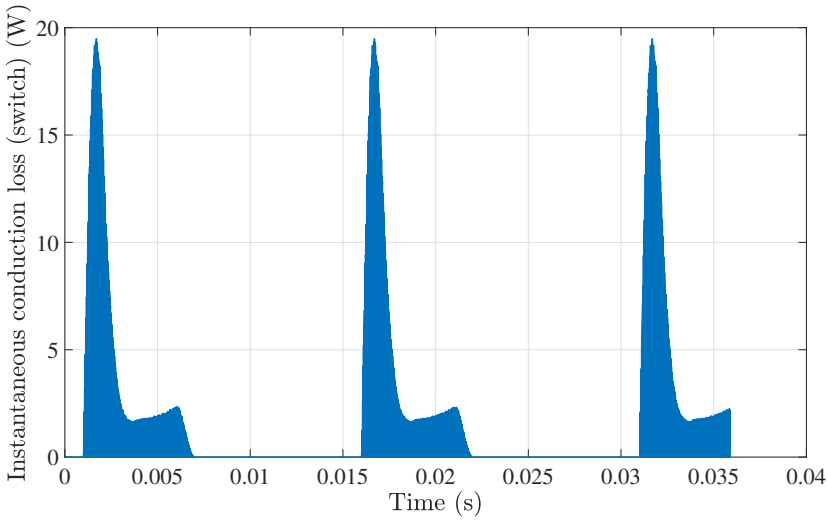
Figure 5.57: The instantaneous conduction losses of the switch
C3M0075120J generated at the operating conditions in Table 5.13.

The instantaneous conduction losses of the diode LSIC2SD120C10 are derived
from the datasheet and fitted with the polynomial in (5.12).

$$P_{cond}(t) = (a_1 T_{dj} + b_1)i_d^2(t) + (a_2 T_{dj} + b_2)i_d(t) + (a_3 T_{dj} + b_3) \quad (5.12)$$

where $a_1 = 0.0003$, $b_1 = 0.0437$, $a_2 = -0.0022$, $b_2 = 0.9811$, $a_3 = 0.0019$, $b_3 = -0.004$,
The instantaneous conduction loss of the diode LSIC2SD120C10 is shown in
Fig. 5.58. This figure is generated at the operating conditions in Table 5.13.

Instantaneous switching losses of the SRM asymmetric H-bridge module

The Instantaneous switching losses of the switch C3M0075120J and the diode
LSIC2SD120C10 are computed at the operating conditions in Table 5.13. The re-
sult is shown in Fig. 5.59 and Fig. 5.60 respectively. The peak value of the switch
loss correspond to the multiplication of the DC-link voltage and the summation of
the peak phase current and the reverse recovery current of the diode.

5.12 Thermal model parameters and results of the SRM asymmetric H-bridge inverter module

The parameters and results of the steady-state and the transient thermal models of
the SRM asymmetric H-bridge inverter module are computed in this section.
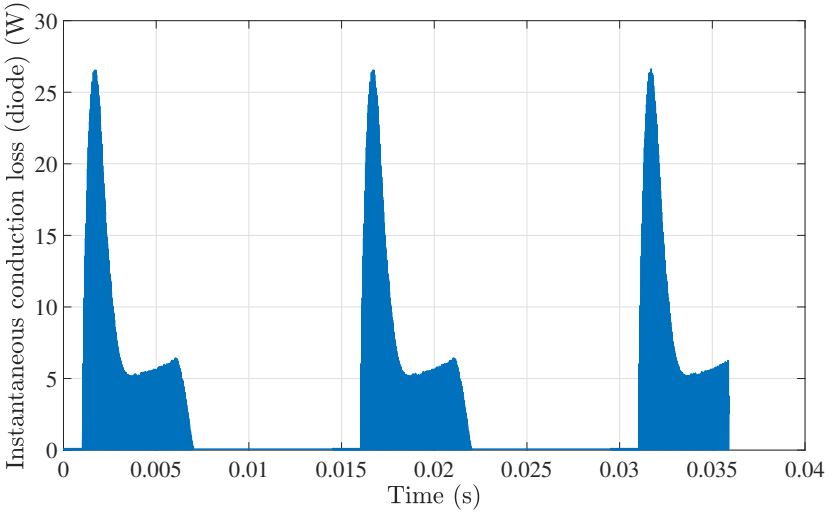
Figure 5.58: The instantaneous conduction losses of the diode LSIC2SD120C10 generated at the operating conditions in Table 5.13.
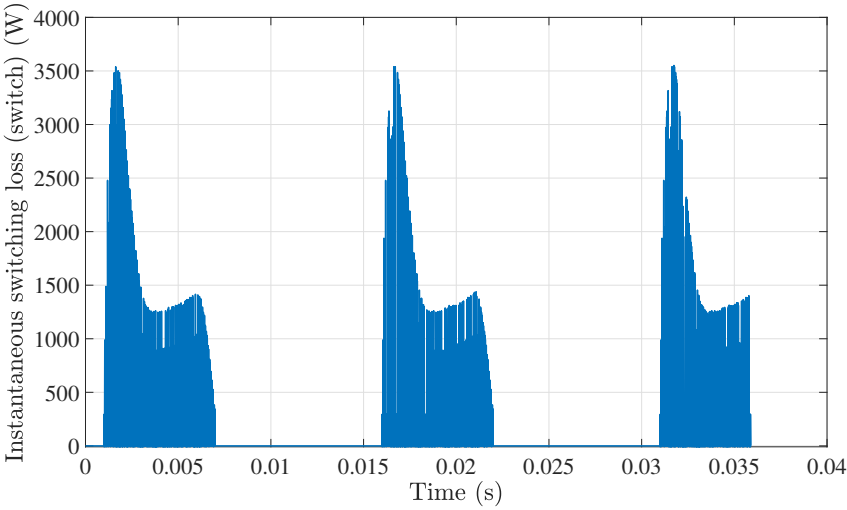

Figure 5.59: The instantaneous switching losses of the switch C3M0075120J generated at the operating conditions in Table 5.13.
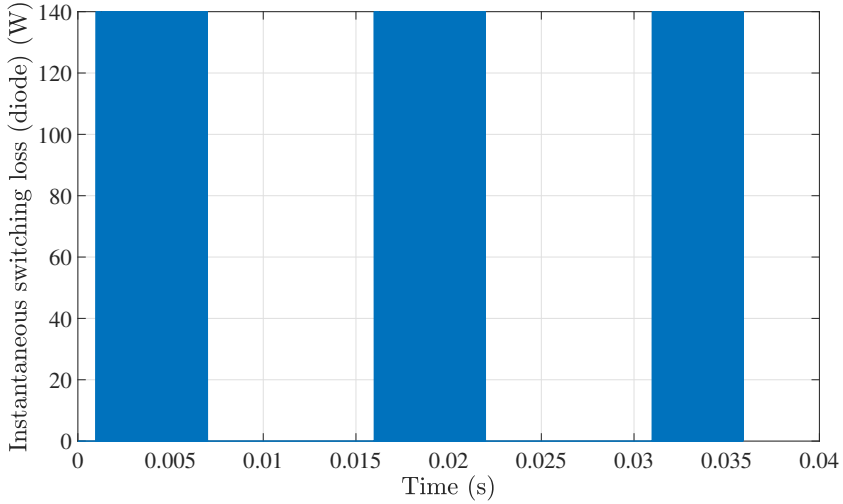
Figure 5.60: The instantaneous switching losses of the diode
LSIC2SD120C10 generated at the operating conditions in Table 5.13.

5.12.1 Calculation of the steady-state thermal model parameters of the SRM asymmetric H-bridge inverter module

Five thermal resistances need to be computed for the steady-state thermal model
of the switch and the diode of the asymmetric H-bridge inverter module. These
thermal resistances are the junction to case thermal resistance of the switch R_{JCs}
and the diode R_{JCd}, the case to PCB thermal resistance of the switch R_{CPs} and
the diode R_{CPd}, the TIM thermal resistance of the switch R_{TIMs} and the diode
R_{TIMd}, the aluminium thermal resistance of the switch R_{ALs} and the diode R_{ALd}
and the convection thermal resistance of the switch R_{convs} and the diode R_{convd}.
The summation of R_{TIMs}, R_{ALs} and R_{convs} gives the PCB to ambient thermal
resistance of the switch R_{PAs}. The summation of R_{TIMd}, R_{ALd} and R_{convd} gives
the PCB to ambient thermal resistance of the diode R_{PAd}. R_{JCs} and R_{JCd} are
extracted from the datasheet and they amount to 1.1°C/W and 0.85°C/W respec-
tively.

Calculation of R_{CPs} and R_{CPd} of the asymmetric H-bridge module

The R_{CPs} and R_{CPd} are calculated by homogenization of the thermal vias pattern
shown in Fig. 5.54 for the switch and diode. The homogenization results in the
equivalent thermal PCB thermal properties listed in Table (5.14) and the thermal
resistances $R_{CPs} = 0.8845$°C/W and $R_{CPd} = 1.4260$°C/W.

Table 5.14: Equivalent thermal properties of the homogenized PCB of the asymmetric H-bridge

Device	Property	Value
switch	k_{xe} (W/m.K)	3.217
	k_{ye} (W/m.K)	3.385
	k_{ze} (W/m.K)	28.215
	C_{pe} (J/kg.K)	1.008×10^3
	ρ_{pe} (kg/m^3)	3.404×10^3
diode	k_{xe} (W/m.K)	3.217
	k_{ye} (W/m.K)	3.385
	k_{ze} (W/m.K)	28.215
	C_{pe} (J/kg.K)	1.198×10^3
	ρ_{pe} (kg/m^3)	3.828×10^3

Calculation of R_{PAs} and R_{PAd} of the asymmetric H-bridge module

The R_{PAs} and R_{PAd} and their three constituting components are computed in the same way described in section (5.6.1). The 3D thermal model generated figures for the calculation of R_{PAs},R_{PAd} and their constituting components (i.e. R_{TIM},R_{AL}, R_{conv}) are shown in Fig. 5.61 and Fig. 5.62 respectively. These figures are generated at 10 litre/min water flow rate and 25°C water inlet temperature.

Full thermal model parameters of the asymmetric H-bridge module

The values of the parameters of the steady-state thermal model of the asymmetric H-bridge inverter module are given in Table 5.15. The total resistance from junction to ambient for the switch R_{JAs} is 6 °C/W and for the diode R_{JAd} is 8.5 °C/W.

The steady state thermal model is verified by 3D thermal simulations at 10 litre/min water flow rate, 25°C water inlet temperature and two losses of 3 W and 4 W in the switch and the diode. The resulting temperature distribution over one asymmetric module at 3 W loss and 4 W loss is shown in Fig. 5.63 (a) and (b) respectively.

The thermal network calculated and the FE computed temperature of the switch and the diode at 3 W and 4 W switch losses are given in Table 5.16 and Table 5.17 respectively. A good correspondence between the thermal network values and the FE values can be noticed.
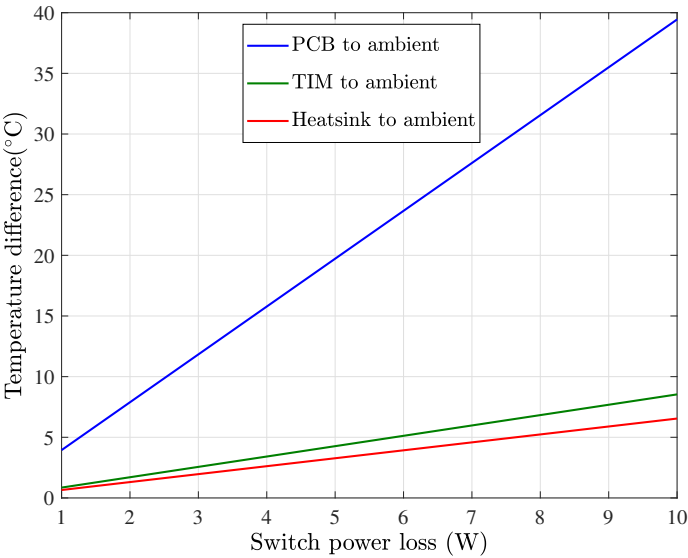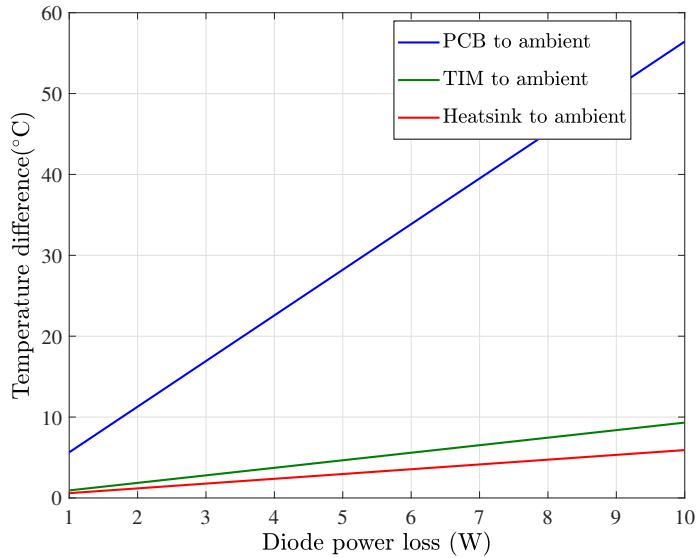
Figure 5.61: The variation of the temperature difference from the PCB bottom surface to ambient, the TIM to ambient, the polygon exposed surface to ambient for the switch C3M0075120J.

Table 5.15: Steady-state thermal model parameters of the asymmetric H-bridge inverter module

Device	Thermal resistance (°C/W)	Value
switch	R_{JCs}	1.1
	R_{CPs}	0.8845
	R_{TIMs}	3.1655
	R_{ALs}	0.2
	R_{convs}	0.65
diode	R_{JCd}	0.85
	R_{CPd}	1.4260
	R_{TIMd}	5.2226
	R_{ALd}	0.34
	R_{convd}	0.59

Figure 5.62: The variation of the temperature difference from the PCB
bottom surface to ambient, the TIM to ambient, the polygon exposed
surface to ambient for the diode LSIC2SD120C10.

(a)   (b)
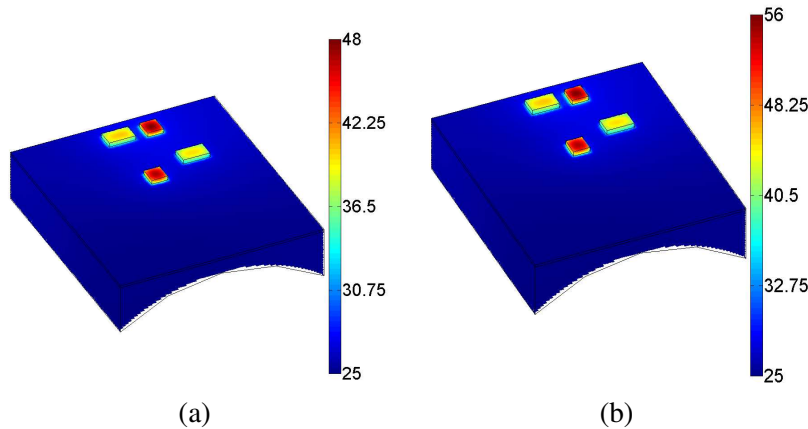
Figure 5.63: The 3D thermal FE temperature distribution over one
asymmetric H-bridge: (a) at 3 W loss in the devices (b) at 4 W loss.

Table 5.16: The computed switch temperature at 3 W and 4 W losses

losses (W)	Thermal network (°C)	FEM (°C)
3	43	44
4	49	50.5

Table 5.17: The computed diode temperature at 3 W and 4 W losses

losses (W)	Thermal network (°C)	FEM (°C)
3	50.5	49.5
4	59	58

5.12.2   Calculation of the transient thermal model parameters of the asymmetric H-bridge inverter module

The junction to case transient thermal models of the switch and the diode are represented by a Cauer network. The parameters of this network are obtained by fitting the thermal impedance curve given in the datasheet of the switch and the diode. The fitting results are shown in Fig. 5.64 and Fig. 5.65 for the switch and the diode respectively.
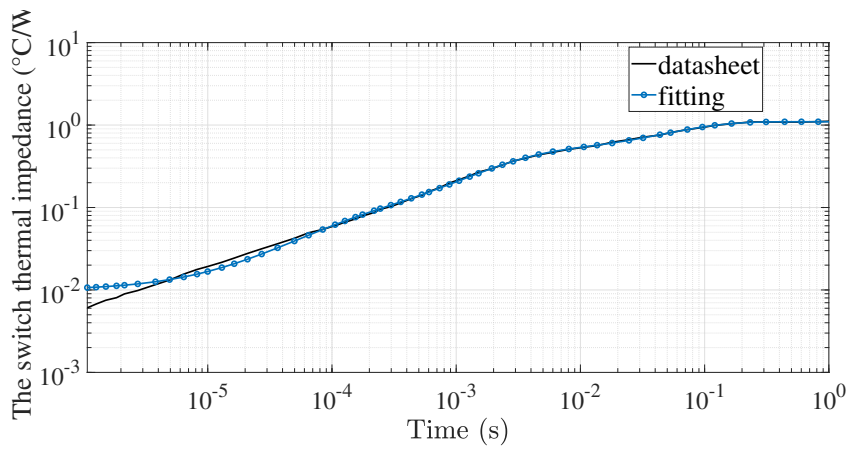
Figure 5.64: The datasheet given and the fitted thermal impedance of the switch C3M0075120J.

The case to ambient thermal models of the switch and the diode are computed by the same way explained in Chapter 4 section (4.3.2). The transient thermal model parameters of the switch and the diode are listed in Table (5.18) and Table
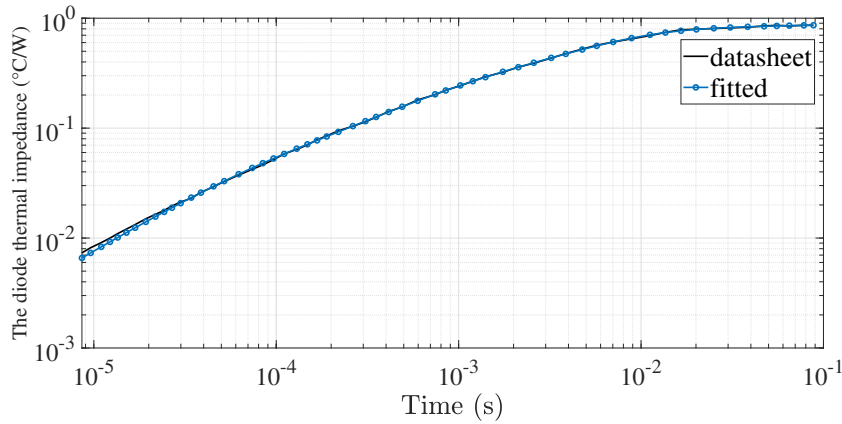
Figure 5.65: The datasheet given and the fitted thermal impedance of the diode LSIC2SD120C10.

(5.19) respectively.

Table 5.18: Transient thermal model parameters of the switch C3M0075120J of the PR integrated SRM converter module

Parameter	Value
R_1 (°C/W)	0.1212
R_2 (°C/W)	0.2969
R_3 (°C/W)	0.1990
R_4 (°C/W)	0.4818
C_1 (J/°C)	0.0020
C_2 (J/°C)	0.0033
C_3 (J/°C)	0.0333
C_4 (J/°C)	0.1026
C_{cp} (J/°C)	0.4022
C_{TIM} (J/°C)	0.1402
C_{AL} (J/°C)	2.4559

Fig. 5.66 (left) shows the instantaneous loss of the switch C3M0075120J resulting at the operating conditions in Table 5.13. The large height needles corre-

Table 5.19: Transient thermal model parameters of the diode LSIC2SD120C10 of the PR integrated SRM converter module

Parameter	Value
R_1 (°C/W)	0.1253
R_2 (°C/W)	0.2143
R_3 (°C/W)	0.4543
R_4 (°C/W)	0.0760
C_1 (J/°C)	0.0016
C_2 (J/°C)	0.0021
C_3 (J/°C)	0.0087
C_4 (J/°C)	0.3806
C_{cp} (J/°C)	0.335
C_{TIM} (J/°C)	0.0713
C_{AL} (J/°C)	1.446

spond to the turn on and the turn off switching loss. The instantaneous junction temperature is shown in Fig. 5.66 (right). The average temperature is 41.6°C and the peak value is 44.8°C. A difference of 3.2°C between the peak and the average value results mainly due to the large switching loss needles at the transition moments of the switch.

Fig. 5.67 (left) shows the instantaneous loss of the diode LSIC2SD120C10 resulting at the operating conditions in Table 5.13. The large height needles correspond to the turn off switching loss. The instantaneous junction temperature is shown in Fig. 5.67 (right). The average temperature is 38.2°C and the peak value is 44.1°C. A difference of 5.9°C between the peak and the average value results mainly due to the large switching loss needles at the transition moments of the diode.

5.13 Conclusion

The geometrical parameters that influence the losses and the temperature of the YASA machine are studied in this chapter. These studies allow an optimal parameter selection. The studied geometrical parameters are the thickness of the inward heat extraction fins, the PM thickness and the air gap length. It is found that the coolest machine results at a certain fin thickness while the most efficient one results
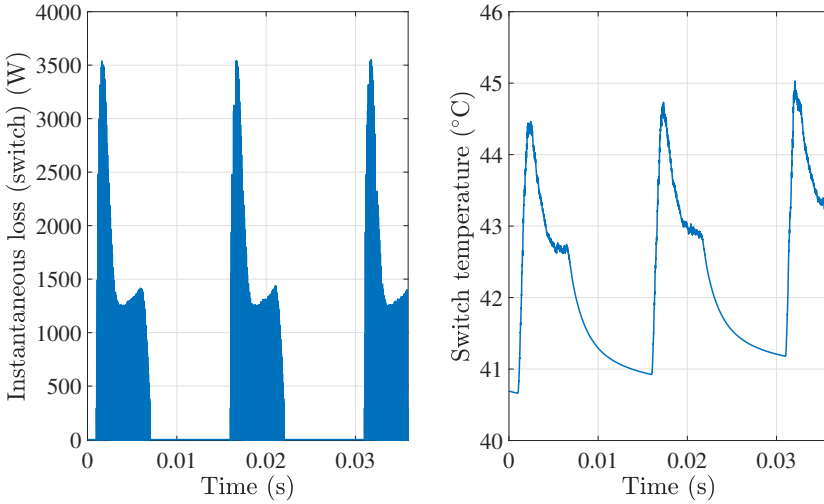
Figure 5.66: The instantaneous loss of the switch C3M0075120J (left) and junction temperature (right) at operating conditions in Table 5.13.
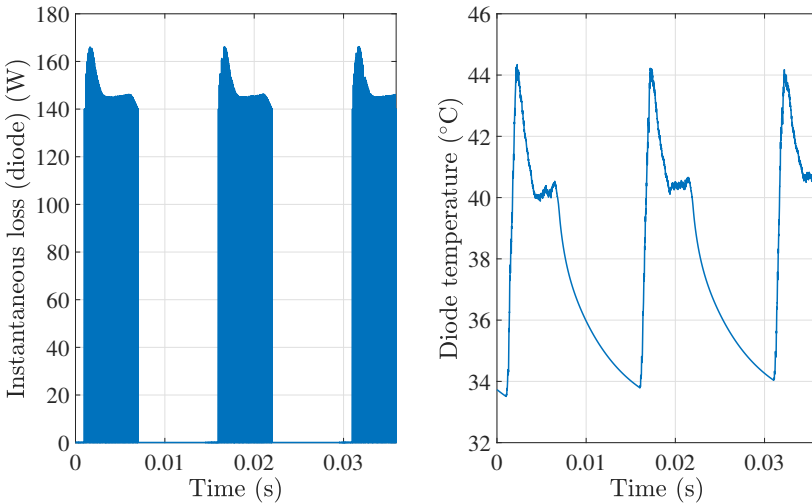

Figure 5.67: The instantaneous loss of the diode LSIC2SD120C10 (left) and junction temperature (right) at operating conditions in Table 5.13.

at different thickness. It is also found that as the thickness of the PM increases, the YASA losses decrease and the temperature as well. The reason behind this is the higher air gap convection coefficient and the lower required stator current at certain

torque. It is found also that as the air gap length increases, the losses increase due to the higher required stator current for the same torque to overcome the higher reluctance and the temperature increases as well due to the higher losses and the lower convection coefficient.

A GaN based half-bridge inverter module is designed and optimized for the CP integrated YASA drive. The heat transfer path from the GaN switches of the half-bridge inverter module to the cooling channel is optimized by populating a thermal via pattern beneath the thermal pad of the switches which reduced the thermal resistance from the switch thermal pad to the bottom of the inverter module PCB by about 98.7%. The radius of the cooling channel is also optimized for optimal heat transfer from the switches and the YASA AFPMSM stator to the cooling fluid.

The parameters of the steady-state and transient thermal models of the GaN switch of the half-bridge are computed after designing the inverter modules. The transient temperature shows a difference of about 4.5°C between the peak and the average temperature of the switch due to the high instantaneous switching losses.

The peak line current that can be injected by one half-bridge inverter module is computed using a computational fluid dynamics model. The temperature of the windings was still far below its rated value. The output power that can be obtained from this integrated drive is calculated and amounts to 4.2 kW. Several techniques for increasing this power are discussed in Chapter 7.

For the PR integration topology for the SRM, the selected topology for the inverter module implementation is the asymmetric H-bridge for its small number of passive components and the possibility to switch a unipolar or a bipolar voltage over the SRM terminals. The SiC technology is selected for the implementation of the asymmetric H-bridge switches and diodes. The design of the asymmetric H-bridge is optimized by populating thermal vias beneath the case of the switch and the diode.

The parameters of the steady-state and transient thermal models of the switches and the diodes of the asymmetric H-bridge are computed after designing the inverter modules. The transient temperature shows a difference of about 3.2°C between the peak and the average temperature of the switch and 5.9°C between the peak and the average temperature of the diode due to the high instantaneous switching losses.

Chapter 6

Experimental Validations of the Circumscribing Polygon and Polygon Retrofitted Integration Topologies

6.1 Introduction

The experimental validations of the modelling introduced in Chapters 3 and 4 for the air cooled YASA machine, the CP integrated YASA drive and the PR integrated SRM are provided in this chapter.

6.2 Experimental setup and results of the air cooled YASA AFPMSM

In this section, the experimental setup of the air cooled YASA machine is described and the modelling validations are provided.

Thermal measurements are conducted and compared with the FE and the LPTN modelling results. Fig. 6.1 shows the experimental setup of the air cooled YASA AFPMSM. The setup consists of a 4 kW YASA machine with key parameters in Table 6.1. The YASA machine is mechanically coupled to an induction machine of 7.5 kW rated power and 3000 rpm rated speed. The induction motor is driven by a commercial drive. The speed/torque setpoint of the commercial drive is generated using a dSPACE 1104 platform.

The stator core temperature and the winding temperaure are measured by the resistance temperature detector (RTD) of the PT100 type. The PM temperature is measured by an infrared temperature sensor (ZTP-135SR). The output of these
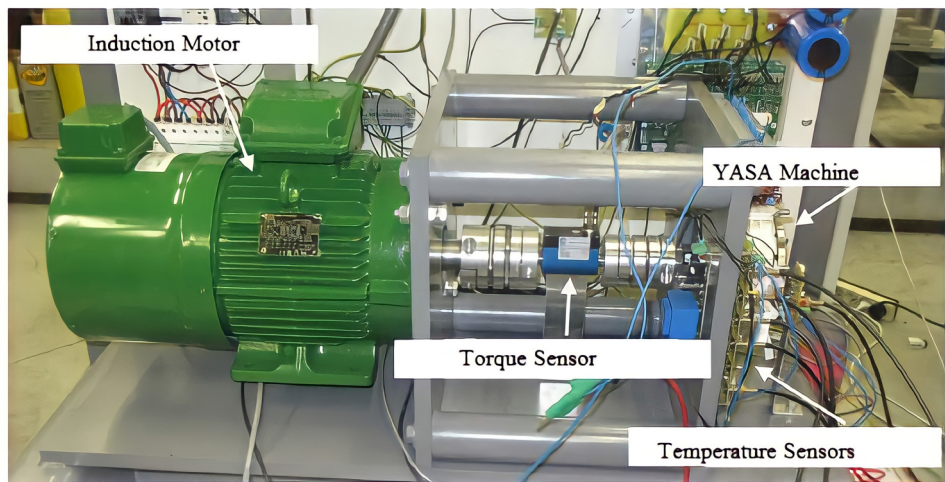
Figure 6.1: The experimental setup of the air cooled YASA machine.

Table 6.1: YASA geometrical parameters

Parameter	Value	Unit
number of poles	16	-
teeth number	15	-
outer diameter housing	195	mm
outer diameter active	148	mm
PM thickness	4	mm
rotor outer radius	74	mm
slot width	11	mm
axial length	60	mm
airgap size ratio	0.0135	-
PM angle span ratio	0.8	-

sensors is signal conditioned by an analog signal conditioning circuit and sampled
every 5 s by the dSPACE 1104.

To validate the LPTN model with well defined losses, the measurements are
conducted at zero core losses and zero magnet losses. The stator core losses and
the magnet losses are eliminated by replacing the magnets with aluminium pieces
with the same shape as the magnets (see Fig. 6.2) [74] and injecting DC-current in

the stator windings in a way that the magnetic flux penetrates the aluminium pieces in one direction at each rotor position. By this way, the only remaining losses are the winding losses.

Figure 6.2: The rotor disk with the aluminium pieces instead of the magnets used in the experimental measurements.

The measurement results are compared to the 3D FE and the LPTN modelling results at 100 W total winding loss and a speed of 1000 rpm. The ambient temperature at which the measurements are performed is 25°C. The winding, the core and the PM temperatures are shown in Fig. 6.3.

It can be seen from Fig. 6.3 that the modelling results are in a good agreement with the experimental measurements. Fig. 6.4 shows the temperature distribution over the stator and the rotor segments at 100 W winding loss, 1000 rpm and 25°C ambient temperature.

The measurements are repeated at 100 W winding loss, 25°C ambient temperature and 2000 rpm. The steady-state results are summarized in Table 6.2. Due to the higher convection coefficients at the higher speed, the steady-state winding temperature reduces by 7°C, the stator core temperature reduces by 8°C and the PM temperature reduces by 0.8°C compared to the 1000 rpm case.

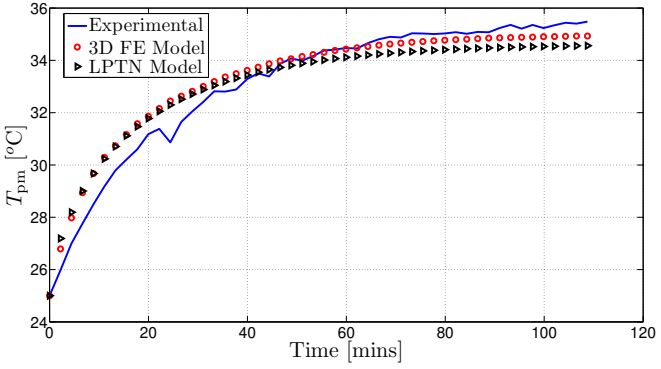## 6.3 Experimental setup and results of the CP integrated YASA AFPMSM

The CP integration concept for the YASA AFPMSM is validated by the three teeth setup shown in Fig. 6.5. A 3D CAD model for this experimental setup is shown in Fig. 6.6 to further illustrate the detailed construction and the materials of the setup
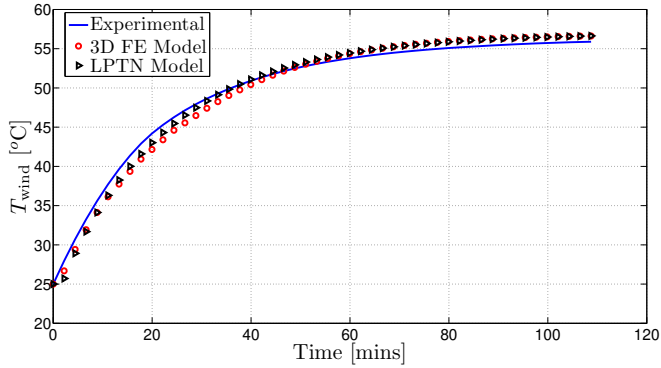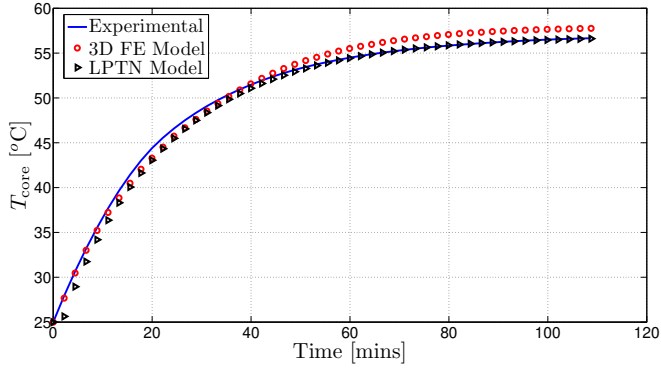
Figure 6.3: The measured temperature of (a) the windings, (b) the stator core and (c) the PMs compared to the 3D finite element and lumped parameter thermal network modelling. These results are obtained at 100 W total winding loss and 1000 rpm at 25°C ambient temperature.
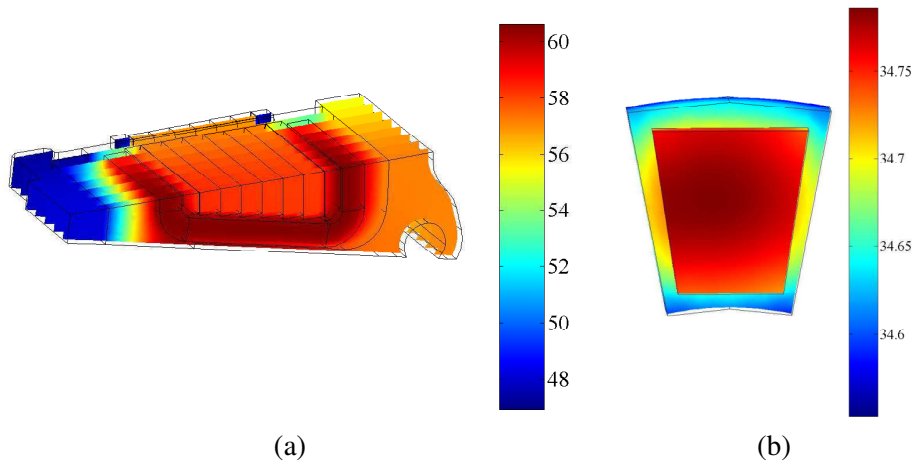
Figure 6.4: The temperature distribution over (a) the stator segment and (b) the rotor segment at 100 W winding loss and 25°C ambient temperature.

Table 6.2: Steady-state temperatures of the YASA machine at 2000 rpm, 100 W winding loss and 25°C ambient temperature

	Experimental	FEM	LPTN
Winding average temperature	49.02	48.53	48.53
stator core average temperature	48.68	48.43	48.43
PM average temperature	34.48	33.72	33.72

components. Table 6.3 contains the materials and the geometrical parameters of the different parts in the setup. Besides the integrated three teeth, the setup has a DC-link board and an $R = 8\ \Omega$, $L = 3$ mH load. The control of the inverter switches and the signal acquisition are performed using the dSPACE MicroLabBox. The in-line current is measured with the on-board sensor (ACHS-7123), the temperature of the switches is measured using the thermal camera (GTC-400), and the temperature of the lower end-winding is measured with the resistance temperature detector (RTD) PT100 sensor. The electrical waveforms are visualized using a 1GHz Tektronix scope. The experimental measurements are performed to compute the switch losses and to validate the modelling of the CP integrated drive. The modelling is validated using DC and pulse width modulated (PWM) waveforms.
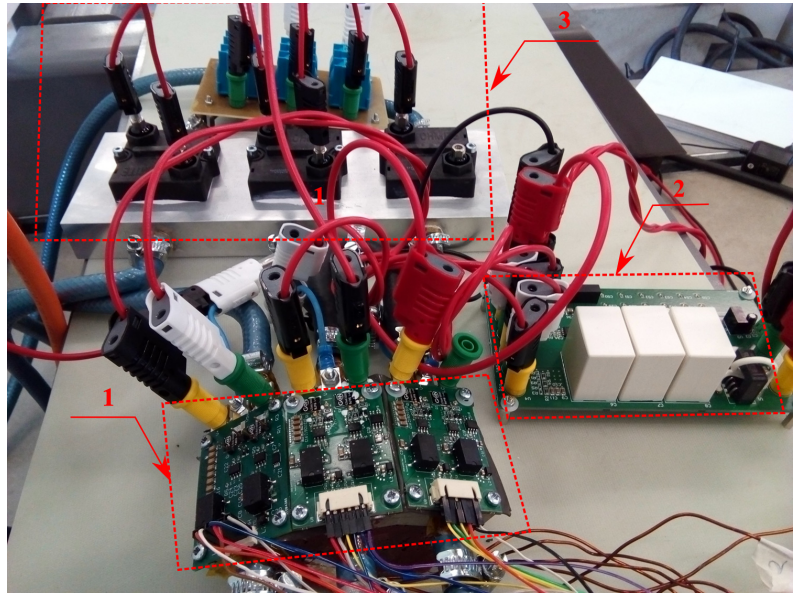
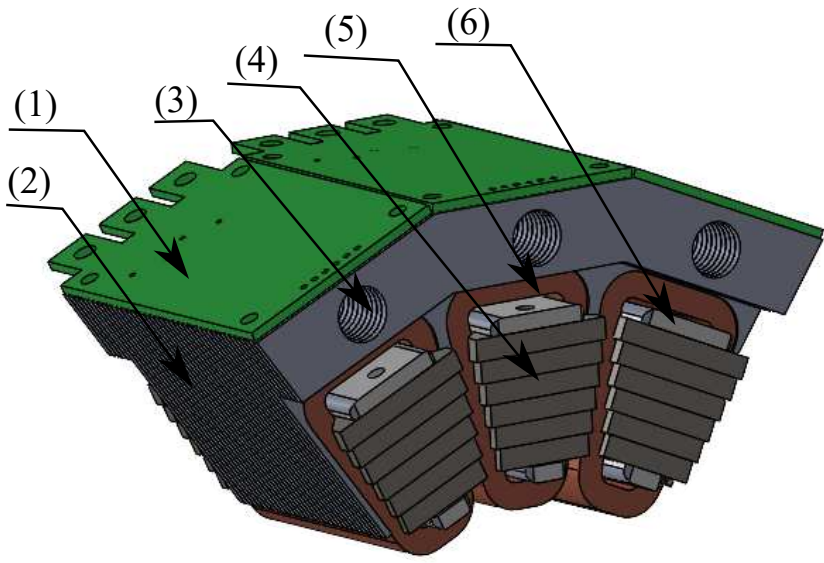Figure 6.5: Experimental setup: (1) The three teeth, (2) The DC link board, (3) The load.

Figure 6.6: 3D CAD model for the three teeth experimental setup: (1)inverter module PCB, (2) aluminium shared cooling structure, (3) cooling channel, (4) core, (5) winding, (6) epoxy infiltrated gap.

Table 6.3: Material specifications of the experimental setup

part	specifications	
	material	geometry
winding	copper	round wire, 0.9 mm diameter, 90 turns
core	M100-23P	0.23 mm laminations
cooling structure	aluminium	2 mm laminations

6.3.1   Switch loss measurements

The conduction and switching losses of the switch are measured using one half-bridge module connected as shown in Fig. 6.7 (a) for the conduction loss measurements and Fig. 6.7 (b) for the switching loss measurement.
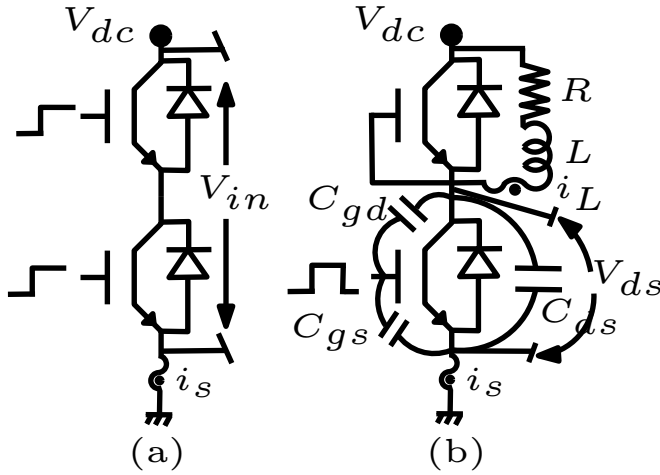
Figure 6.7: The schematic diagram for the circuit used for (a) conduction loss measurements, (b) switching loss measurements.

The two switches of the half-bridge in Fig. 6.7 (a) are turned on and a variable DC-voltage is applied between the drain of the upper switch and the source of the lower switch. For different DC-voltages, this voltage is measured using the differential probe (RS 729-6677). The source current of the lower device is measured using the current probe (TCPA 300). All waveforms are visualized using a 1GHz scope. The junction temperature is measured using the thermal camera (GTC-400). The measurements are done at 1 litre/min water flow rate and 25 °C inlet temperature. From these measurements, the measured drain to source resistance $R_{ds}(T)$ of one device is calculated and plotted in Fig. 6.8.
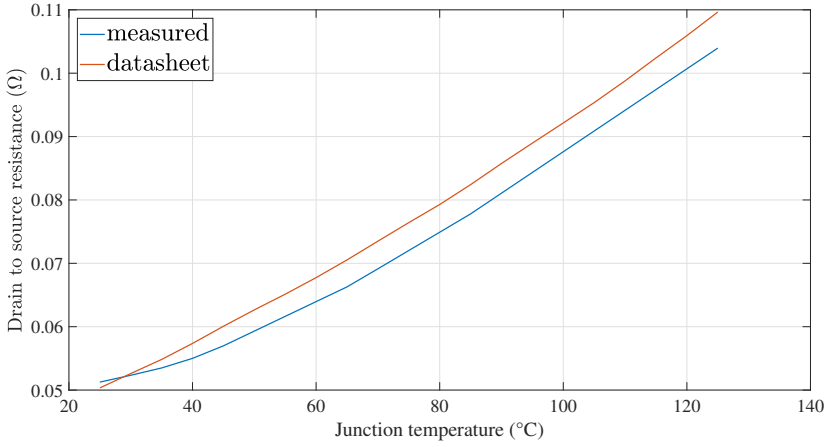
Figure 6.8: Measured switch resistance R_{ds} versus junction temperature.

Using the circuit shown in Fig. 6.7 (b) with the upper transistor kept off and the lower transistor switched with f_s=10 kHz, the loss of the lower switch is measured and compared to the values calculated using the method explained in Chapter 4 section (4.2). The measurements are performed at 175 V DC-link voltage, 8.4 A switch current and different junction temperatures. Fig. 6.9 shows V_{ds}, i_s, V_{gs} of the lower switch and i_L as well at 51°C junction temperature. The ringing that can be noticed in the current waveform results from the resonance between the output capacitance of the switch and the parasitic inductance of the current probe.

The total switch loss is calculated from (6.1) using the math mode of the scope, the conduction loss is calculated using R_{ds} and the rms value of the current calculated by the scope and the switching loss is calculated from the difference. Fig. 6.10 shows the total loss, the conduction loss, and the switching loss at different junction temperatures measured and calculated. It can be noticed that the analytical model overestimates the conduction loss a bit and underestimates the switching loss a bit but the total loss is in a good agreement with the measurements.

$$P_{swtm} = \int_0^{T_s} V_{ds}(t)i_s(t)dt \qquad (6.1)$$

where P_{swtm} is the total switch loss, $T_s = \frac{1}{f_s}$.

6.3.2 Validation of the CP integration modelling using DC waveforms

The DC measurements are performed using the circuit connections in Fig. 6.11 for the three half-bridge inverter modules and the three coils. The inverter modules are supplied from an adjustable DC-source and the three coils are supplied from
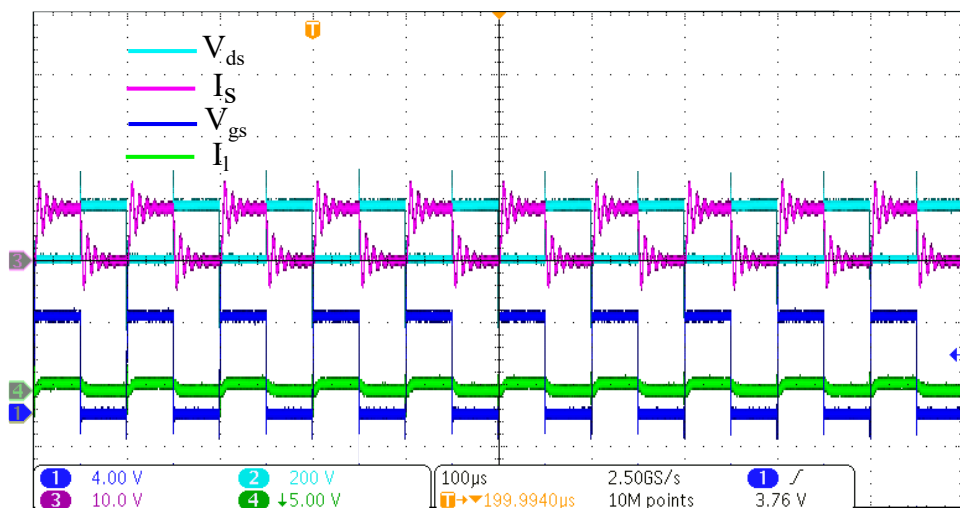
Figure 6.9: Switch loss measurements waveforms measured at 175 V DC-link voltage, 8.4 A switch current and 51°C junction temperature.
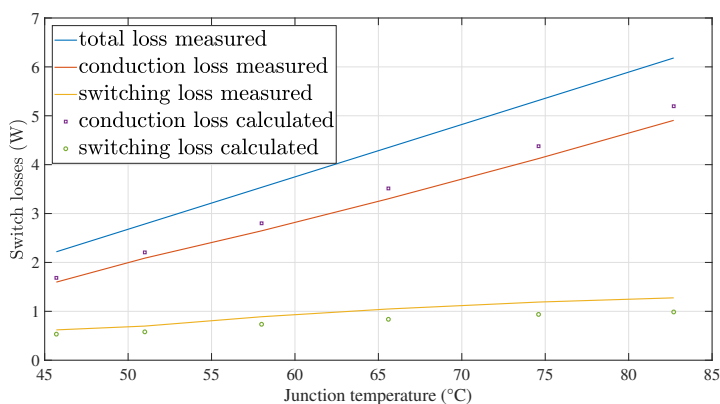

Figure 6.10: Switch loss measurements measured at 175 V DC-link voltage, 8.4 A switch current and different junction temperatures.

a different adjustable DC-source. The measurements are conducted at 25°C water inlet temperature and 1 Litre/min water flow rate. The objective of these measurements is the calculation of the total thermal resistance from junction to ambient of the switch GS66508B.

The DC-source of the coils is adjusted until a total steady-state power loss of 75 W is reached. The junction temperature of the switch is recorded at different switch losses and the junction temperature rise above the water temperature is plotted versus the switch losses as shown in Fig. 6.12. The slope of the curve of Fig.
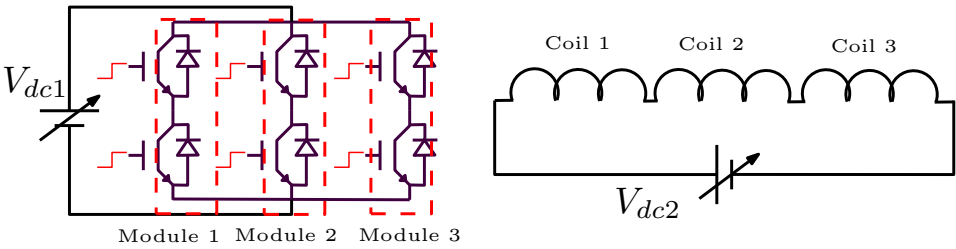
Figure 6.11: The connection of the inverter modules (left) used to generate Fig. 6.12 and the coils connection used to generate 75 W total loss in the three coils (right).

6.12 gives the thermal resistance from the junction of the switch to the cooling water. The value of this thermal resistance is 13.498°C/W which is in a good agreement with the value derived in Chapter 5 section (5.6.1). The switch losses can be estimated from this thermal resistance and the water inlet temperature.
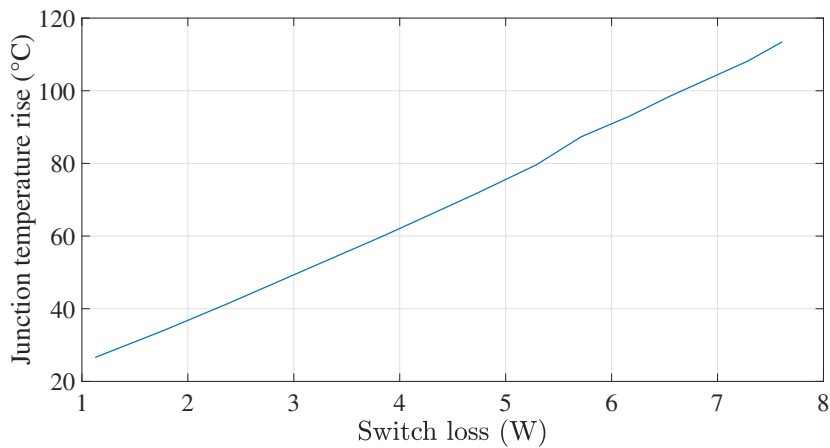

Figure 6.12: The measured junction temperature rise versus the switch loss at 25°C water inlet temperature and 1 litre/min water flow rate.

The temperature distribution over the three inverter modules at 6 W loss per switch, 20°C water inlet temperature and 1 Litre/min water flow rate is shown in Fig. 6.13. The junction temperature reaches 101.6°C which is in a good agreement with the value calculated from the steady-state thermal model. It can be noticed that the temperature of the low power driving components remains at low value which ensures high operation reliability of the inverter modules.
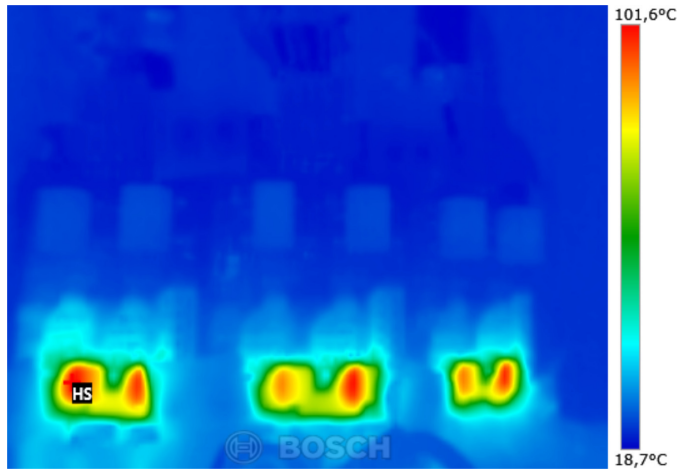
Figure 6.13: The converter module temperature distribution at 6 W loss per switch at 20°C water inlet temperature and 1 Litre/min water flow rate.

6.3.3 Validation of the CP integration modelling using PWM waveforms

To evaluate the performance of the CP integration topology with real PWM waveforms, the three half-bridge inverter modules are operated as a three-phase inverter. The PWM technique used is the sinusoidal one with a switching frequency f_s of 10 kHz. The measurements are carried out at 175 V DC-link voltage and the peak line current is adjusted to 9.5 A.

The measured output phase voltage, current and power are shown in Fig. 6.14. The measured average output power is 1094.5 W. The measured input DC voltage, current and power are shown in Fig. 6.15. The average input power is 1115 W. The total loss in the three half-bridge inverter modules is 20.5 W which means a switch loss of 3.41 W.

The temperature of one of the inverter modules is shown in Fig. 6.16. The junction temperature reaches 67.9°C. The thermally estimated loss corresponding to this temperature is 3.2 W which is in a good correspondence with the electrically measured one.

The temperature of the stator elements (core and windings) is also measured with the thermal camera and a PT100 RTD temperature sensor placed on the bottom end-winding. Fig. 6.17 shows the core temperature of the three teeth which equals 54 °C. Fig. 6.18 shows the bottom end-winding temperature of the three teeth which equals 58.7°C. The transient bottom end-winding temperature is measured with the PT100 sensor and shown in Fig. 6.19. The temperature measured with the thermal camera is in good agreement with the value measured by the
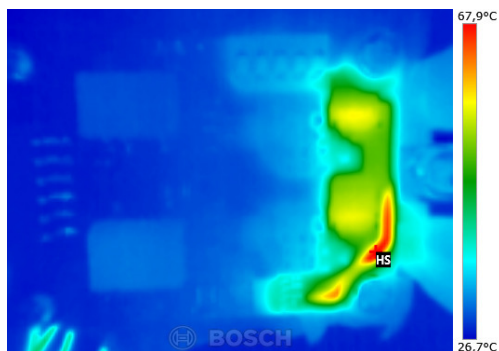
Figure 6.14: The measured phase current, voltage and power measured at 9.5A peak phase current.

Figure 6.15: The measured DC-link voltage, current and power at $V_{dc} = 175$ V.

PT100 RTD.

To validate the accuracy of the CFD model in predicting the stator elements temperature, the simulation is performed at 1 litre/min water flow rate, 25°C water inlet temperature, 25 W loss per winding, 3.42 W loss per switch. The simulation result is shown in Fig. 6.20. The core temperature is 52.58 °C, the bottom end-winding temperature is 57.77°C and both are in a good agreement with the measurements presented in Fig. 6.17 and Fig. 6.18.

Figure 6.16: The measured inverter module temperature distribution at 175 V DC-link voltage, 9.5 A peak line current, 1 litre/min water flow rate and 25°C water inlet temperature.
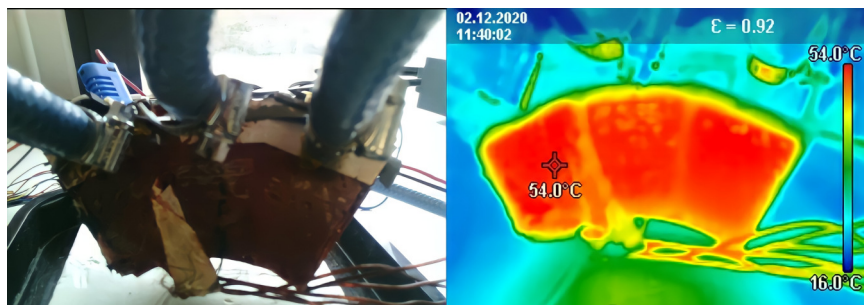

Figure 6.17: The measured temperature distribution over the core of the three teeth at 3.42W switch loss, 25W winding loss and 1 litre/min flow rate.
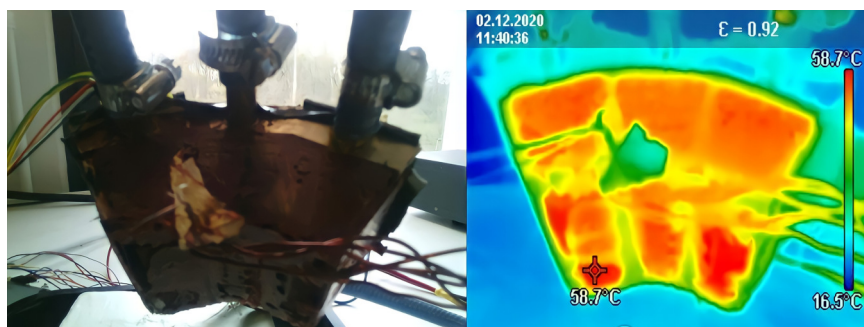

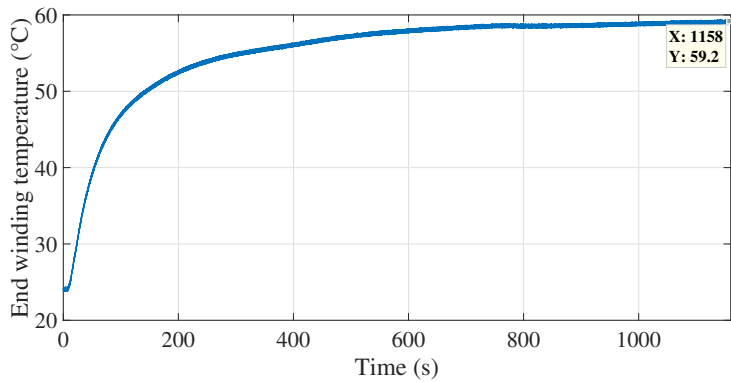Figure 6.18: The measured temperature distribution over the bottom end-winding of the three teeth at 3.42W switch loss, 25W winding loss and 1 litre/min flow rate.

Figure 6.19: The measured transient temperature of the bottom end-winding measured with PT100 RTD sensor at 3.42W switch loss, 25W winding loss and 1 litre/min flow rate.
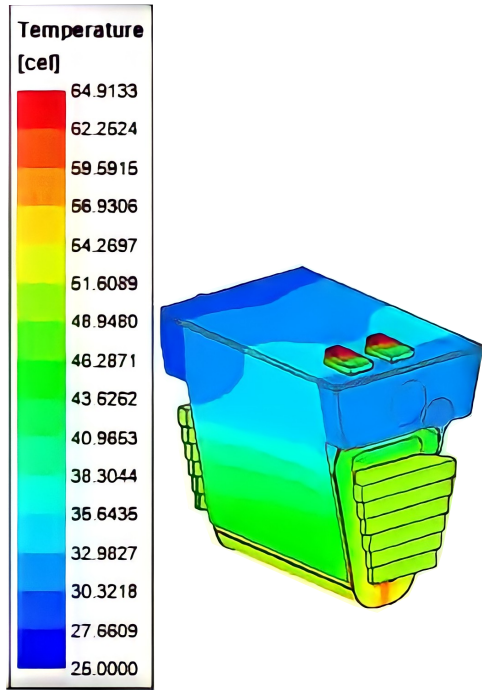

Figure 6.20: The simulated temperature distribution at 3.42W switch loss, 25W winding loss and 1 litre/min flow rate.

6.4 Experimental setup and results of the PR integrated SRM

Fig. 6.21 is a picture for the implemented PR integrated SRM drive. The full experimental setup is shown in Fig. 6.22. It consists of the PR SRM drive, the load induction machine and the torque sensor. The torque is measured with a torque sensor (DR-2643-P). The phase currents are measured with the on-board sensor (ACHS-7123). The position is measured with a resolver (RE-15-1-A14). The phase torque is estimated from the measured currents and position. The temperature of the power converter module is measured using the thermal camera (GTC400). The winding temperature is measured using the resistance temperature detector (PT100).
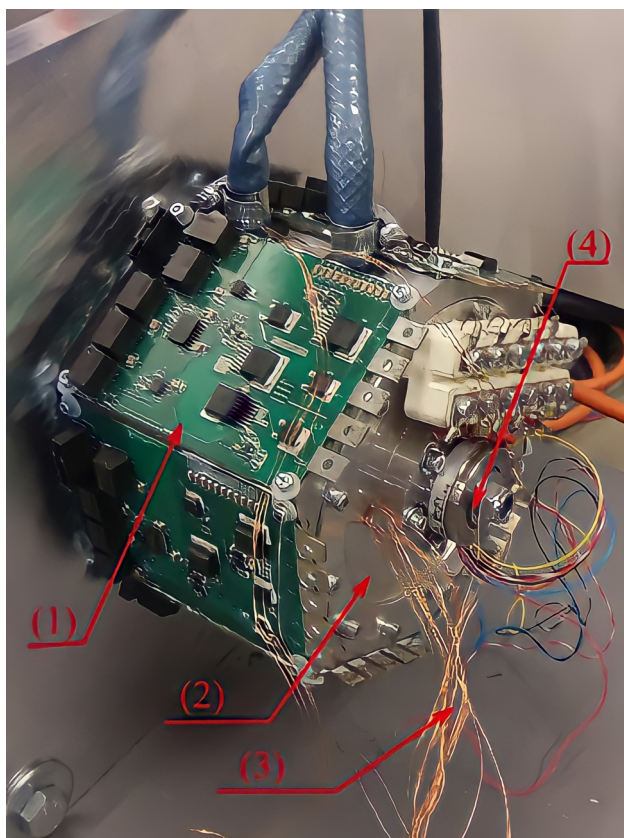

Figure 6.21: The implemented PR integrated SRM drive: (1) asymmetric H-bridge converter module, (2) SRM, (3) PT100 temperature sensor, (4) resolver.

The signal acquisition and the control algorithm are implemented on the MicroLabBox dSpace. The converter is switched at a frequency of 20 kHz and the

control loop is executed every 50 μs. The induction machine regulates the speed at the torque regulated by the SRM.
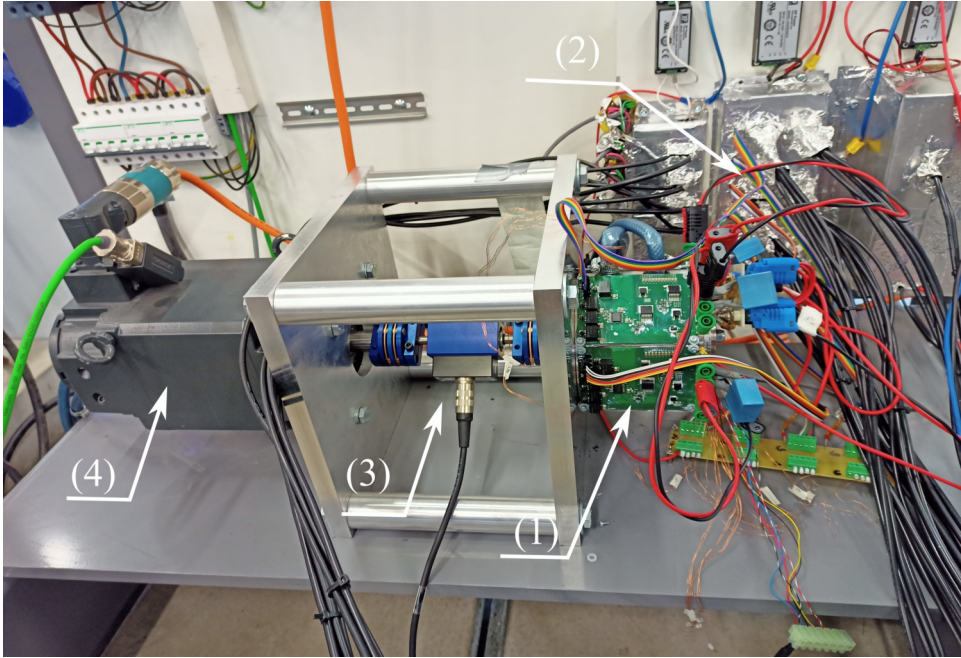

Figure 6.22: The full experimental setup: (1) The PR integrated SRM drive, (2) DC-link board, (3) Torque sensor, (4) The load induction machine.

6.4.1   Validation of the SRM modelling

The temperature of the windings is measured at 2 Nm and 1000 rpm and compared to the results obtained from the FEM and the LPTN introduced in Chapter 3 section (3.8). The operating conditions and heat sources at 2 Nm and 1000 rpm are listed in Table 6.4.

Fig. 6.23 shows the measured phase currents and torques at 2 Nm and 1000 rpm. The currents and the torques are in a good agreement with the simulated ones in Fig. 6.24 but without the high frequency switching ripples as the sampling frequency is equal to the switching frequency.

The SRM winding temperature at 2 Nm and 1000 rpm is shown in Fig. 6.25. The measured steady-state temperature at this operating point is 138°C. The steady-state temperature calculated by the FEM and the LPTN is 135.4°C. A 2.6°C temperature difference between the measured temperature and the calculated one from the models is found. As the models calculate the average temperature and the measurements are performed at certain locations in the windings, this difference

Table 6.4: The operating conditions at 2 Nm and 1000 rpm operation of the SRM

Variable	Value
Total winding losses (W)	410
Total stator core losses (W)	2.6
Total rotor core losses (W)	1.8
Switch losses (W)	2.7
Diode losses (W)	1.4
Water inlet temperature (°C)	25
Water flow rate (Litre/min)	10
h_{SRM} (W/m^{2}K)	1375
h_{PR} (W/m^{2}K)	910
V_{dc} (V)	200

could result from the small temperature gradient from one location to the other. The accuracy of the material properties would also be one of the reasons of that difference. The approximations made in the calculation of the thermal resistance of the parts with irregular shapes is also one of the reasons. The difference of the transient of the temperature calculated from the FEM and the LPTN compared to the measurements is mainly due to the accuracy of the specific heat capacity of the different components in the path of heat transfer from the windings to the water.

The stator core temperature is shown in Fig. 6.26. It reaches 43°C. The temperature difference between the windings and the stator core can be explained by looking to the temperature distribution and the heat flux path shown in Fig. 6.27 and Fig. 6.28. It can be observed from Fig. 6.28 that the heat generated by the effective winding part of the coil flows axially towards the end-winding insert and then radially towards the water jacket. The reason behind the initial axial flow of the heat instead of direct radial flow to the water jacket through the stator core and the end-winding insert is the epoxy layer with small thermal conductivity in the cavity between the coil and the stator core. This also explains the temperature difference between the end-winding insert surface and the stator core surface in contact with the water jacket.

The large temperature gradient on the interface between the coil and the stator core results from the small thermal conductivity of the slot liner. The high temperature gradient on the coil in the radial direction is due to the small thermal conductivity of the coil in the radial direction. It can also be noticed that in the
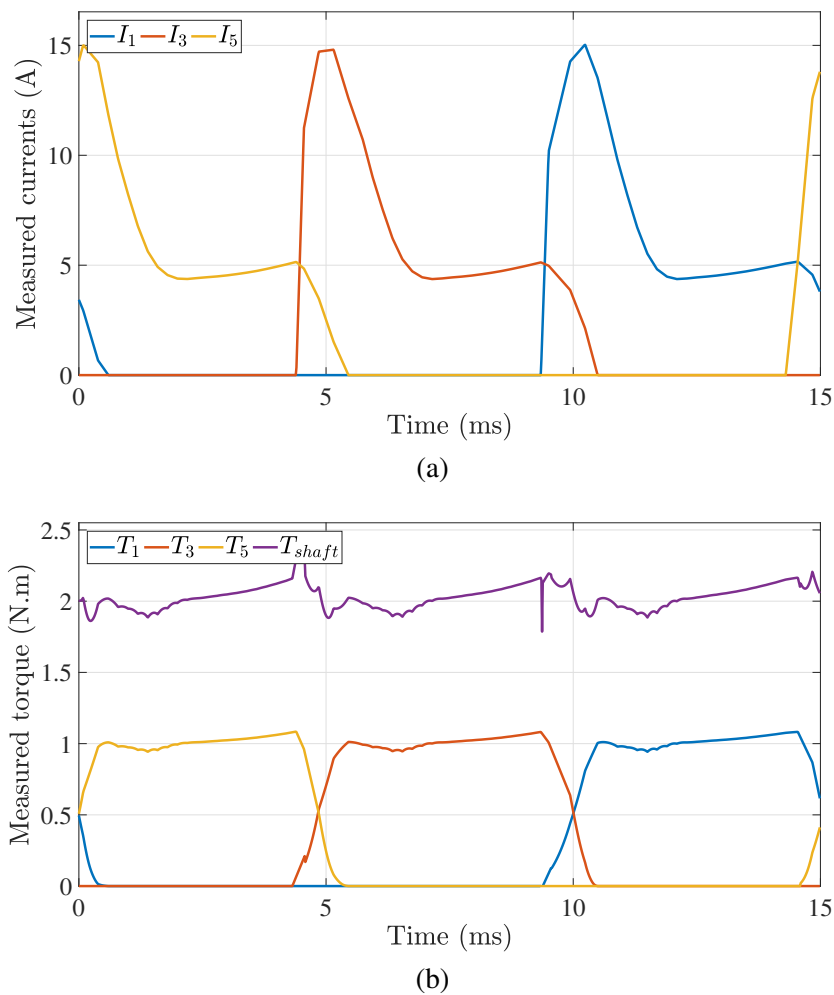
Figure 6.23: The measured coil currents (a) and torques (b) at 2 Nm and 1000 rpm.

coil part away from the water jacket (the red part in Fig. 6.28), the heat flows axially (due to the high axial thermal conductivity of the coil) to reach the water jacket via the end-winding insert. This explains the high local heat flux on the interface between the coil and the end-winding insert in the axial direction. For the coil part near the water jacket, the heat flux propagates radially towards the water jacket through the end-winding insert. This explains the high local heat flux on the boundary between the coil and the end-winding insert in the radial direction.

The air temperature used for the boundary condition of the air gap exposed surfaces is calculated from the LPTN. Fig. 6.29 shows the temperature of the air
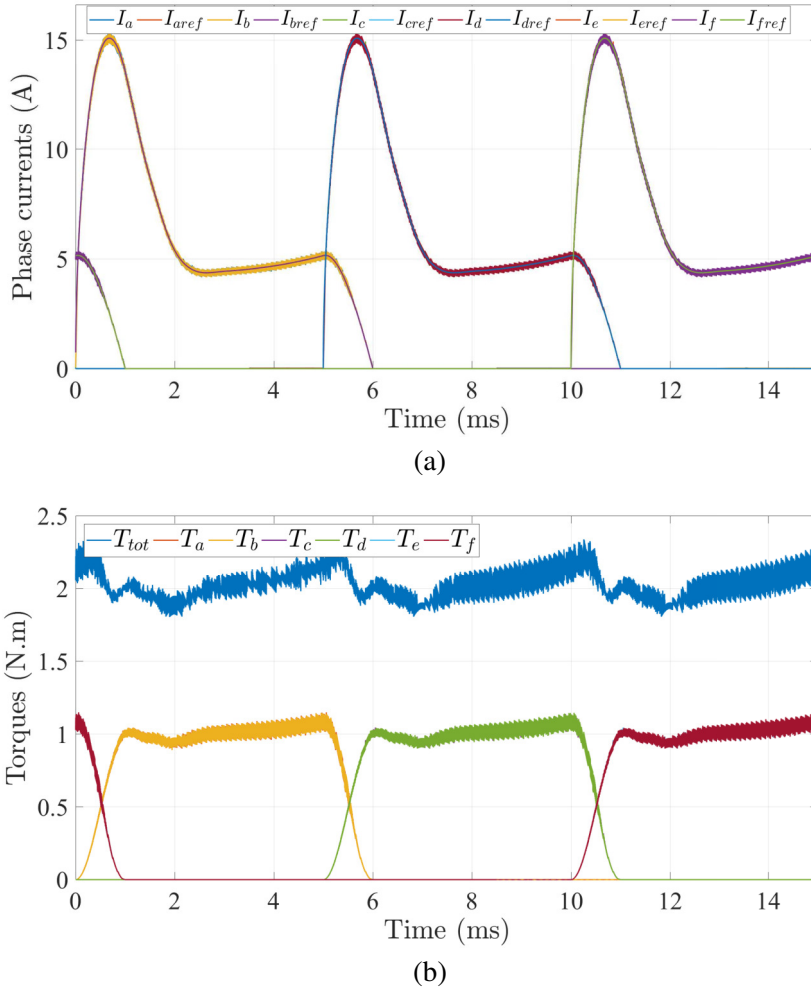
(a)

(b)

Figure 6.24: The simulated phase currents (a) and torques (b) at 2 Nm and 1000 rpm.

and the rotor at 2 Nm and 1000 rpm. At steady-state the air temperature reaches 55°C. The transient rate of heat transfer to the air gap assuming that the heat flows from the stator to the air gap is shown in Fig. 6.29. The following can be noticed from Fig. 6.29 and Fig. 6.30.

- Initially the heat transfers from the stator to the air gap. This can be noticed from the positive value of the heat flux. This initial direction of the heat transfer from the stator to the air gap is logical because of the much higher losses in the stator windings and core compared to the rotor core. These
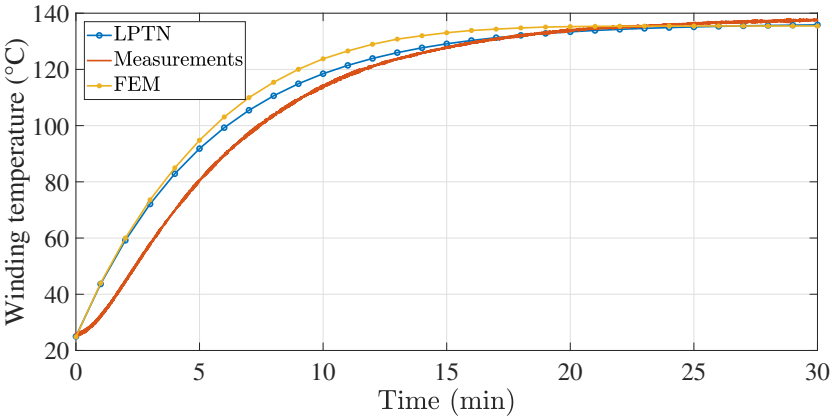
Figure 6.25: The winding temperature of the SRM at 2 Nm and 1000 rpm. This temperature is obtained at the operating conditions given in Table 6.4.
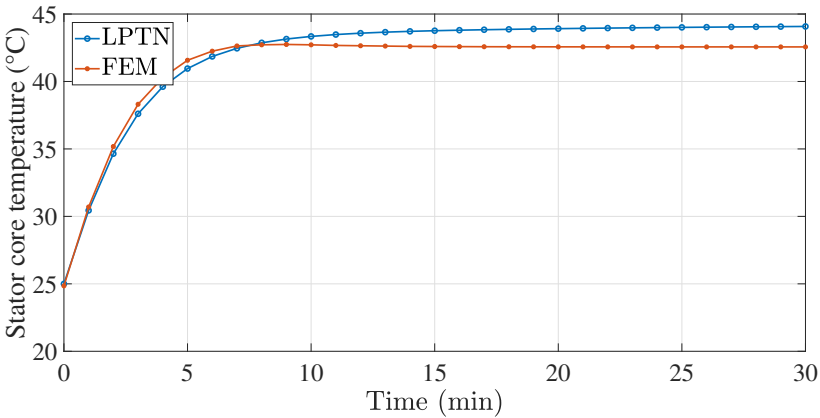

Figure 6.26: The stator core temperature of the SRM at 2 Nm and 1000 rpm. This temperature is obtained at the operating conditions given in Table 6.4.

higher losses in the stator cause faster temperature rise of the stator above the air temperature compared to the rotor.

- The temperature rise of the air and the heat losses of the rotor cause temperature rise of the rotor.

- The above process continues until the stator temperature reaches steady-state. The stator reaches steady-state faster than the rotor because of the high
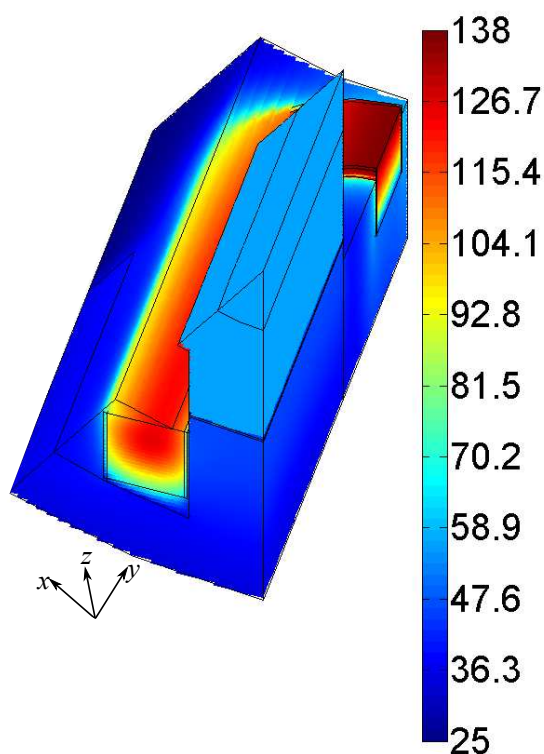
Figure 6.27: The temperature distribution over one quarter tooth of the SRM. This temperature distribution is obtained at the operating conditions given in Table 6.4.
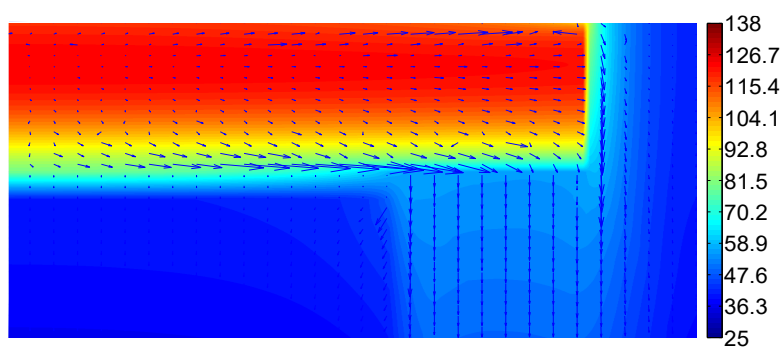

Figure 6.28: The temperature distribution and the heat flux lines obtained on a cross-section on the yz-plane in the middle of the coil. This temperature distribution is obtained at the operating conditions given in Table 6.4.

rate of heat evacuation to the water jacket resulting from the high convection coefficient and the steady water temperature.

• Right at the moment the stator reaches steady-state, the heat transfer from the stator to the air gap becomes zero which means that the rate of heat generation in the stator becomes equal to the rate of heat evacuation in the water.

• Once the stator reaches steady-state, the rotor temperature rises above the air gap temperature until the rotor temperature and air gap temperature reach steady-state. This makes sense because the only heat transfer path of the rotor is the path to the air gap.

• The steady-state temperature difference between the rotor and the air gap is 1.75°C. At this temperature difference the rate of heat generation in the rotor (the rotor power loss) equals the rate of heat evacuation in the air gap.

The steady-state temperature distribution of the rotor and the heat transfer in the air gap are shown in Fig. 6.31. A uniform temperature distribution over the rotor can be noticed due to its homogeneous structure and high thermal conductivity. The heat transfer from the rotor to the air gap and then to the stator can be noticed.
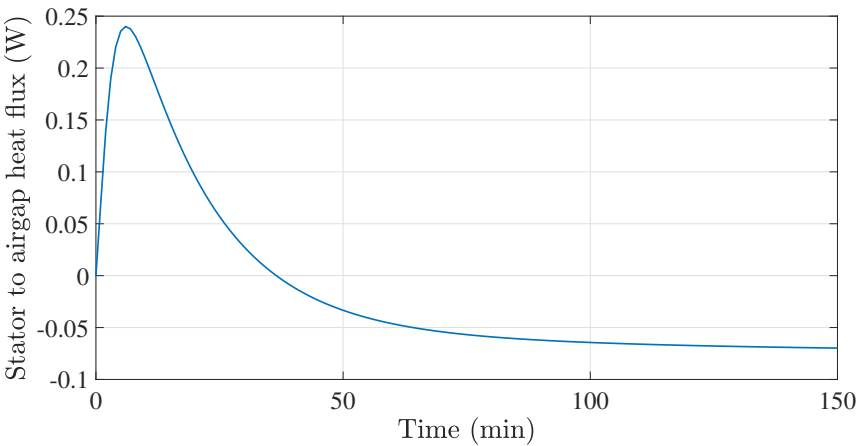

Figure 6.29: The rate of heat transfer from the stator to the air gap.

The measurements are performed at another operating point of (1Nm, 2000rpm). The measured phase currents and torques at this operating point are shown in Fig. 6.32 (a) and (b) respectively. The phase current waveform has the same pattern as the one required with the operating point (2 Nm, 1000 rpm) but with only half of its value as the torque is halved.
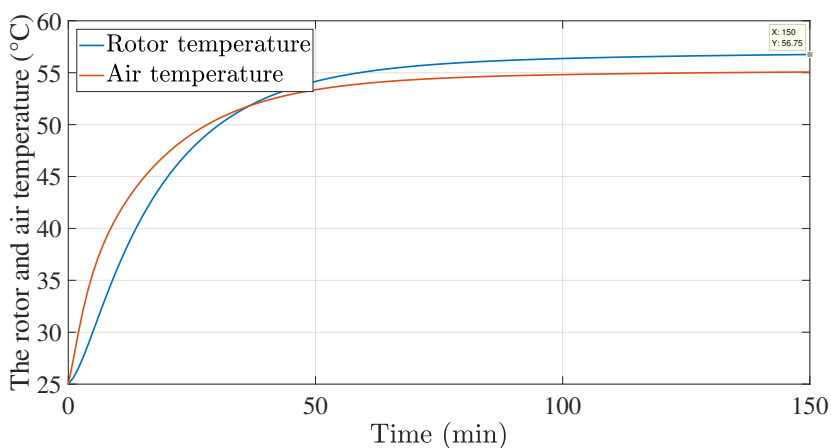
Figure 6.30: The rotor and the air temperature of the SRM at the operating conditions in Table 6.4.
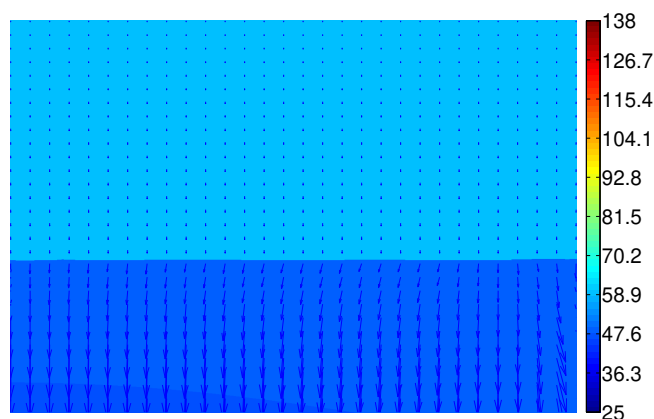

Figure 6.31: The rotor temperature distribution and the air gap heat transfer of the SRM obtained on a cross-section on the yz plane in the middle of the rotor part at the operating conditions in Table 6.4.

The losses of the stator windings, stator core and rotor core at the operating point (1 Nm, 2000 rpm) are 140W, 4.75W and 4.4W respectively. The temperature distribution over the stator and rotor segments at this operating point is shown in Fig. 6.33. The maximum stator winding temperature is 63.5°C.
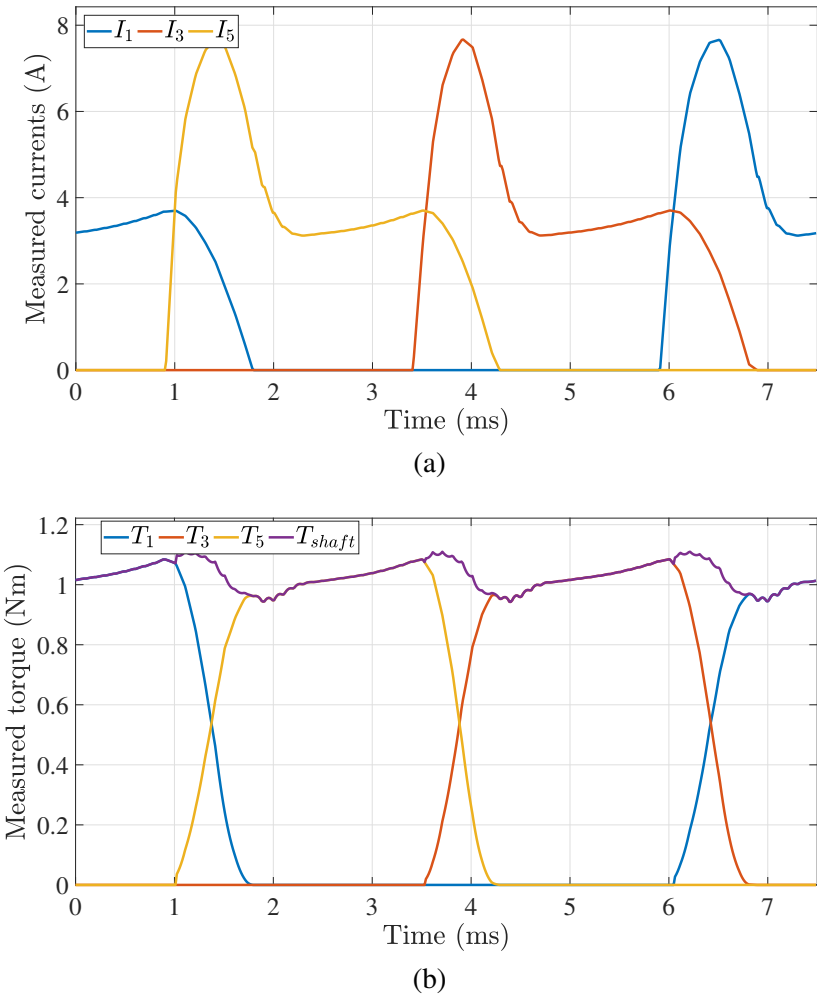
(a)

(b)

Figure 6.32: (a) Measured coil currents, (b) Produced torques at (1 Nm, 2000 rpm).

6.4.2 Validation of the asymmetric H-bridge modelling

The steady-state thermal model of the asymmetric H-bridge of the PR integrated SRM drive is validated in this section. The converter switching performance is also evaluated in this section.
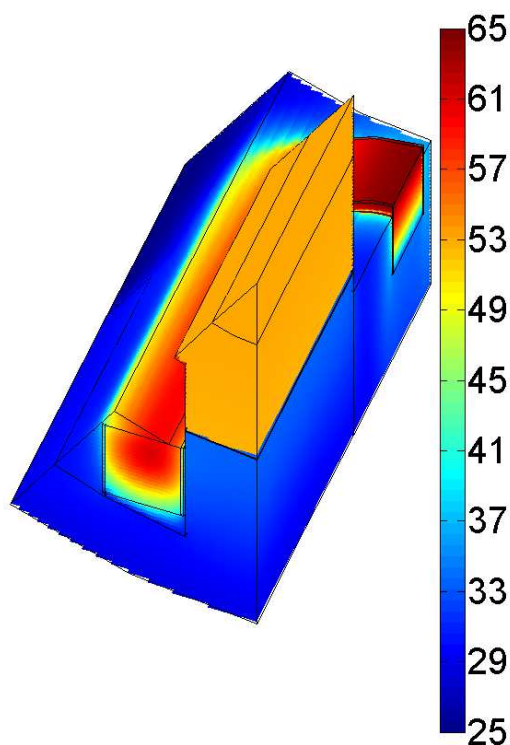
Figure 6.33: Temperature distribution over one quarter tooth of the SRM. This figure is generated at the operating point (1 Nm, 2000 rpm).

**Measurements of the steady-state thermal resistance**

The junction temperature rise of the switch C3M0075120J is measured at three different switch losses 1.9 W, 3.5 W and 5.4 W at 10 litre/min water flow rate and 25°C water inlet temperature. These switch losses are obtained by injecting DC current in the switches. The losses in the diodes are zero. The temperature distribution over the asymmetric H-bridge module at each power loss is shown in Fig. 6.34.

Fig. 6.35 shows the measured junction temperature rise of the switch versus the measured switch power loss. The slope of this curve gives the thermal resistance of the switch from junction to case. The slope of this curve is 6.2°C/W which confirms the accuracy of the thermal model presented in Chapter 5 section (5.12.1).

The diode thermal resistance is measured by the same way explained for the switch and the resulted junction to case thermal resistance is 8.65°C/W which is in a good agreement with the value obtained by the thermal network as presented in Chapter 5 section (5.12.1).
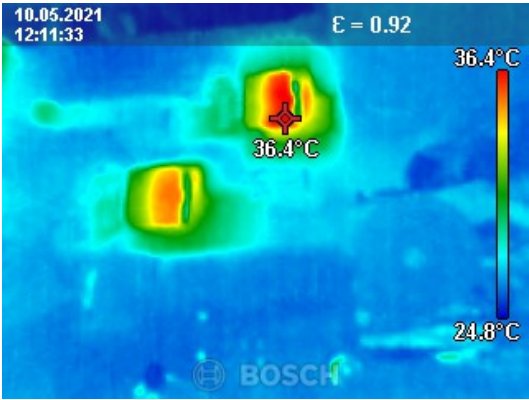
(a)
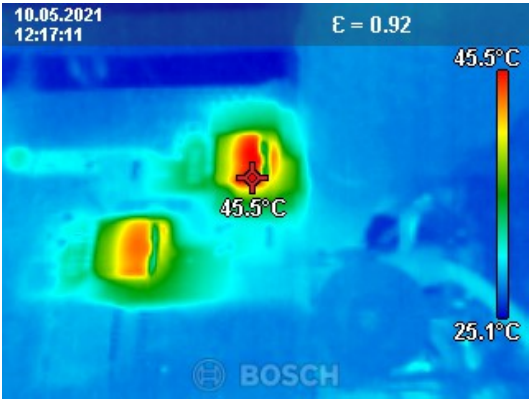
(b)
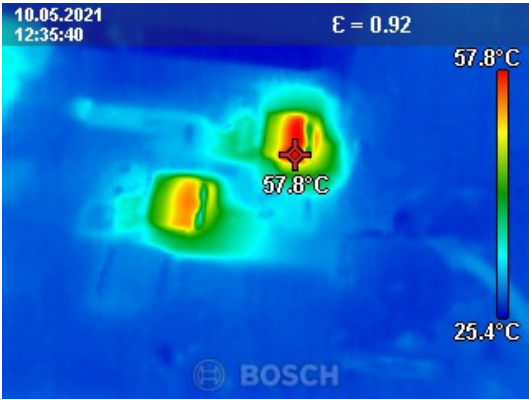
(c)

Figure 6.34: The measured junction temperature of the switch C3M0075120J at (a) 1.9 W loss per switch, (b) 3.5 W loss per switch and (c) 5.4 W loss per switch.
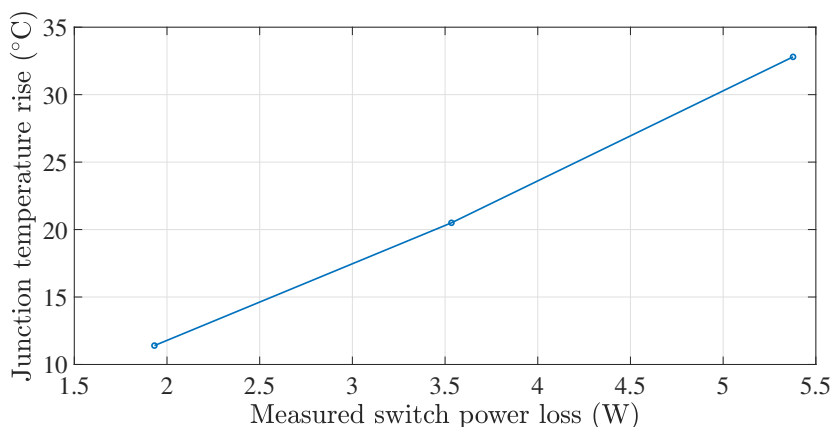
Figure 6.35: The measured junction temperature rise of the switch C3M0075120J versus switch loss.

Temperature distribution at rotating condition

The 3D thermal model presented in Chapter 4 section (4.4.1) of the asymmetric H-bridge is used to compute the temperature distribution over one integrated module and then the result is compared with the measurements.

The temperature distribution is calculated at the operating conditions in Table 6.4. Fig. 6.36 shows the temperature distribution over one integrated converter module. The junction temperature of the switch and the diode reaches 41.2°C and 37.8°C respectively.

Fig. 6.37 is a cross section in the xz-plane in the middle of the upper switch and diode. It can be noticed from this figure the high temperature gradient over the 1 mm TIM. This is due to its small thermal conductivity (4.4 W/mK) in comparison to the PCB thermal conductivity in the z direction and the conductivity of the aluminium housing. The heat dissipated by the switch and the heat dissipated by the diode flow vertically down towards the exposed area (the water jacket) and then they divert in two different directions towards the low temperature areas of the exposed area.

The measured temperature distribution over one asymmetric H-bridge is shown in Fig. 6.38. The switch and diode temperature are 41.6°C and 38.2°C respectively. The measured temperature values are in good agreement with the simulated one in Fig. 6.36. It can be seen that the temperature of the low power driving components remains low.

The switch and diode losses at the operating point (1 Nm, 2000 rpm) are 1.8 W and 0.9 W respectively. The simulated temperature distribution over one asymmetric H-bridge module at this operating point is shown in Fig. 6.39. The junction temperature of the switch and the diode reaches 36°C and 33°C respectively. The
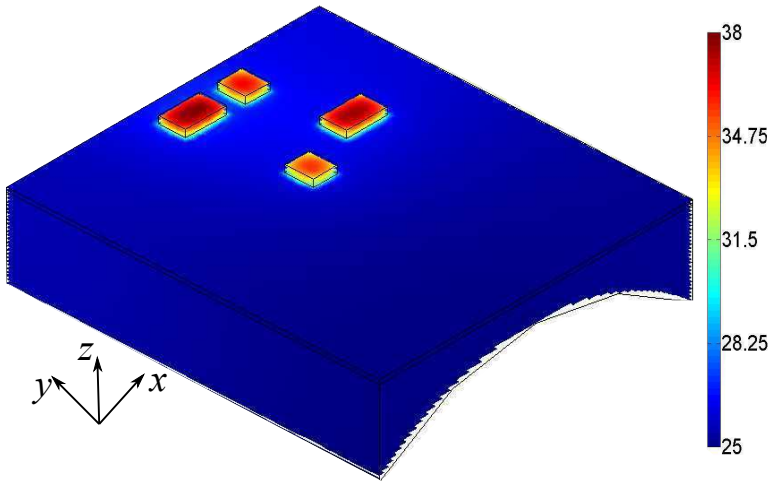
Figure 6.36: The temperature distribution over one integrated converter module. This figure is generated at the operating conditions in Table 6.4.
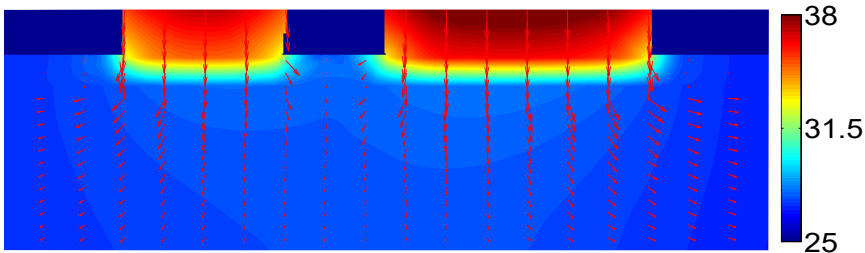
Figure 6.37: The temperature distribution and the heat flux lines of one integrated SRM module on an xz-plane in the middle of the upper switch and the upper diode. Only part of the polygon length in the x direction is taken. The red arrows represent the heat flux lines. This figure is generated at the operating conditions in Table 6.4.

junction temperature is lower than the case (2 Nm, 1000 rpm) due to the smaller switch and diode losses resulting from a smaller switched current at the smaller load torque.

The measured temperature distribution over one asymmetric H-bridge at (1 Nm, 2000 rpm) is shown in Fig. 6.40. The temperature of the switch and diode is 36.2°C and 33.8°C respectively. These values are in a good agreement with the simulated ones.

The efficiency map of the whole drive (SRM and asymmetric H-bridge) is shown in Fig. 6.41. The efficiency increases as the operating point approaches
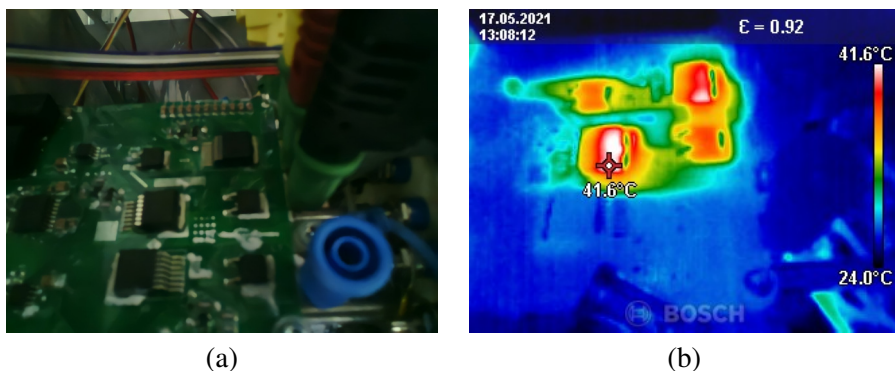
Figure 6.38: The measured temperature distribution over one asymmetric H-bridge at 2 Nm and 1000 rpm, 10 litre/min water flow rate and 25°C water inlet temperature: (a) The real picture, (b) The thermal picture.
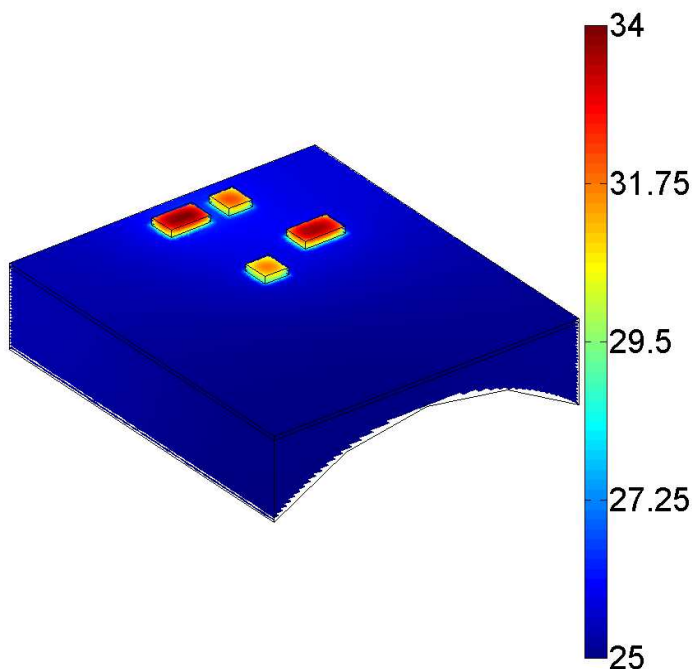
Figure 6.39: Temperature distribution over one integrated converter module. This figure is generated at the operating point (1 Nm, 2000 rpm).

(a)   (b)
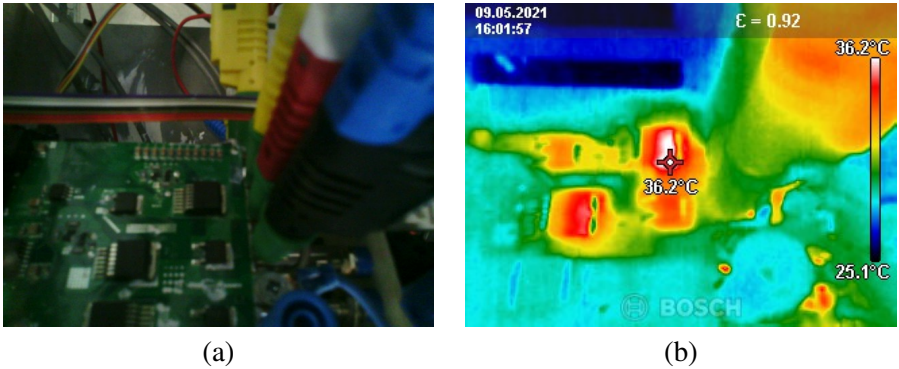
Figure 6.40: Measured temperature distribution over one asymmetric
H-bridge at (1 Nm, 2000 rpm): (a) The real picture, (b) The thermal
picture.

the rated value. The efficiency at the rated torque of 3 Nm and a speed of 5500 rpm
is 84%.
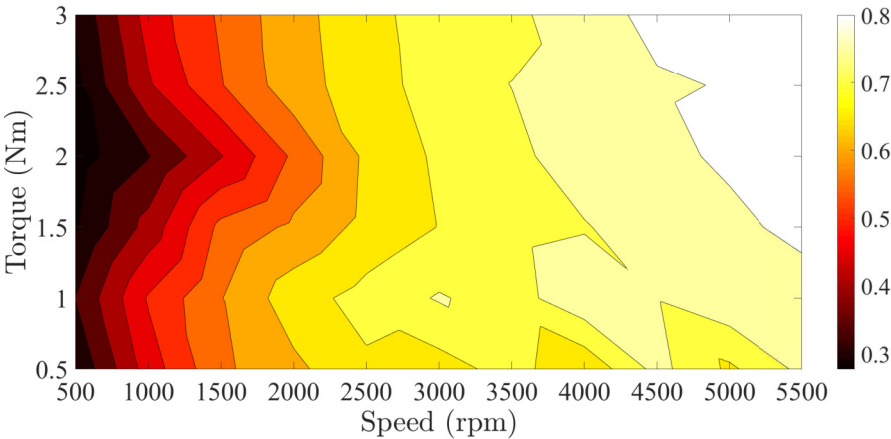
Figure 6.41: Efficiency map of the SRM drive.

The measured electrical and thermal performance of the implemented PR inte-
grated SRM drive confirm the feasibility of the proposed PR integrated drive as a
compact physical integration solution.

Asymmetric H-bridge switching performance

The switching performance of the asymmetric H-bridge is assessed by operating
the asymmetric H-bridge as a two-quadrant chopper with the motor winding as the

load. The motor current, the switch voltage, the switch current and the DC-link current are measured at 200 V DC-link voltage, 20 kHz switching frequency, 0.4 switch duty cycle, 25°C water inlet temperature and 10 litre/min water flow rate. These waveforms are shown in Fig. 6.42. It can be noticed that small voltage spikes appear on the switch voltage but high common mode current can be seen on the motor winding current waveform at the commutation moments of the converter. This common mode current can be mitigated by slowing down the switch transition speed or by designing a common mode filter. At these operating conditions, the motor winding current is 4 A with small ripples. The converter temperature distribution is shown in Fig. 6.43. The switch temperature reaches 50°C and the diode temperature reaches 41°C.

6.5   Conclusion

The FE and the LPTN models built for the air cooled YASA machine in Chapter 3 are validated by experimental measurements. Good agreement between the models and the experimental measurements is observed.

An experimental three teeth integrated setup is built to asses the feasibility of the circumscribing polygon integration topology. Several electrical and thermal measurements are performed using DC and PWM waveforms. These measurements confirm the feasibility of the circumscribing polygon integration topology.

A full rotating setup for the PR integrated SRM is built and experimental measurements for the temperature of the machine and the asymmetric H-bridge are conducted to validate the modelling tools. The results ensure a proper operation of the PR integrated drive and a good agreement between the models and the measurements is found.

Figure 6.42: The measured asymmetric H-bridge converter waveforms at 200 V DC-link voltage, 20 kHz switching frequency, 25°C water inlet temperature and 10 litre/min water flow rate.
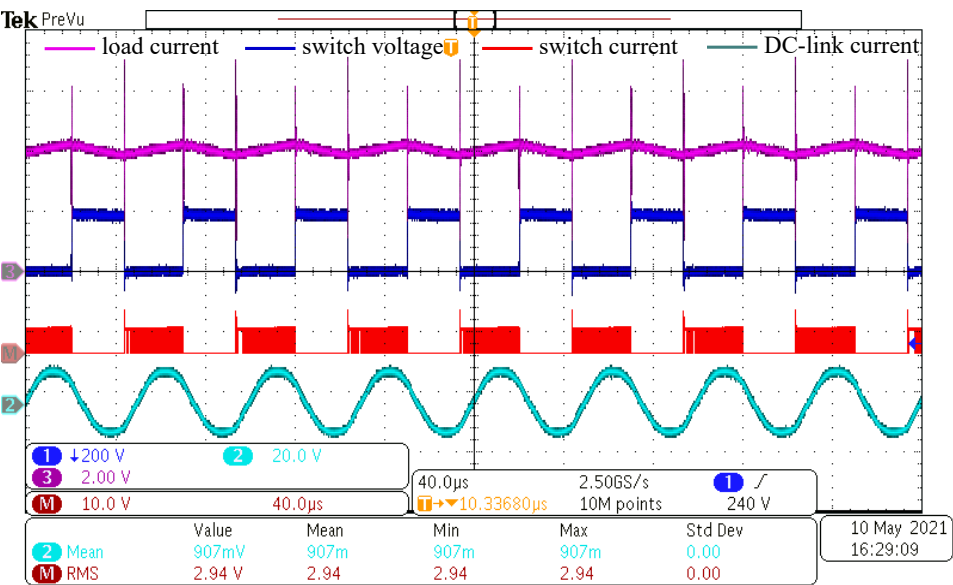

Figure 6.43: The temperature distribution over one asymmetric H-bridge module at 200 V DC-link voltage, 20 kHz switching frequency, 25°C water inlet temperature and 10 litre/min water flow rate.

Chapter 7

Multiphysics Design of an Integrated DC-link Structure with Distributed Capacitance for the YASA Integrated Drive

7.1   Introduction

The DC-link structure of electric motor drives consists of the DC-link capacitors and the DC-link bus bar. The DC-link capacitors smooth and hold the DC-link voltage by supplying the DC-link current ripple [127]. The selected DC-link capacitors should be capable of supplying the required DC-link current ripple without excessive heating. The DC-link bus bar provides a mechanical mounting structure for the capacitors and electrically connects the DC-source, the capacitors and the converters together [128]. The DC-link bus bar should be designed to have a low AC inductance to reduce the voltage spike amplitude over the converter switches [129].

The authors in [127, 130, 131] address the design of the DC-link capacitor for three-phase drives with a single set of stator windings. The authors in [132, 133] handle the influence of the pulse width modulation (PWM) carriers interleaving on the design of the capacitor of the three-phase drives with dual stator winding. In [134], the authors illustrated the possibility of using carrier interleaving with IMMDs but no closed form generic design equations are given.

For the DC-link bus bar design, the authors in [135–137] study the influence of the bus bar geometry for three-phase inverters implemented using commercial half-bridge modules on the value of the parasitic inductance. None of these studies address the design of an integrated bus bar structure feasible for IMMDs given their special structure and high ambient temperature.

In this chapter, a generic design methodology for the proposed DC-link structure feasible for reconfigurable modular integrated drives is provided and applied

on a fifteen stator coils circumscribing polygon integrated axial flux drive. The design process presented in this chapter involves the determination of the required DC-link capacitance for each configuration and the multi-physics design of the bus bar. An electromagnetic FE model and thermal model are developed for the proposed DC-link structure to ensure that the electrical and the thermal stresses on the components of the DC-link structure are within the rated values.

The electromagnetic FE model is used to extract the DC-link structure parasitics so that the DC-link voltage spike can be estimated, and to compute the loss density distribution in the bus bar. This loss density distribution is used as an input to a thermal model for the DC-link structure to compute the temperature distribution. In this way, both the electrical and the thermal stresses on the bus bar can be evaluated to ensure reliable operation in the high ambient temperature environment of the integrated drive.

7.2 Mechanical construction of the integrated DC-link structure

Fig. 7.1 shows the integrated DC-link structure assembled with the CP fifteen stator coils integrated axial flux drive. From this figure, the DC-link structure doesn't increase the outer diameter of the integrated machine/converter structure. Instead, it occupies a distance in the axial direction corresponding to the width of the capacitor module plus twice the bus bar thickness plus the insulation layer.

Fig. 7.2 (a) shows the DC-link structure with both the capacitors and the bus bar together. It consists of a ring shaped bus bar with the DC-link capacitors arranged circumferentially pointing radially inward. In this way, the bus bar and the capacitors are integrated with the machine/converter structure without influencing the outer diameter which enhances the compactness of the drive.

Fig. 7.2 (b) shows an exploded view for the bus bar part of the DC-link structure. It consists of a positive plate, a negative plate and an electrical insulation layer between them. Each plate has an input tab for the DC-source, a connection terminal for the module capacitor and a connection terminal for the converter input source. A short distance of 17.5 mm between the capacitor terminal and the converter DC-input terminal is achieved which results in a small AC parasitic inductance, and hence, smaller voltage spike over the switches. A relatively longer average distance of 115 mm between the DC-source input tab and the converter input terminal is achieved which results in a relatively greater DC parasitic inductance, and hence, a smoother DC-source current and smaller DC-source stress will result.

The conducting plates can be made of copper or aluminium [135]. Using aluminium plates results in a lighter drive due to the smaller mass density of aluminium compared to copper, but higher loss, and hence, temperature will result due to the smaller electrical and thermal conductivity of the aluminium. The in-
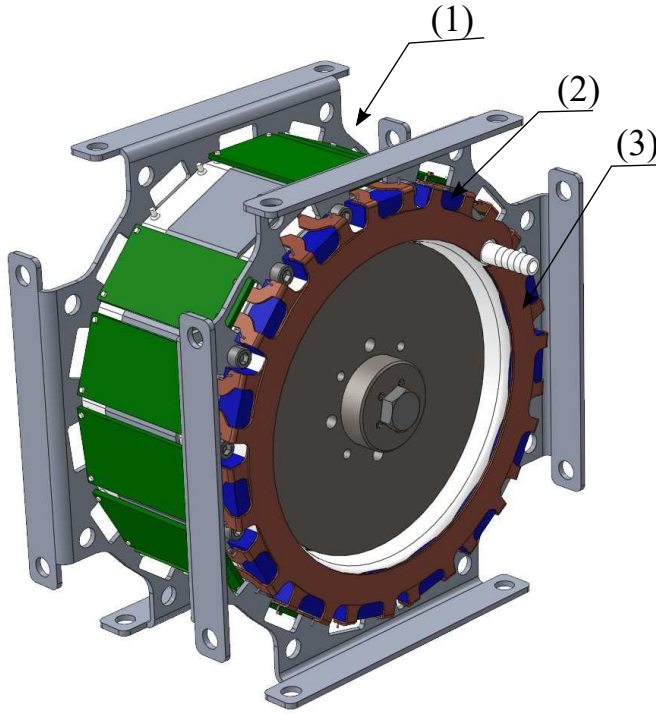
Figure 7.1: The integrated DC-link structure assembled with the CP integrated axial flux machine: (1) CP integrated drive, (2) DC-link capacitor, (3) DC-link bus bar.

sulation layer can be made of kapton, mylar, nomex or epoxy glass (FR4) [136]. Table 7.1 contains the main properties of the insulation materials. Here, E is the breakdown strength, ϵ_r is the relative permittivity and K_{th} is the thermal conductivity. As the maximum bus bar temperature is limited by the rated temperature of the insulation layer, kapton represents the optimal choice from the thermal point of view.

7.3   Design of the DC-link structure

The design of the integrated DC-link structure involves the determination of the DC-link capacitors for each possible configuration of the modular drive and the multi-physics analysis of the mechanical outline of the integrated bus bar part of the DC-link structure.

(a)   (b)

Figure 7.2: The DC-link structure (a): (1) The bus bar structure, (2)
The DC-link capacitors. DC-link bus bar structure (b): (1) Positive
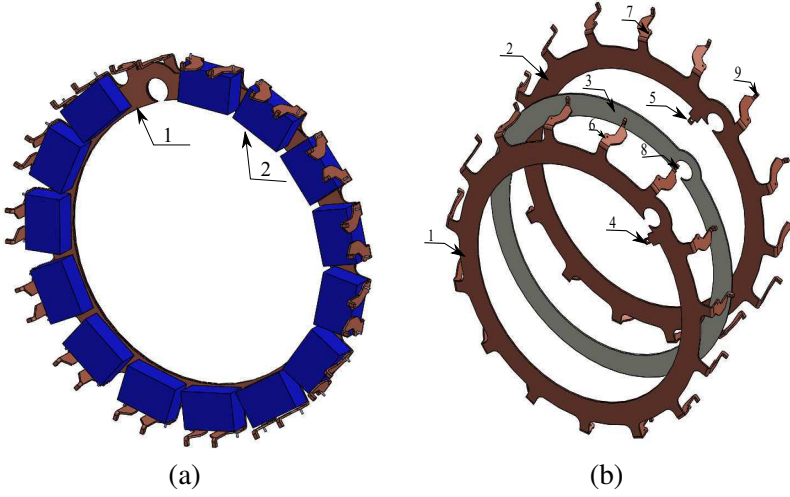plate, (2) negative plate, (3) insulation layer, (4) DC-input plus, (5)
DC-input minus, (6) capacitor plus terminal, (7) capacitor minus ter-
minal, (8) converter module plus input, (9) converter module minus
input.

Table 7.1: Properties of insulation materials

Material	E (kV/mm)	ϵ_r	rated temperature (°C)	K_{th} (W/m.K)
Kapton	196	3.7	400	0.4
Mylar	295	3.3	105	0.14
Nomex	17-33	1.6	220	0.157
FR4	49	4.3	140	0.31

7.3.1 Selection of the DC-link capacitors

The main specifications of the DC-link capacitors are the root mean square (rms)
ripple current rating, the voltage rating and the value of the capacitance. For each
stator winding connection, the rms value of the DC-link ripple current depends
on the pulse width modulation (PWM) technique, the peak line current $i_{linepeak}$,
the power factor, the modulation index (M) and the interleaving angle (K) if it
applies [131]. The rated voltage depends on the DC-link voltage value. The value
of the capacitance depends on the tolerated DC-link peak-to-peak voltage ripple,

the converter switching frequency and the current ripple to be supplied [138].

Generic capacitor sizing method

The DC-link capacitor sizing procedure starts by calculating the frequency spectrum of the DC-link current waveform. From this spectrum, all the DC-link capacitor specifications can be calculated (i.e. the rms value of the capacitor ripple current, the value of the required DC-link capacitance).

Starting from the DC-link current spectrum equations developed in [132] for six-phase machines divided into two three-phase winding sets, equations (7.1, 7.2) are derived for calculating the DC-link current harmonics ($i_{ch}(n, m)$) for sinusoidal pulse width modulation (SPWM) and equations (7.3, 7.4) for space vector pulse width modulation (SVPWM). These equations are applicable at general g number of stator winding groups and N number of phases per group and any operating condition of peak line current $i_{linepeak}$, power factor angle ϕ, modulation index M and interleaving angle K.

$$i_{ch}(n, m) = \frac{i_{linepeak}}{2\pi^2} \sum_{s=1}^{g} \sum_{h=1}^{N} \int_{y_{min}}^{y_{max}} f(x, y) dy dx \tag{7.1}$$

$$\begin{cases} f(x, y) &= \cos(x - \phi + n\theta) e^{i(my+nx)} \\ y_{min} &= \frac{\pi}{2}(1 - M \cos(x + n\theta)) + K \\ y_{max} &= \frac{\pi}{2}(3 + M \cos(x + n\theta)) + K \end{cases} \tag{7.2}$$

$$i_{ch}(n, m) = \frac{i_{linepeak}}{\pi^2} \sum_{s=1}^{g} \sum_{h=1}^{N} \sum_{i=1}^{3} \int_{x_{min}}^{x_{max}} \int_{y_{min}}^{y_{max}} f(x, y) dy dx \tag{7.3}$$

$$\begin{cases} f(x, y) &= \cos(x - \phi + \theta) e^{i(my+nx)} \\ x_{min,i} &= (i - 1)\frac{\pi}{3} \\ x_{max,i} &= i\frac{\pi}{3} \\ y_{min} |_{i=(3,1)} &= \frac{\pi}{2}\left(1 - \frac{\sqrt{3}}{2} M \cos(x \pm \frac{\pi}{6} + \theta)\right) + K \\ y_{min} |_{i=2} &= \frac{\pi}{2}\left(1 - \frac{3}{2} M \cos(x + \theta)\right) + K \\ y_{max} |_{i=(3,1)} &= \frac{\pi}{2}\left(3 + \frac{\sqrt{3}}{2} M \cos(x \pm \frac{\pi}{6} + \theta)\right) + K \\ y_{max} |_{2} &= \frac{\pi}{2}\left(3 + \frac{3}{2} M \cos(x + \theta)\right) + K \end{cases} \tag{7.4}$$

The DC-link capacitor current harmonics are located at the switching frequency f_s and multiples of it and their side-bands [134]. The frequency of these harmonics can be expressed as $mf_s + nf_o$. Here,(n ,m) are positive integers and f_o is the inverter output fundamental frequency.

From the capacitor harmonic current components $i_{ch}(n, m)$, the capacitor rms ripple current I_{crms} can be calculated from (7.5).

$$I_{crms} = \sqrt{\sum_{m=1}^{\infty} \sum_{n=-\infty}^{\infty} i_{ch}^2(n,m)} \tag{7.5}$$

The value of the needed DC-link capacitance can be calculated from the maximum permissible peak-to-peak ripple voltage $V_{ppripple}$ and the equivalent most dominant harmonic component of the capacitor current I_{mde}. The value of $V_{ppripple}$ is usually limited to 1% of the DC-link voltage V_{dc} [20]. I_{mde} can be calculated from (7.6). The minimum required DC-link capacitance C_{min} can be calculated from (7.7). Here, $I_{chpea}(n, m_{md})$ is the peak value of the most dominant harmonic capacitor current with harmonic frequency $f_{md} = m_{md}f_s$ and its side-bands.

$$I_{mde} = \sqrt{\sum_{n=-\infty}^{\infty} I_{chpea}^2(n, m_{md})} \tag{7.6}$$

$$C_{min} = \frac{I_{mde}}{\pi f_{md} V_{ppripple}} \tag{7.7}$$

Equation (7.7) gives the value of the total needed DC-link capacitance. For the IMMDs, the module capacitance can be obtained by dividing C_{min} by the total number of modules n_{mod}.

A commercial capacitor can be selected with a capacitance greater than $\frac{C_{min}}{n_{mod}}$, a rated rms ripple current greater than $\frac{I_{crms}}{n_{mod}}$ and rated voltage greater than V_{dc}.

After selecting a commercial capacitor, the capacitor power loss and hotspot temperature can be calculated considering the practical capacitor equivalent circuit shown in Fig. 7.3. The practical capacitor model consists of the parallel combination of a pure capacitor C and insulation resistance R_i connected in series with equivalent series resistance ESR and equivalent series inductance ESL. Two loss components dissipate in the capacitor, one in R_i designated by P_d and the other in ESR designated by P_t. Both loss components and the capacitor hot spot temperature can be calculated from (7.8).

$$\begin{cases} P_d & = \frac{1}{2}C\tan(\delta)\sum_{m=1}^{\infty}\sum_{n=-\infty}^{\infty} V_{pph}^2 f_h \\ P_t & = \sum_{m=1}^{\infty}\sum_{n=-\infty}^{\infty} I_{chrms}^2(n,m)ESR(n,m) \\ \theta_{hotspot} & = \theta_{ambient} + (P_d + P_t)R_{th} \end{cases} \tag{7.8}$$

Here, C is the value of the selected capacitance, $\tan(\delta)$ is the dielectric loss tangent, V_{pph} is the peak-to-peak ripple voltage resulting from the harmonic with frequency (f_h), I_{chrms} is the harmonic current rms value for one module capacitor, ESR is the equivalent series resistance at the harmonic (n, m), P_d is the dielectric loss component, P_t is the loss in the ESR, $\theta_{ambient}$ is the maximum allowable
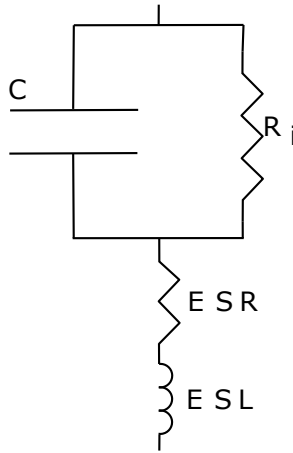
Figure 7.3: The capacitor practical circuit model.

ambient temperature, $\theta_{hotspot}$ is the maximum allowable capacitor hotspot temperature, R_{th} is the maximum thermal resistance of the capacitor from its hotspot to the ambient. $\tan(\delta)$, R_{th}, ESR are all extracted from the datasheet of the selected capacitor.

In variable speed drives, the power factor and the modulation index M both vary with the load and so does the capacitor current. For identification of the (PF, M) that result in the maximum capacitor current stress, the family of curves in Fig. 7.4 are generated for the winding connection in Fig. 7.13 at rated line current and an interleaving angle of 85°. The maximum capacitor current stress resulted at the operating point (PF=1, M=0.6). The same result is reported in [131] for the three-phase machines. Therefore, the capacitance value and the current stress of the DC-link capacitors are evaluated at (PF=1, M=0.6).

Fig. 7.5 is a flow chart that summarizes the generic capacitor design process. The described design procedure is applied on the different possible phase connections of the fifteen-phase YASA AFPMSM.

Required capacitance for three-phase operation

Fig. 7.6 shows the windings connection in case of three-phase operation of the YASA AFPMSM. Each phase is composed by connecting five coils in series. The capacitor sizing is done for the values listed in Table 7.2 and a DC-link voltage of 400 V.

The harmonic spectrum of the capacitor current is calculated and reported in Fig. 7.7 for SPWM and SVPWM. It can be noticed from the current spectrum that the most dominant harmonic current component is located at $2f_s$ for both PWM
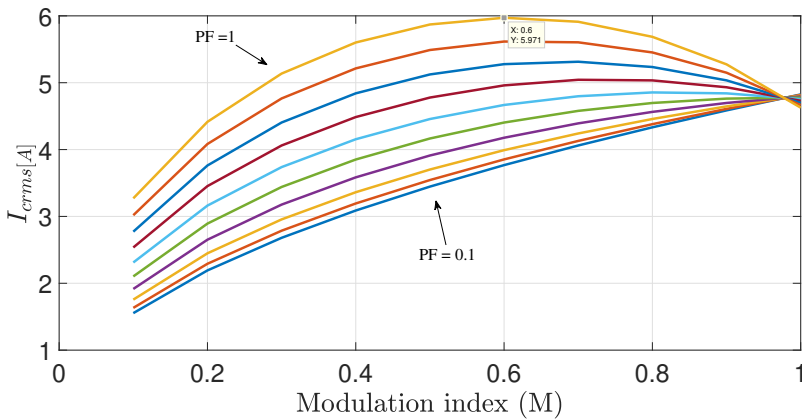
Figure 7.4: Capacitor rms current versus modulation index at different values of power factor for the topology in Fig. 7.13 at rated line current and 85° interleaving angle.

techniques. The values of the side-band harmonics in case of SVPWM are much higher than the case of SPWM resulting in a higher capacitor rms ripple current and bigger capacitance requirement.

Table 7.2: The values at which the capacitor sizing is done

Variable	Value
Peak line current $i_{linepeak}$(A)	12.7
Modulation index (M)	0.6
Switching frequency f_s (kHz)	50
Peak-to-peak voltage ripple V_{ripple}	1%

The value of the per module capacitor rms ripple current in case of SPWM is evaluated as 1.92 A and the value of the minimum needed per module capacitance is 2 μF.

The film capacitor FB27A6J0335C from AVX with the key specifications in Table. 7.3 is selected and the circuit in Fig. 7.6 is simulated at the rated operating conditions to verify the analytical design method. The used inverter load is an RL load with R=8 Ω, L=1mH to get a nearly sinusoidal current waveform with peak value of 12.7 A and displacement power factor of 0.97 at the fundamental frequency of 333.3 Hz.
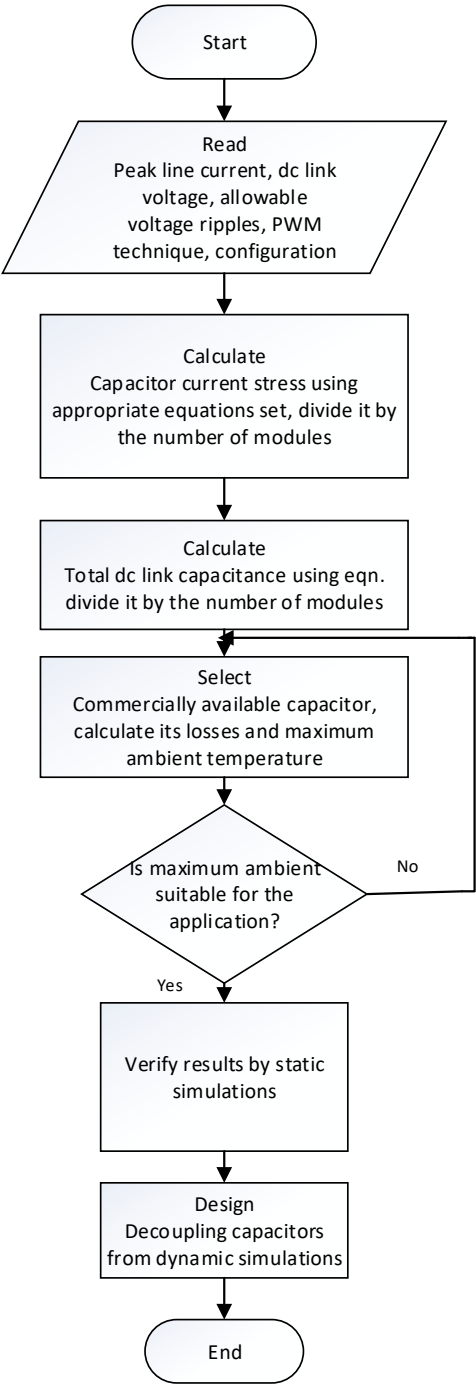
Figure 7.5: Generic DC-link capacitor design flow chart.
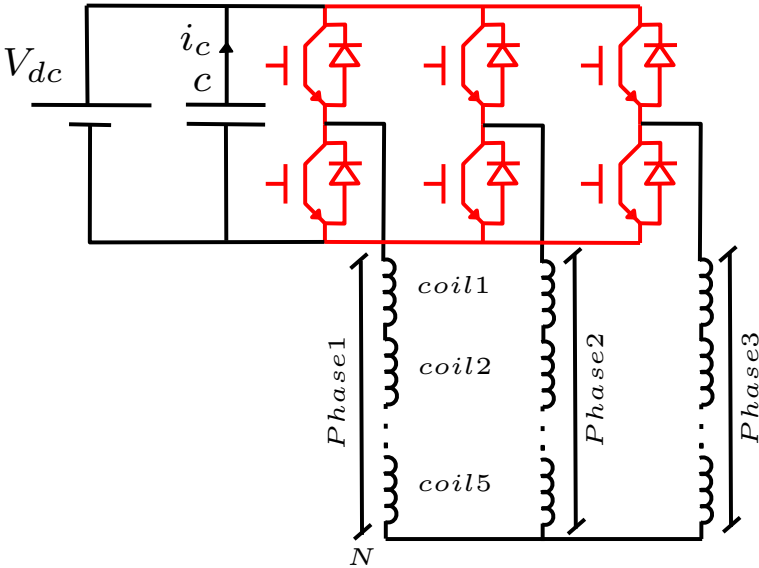
Figure 7.6: The phase connection in case of three-phase operation.
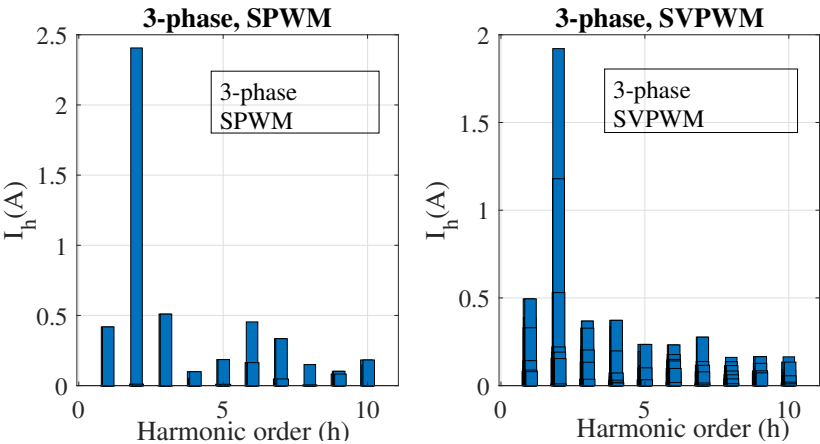
Figure 7.7: The harmonic spectrum of the capacitor current in case of
three-phase connection: SPWM (left), SVPWM (right), h=$\frac{f_h}{f_s}$.

Fig. 7.8 shows the three-phase currents with peak value of 12.7 A and fre-
quency 333.3 Hz.

Fig. 7.9 depicts the per module capacitor current for five switching cycles.
Its rms value is 1.882 A which indicates good correspondence with the analytical

Table 7.3: Selected capacitor key specifications

Variable	value
rated voltage (V)	550
rated rms ripple current (A)	5
Capacitance (μF)	3.3
ESR (mΩ)	22
$\tan(\delta)$	2e-4
thermal resistance R_{th} ($^\circ$C/W)	27.3
rated hotspot temperature ($^\circ$C)	100
ESL (nH)	25
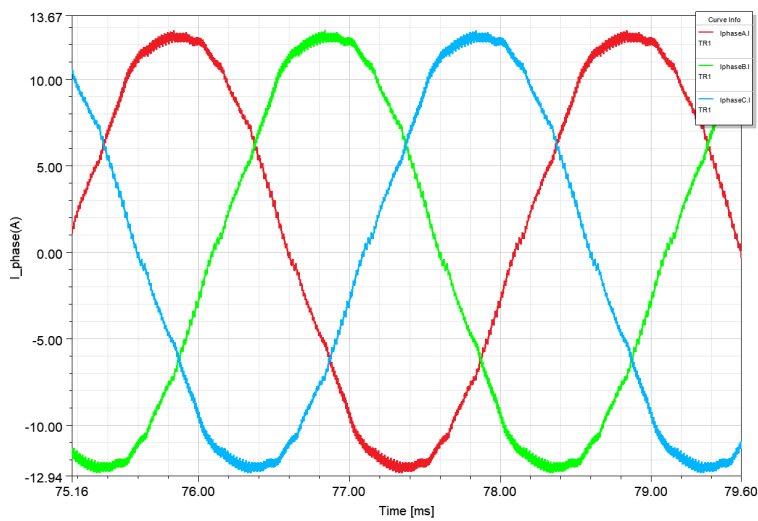
Figure 7.8: The three-phase currents resulting from the simulation of the circuit in Fig. 7.6 at 12.7 A peak line current.

estimation of 1.92 A.

Fig. 7.10 shows the DC-link voltage. It can be observed that the peak-to-peak voltage is 7.74 V while the average voltage is 400 V, which corresponds to 1.9% peak-to-peak ripple. The peak-to-peak ripple is a bit higher than the design value due to the contribution of the ESR, ESL and the neglected harmonics, but the value is still acceptable for motor drives applications.

Figure 7.9: The per module capacitor current for five switching cycles.

Figure 7.10: The DC-link voltage in case of static simulations and three-phase operation.

Required capacitance for five-phase operation

In this configuration, every three stator coils are connected in series to form one phase as shown in Fig. 7.11. To have the same power as in the case of the 3-phase,
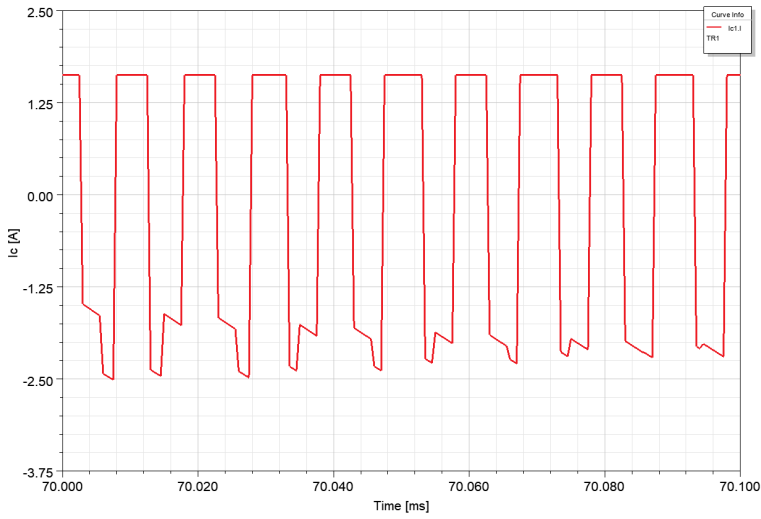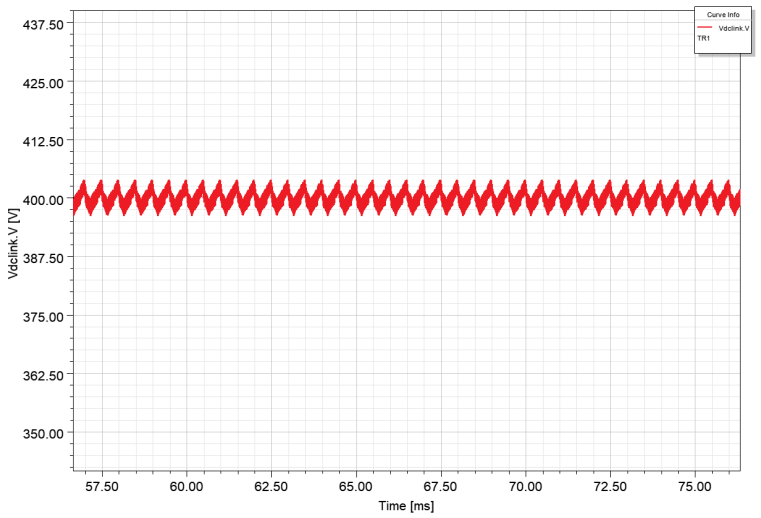
the DC-link voltage is set to 240 V while the phase current will remain the same.
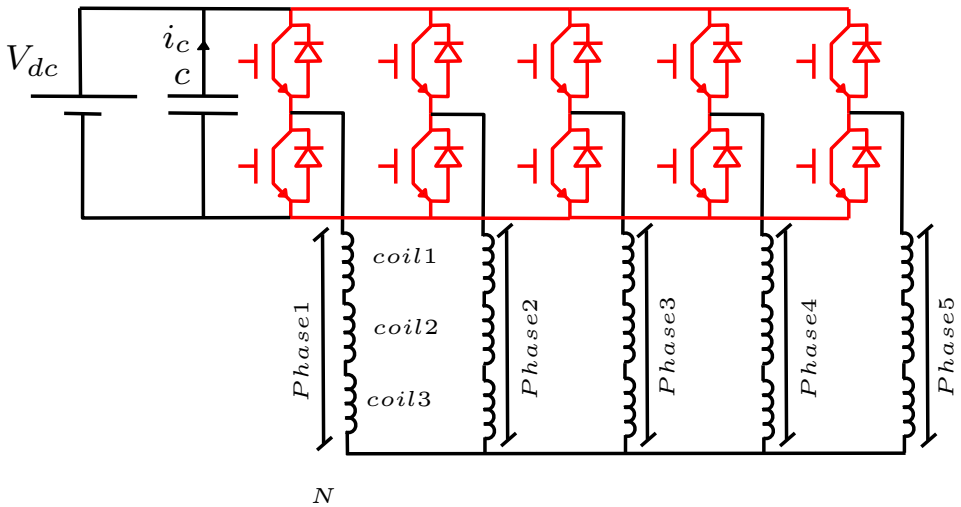

Figure 7.11: The connection in case of five-phase operation.

The capacitor current spectrum has the most dominant harmonic at $2f_s$ with lower current ripple requirement in case of SPWM, the same conclusions drawn in case of three-phase operation. The per module capacitor rms ripple current in case of SPWM is 1.8 A and the minimum per module capacitance needed is 3.2 μF.

A higher per module capacitance is needed compared to the three-phase case due to the lower absolute peak-to-peak ripple voltage requirement. A smaller voltage rated capacitors is needed. A bit smaller per module capacitor ripple current results due to the higher number of capacitor modules, but still the total DC-link current ripple is higher than in the case of three-phase.

Required capacitance for fifteen-phase operation

In case of fifteen-phase operation, the stator coils can be connected to have one common neutral point as in Fig. 7.12, divided into five groups with three coils in each group as in Fig. 7.13 or divided into three groups with five coils in each group as in Fig. 7.14. For the connections in Fig. 7.13 and Fig. 7.14, the PWM carriers can be shifted by an interleaving angle K as shown in Fig. 7.15 to further reduce the DC-link current stress. Each configuration has its own torque-speed and fault-tolerance characteristics.

For fifteen-phase operation, the DC-link voltage is scaled down to 80 V and the current is kept the same for obtaining the same output power. In case of fifteen-phase operation with one neutral (Fig. 7.12), the resulting most dominant harmonic

222
Multiphysics Design of an Integrated DC-link Structure with Distributed
Capacitance for the YASA Integrated Drive
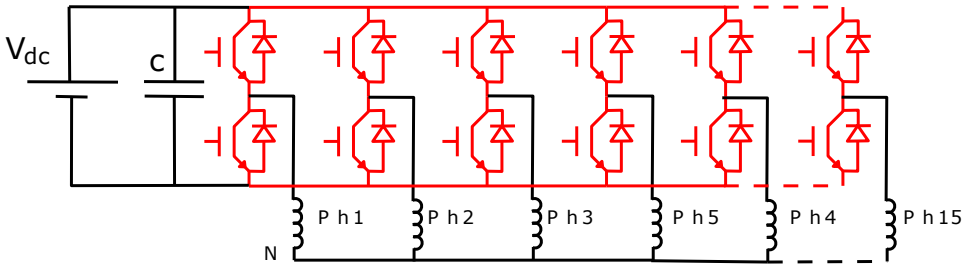
Figure 7.12: The connection in case of fifteen-phase operation with one common neutral.
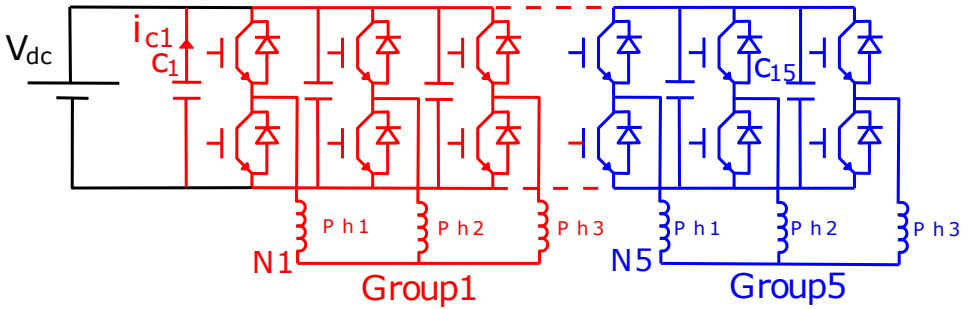
Figure 7.13: The connection in case of fifteen-phase divided as five groups with three-phase in each group.
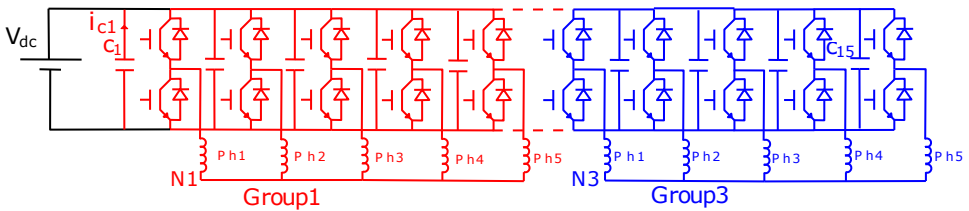
Figure 7.14: The connection in case of fifteen phases divided as three groups with five-phase in each group.

is $2f_s$ with lower rms ripple current in case of SPWM compared to SVPWM technique. The same result is obtained in case of three-phase and five-phase operation. The value of the needed per module capacitance in this case is 9.5 μF with ripple current value of 1.75 A for SPWM technique.

For the calculation of the DC-link capacitor for the connections in Figs. 7.13
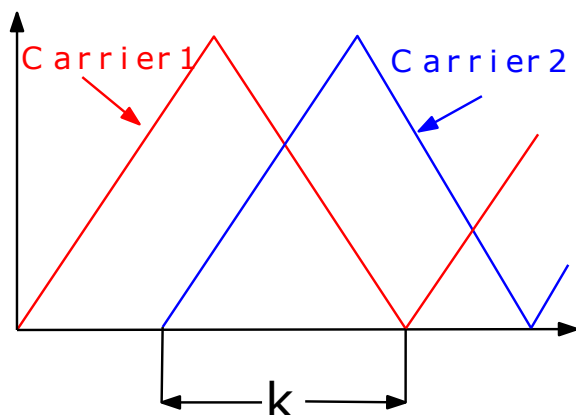
Figure 7.15: Illustration of carrier interleaving.

and 7.14, the optimal interleaving angle K should be calculated first. Figs. 7.16 and 7.17 show the rms current of the DC-link capacitor versus the interleaving angle for the connections in Figs. 7.13 and 7.14 respectively. It can be seen that a great reduction in the capacitor rms current occurs at the optimal interleaving angle. The smaller capacitor current is noticeable in case of SPWM. The optimal interleaving angle for the connection in Fig. 7.13 is 70° and 60° for the connection in Fig. 7.14.
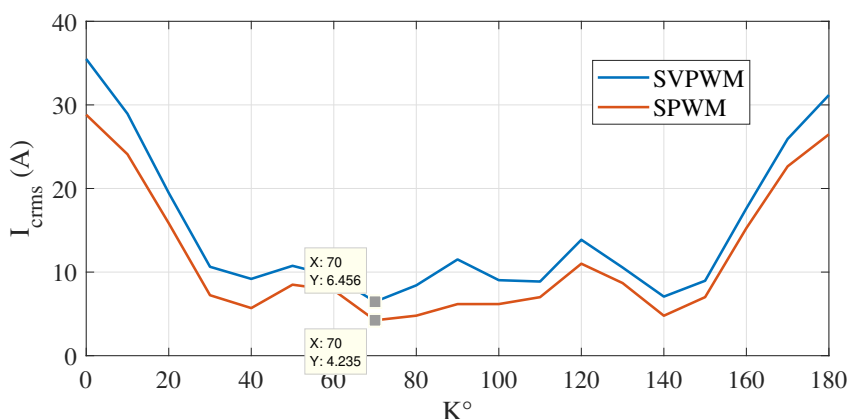
Figure 7.16: The capacitor ripple current for the configuration in Fig. 7.13 versus the interleaving angle.

Fig. 7.18 (left) and (right) show the simulated capacitor current waveform with
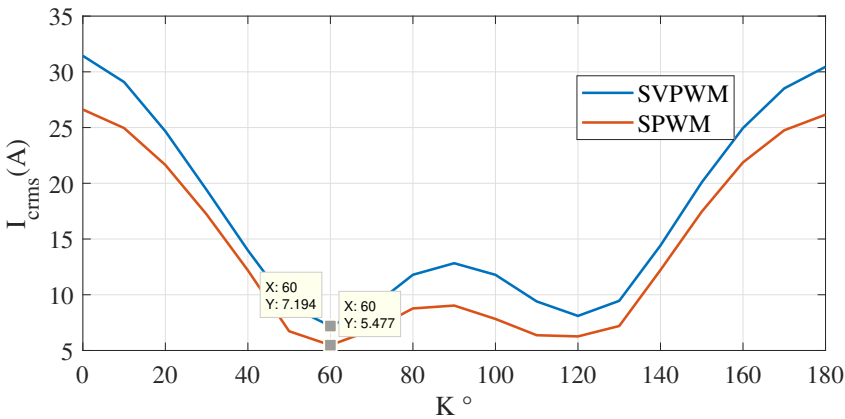
Figure 7.17: The capacitor ripple current for the configuration in Fig.
7.14 versus the interleaving angle.

its rms value at (f_s=50 kHz), SPWM, in case of zero and 70° interleaving angle for
the phase connection in Fig. 7.13. The simulation results confirm the analytically
calculated rms current (see Fig. 7.16) and the great reduction in the capacitor rms
current at the optimal interleaving angle.
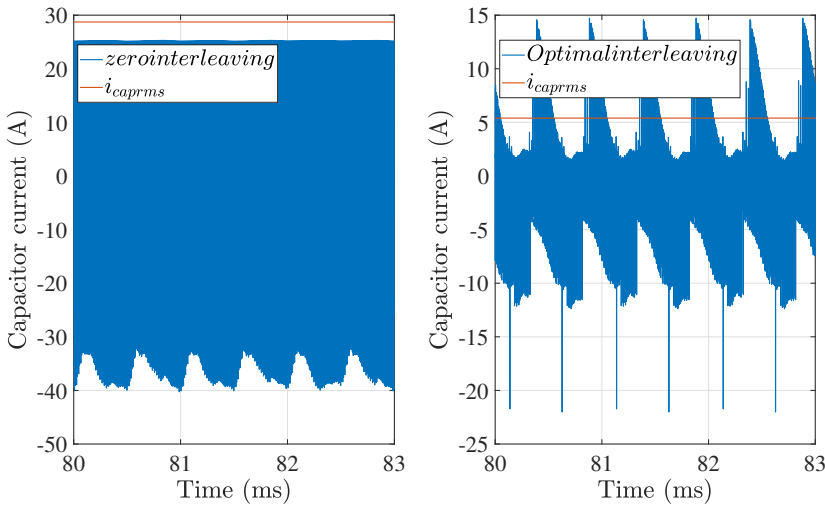
Figure 7.18: The simulated capacitor current at zero (left) and 70°
(right) interleaving angle for the topology in Fig.7.13.

The capacitor harmonic current spectrum for the connection in Fig. 7.13 at 70° interleaving angle is shown in Fig. 7.19. It can be seen that the frequency of the dominant harmonic component is $5f_s$ which is higher than the $2f_s$ component resulted for the connections with single neutral point. This high frequency of the most dominant harmonic current component leads to smaller DC-link capacitance requirement. It can also be seen that the side-band harmonics in the case of SVPWM are more significant than the case of SPWM which explains the higher capacitor rms current value as depicted in Figs. 7.16 and 7.17. For the connection in Fig. 7.16, in case of SPWM, the per module capacitor rms current is 0.3 A and the minimum required capacitance is 0.5 μF at the optimal interleaving angle. For the connection in Fig. 7.17, the per module capacitor rms current is 0.4 A and the minimum required capacitance is 0.65 μF at the optimal interleaving angle.
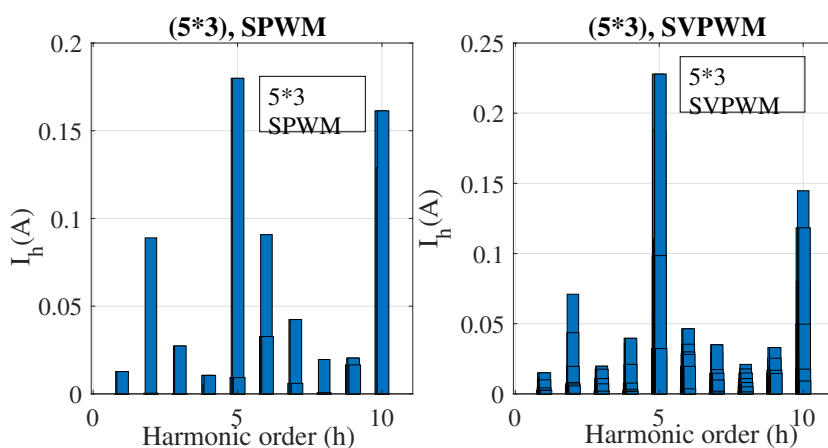
Figure 7.19: The capacitor current harmonic spectrum of the capacitor current in case of connection in Fig. 7.13.

The specifications of the per module capacitor for each phase connection are summarized in Table 7.4.

7.3.2   Bus bar electro-thermal analysis

An electromagnetic and thermal analysis for the bus bar part of the DC-link structure shown in Fig. 7.2 is carried out in this part.

Bus bar electromagnetic analysis

The electromagnetic analysis of the DC-link bus bar is performed for both the evaluation of the parasitic parameters of the bus bar [128] and for evaluation of the electromagnetic loss distribution in the bus bar.

Table 7.4: Per module DC-link capacitor specifications for each phase connection

Variable	Connection	Value
Minimum rated voltage (V)	3-ϕ	400
	5-ϕ	240
	15-ϕ	80
	5×3-ϕ	80
	3×5-ϕ	80
Minimum ripple current rating (A)	3-ϕ	1.92
	5-ϕ	1.8
	15-ϕ	1.75
	5×3-ϕ	0.3
	3×5-ϕ	0.4
Minimum capacitance (μF)	3-ϕ	2
	5-ϕ	3.2
	15-ϕ	9.5
	5×3-ϕ	0.5
	3×5-ϕ	0.65

Fig. 7.20 illustrates the different parasitic inductances in the commutation loop of the half-bridge converter module. The DC-link bus bar contributes with L_+ and L_- to the loop inductance L_{loop}. The maximum possible DC-link voltage V_{dc} that can be applied to the converter terminals depends on the commutation loop inductance, the switching speed of the converter switches and the rated voltage of the switches (7.9). Since the converter modules are implemented using GaN technology which is characterized by the very high switching speed [11], any small parasitic inductance contributes considerably to the switch voltage spike $L_{loop}\frac{di}{dt}$.

$$\begin{cases} V_{ds} & = V_{dc} + L_{loop}\frac{di_{a1}}{dt} \\ L_{loop} & = L_+ + L_- + ESL + L_{PCB} \\ L_{PCB} & = L_1 + L_2 + L_3 \end{cases} \qquad (7.9)$$

where, V_{ds} is the switch voltage, i_{a1} is the switch current during commutation, ESL is the capacitor equivalent series inductance, L_{PCB} is the parasitic induc-
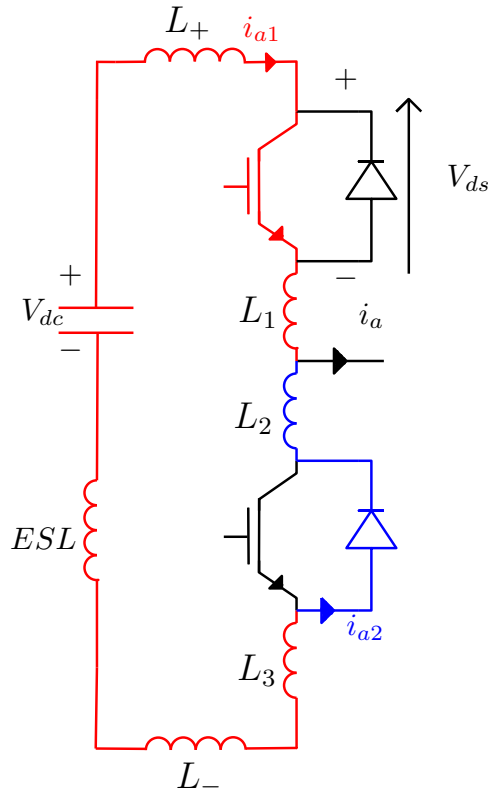
Figure 7.20: Half-bridge commutation loop parasitics.

tance of the converter PCB.

The per module equivalent circuit between the DC-input tabs and the converter module can be represented by Fig. 7.21. It contains both the AC parasitics L_{AC}, R_{AC}, C_{int} between the capacitors and the converter modules and the DC parasitics L_{DC}, R_{DC} between the DC input tabs and the converter modules. L_{AC} contributes to the voltage spike on the switches, C_{int} is an intrinsic capacitance that smooths the DC-link voltage, R_{AC} dissipates the AC loss and part of the DC loss, L_{DC} further smooths the input DC current along with the DC-source inductance L_s, R_{DC} dissipates part of the DC loss.

Table 7.5 lists the per module parasitic values for the DC-link bus bar in case of copper and aluminium plates of 1 mm thickness with 50μm of kapton as an insulation layer.

For evaluation of the loss density distribution in the bus bar needed for the thermal analysis, both the DC-source current and the capacitor rms current should be evaluated first. The bus bar highest loss occurs at the lowest DC-link voltage

228
Multiphysics Design of an Integrated DC-link Structure with Distributed
Capacitance for the YASA Integrated Drive
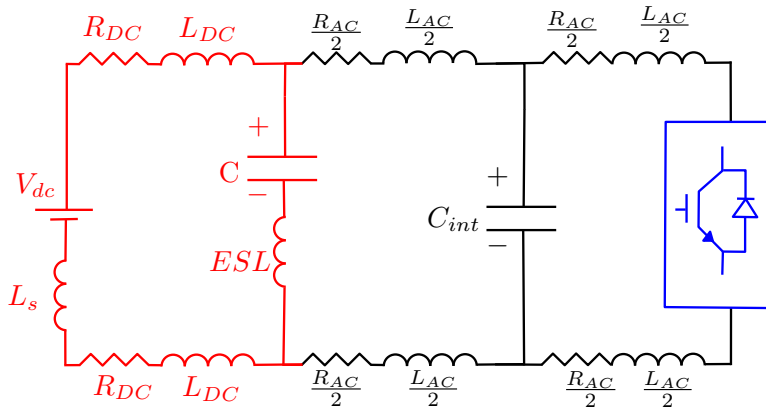
Figure 7.21: Per module bus bar equivalent circuit.

Table 7.5: Values of the bus bar parasitic parameters

Plate material	Parameter	Value
Copper	$R_{dc}(m\Omega)$	1.125
	$L_{dc}(nH)$	409
	$R_{AC}(m\Omega)$	0.3
	$L_{AC}(nH)$	16.04
	$C_{int}(pF)$	36.08
Aluminium	$R_{dc}(m\Omega)$	1.725
	$L_{dc}(nH)$	409
	$R_{AC}(m\Omega)$	0.3
	$L_{AC}(nH)$	16.04
	$C_{int}(pF)$	36.08

and highest capacitor rms current which corresponds to the fifteen-phase operation
without interleaving. Assuming 90% drive efficiency η, 17 kW rated output power
P_r and V_{dc}= 80 V, the DC-source current I_{dc} is calculated from (7.10) and amounts
to 236 A. For the capacitor rms current, the worst case occurs at zero interleaving
angle for the connection in Fig. 7.13 where the current amounts to 35 A (see Fig.
7.16).

$$I_{dc} = \frac{P_r}{\eta V_{dc}} \tag{7.10}$$

Both the AC and the DC-current are injected in the bus bar and the loss density is evaluated in case of copper plates (Fig. 7.22) and aluminium plates (Fig. 7.23). It can be seen that the maximum loss density is located at the input DC tabs due to the higher DC-current compared to the AC one and also the total DC-current of the fifteen modules is passing through the input tabs unlike the AC-current that divides over the fifteen capacitors. The maximum loss density is 1.53 times higher in case of aluminium plates compared to copper plates due to the lower electrical conductivity of the aluminium.

Bus bar thermal analysis

A thermal model is built to evaluate the temperature of the bus bar components to ensure that the insulation temperature is below its rated value given the high ambient temperature inside an integrated drive. Assuming an ambient temperature of 50°C, natural air convection and the loss density distribution in Figs. 7.22 and 7.23, the temperature field is evaluated and shown in Figs. 7.24 and 7.25 for the plates and the insulation layer in case of copper and aluminium plates respectively. The thermal properties of the materials used in the simulation are given in Table 7.6. Here, ρ and C_p are the mass density and the specific heat capacity respectively.

The insulation temperature rises 97.3°C and 165.8°C above the ambient for the copper and the aluminium plates respectively. For both materials, the insulation temperature stays below the rated value of the Kapton material (400°C). The 68.5°C more temperature rise in case of aluminium plates is due to the higher loss density and the lower thermal conductivity of the aluminium. It can be seen also the higher temperature gradient in case of aluminium plates due to the lower thermal conductivity. The maximum insulation temperature is 15% and 28.5% higher than the average in case of copper and aluminium plates respectively.

7.4   Influence of the parasitics

The influence of the DC-link structure parasitics on the converter DC terminal voltage, output phase voltage and output line voltage is assessed by simulating the circuit in Fig. 7.21. The converter is modelled using the dynamic behaviour of the GaN switch GS66508B used in the implementation of the converter modules.

Due to the high transition speed of the GaN switches [11], any small parasitic inductance in the commutation loop contributes considerably to the voltage stress on the switches and the bus bar insulation during turn-off transition of the switches. Fig. 7.26 (left) shows the resulted converter module terminal voltage. A spike of 73 V above the 400 V DC-voltage can be observed.

Figure 7.22: The bus bar loss density distribution due to the AC and
the DC-current in case of copper plates.

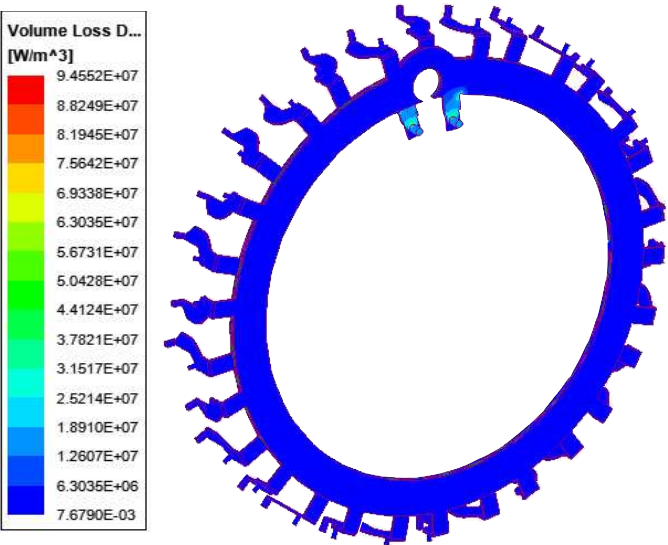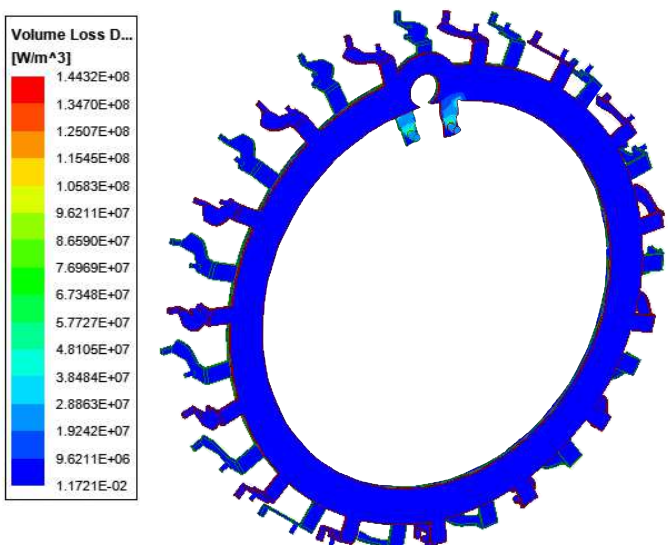Figure 7.23: The bus bar loss density distribution due to the AC and
the DC-current in case of aluminium plates.
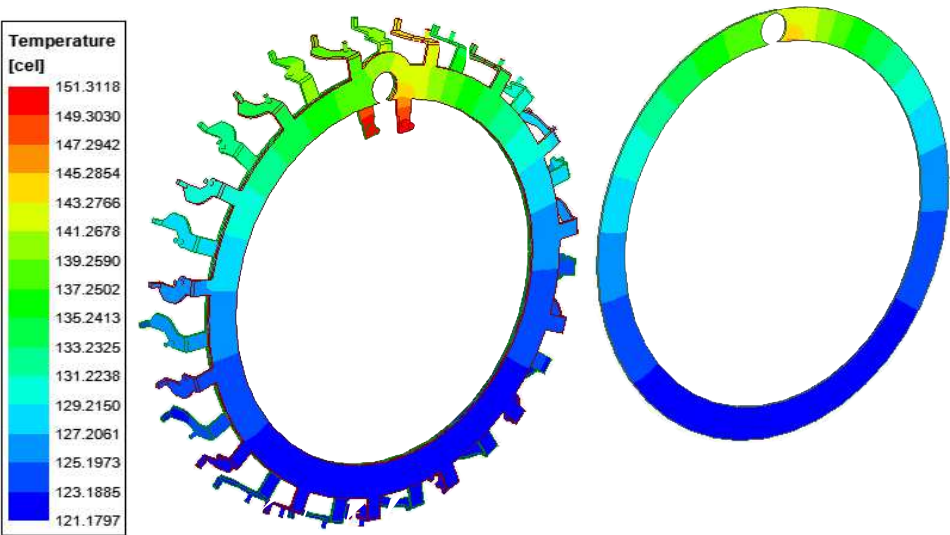
Figure 7.24: The bus bar temperature distribution in case of copper plates with plate temperature (left) and insulation temperature (right).
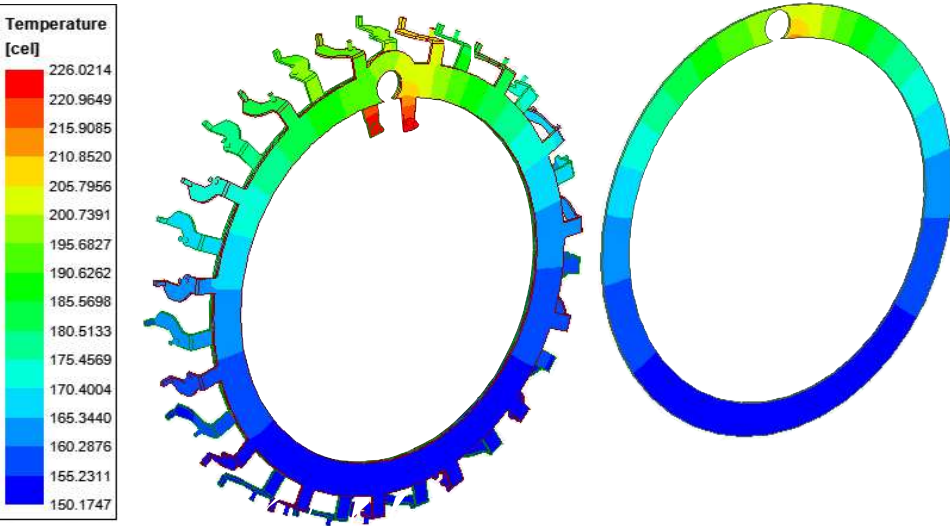
Figure 7.25: The bus bar temperature distribution in case of aluminium plates with plate temperature (left) and insulation temperature (right).

232
Multiphysics Design of an Integrated DC-link Structure with Distributed
Capacitance for the YASA Integrated Drive

Table 7.6: Thermal properties of the bus bar materials

Material	K_{th} (W/m.K)	ρ (kg/m^3)	C_p (J/kg.K)
Copper	385	8890	392
Aluminium	167	2712	896
Kapton	0.4	1330	1420
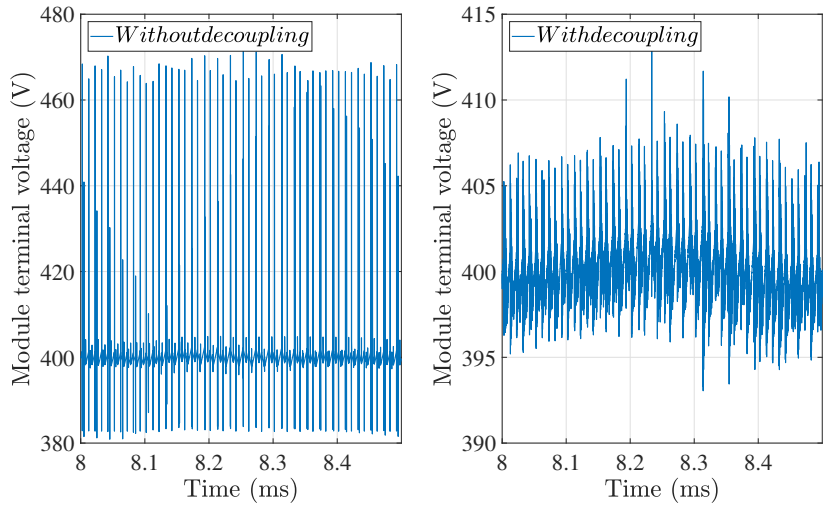
Figure 7.26: The module terminal voltage spike due to the DC-link parasitics (left) and spike reduction by decoupling (right).

The influence of adding four 0.1 μF ceramic capacitors close to the terminals of the converter module is shown in Fig. 7.26 (right). The additional capacitors reduce the voltage spike to 12 V.

The effect of the parasitics on the line voltage with and without the decoupling capacitors is evaluated and reported in Fig. 7.27. It can be seen that the effect on the DC-link voltage waveform is directly reflected on the line voltage.

The effect of the parasitics on the phase voltage with and without the decoupling capacitors is evaluated and reported in Fig. 7.28. A smaller influence on the phase voltage spike can be noticed as it is affected by the transient switching behaviour of only one inverter leg. The decoupling capacitors are reducing the phase voltage spike by about 23 V.

Figure 7.27: The line voltage spike due to the DC-link parasitics (left) and spike reduction by decoupling (right).

Figure 7.28: The phase voltage spike due to the DC-link parasitics (left) and spike reduction by decoupling (right).

7.5 Experimental validation

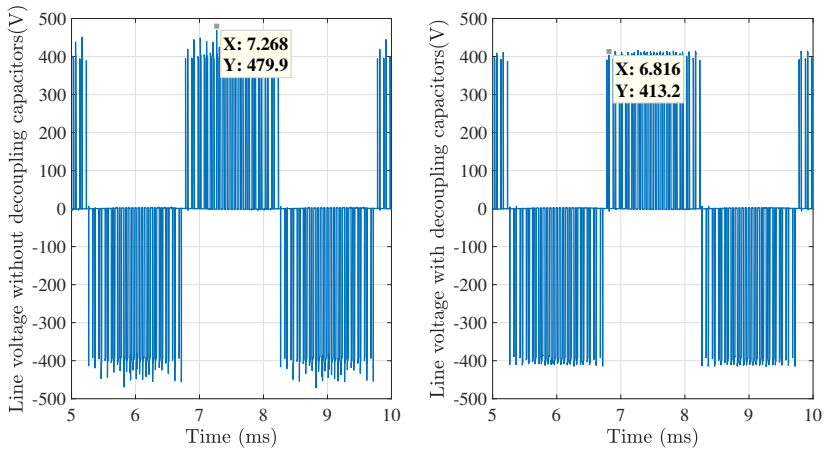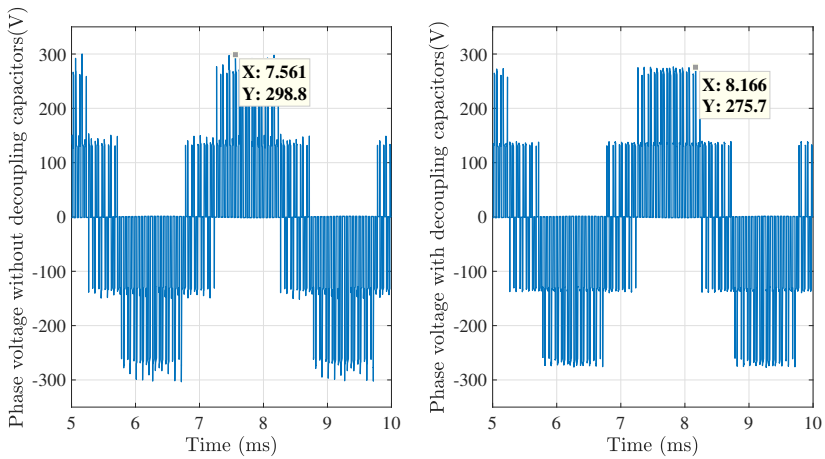Experimental measurements are performed on the three-teeth integrated setup presented in Chapter 6 section (6.3). The three modules are operated as three-phase inverter supplying an $R = 11.5\Omega, L = 3$ mH load. The line currents are mea-

sured with the on-board current sensor ACHS-7123 while the capacitor currents are measured using the current probe TCPA300 with the static transfer function of 10 A/mV. All waveforms are visualized using a Tektronix 1 GHz bandwidth scope. The sinusoidal PWM technique is utilized and the control pulses are generated using a dSPACE MicroLabBox.

The capacitor current is measured at a switching frequency 10 kHz, a fundamental frequency of 50 Hz, and three different peak line currents of 7.5 A, 5.5 A and 3.8 A to compare the measured rms value with the calculated value (7.6). With the value of the RL load used and 50 Hz, the resulting power factor is 0.997, near to unity to evaluate the worst case capacitor current value [131]. Fig. 7.29 shows the measured three-phase line currents in case of 7.5 A peak.
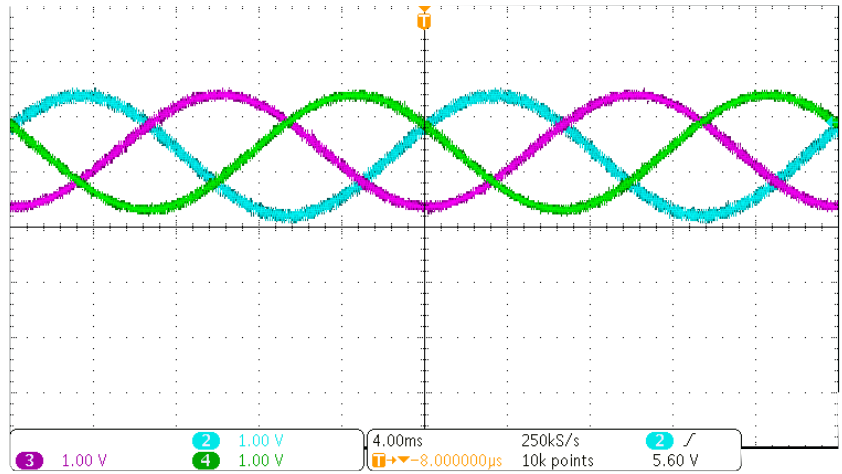
Figure 7.29: The three-phase currents with 7.5 A peak value. The scales are 4A/div and 4ms/div.

The capacitor current at 7.5 A peak line current is shown in Fig. 7.30 for ten power cycles and Fig. 7.31 for ten switching cycles. The measured and the calculated capacitor rms current at different peak line currents are reported in Table 7.7 as well as the percentage error between them.

The difference between the measured and the calculated current is mainly resulting from the influence of the parasitics and the decoupling capacitors.

The influence of the switching frequency on the capacitor current is visualized by measuring the capacitor current at a constant peak line current of 6.5 A and two different switching frequencies (10 kHz, 30 kHz). Fig. 7.32 shows the measured capacitor current at 10 kHz and Fig. 7.33 at 30 kHz with the rms value marked on the graph. A 20.6% increase in the capacitor rms current can be observed at 10 kHz. The reason of the decrease of the capacitor current with the increase in the switching frequency is the higher inductive impedance of the DC-link that further
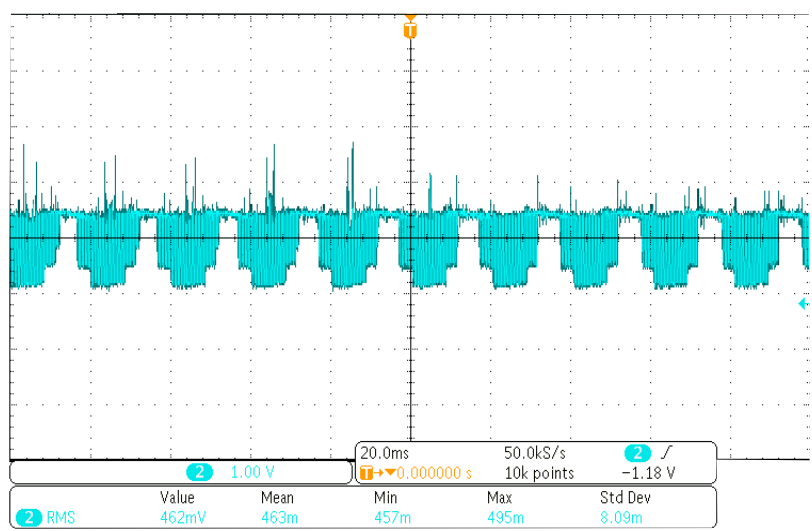
Figure 7.30: The capacitor current for 10-power cycles. The scales are 4A/div and 20ms/div.
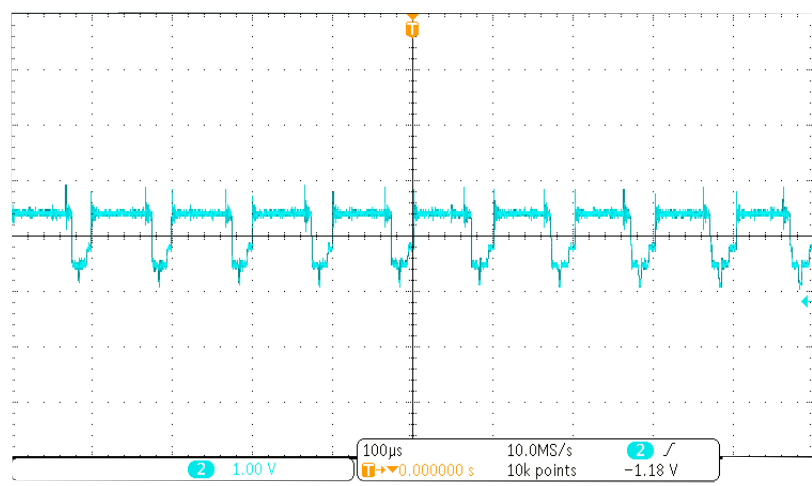
Figure 7.31: The capacitor current for 10-switching cycles. The scales are 4A/div and 100μs/div.

smooths the current at the higher switching frequency.

The estimation of the capacitor power loss using equation (7.8) is assessed by measuring the capacitor temperature at two different line currents (5.5 A, 3.8

Table 7.7: capacitor measured and calculated rms current

Peak line current (A)	capacitor rms current		% error
	measured	calculated	
7.5	4.62	4.35	-5.7
5.5	3.41	3.2	-6.1
3.8	2.48	2.35	-5.3
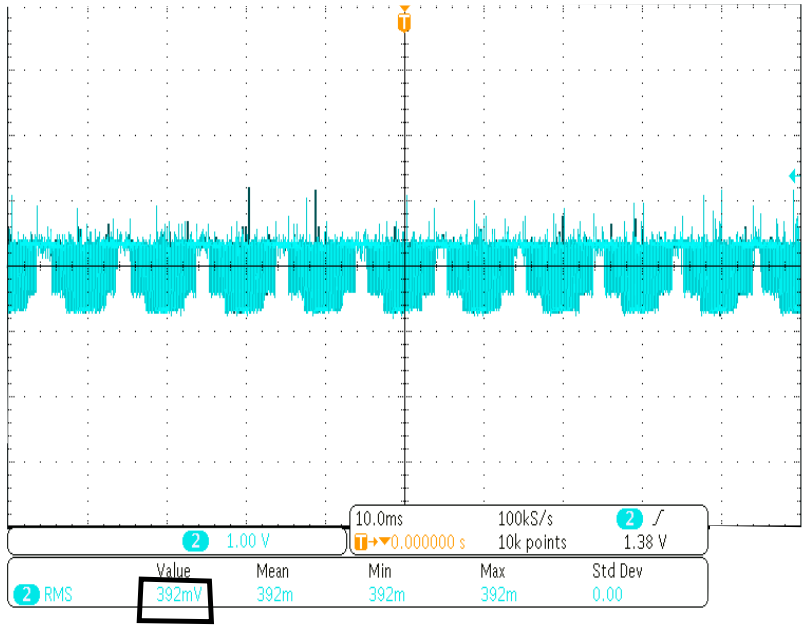
Figure 7.32: The capacitor current at 10 kHz switching frequency. The scales are 4A/div and 10ms/div.

A) and comparing the thermally measured power with the electrically calculated power. Both measurements are captured at ambient temperature of 25°C and free air convection. The capacitor is covered with a black tape for a better emissivity and temperature measurement accuracy. The resulted hot spot temperature is 36.7°C and 34.1°C for 5.5 A and 3.8 A peak line current respectively.

Table 7.8 contains the capacitor power loss measured thermally and calculated electrically with the percentage difference between both of them. The difference between the measurements and the calculations can be explained as follows: the variation of the ESR and the thermal resistance of the capacitors with temperature
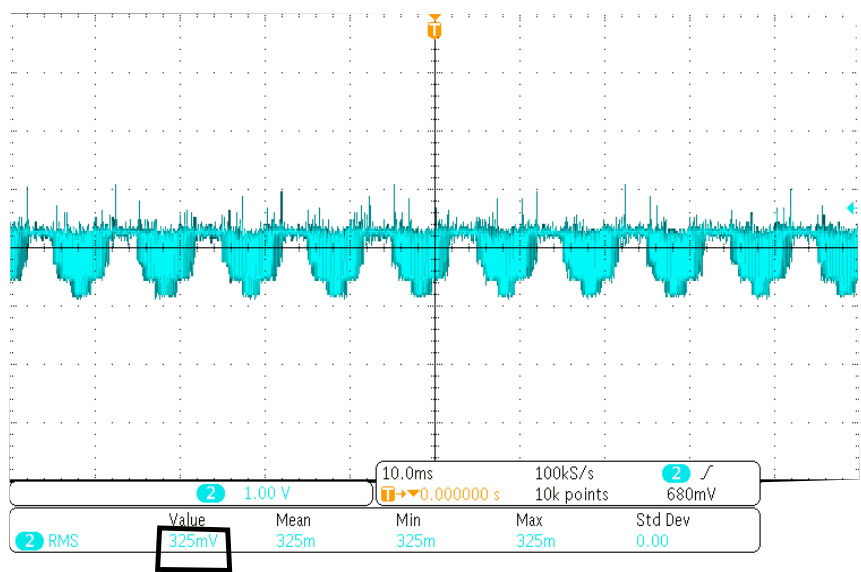
Figure 7.33: The capacitor current at 30 kHz switching frequency. The scales are 4A/div and 10ms/div.

is not given in the datasheet of the selected part instead, fixed values at 25°C are given. Neglecting the variation of these parameters with temperature introduces an error in the calculation of the capacitor losses. The capacitor temperature is measured with the thermal camera (GTC 400). The measured value has an error of ±3°C. This represents the measurement error. Since the measured capacitor temperature is less than 37°C, the contribution of the thermal camera measurement error is expected to be the main reason of the discrepancy.

Table 7.8: capacitor measured and calculated losses

Peak line current (A)	capacitor loss		% error
	measured	calculated	
5.5	0.508	0.594	16.9
3.8	0.3957	0.464	17.2

Fig. 7.34 shows the manufactured DC-link bus bar installed on the stator of the circumscribing polygon integrated YASA axial flux drive. The bus bar is manufactured from aluminium of 1mm thickness. The thermal performance of the bus bar is tested by injecting 55 A (to limit the temperature of the wires connecting

the DC-source to the bus bar) in the DC-input tabs at ambient temperature of $25°C$ and the resulted temperature distribution is reported in Fig. 7.35. At such current, the bus bar hot spot at the input tabs reaches $110°C$. This is much smaller than the rated value of the kapton, an indication of the possibility to inject higher input current.

7.6   Conclusion

An integrated DC-link structure topology for reconfigurable modular motor drives is designed and extensively analysed in this chapter. This DC-link structure has many advantages for the reconfigurable modular integrated drives. It combines both the capacitors and the bus bar together and integrates them with the modular integrated converter/machine structure without increasing the outer diameter of the drive which enhances the compactness of the integrated drive. The per module AC parasitic inductance from the capacitor terminals to the inverter input terminals is calculated to be 16 nH which is a small value compared to the ESL resulting in a small voltage stress on the switches. The per module DC parasitic inductance is also calculated to be 409 nH which is a relatively high value. This DC inductance smooths the DC-source current which results in lower electrical and thermal stresses on the input DC-source.

Considering the high ambient temperature inside the integrated drive, the electromagnetic loss density distribution of the bus bar is computed and used as an input to a thermal model to compute the bus bar temperature. The calculated temperature is proven to be tolerable by the bus bar components.

Generic analytical equations for the design of the DC-link capacitors for the different configurations of the YASA drive are provided.

Experimental validations are performed to assess the accuracy of the analytical design method of the DC-link capacitors and bus bar. The measurements confirm a good accuracy of the analytical method and good multiphysics modelling of the bus bar.
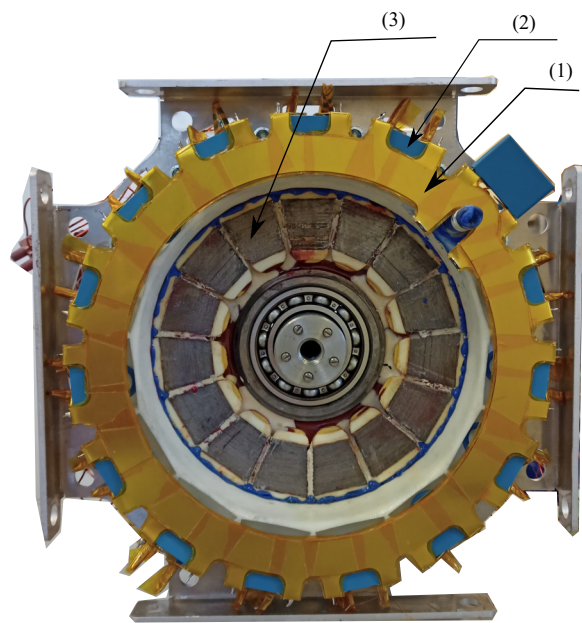
Figure 7.34: The manufactured stator of the integrated drive with the bus bar installed: (1) the DC-link bus bar, (2) the DC-link capacitor, (3) the stator teeth.
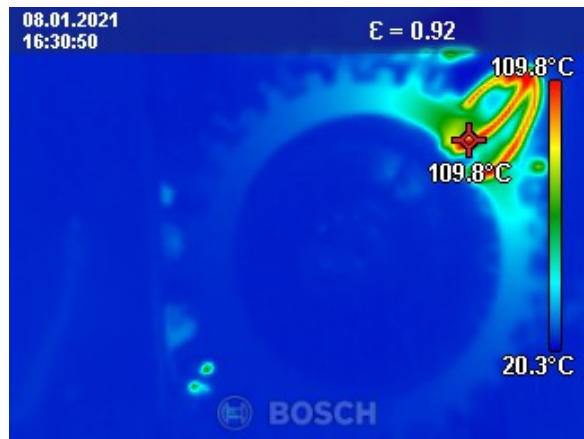
Figure 7.35: The temperature distribution over the bus bar measured at 55 A input DC-current.

Chapter 8

Power Density of the Circumscribing Polygon Integration Topology for the YASA Integrated Drive

8.1   Introduction

The power density of the electric motor drive is determined by the total volume or the total mass of the drive and the rated power that can be delivered by this volume or this mass [6]. Therefore, an enhancement in the power density can be achieved if a reduction in the volume or the mass for the same power is established or higher power can be obtained from the same volume or mass, or in best case the reduction of the volume or the mass and the boosting of the power at the same time.

As explained in the previous chapters, the integration of the electric machine and the power converter contributes in the reduction of the volume and the weight of the drive which enhances the power density. Besides the integration, the modularity facilitates the design of the cooling system by distributing the total power over several modules.

In integrated modular motor drives (IMMDs) with shared cooling for the electric machine and the power converter, the maximum power that can be obtained from the drive depends on the maximum current that can be injected by one converter module without exceeding the junction temperature limit of the switches and the maximum current that can be tolerated by the machine windings without exceeding the winding insulation temperature limit.

The maximum current that can be injected by one converter module depends on the power loss characteristics of the switch and the cooling capacity of the shared cooling system. As a consequence, selection of the semiconductor technology with low losses (i.e. WBG devices) and the optimal design of the shared cooling struc-

ture are the key points in maximizing the thermally tolerable switch current. In this perspective, the selected GaN switch for the converter implementation enhances the maximum current that can be injected by one module.

The maximum current that can be tolerated by the machine windings depends on the power loss characteristics of the windings and the core, and the cooling capacity of the shared cooling structure [139]. So, the optimal selection of the winding type and core material and the optimal design of the cooling system are the key techniques for maximizing the thermally tolerable winding current. Since the studied machine in this work is the Yokeless and segmented armature (YASA) axial flux permanent magnet machine (PMSM) with concentrated windings, the winding losses are expected to be low compared to the distributed winding machines due to the shorter end-windings [17]. The absence of the yoke and the selection of grain oriented core material are both contributing to the reduction of the core loss [72].

In this chapter, the power density of the circumscribing polygon (CP) integrated drive developed for the YASA AFPMSM is studied and several techniques for boosting the power density of this reference design are investigated using the CFD simulations and experimental measurements.

8.2   IMMDs phase configurations

The non-integrated YASA drive is designed to operate as three-phase machine at 400V DC-link voltage. Each phase is formed by connecting five-stator coils in series as shown in Chapter 7 Fig. 7.6. The same machine can be operated as five-phase if three stator coils are connected in series to form one phase as shown in Chapter 7 Fig. 7.11 and the DC-link voltage is scaled down to 240V. The five-phase operation could lead to a higher torque density if third-harmonic injection technique is utilized [140]. Fifteen-phase operation is also possible in three different ways at 80V DC-link voltage. Fifteen-phase operation is possible either with one common neutral as shown in Chapter 7 Fig. 7.12 or with five groups with three phases in each group as shown in Chapter 7 Fig. 7.13, or three groups with five phases in each group as shown in Chapter 7 Fig. 7.14. The fifteen-phase operation shown in Fig. 7.13 and Fig. 7.14 has fault-tolerance operation capability.

Due to the different DC-link voltage of the different phase connections, the switch losses, specifically the switching loss part is expected to be different if all other operating conditions (i.e. the switching frequency, the line current, the power factor, the modulation index) remain the same. Thanks to the low switching losses of the GaN devices, this difference is not expected to be high.

8.3   Power density and efficiency of the reference design

The power density of the integrated drive can be calculated as the ratio of the maximum power that can be obtained from the integrated drive to its volume or

alternatively to its mass. The power density indication derived from dividing by the volume is used in applications with limited space for the drive while the indication derived by mass division is important in applications that require low DC-source power consumption. Both indicators are derived for the CP drive in this part.

The power that can be obtained from the drive is limited by the maximum possible speed and the maximum torque that can be obtained from the machine. The maximum speed is limited by mechanical constraints. The maximum torque is limited by the maximum current that can be injected in the windings. In IMMDs with shared cooling, the maximum current that can be injected in the winding is limited by the switch junction temperature and the winding insulation class.

The maximum current that can be injected in the winding without exceeding the insulation thermal limit is evaluated using the CFD model. The following steps are performed to calculate the maximum winding current:

1. At 1 litre/minute water flow rate and 25°C water inlet temperature, the winding loss is increased until the winding maximum temperature reaches 115°C (the extra margin until reaching the winding insulation rated temperature is left for the core loss).

2. The winding loss and the average winding temperature resulting from step 1 are recorded.

3. The winding resistance is computed using (8.1) and the winding current is computed from (8.2).

4. Using the current calculated in step 2, the core loss is computed from [72] and injected in the CFD model to evaluate the new winding maximum temperature. If the maximum temperature is lower than the limit of the insulation, the computed current is recorded. If not, the current is decreased, the new winding and the core losses are computed and the new maximum temperature until reaching a value lower than the rated winding temperature.

$$R_{coilhot} = R_o(1 + \alpha(T_{wdg} - T_o)) \qquad (8.1)$$

where, R_o is the winding resistance at 25°C, α is the resistance temperature coefficient which equals 0.393%/°C for copper, and T_{wdg} is the average winding temperature.

$$I_{wdg} = \sqrt{\left(\frac{P_{losscoil}}{R_{coilhot}}\right)} \qquad (8.2)$$

where, I_{wdg} is the maximum possible winding current, $P_{losscoil}$ is the maximum coil loss computed.

8.3.1 Application example

Applying the above steps results in a maximum winding temperature of 115°C with R_o=138.9 mΩ at 73W per module winding loss and zero core loss, this result is shown in Fig. 8.1 (a). The average coil temperature is 101.5°C and the corresponding coil resistance is 186.5 mΩ. The resulting winding current is 19.8A. The core loss per module is computed and amounts to 9W. Fig. 8.1 (b) shows the module temperature distribution with the core loss considered. The winding maximum temperature is 127°C which is still affordable by insulation class B and higher.

(a)   (b)
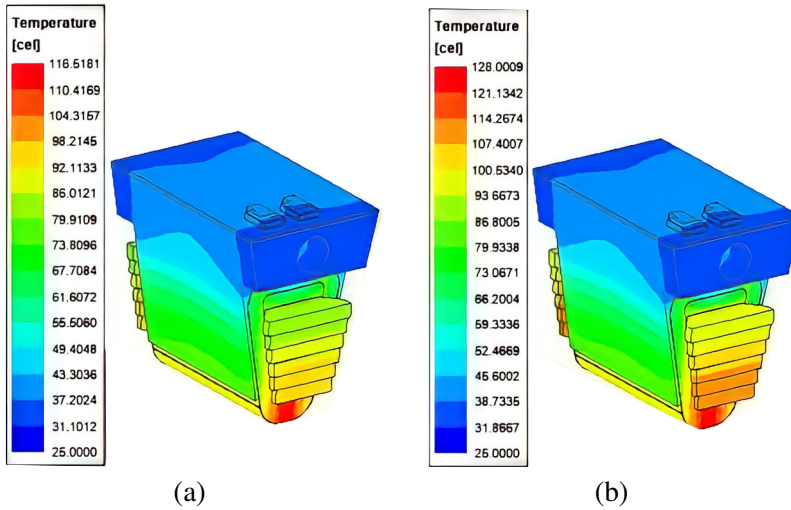
Figure 8.1: The module temperature distribution (a) in case of 73W winding loss per module and no core loss (b) in case of 73W winding loss per module and 9W core loss.

The maximum winding current that can be injected with one inverter module without exceeding the rated junction temperature of the switch is computed at the rated operating conditions in Table 8.1 as follows:

1. The switch loss that results in 115°C thermal pad temperature is computed using the CFD model.

2. From the switch loss versus temperature model, the peak winding current that results in the switch loss in step 1 is calculated.

Applying the above steps results in 115°C thermal pad temperature at 8.5W switch loss. The corresponding junction temperature can be calculated from (8.3) and amounts to 119.25°C. From Fig. 8.2 (a), (b), (c), the peak line current that can be injected by one inverter module in case of three-phase, five-phase, fifteen-phase

Table 8.1: The operating conditions at which the maximum current injected by one switch is computed

Parameter	Value
Modulation index (M)	1
Switching frequency (f_s) (kHz)	50
Fundamental frequency (f_o) (Hz)	333.3
Power factor (pf)	0.85
$V_{dc}\vert_{3-phase}$ (V)	400
$V_{dc}\vert_{5-phase}$ (V)	240
$V_{dc}\vert_{15-phase}$ (V)	80

operation is 14A, 15.5A, 16.5A respectively which corresponds to 9.8A, 10.9A, 11.6A rms respectively. Due to the low switching loss of the GaN device, the difference in the maximum current that can be injected at each connection is not high.

$$T_j = T_{tp} + R_{jc}P_{swloss} \tag{8.3}$$

where, T_j is the junction temperature, T_{tp} is the thermal pad temperature, R_{jc} is the junction to case thermal resistance which amounts to 0.5 °C/W for the selected switch, P_{swloss} is the switch loss.

At 9.8A rms line current, the per module winding loss is 14.6W and the per module core loss is 3W. Fig. 8.3 shows the temperature distribution over one integrated module at these power losses. The resulting winding maximum temperature is 51.5°C.

For the calculation of the power density, the total volume, the total mass and the total power of the integrated drive should be calculated for each phase connection. The total drive power P_{drive} can be calculated from (5.11) for each phase number n_{phase}. The total drive volume is calculated from the axial length of the integrated drive which equals 105.5mm and the outer diameter which equals 212.7mm. The resulting volume equals 3.75l. The mass of each component of the drive and the total mass are given in Table 8.2.

For this reference design, the windings can tolerate up to 19.8A rms current but the converter module can only inject up to 11.6A in case of fifteen-phase operation. So, the power density is limited by the switch junction temperature for this design. The power density of this design for fifteen-phase operation is 1.12kW/l or 0.33kW/kg.

The total output power of the inverter is 4.2kW, the total inverter loss is 255W

(a)

(b)

(c)
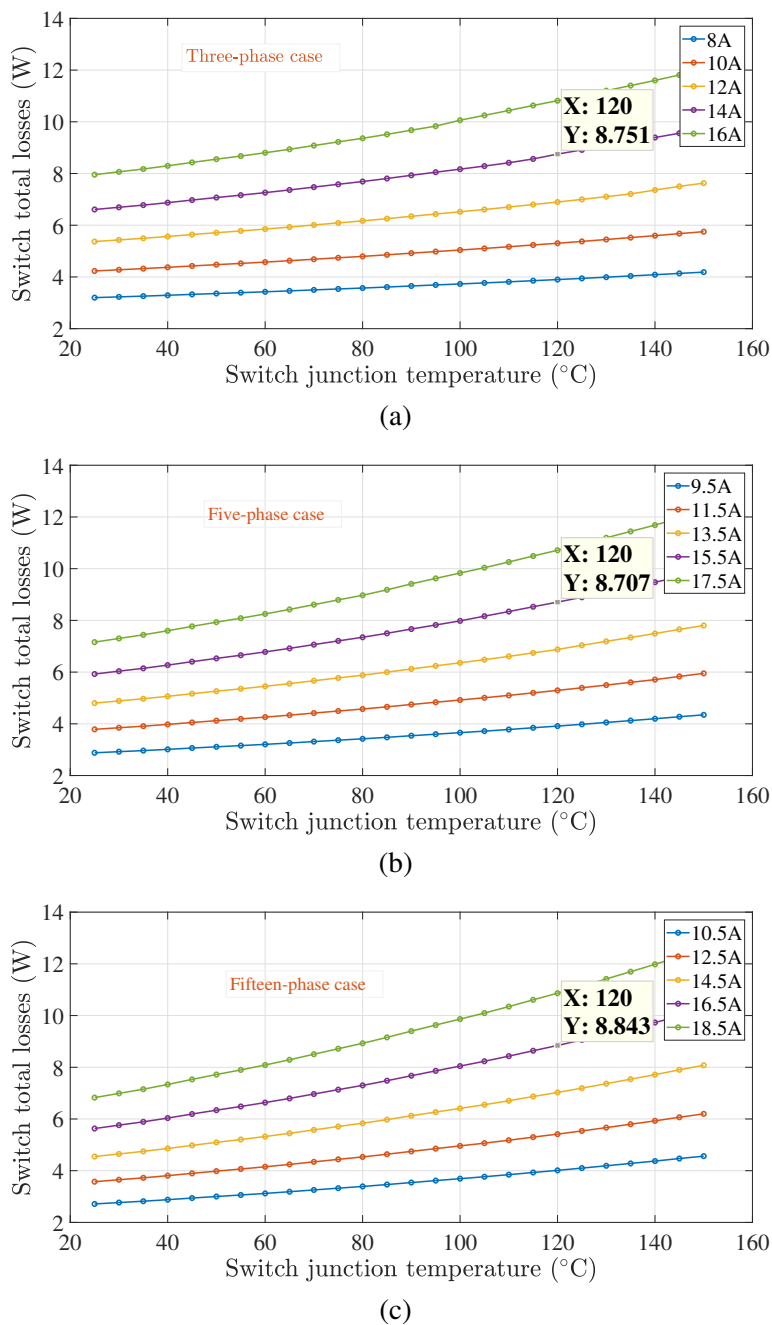
Figure 8.2: The switch loss versus the junction temperature at the operating conditions in Table 8.1 in case of (a) three-phase operation, (b) five-phase operation, (c) fifteen-phase operation.
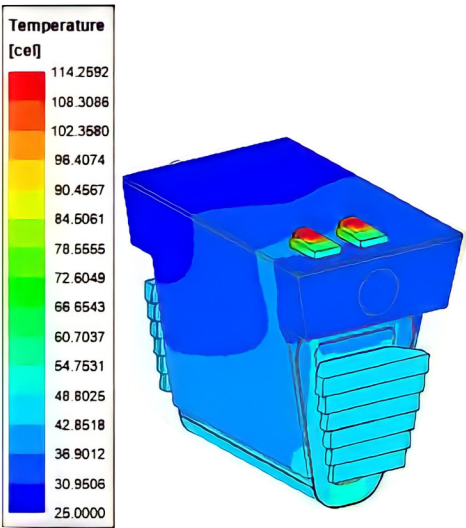
Figure 8.3: Temperature distribution over one integrated module at 14.6W per module, 3W per module loss and 8.5W per switch loss in case of reference design system.

Table 8.2: The mass of the integrated drive components

Drive part	Mass (kg)
rotor disks	2.13
magnets	0.6
shaft	0.9
bearing	0.28
stator core	2.8
stator winding	2.9
shared cooling structure	2.2
converter modules	0.26
DC-link structure	0.5
Total mass	12.57

and the total machine loss is 264W. This results in inverter efficiency of 94.3% and total drive efficiency of 88.4%.

8.4   Power density boosting techniques

The power density of the integrated drive can be enhanced by boosting the current that can be injected by one inverter module and tolerated by the machine windings without violating the thermal limits of both. In this section, techniques for boosting the current of one inverter module and/or the current of the windings are studied.

8.4.1   Parallel operation of the inverter modules

In case of three-phase and five-phase operation, the drive power density can be enhanced by supplying each phase from several parallel connected inverter modules.

Since the shared cooling structure can accommodate up to fifteen-inverter modules, up to five-modules per phase can be used in case of three-phase operation as shown in Fig. 8.4 (a) and up to three-modules per phase can be used in case of five-phase operation as shown in Fig. 8.4 (b).
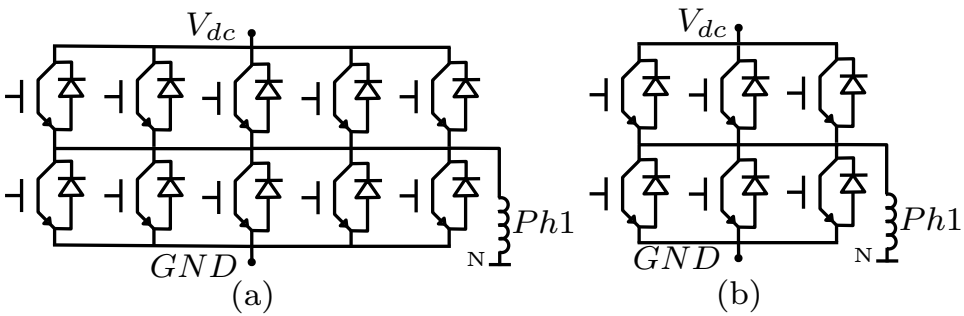
Figure 8.4: Possible number of parallel connected converter modules per phase in case of (a) Three-phase operation, (b) Five-phase operation.

By this parallel connection of the inverter modules, the full 19.8A rms of the winding can be supplied without overheating the switches. The 73W per module winding loss and the 9W per module core loss will result while the switch loss will be 8.5W. The temperature distribution over one module in this case is shown in Fig. 8.5. The power density using this approach becomes 1.92kW/l or 0.57kW/kg. This method is applicable only in case of three-phase and five-phase operation but not in case of fifteen-phase.

If the 19.8A rms which is 28A peak of the stator winding is supplied by two converters connected in parallel, each converter contributes by 14A peak line current.

For the three-phase case, the total output power of the inverter is 7.2kW, the total inverter loss will be 102W, the efficiency of the inverter will be 98.6%. The total machine loss will be 1230W and the total drive efficiency will be 81.8%.

Figure 8.5: Temperature distribution over one integrated module in case of two-parallel inverter modules per phase, 73W per coil winding loss, 9W core loss and 8.5W switch loss.

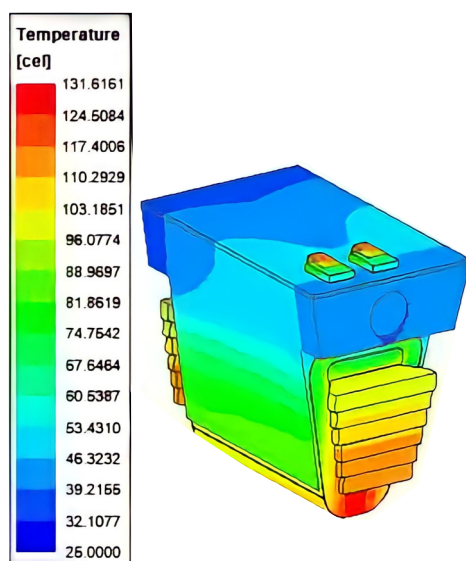For the five-phase case, the total output power of the inverter is 7.2kW, the total inverter loss will be 146.5W, the efficiency of the inverter will be 98%. The total machine loss will be 1230W and the total drive efficiency will be 81.3%.

8.4.2 Optimal choice of the thermal interface material (TIM)

The reference design system is implemented using the TIM material (TIM1) with thermal conductivity of 4.4W/m.K and 1mm thickness. The high thermal conductivity facilitates the heat-transfer but the big thickness degrades it. Another TIM choice (TIM2) with a thermal conductivity of 0.12W/m.K and a thickness of 0.025mm is investigated. From the CFD model with the case of TIM2, the switch thermal pad temperature reaches 115°C at 22W switch loss and the junction temperature reaches 126°C. At such tolerable switch loss, the peak line current that can be injected by one converter module is 25A (see Fig. 8.6) which corresponds to 17.7A rms. At this current, the per module winding loss is 57.1W and the core loss per module is 7.5W. The module temperature distribution at such losses is shown in Fig. 8.7. The resulting power density in case of fifteen-phase operation when using TIM2 is 1.7kW/l or 0.51kW/kg. The choice of the TIM material and dimensions influences the temperature of the switches only and not the machine elements as it exists mainly in the path of the heat generated by the switches. This method is applicable for all phase connections.
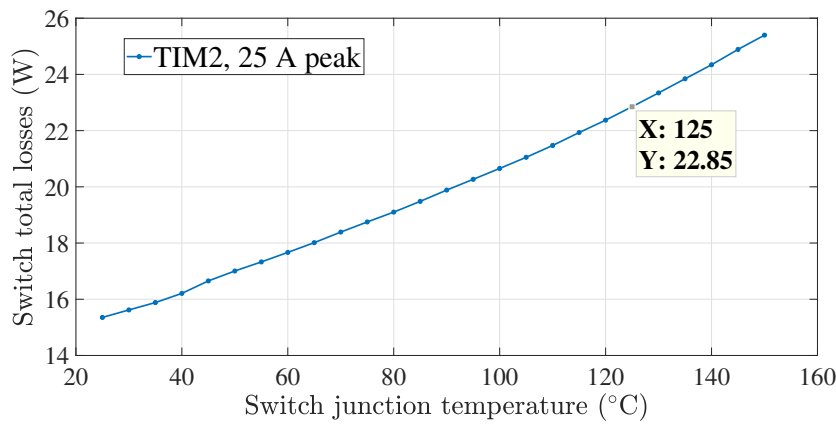
Figure 8.6: The switch loss versus the junction temperature at 25A peak line current in case of using TIM2.
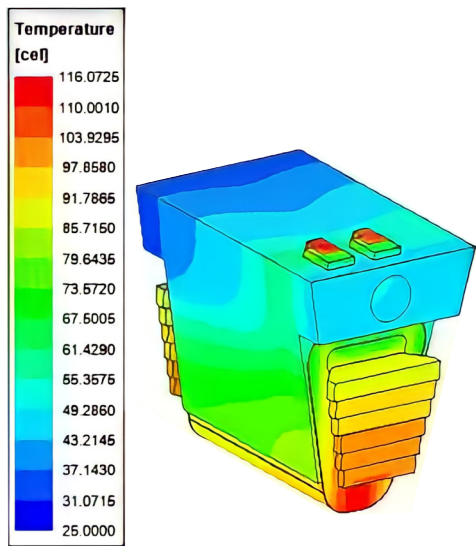
Figure 8.7: Temperature distribution over one integrated module at 57.1W per module winding loss, 7.5W per module core loss and 22W switch loss using TIM2.

In case of fifteen-phase operation, the total output power of the inverter is 6.4kW, the total inverter loss will be 660W, the efficiency of the inverter will be 91%. The total machine loss will be 969W and the total drive efficiency will be 77%.

8.4.3 Shared cooling structure material

The shared cooling structure of the reference design system is made of aluminium. The influence of using copper instead is evaluated in this part. Using copper instead of aluminium results in winding maximum temperature of 115°C at 83W per module winding loss compared to 73W in the case of the reference design system. The corresponding winding current is 21 A compared to 19.8A in the reference design case. A switch thermal pad temperature of 115°C results at switch loss of 8.7W. So, using copper instead of aluminium boosts the winding current a bit without much increase in the switch current. Since the maximum switch current remains the same as the reference case, the temperature distribution over one module is computed at 14.6W winding loss, 3W core loss and 8.5W switch loss, the same values of the reference design system. The result is shown in Fig. 8.8. A reduction of 3°C in the winding maximum temperature and the switch temperature compared to the aluminium case is observed. This method results in the same volumetric power density as the reference one and a smaller mass power density due to the higher copper mass density.
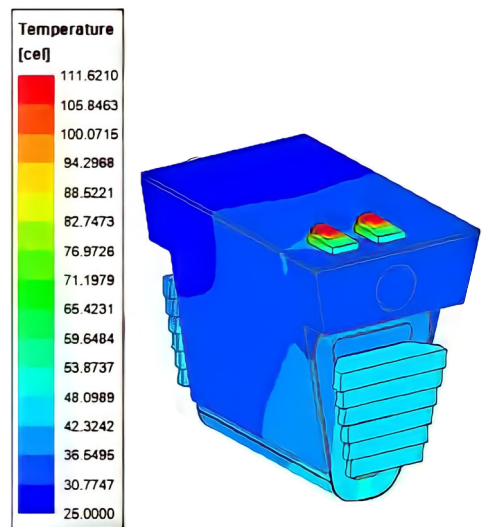
Figure 8.8: Temperature distribution over one integrated module at 14.6W per module, 3W per module loss and 8.5W per switch loss in case of copper shared cooling structure.

8.4.4 Number of cooling channels per module

The influence of the number of the cooling channels on the maximum winding current and the maximum switch current is evaluated by considering three-cooling channels per module instead of only one. Using this method, a winding maximum

temperature of 115°C results at 85W per module winding loss. The corresponding winding current is 21.4A. A switch thermal pad temperature of 115°C results at 10.2W switch loss, the corresponding switch junction temperature is 120.1°C. The maximum line current that can be injected by one converter module in case of fifteen-phase operation is 17.85A (see Fig. 8.9) which corresponds to 12.62A rms. The per module winding loss at such current is 29.7W, the per module core loss is 4.3W. The temperature distribution over one module is shown in Fig. 8.10. The resulting power density of this method in case of fifteen-phase operation is 1.21kW/l or 0.36kW/kg.
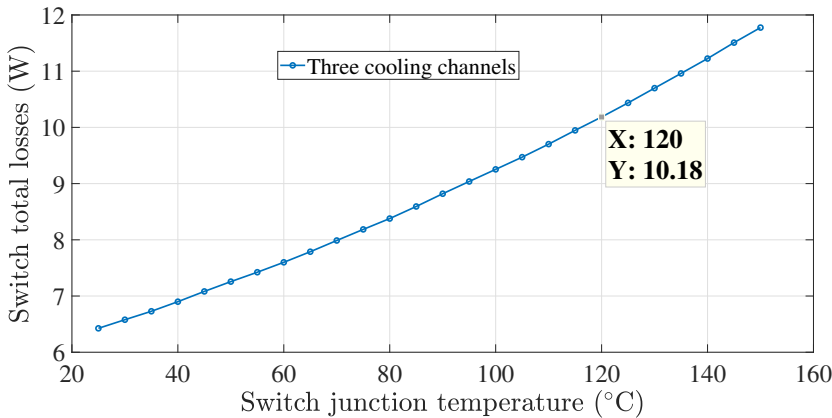
Figure 8.9: The switch loss versus the junction temperature at 17.85A peak line current in case of three cooling channels per module.

In case of fifteen-phase operation, the total output power of the inverter is 4.6kW, the total inverter loss will be 306W, the efficiency of the inverter will be 93.8%. The total machine loss will be 510W and the total drive efficiency will be 83.4%.

8.5   Combined Techniques

By combining the usage of TIM2, the copper housing and the three cooling channels per module, the highest winding current and switch current can be obtained and therefore, the highest power density. By this combination of methods, the switch thermal pad reaches 115°C at 35W loss and the junction temperature reaches 132.5°C. The maximum line current that can be injected by one inverter module is 31.5A (see Fig. 8.11) which corresponds to 22.3A rms. The per module winding loss and core loss at this current are 92.7W and 11W. The temperature distribution over one module at these losses is shown in Fig. 8.12. As can be seen the winding maximum temperature reaches 129.3°C. The power density achieved

Figure 8.10: Temperature distribution over one integrated module at 29.7W per module winding loss, 4.3W per module core loss and 10.2W switch loss in case of three cooling channels per module.

with these combined methods is 2.14kW/l.
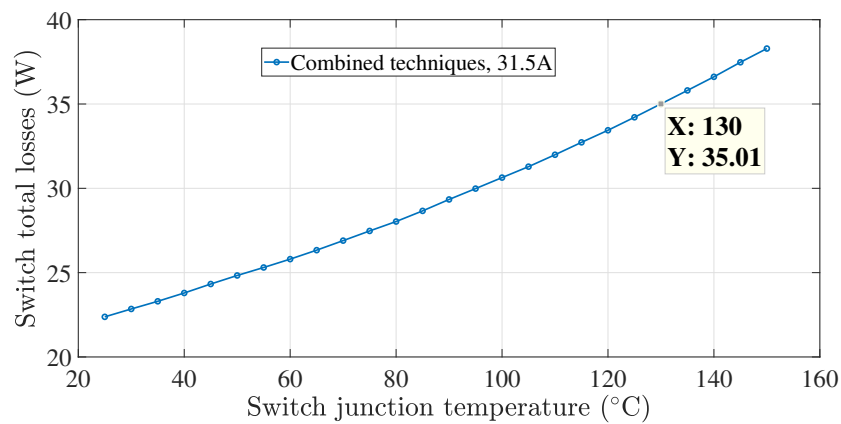
Figure 8.11: The switch loss versus the junction temperature at 31.5A peak line current in case of combined power density boosting techniques.

Compared to a power density of 1.43 kW/l reported in [6] for an integrated drive based on an air cored axial flux machine and a GaN based modular converter, the achievable power density of 2.14 kW/l is an indication for the effectiveness of
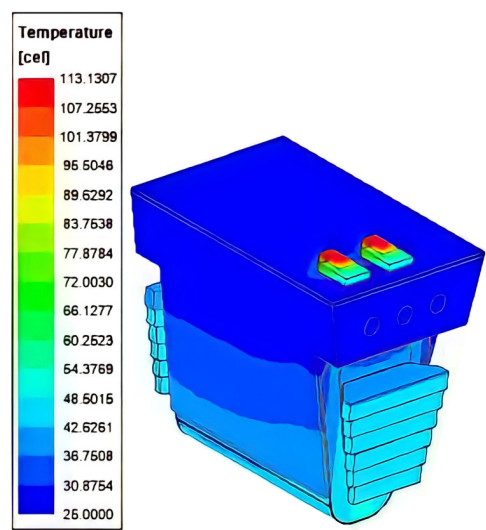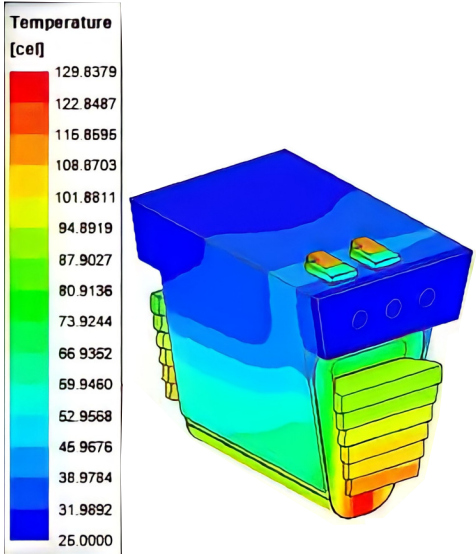
Figure 8.12: Temperature distribution over one integrated module at 92.7W per module winding loss, 11W per module core loss and 35W switch loss in case of combined power density boosting techniques.

the presented power density boosting techniques.

In case of fifteen-phase operation, the total output power of the inverter is 8.02kW, the total inverter loss will be 1050W, the efficiency of the inverter will be 88.5%. The total machine loss will be 1500W and the total drive efficiency will be 72%.

Fig. 8.13 shows the normalized power density of each power density enhancement technique with respect to the reference design system. Fig. 8.14 shows the normalized efficiency. From Fig. 8.13 and Fig. 8.14, the compromise between the power density and the efficiency of the integrated drive can be seen.

8.6   Experimental validation

The different power density enhancement techniques are assessed by experimental measurements on the three teeth setup explained in Chapter 6 section (6.3). The setup has one cooling channel per module and an aluminium shared cooling structure.

8.6.1   Parallel operation assessment

The effectiveness of the parallel operation on the power density is validated experimentally using DC and PWM waveforms. The thermal interface material used is
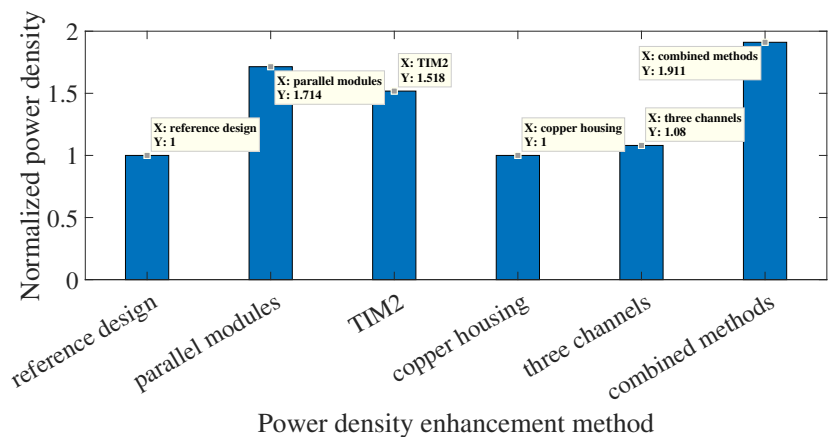
Figure 8.13: The influence of the power density enhancement techniques on the volumetric power density of the integrated drive.
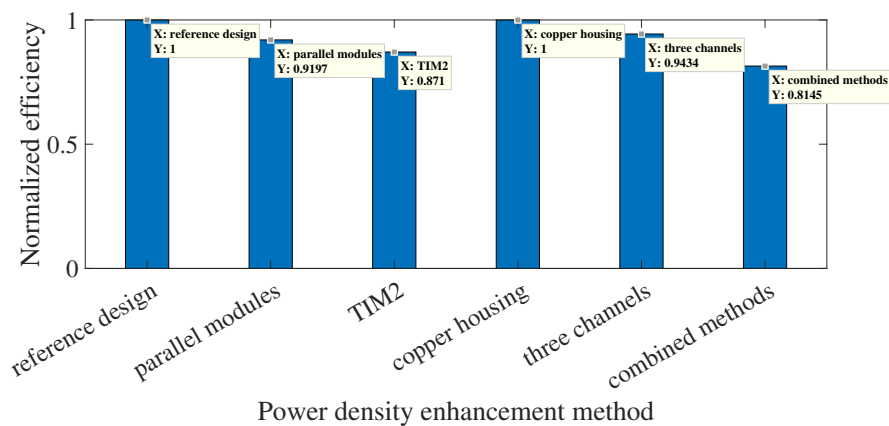
Figure 8.14: The influence of the power density enhancement techniques on the efficiency of the integrated drive.

TIM1.

Parallel operation with DC-waveforms

To show the effectiveness of the parallel operation of the converter modules, the converter modules and the windings are connected as shown in Fig. 8.15 (a) for a single converter connected in series with the three coils and Fig.8.15 (b) for two converters in parallel and connected in series with the three coils.

The injected winding current is 9.5A and 17.2A for the case of one module in
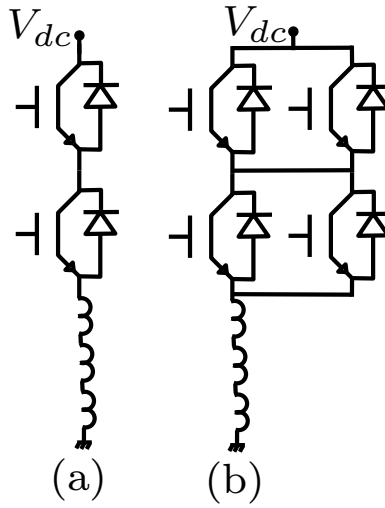
Figure 8.15: Converter modules and stator coils connection in case
of (a) One module in series with the windings, (b) Two modules in
parallel in series with the windings.

series with the windings and two modules in parallel respectively. The water flow
rate is 1 litre/minute and the inlet temperature is 25°C. The winding temperature
and the switches temperature are reported in Fig. 8.16 and Fig. 8.17 respectively
for both cases. It can be noticed that the current that can be injected in the windings
in case of parallel operation is increased by a factor of 1.81 without exceeding the
junction temperature of the switches which proves the effectiveness of the parallel
operation of the converter modules.

Parallel operation with PWM-waveforms

The circuit shown in Fig.8.18 (a) and (b) is used to evaluate the effectiveness of
the parallel operation with PWM waveforms. The upper transistor(s) is (are) kept
off and the lower transistor(s) is (are) switched with f_s=10kHz. The load used is
R=8Ω, L= 3 mH. The load current is increased until the junction temperature of
the switch reached 109°C.

Fig. 8.19 shows the electrical waveforms of the lower switch and the load at
which the switch junction temperature reached 109°C in case of the circuit con-
nection in Fig. 8.18 (a). The rms of the load current is 7.7A and the peak current is
12.4A. The DC-link voltage is 130V. Fig. 8.20 (a) and (b) shows the temperature
distribution over the inverter module with 109°C junction temperature.

Fig. 8.21 shows the electrical waveforms of the lower switch and the load at
which the switches junction temperature reached 109°C in case of the circuit con-
nection in Fig. 8.18 (b). The rms of the load current is 12.3A and the peak current
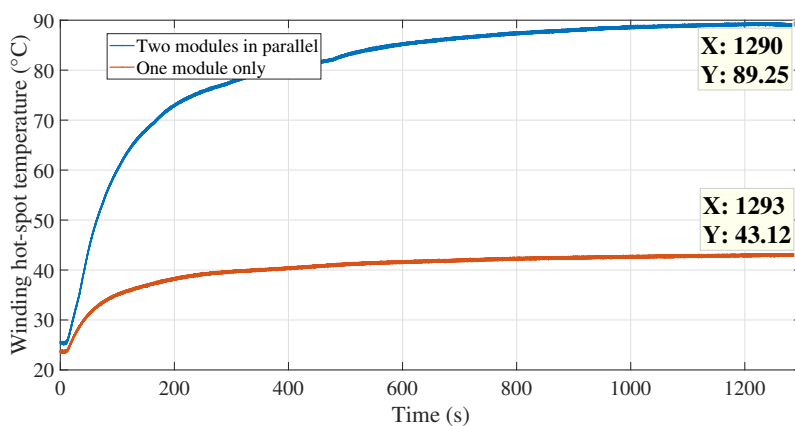
Figure 8.16: Winding temperature in case of one converter module and two modules in parallel at 9.5A and 17.2A.

Figure 8.17: Switch temperature in case of (a) one module supplying 9.5A winding current and (b) two modules in parallel supplying 17.2A winding current.

is 16.4A. The DC-link voltage is 160V. Fig. 8.22 (a) and (b) shows the temperature distribution over the inverter module with 109°C junction temperature. The load rms current in case of parallel operation is not exactly double the value in case of single module due to the higher DC-link voltage in case of parallel operation.
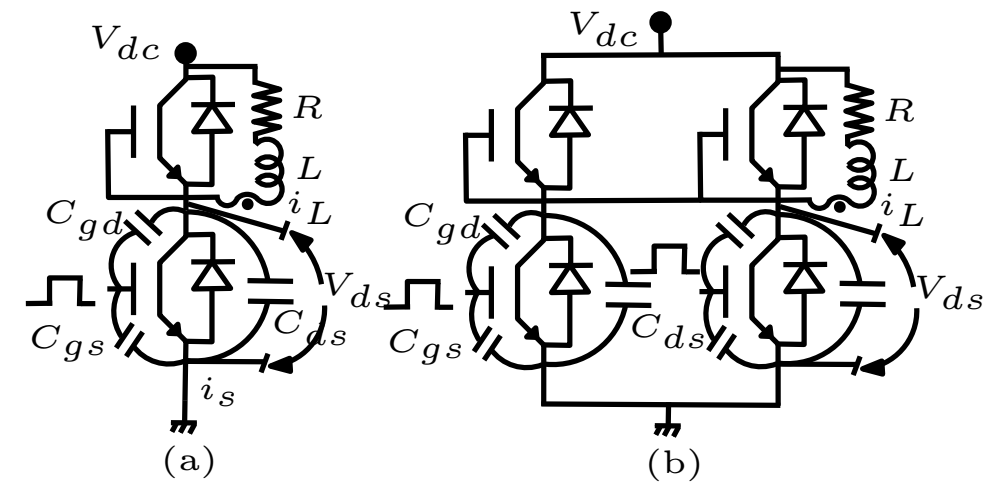
Figure 8.18: The schematic used to assess the operation with PWM
waveforms (a) single module, (b) two-converter modules in parallel.
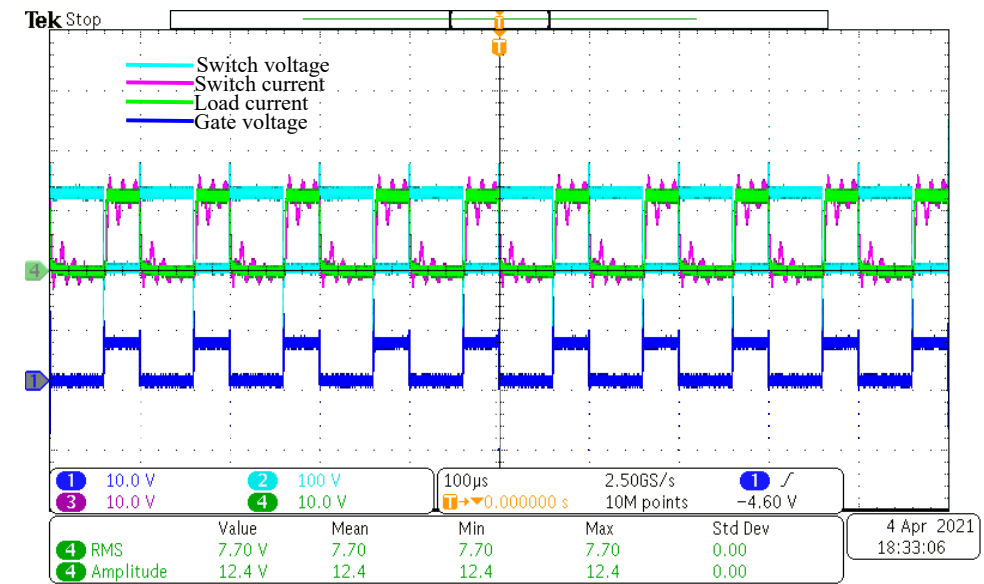
Figure 8.19: The electrical waveforms for the connection in Fig. 8.18
(a): the lower switch gate voltage, drain to source voltage, switch
current and load current measured at f_s=10kHz.

(a) (b)

Figure 8.20: The thermal image for the connection in Fig. 8.18 (a):
(a) inverter module real picture, (b)inverter module temperature dis-
tribution with junction temperature of 109°C.
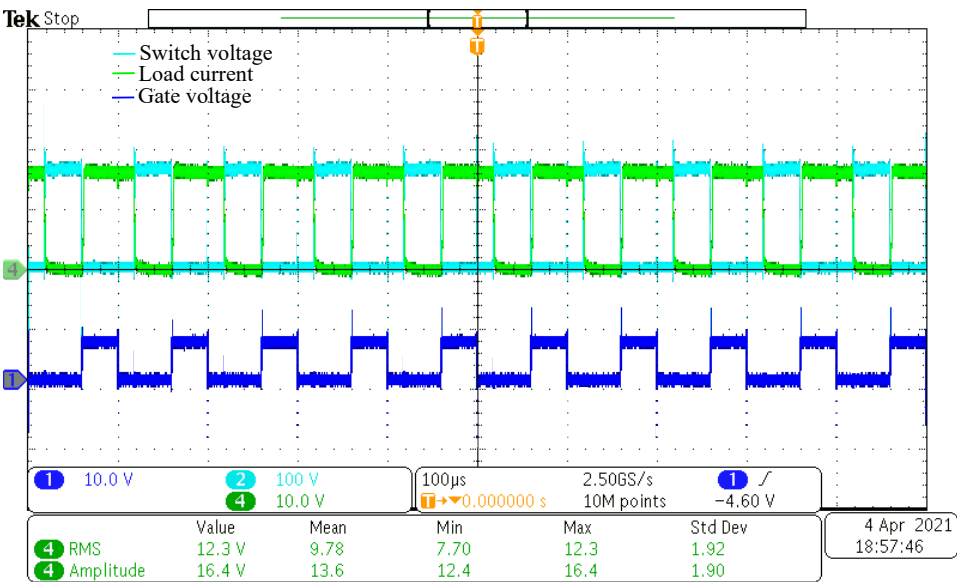
Figure 8.21: The electrical waveforms for the connection in Fig. 8.18
(b): the lower switch gate voltage, drain to source voltage, switch
current and load current measured at f_s=10kHz.

(a)   (b)
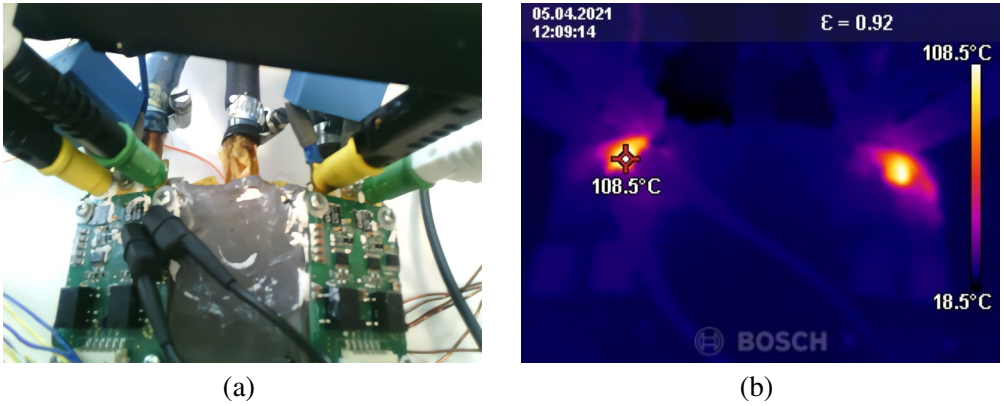
Figure 8.22: The thermal image for the connection in Fig. 8.18 (b):
(a) inverter module real picture, (b) inverter module temperature dis-
tribution with junction temperature of 109°C.

8.7   Conclusion

In this chapter, the power density of the circumscribing polygon integration topol-
ogy developed for the YASA AFPMSM is evaluated and five different power den-
sity boosting techniques are evaluated.

The power density boosting techniques evaluated in this chapter are the par-
allel operation of the converter modules, using optimal thermal interface material
(TIM2), using copper housing instead of the aluminium one, using three cooling
channels per module instead of only one and finally all these techniques are com-
bined together.

The power density of the reference designed system implemented using one
converter module per phase, TIM1, aluminium housing and one cooling channel
per module is 1.12kW/l or 0.33kW/kg.

The parallel operation of the converter modules boosts the power density of
the drive by a factor of 1.714. Using TIM2 as a thermal interface material boosts
the power density by a factor of 1.51. The copper housing doesn't influence the
maximum current that can be injected by the converter modules and hence, it only
increases the weight of the drive without boosting the output power. Using three
cooling channels per module enhances the power density by a factor of 1.08. By
combining these power density boosting techniques, the power density is boosted
by a factor of 1.9.

The efficiency is compromised with the power density boosting. The normal-
ized efficiency in case of combined power density boosting techniques becomes
0.81.

Chapter 9

Reconfigurable Modular Fault-Tolerant Converter Topology for SRM Drives

9.1   Introduction

The switched reluctance motors (SRMs) have a rugged and modular stator pole construction. The absence of the windings and the permanent magnets in the rotor makes the SRMs more reliable and lighter compared to the other conventional machines [141]. The magnetic independence of the stator coils makes the SRMs excellent fault tolerant drives [142]. The airgap torque generated by this machine is proportional to the square of the coil current which makes them high starting torque machines which is an important feature for the traction applications. These excellent properties of the SRMs make them attractive and competitive in many applications such as hybrid electric vehicles (HEVs), generators in aircrafts and in wind turbines [143]- [144]- [145].

The main drawbacks of the SRMs are the high torque ripple and low torque/power density, low efficiency and acoustic noise [146]. The performance can be improved by advanced instantaneous torque control techniques [101]- [147], improved machine design [148]- [149] and novel converter topologies [150].

The torque ripple during phase commutation can be minimized by distributing the required torque over the ingoing and the outgoing phases instantaneously so that the summation of their produced torques remains constant and equal to the desired torque [105]. This method can be applied by using the torque sharing function (TSF) concept [103].

Several converter topologies are existing in literature for driving the SRM. The most commonly used topology is the asymmetric H-bridge owing to its low passive components requirement and modular construction [96]. Several asymmetric H-bridge based converter topologies with front-end converters for boosting the DC-

link voltage are proposed in literature [151]- [152]. Boosting the DC-link voltage can further improve the torque production of the SRM.

Multilevel converters derived from the asymmetric H-bridge are proposed in [153]- [141]. In [153], a multilevel converter with a front-end converter is presented, in which phase current rise and fall are accelerated without increasing the torque ripple. The drive efficiency is also improved by $2\%-4\%$. The addition of the front-end converter complicates the structure and results in a costly and more expensive structure. In [141], the performance of asymmetric three-level neutral point diode clamped converter is compared with a conventional asymmetric H-bridge. Lower current ripple, lower noise, and higher efficiency are obtained from the three-level converter. Since each leg in the three-level converter contains four power switches, the control is more complicated than the asymmetric H-bridge and the cost is higher.

Both conventional and modular driving techniques can be applied on the SRM [154]. In the conventional driving method, depending on the number of the stator poles, a number of stator coils are connected together to form one phase. This phase is driven from one asymmetric H-bridge. This driving technique has the advantage of small number of converter modules and better performance in the low speeds [155] but it lacks fault tolerance. Wider speed range and fault tolerant operation can be obtained with modular driving but on the cost of lower performance at low speeds [7].

To get the benefits of the conventional and the modular driving techniques, a reconfigurable converter topology is presented in this chapter. A unidirectional switch is added to the asymmetric H-bridge module in a way that makes it possible to reconfigure the converter to work in the conventional and the modular way by toggling this switch. The converter operation is studied by simulations and on an experimental setup.

9.2   Conventional versus Modular driving

The 6/4 SRM with the magnetic construction in Fig. 9.1 introduced in previous chapters is considered for studying the converter topology presented in this chapter. In the conventional driving method, each two diagonally opposite coils are connected in series and driven by one asymmetric H-bridge as shown in Fig. 9.2. In the modular driving method, each stator coil is driven from one separate asymmetric H-bridge as shown in Fig. 9.3.

Thanks to the magnetic independence of the stator coils, the total shaft torque can be synthesized from the torque pulses generated by each coil [96]. This feature makes it possible to obtain torque in case of fault in one coil or one converter module by controlling each coil from one separate converter (i.e. the modular driving method).
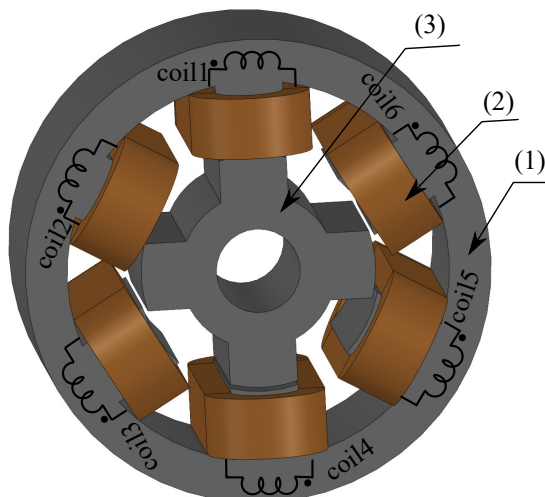
Figure 9.1: Magnetic construction of the 6/4 switched reluctance machine: (1) stator iron, (2) stator coils, (3) rotor iron. The stator coils are labelled coil1, coil2, coil3, coil4, coil5, coil6.
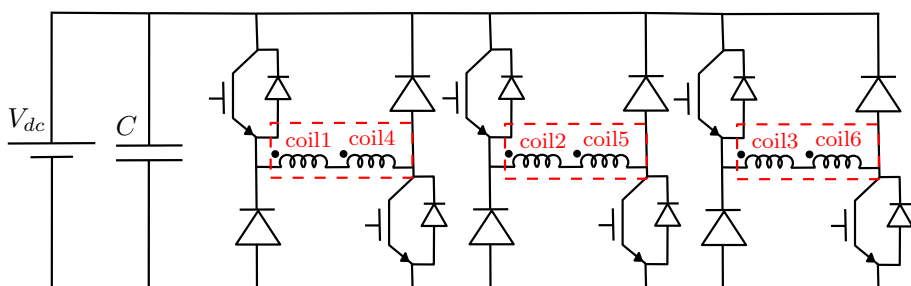
Figure 9.2: 6/4 SRM conventional driving method with the stator coils shown in Fig. 9.1.

9.3   Proposed converter topology

Although being valid for any SRM stator/rotor pole combination, the idea is illustrated on a 6/4 SRM case study. Fig. 9.4 (a) shows the proposed converter topology for the case study in Fig. 9.1. The basic building structure of the proposed converter for two diagonally opposite stator coils (i.e. coil1, coil4) is shown in Fig.
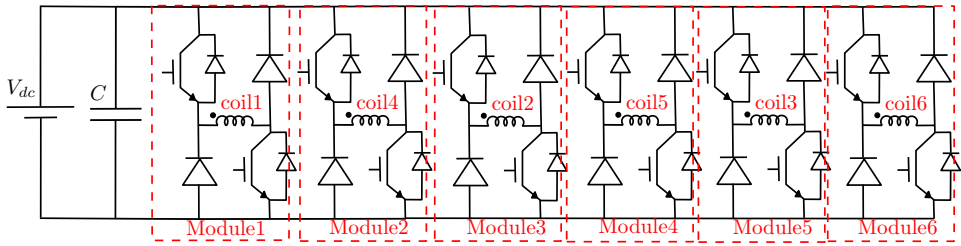
Figure 9.3: 6/4 SRM modular driving method with each module labelled in red.

9.4 (b). A unidirectional current switch is added to the asymmetric H-bridge. The switch consists of one MOSFET and one diode connected in series. The drain of the MOSFET is connected to one coil terminal and the cathode of the diode is connected to a terminal of the diagonally opposite coil. The proposed reconfigurable converter topology can be generally applied on a n_s coils SRM by implementing $\frac{n_s}{2}$ of the modular converter with the reconfiguration switch and $\frac{n_s}{2}$ modules without the reconfiguration switch.

9.3.1   conventional operation

In the conventional mode of operation, the MOSFET of the added switch is turned on to connect the diagonally opposite coils in series to form one phase of the machine. The control of that phase takes place by leg 1 and leg 4 while leg 2 and leg 3 stay off as illustrated in Fig. 9.5 (a). The added switch turns and stays on during the conventional mode of operation. Therefore, no switching losses take place in the added switch.

The pulse width modulation (PWM) signals of the main switches and reconfiguration switches and the output phase voltage in the conventional mode of operation are shown in Fig. 9.6. As the reconfiguration switches remain on in the conventional mode of operation, their duty cycle is set to unity. This results in series connection of coils (1,4) to form phase A, coils (2,5) to form phase B and coils (3,6) to form phase C. The duty cycles of the main switches of each phase designated (duty A, duty B, duty C) in Fig. 9.6 are compared to a carrier waveform with a frequency equal to the switching frequency of the converter to generate the switching pulses of the main switches. For example, the pulses designated (pulses A) in Fig. 9.6 are driving the power switches of leg1 and leg4 (the active legs) in Fig. 9.5 (a) to control phase A. The duty cycle of the power switches of the inactive legs shown in dashed grey in Fig. 9.5 (a) remains zero for all time of conventional mode of operation. The same but shifted pulse pattern is generated to drive phase B and phase C as shown in Fig. 9.6.

The shift angle between pulses of the phases (θ_{sh}) depends on the rotor pole

(a)

(b)
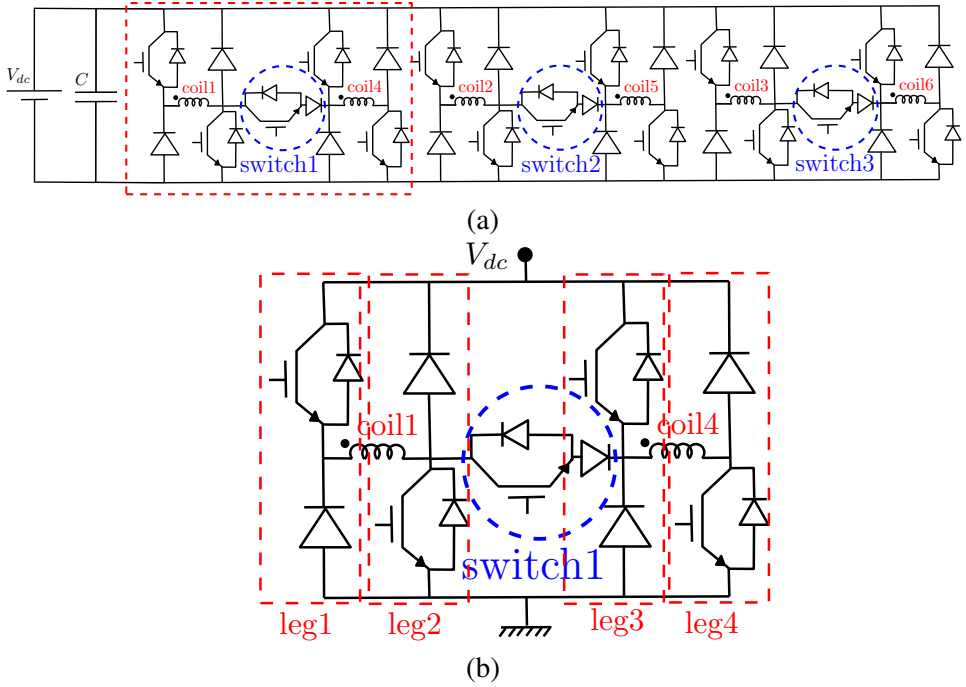
Figure 9.4: (a) Proposed reconfigurable SRM converter structure considering 6 stator coils machine with the added switches marked in blue and the basic building structure marked in red, (b) A zoom on the proposed converter structure for two diagonally opposite stator coils.

pitch and the number of phases. θ_{sh} can be calculated from (9.1). This angle is also shown in Fig. 9.6. It can be seen from Fig. 9.6 that the resulting output phase voltage is swinging between V_{dc} and -V_{dc} during the phase conduction period.

$$\theta_{sh} = \frac{360°}{P_r \times N_{ph}} \tag{9.1}$$

where P_r is the number of rotor poles and N_{ph} is the number of phases.

9.3.2   modular operation

In the modular mode of operation, the added switch is turned off and each coil is driven from one asymmetric H-bridge as shown in Fig. 9.5 (b).

The PWM signals of the main switches and reconfiguration switches and the output phase voltage in the modular mode of operation are shown in Fig. 9.7. The reconfiguration switches remain off in this mode, and hence, their duty cycle remains zero. The duty cycle of the main switches of each module designated (duty
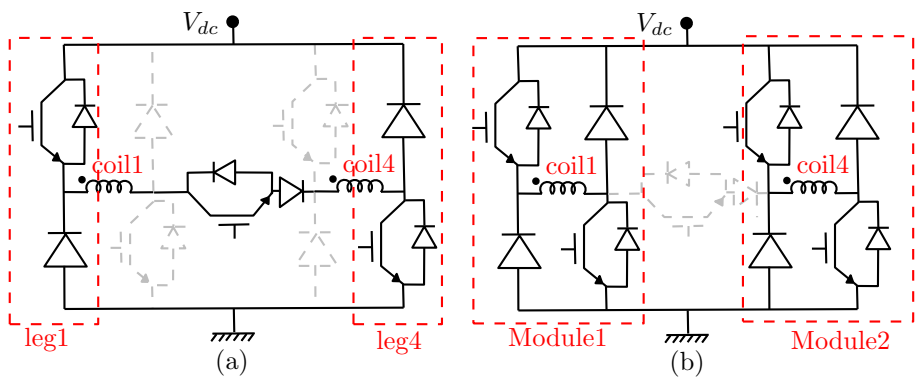
Figure 9.5: Configuration of the proposed converter in (a) conventional mode of operation, (b) modular mode of operation.
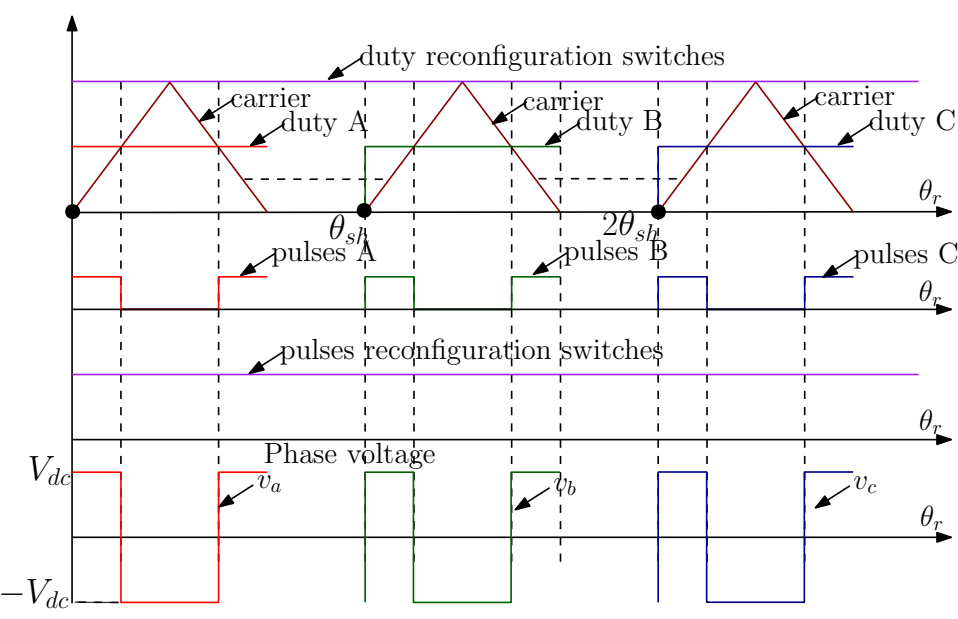
Figure 9.6: PWM signals of the main switches and reconfiguration switches and the output phase voltage in case of conventional operation. (duty A, duty B, duty C) are the duty cycles of the power devices of the active legs driving phase A, B and C respectively. θ_{sh} is the shift angle between pulses of the different phases. The waveforms of Phase A, B and C are shown in red, green and blue respectively.
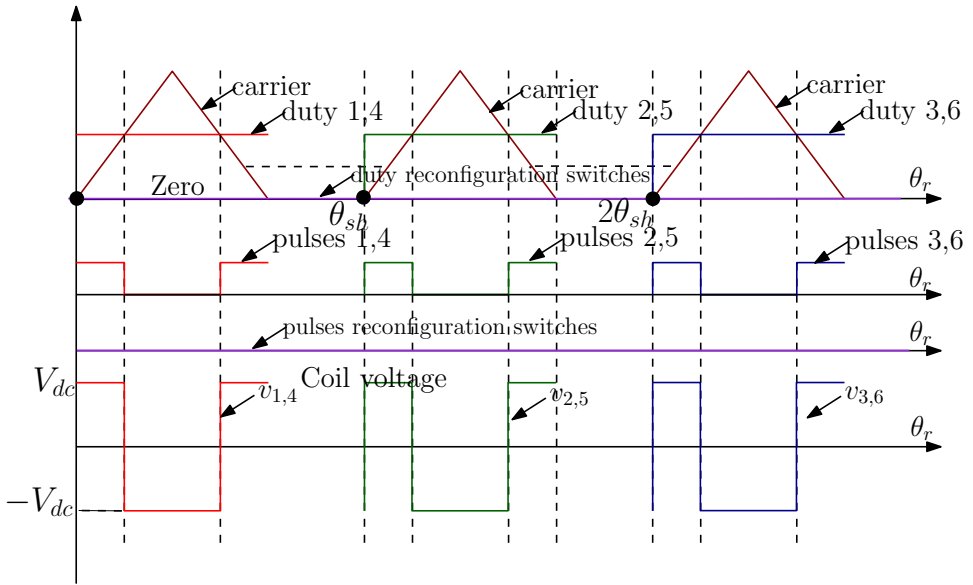
Figure 9.7: PWM signals of the main switches and reconfiguration switches and the output phase voltage in case of modular operation. (duty 1,4, duty 2,5, duty 3,6) are the duty cycles of the power devices of the modules driving coils (1,4), (2,5) and (3,6) respectively. θ_{sh} is the shift angle between pulses of the different phases. The waveforms of coils (1,4), (2,5) and (3,6) are shown in red, green and blue respectively.

1,4, duty 2,5, duty 3,6) in Fig. 9.7 is compared with a carrier waveform with a frequency equivalent to the switching frequency of the converter to generate the switching pulses of the main switches. The converter modules of each two diagonally opposite coils such as (Module1 and Module2) in Fig. 9.5 (b) are switched simultaneously as these coils see the same magnetic circuit at each rotor position. Therefore, the pulses of the main switches of these converter modules are the same. For example, pulses 1,4 shown in Fig. 9.7 are driving the main switches of Module1 and Module2 shown in Fig. 9.5 (b). The same but shifted pulse pattern is generated to drive (coils 2,5) and (coils 3,6). These pulses are designated (pulses 2,5) and (pulses 3,6) in Fig. 9.7. The shift angle is θ_{sh}. The resulting coil voltage is bipolar and swinging from V_{dc} to -V_{dc} as shown in Fig. 9.7.

9.4   Performance indicators of SRM drive

The same dynamic model of the closed loop torque controlled SRM presented in Chapter (3) section (3.6) is used to evaluate the performance of the SRM driven by

the proposed converter topology in Fig. 9.4 in each mode of operation.

The peak-to-peak torque ripple is one of the performance indices used to evaluate the performance of the SRM driven by the proposed converter topology in conventional, modular and faulty mode of operations. The peak-to-peak torque ripple $\hat{T}_e$ can be calculated from (9.2).

$$\hat{T}_e = 100 * \left(\frac{max\left(T_e(\theta)\right) - min\left(T_e(\theta)\right)}{\overline{T_e}} \right) \tag{9.2}$$

where $\overline{T_e}$ is the average torque.

The total converter losses are used as a performance index of the proposed converter in the conventional and modular mode of operation of the SRM. These losses are computed as explained in Chapter (4) section (4.2.1) considering the SiC switch C3M0075120J and the SiC diode LSIC2SD120C10.

Since the size of the DC-link capacitor C determines the size of the converter, the required DC-link capacitance for each driving technique should be determined. C is calculated from (9.3).

$$\begin{cases} C & = \frac{\Delta Q}{\Delta V} \\ \Delta Q & = \int i_c(t) \mid_{ch/disch} dt \end{cases} \tag{9.3}$$

where ΔQ is the amount of charge that the capacitor gains or loses every switching cycle, ΔV is the peak to peak capacitor voltage ripple, $i_c(t)$ is the capacitor current during charging or discharging. The capacitor is sized to have $\Delta V = 1\% V_{dc}$.

9.5 Simulation results

The SRM driven by the proposed converter topology in Fig. 9.4 is simulated the healthy and faulty condition in conventional and modular modes of operation. Fig. 9.8 shows the torque-speed range of the SRM considered for the study in this chapter in case of conventional and modular driving methods. This figure is generated at 800V DC-bus voltage and 4A rms rated coil current. As can be seen, the range of the speed that can be obtained at the rated torque is 5500 rpm in case of conventional driving and extended to 12000 rpm in case of modular driving.

The speed prolongation in case of modular operation results from the halved phase impedance in case of modular operation (one coil per phase in the modular case and two coils connected in series in the conventional case) for the same DC-link voltage (rated voltage of one coil). This means that the rated torque (rated current) can be obtained at higher speed (back-emf). This can be represented by (9.4).

$$i_x = \frac{v_x - v_{back}}{Z_x} \tag{9.4}$$
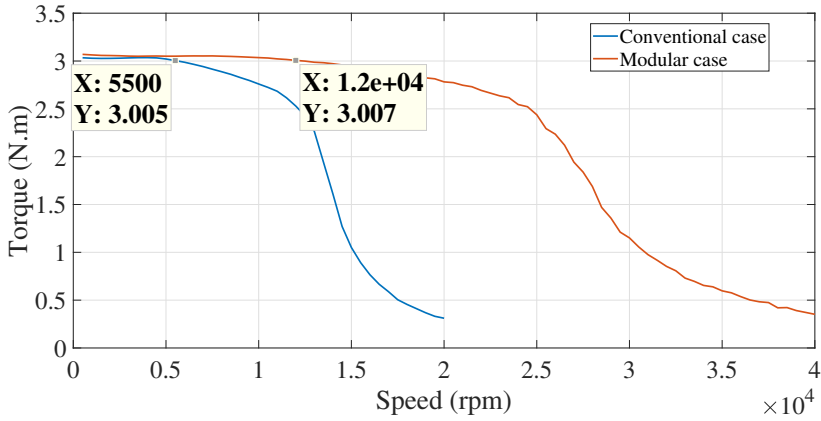
Figure 9.8: Torque-speed range of the 6/4 SRM in case of conventional and modular driving methods at 800V DC-bus voltage and 4A rms rated coil current.

where i_x is the phase current, v_x is the phase terminal voltage, v_{back} is the back-emf and Z_x is the phase impedance.

The simulation results reported in the following sections are obtained at the turn-on (θ_{on}) and turn-off (θ_{off}) angles that minimize the peak-to-peak torque ripple in (9.2). θ_{on} and θ_{off} are shown in Fig. 9.9 for the conventional, modular and faulty conditions for the full torque-speed range of each mode.

9.5.1 Healthy operation

The simulation results for healthy operation in the full speed range up to 12000 rpm are presented in this part.

Speeds < 5500 rpm

For the speeds lower than 5500 rpm, the converter can be configured to operate in either the conventional or the modular mode. The peak-to-peak torque ripple $\hat{T}_e(\theta)$, the total converter loss ($P_{convloss}$), the rms current of the DC-link capacitors (I_{crms}) and the required DC-link capacitance C are calculated up to 5500 rpm and 3Nm output torque for both the conventional and the modular driving modes.

Fig. 9.10 (a) and (b) show the peak-to-peak torque ripple for the conventional and the modular driving methods respectively. The peak-to-peak torque ripple in case of the modular driving is higher in the whole region of the torque-speed curve. The global maximum peak-to-peak torque ripple is 24% in case of conventional driving and 35% in case of modular driving. This can be explained as follows: the torque ripples of the SRM are the commutation ripples and the switching ripples.
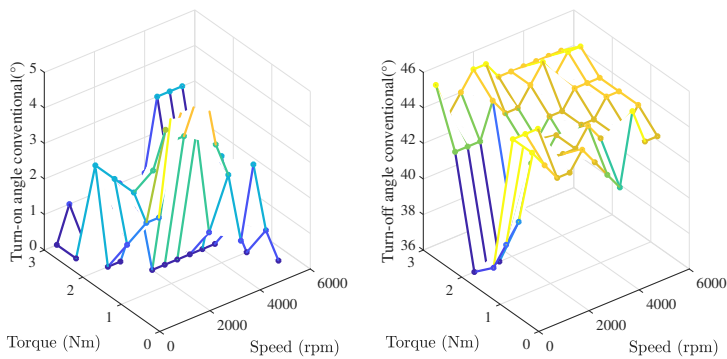
(a)
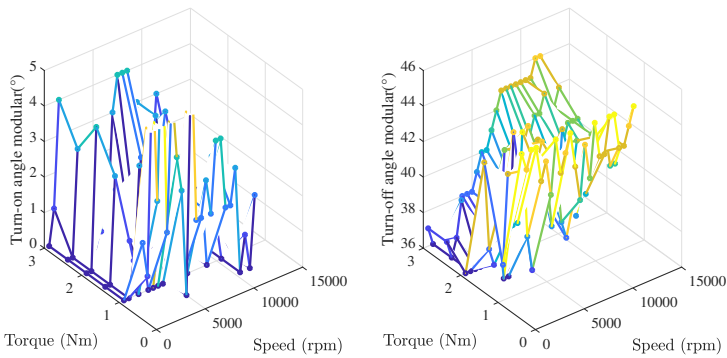
(b)
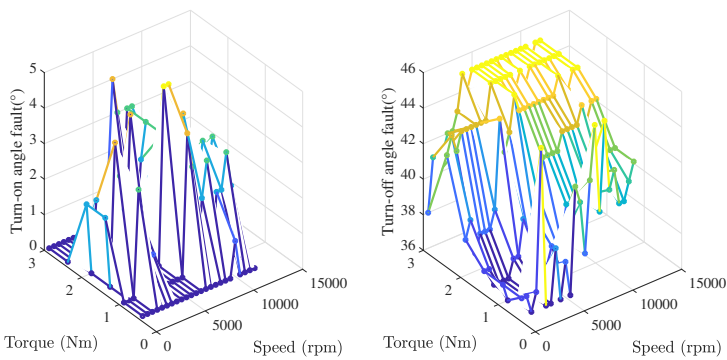
(c)

Figure 9.9: (a) Turn-on and turn-off angles in case of conventional mode of operation for full torque-speed range, (b) Turn-on and turn-off angles in case of modular mode of operation for full torque-speed range, (c) Turn-on and turn-off angles in case of faulty condition for full torque-speed range.

The commutation ripples occur due to the approximation error of the inverse torque function presented in Chapter 3 section (3.6). This approximation error increases with the current. As the current required for having certain torque in case of modular driving is expected to be higher than or at least equal the case of conventional driving, the commutation ripple is expected to be higher. Due to the smaller coil inductance in case of modular driving compared to the phase inductance in case of conventional driving, the switching current ripples, and hence, the switching torque ripples are expected to be higher.

(a)

(b)
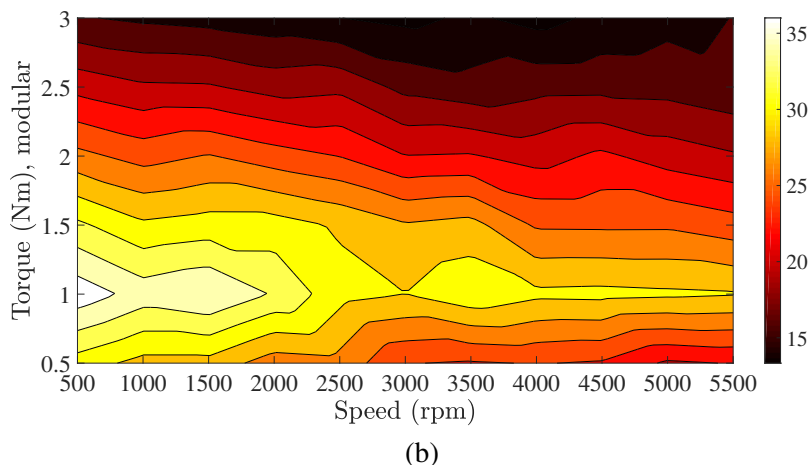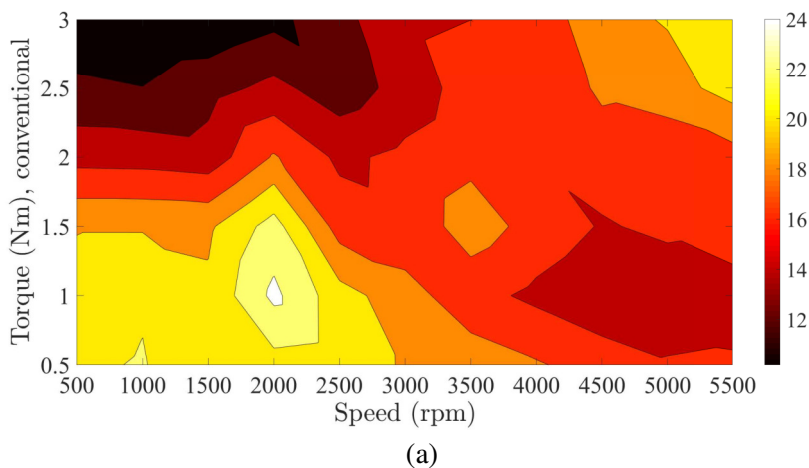
Figure 9.10: The peak-to-peak torque ripple in % of the SRM drive up to 5500 rpm in case of (a) conventional driving, (b) modular driving.

Fig. 9.11 (a) and (b) show the currents and the torques of the three phases in case of conventional driving at (3Nm, 5500 rpm). Fig. 9.12 (a) and (b) show the

currents and the torques of the six coils in case of modular driving at (3Nm, 5500 rpm). As can be noticed, the shaft torque is well tracking the reference torque with very small variation around the reference.

(a)

(b)
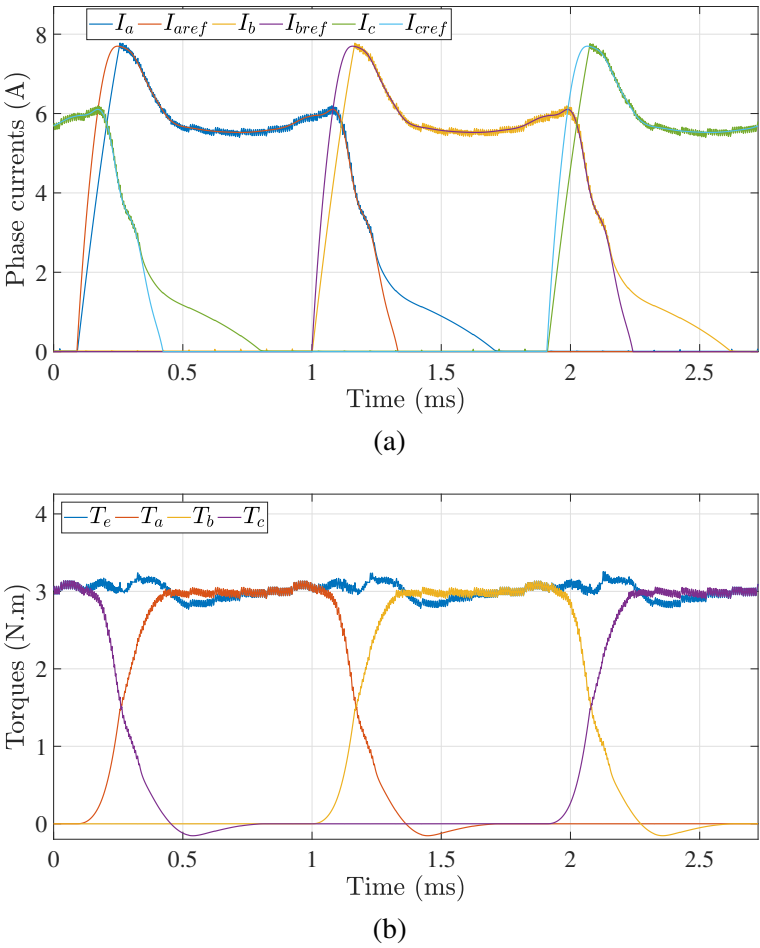
Figure 9.11: The phase currents (a) and torques (b) in case of conventional operation at 3Nm and 5500 rpm.

The shaft torque ripple has a high frequency component and a low frequency component. The high frequency component results from the switching action of the converter. It can be noticed from Fig. 9.11 and Fig. 9.12 that the high frequency ripples in case of conventional driving are smaller than the case of the modular driving due to the smaller coil inductance (one coil in case of modular driving) compared to the phase inductance (two-coils in series in case of conventional driving). The higher the inductance, the smoother the current, and hence,
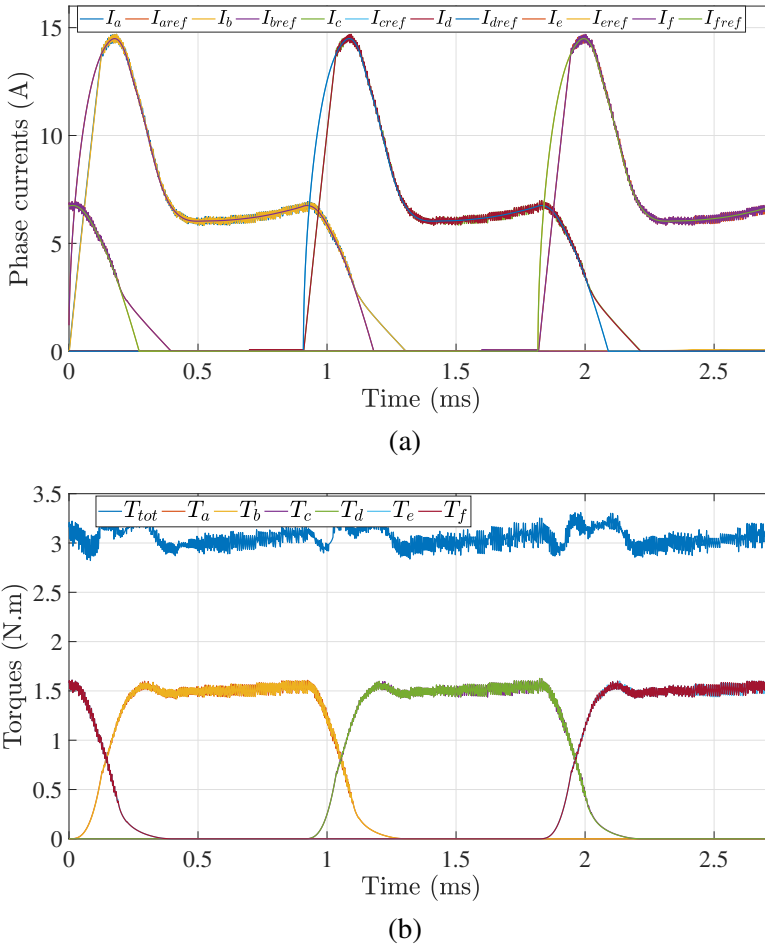
Figure 9.12: The phase currents (a) and torques (b) in case of modular operation at 3Nm and 5500 rpm.

the smoother the phase produced torque. The low frequency torque ripples result at the commutation moments due to the error in the calculated phase reference current from [107] and the actual required phase current. Another reason of the low frequency torque ripples is that the rate of change of the reference current at the beginning and the end of the phase conduction is higher than the maximum rate of change that can be achieved by applying the full DC-link voltage with unity duty cycle over the terminals of the windings. This results in some deviation between the reference current and the feedback current which in turn results in deviation in torque and torque ripples.

The total converter loss in case of conventional and modular driving is shown

in Fig. 9.13 (a) and (b) respectively. The total converter loss in case of modular operation is higher than double the losses in case of conventional operation. The reason behind that is the higher number of converter modules in case of modular driving switching the same or a bit higher current waveform as the conventional case.

(a)

(b)
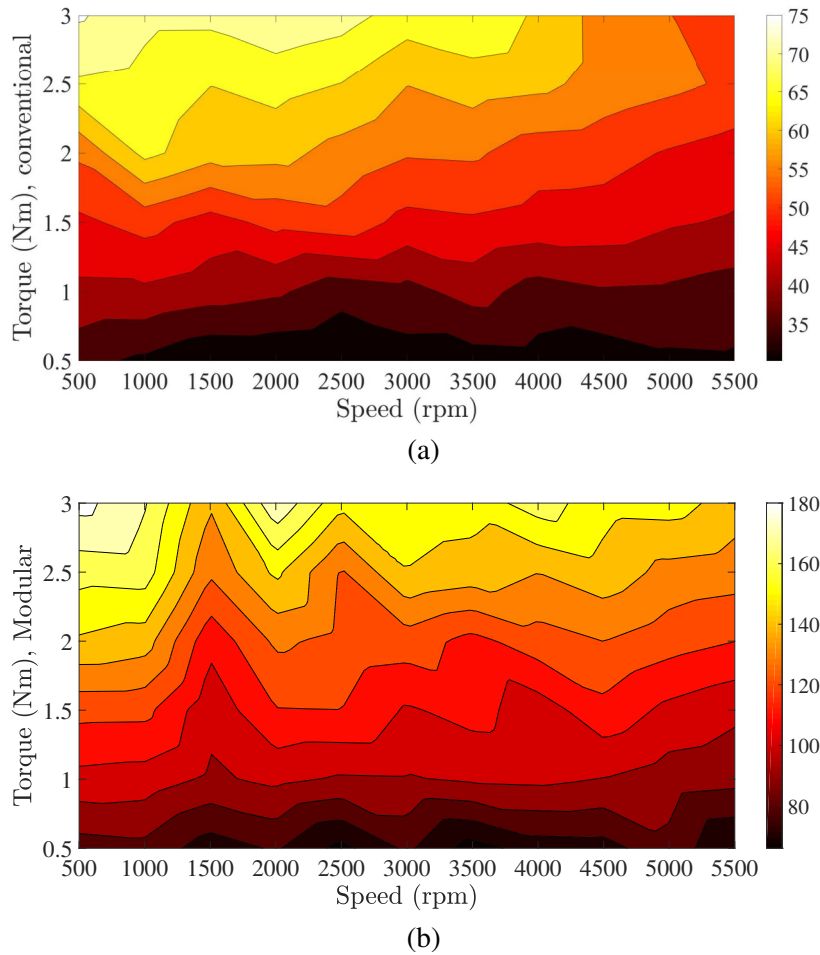
Figure 9.13: The total converter loss up to 5500 rpm (W) in case of (a) conventional driving, (b) modular driving.

The rms current of the DC-link capacitors for the conventional case and the modular case is shown in Fig. 9.14 (a) and (b) respectively. The required rms current rating of the DC-link capacitors in case of modular operation is double the value required in case of the conventional operation. The reason is the same as the one for higher converter loss in case of modular driving.

(a)

(b)
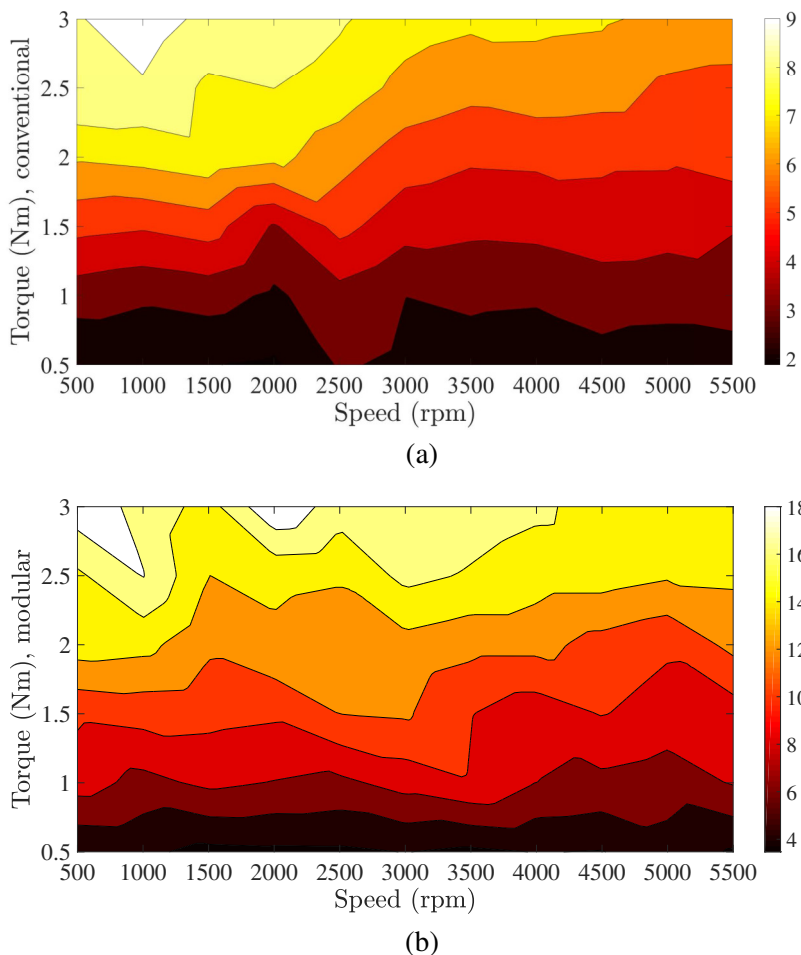
Figure 9.14: The rms current (A) of the DC-link capacitors in case of
(a) conventional driving, (b) modular driving.

The required DC-link capacitance for the conventional case and the modular
case is shown in Fig. 9.15 (a) and (b) respectively. The DC-link capacitance is
sized assuming 1% peak-to-peak DC-link voltage ripple. The required DC-link
capacitance in case of modular driving is double the value in case of conventional
driving because the DC-link current ripple in case of modular driving results from
the summation of six current waveforms instead of three, and hence, the DC-link
ripple current is expected to be its value at the case of conventional driving.

From the above analysis, for the speeds lower than 5500 rpm, the conventional
driving has much better performance than the modular driving.
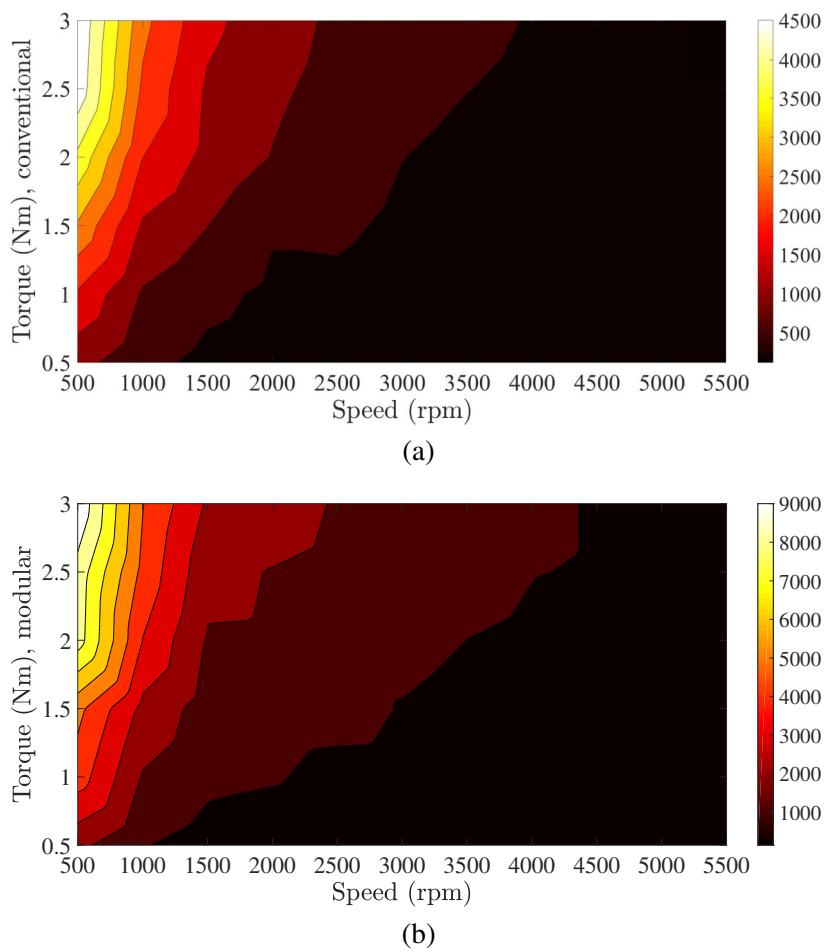
Figure 9.15: The required DC-link capacitance (μ F) in case of (a) conventional driving, (b) modular driving.

Speeds $>$ 5500 rpm

For the speeds $>$ 5500 rpm, the converter should operate in the modular driving mode. Fig. 9.16 (a), (b) and (c) shows the peak-to-peak torque ripple, the rms current of the DC-link capacitors and the converter loss in the speed range from 6000 rpm to 12000 rpm respectively. The performance of the modular driving at this speed range is much better than at lower speeds. So, by configuring the converter to operate in the conventional driving mode in the speeds lower than 5500 rpm and in the modular one for higher speeds, the worst case peak-to-peak torque ripple will be 26%, the highest converter loss will be 140W, and the highest DC-link rms current will be 15A.
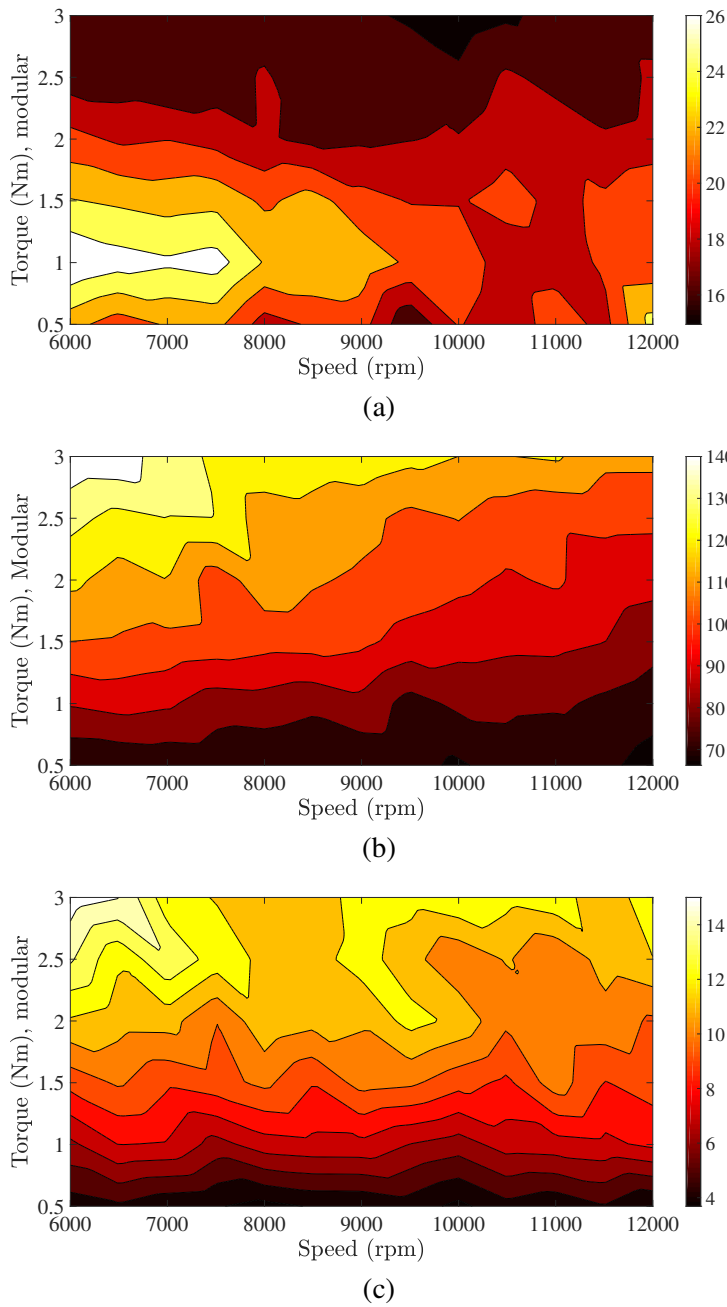
Figure 9.16: The performance maps for the speed range 6000 rpm to 12000 rpm: (a) The peak-to-peak torque ripple (%) map, (b) The total converter loss (W) map,(c) The DC-link capacitors rms current (A) map.

The reference and the feedback currents of the six phases at (3Nm, 12000 rpm) are shown in Fig. 9.17 (a). The torques of the six phases and the total shaft torque are shown in Fig. 9.17 (b). The torque ripples are caused at the phase commutation moments due to the approximations of the inverse torque function. The converter switching is also causing ripples.

(a)

(b)
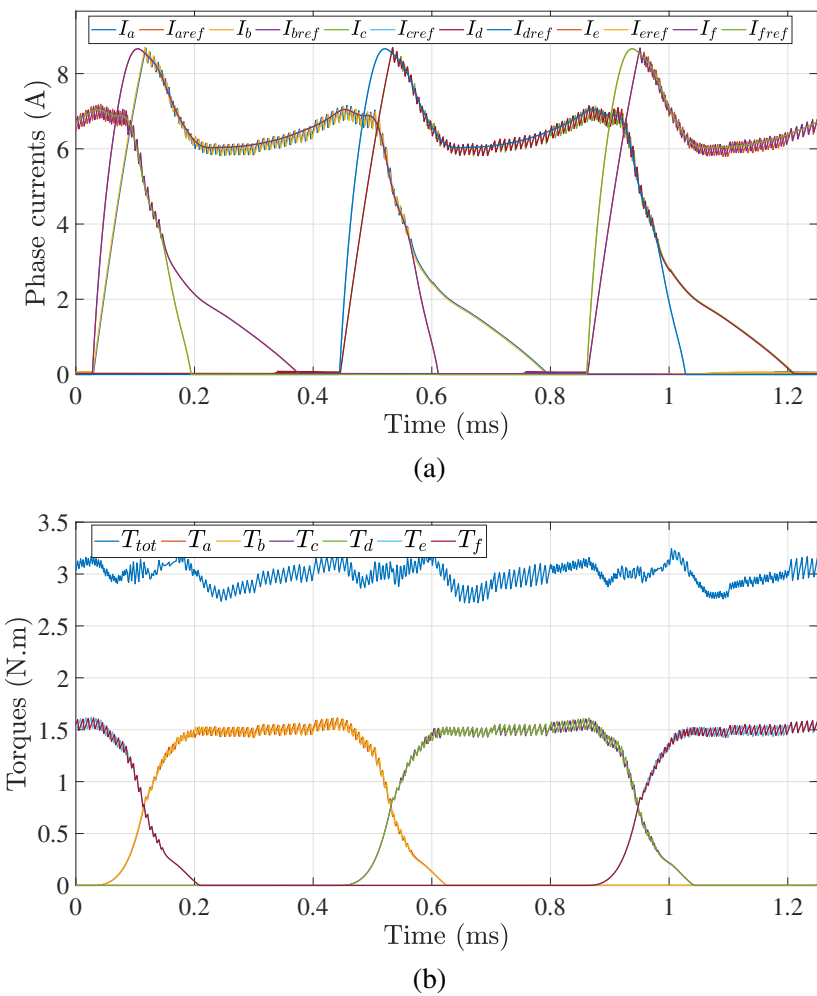
Figure 9.17: The phase currents (a) and torques (b) at 3Nm and 12000 rpm.

Modes transition

Fig. 9.18 (a) and (b) show the phase currents and torques at 3Nm and the speeds 5500 rpm and 7000 rpm. The converter reconfigures automatically at the time instant of 3 ms from the conventional mode of operation to the modular one. Smooth transition from the conventional to the modular mode can be noticed with continuous output torque.

(a)

(b)
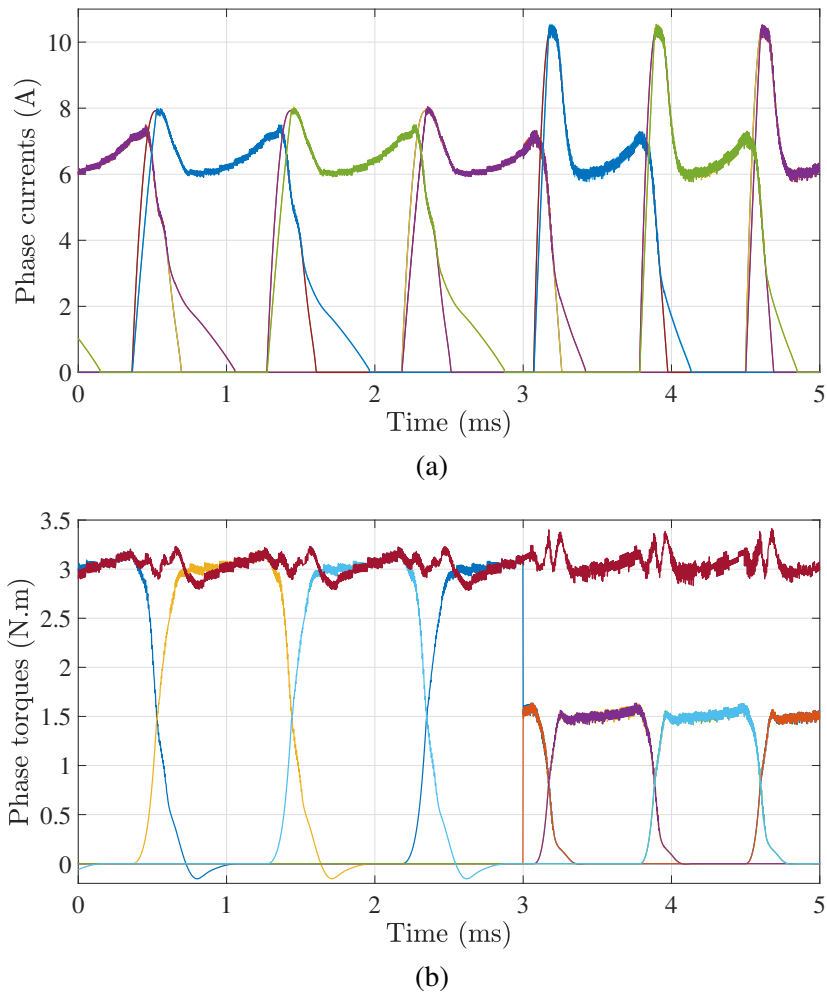
Figure 9.18: The phase currents (a) and torques (b) at 3Nm at the speeds 5500 rpm and 7000 rpm with the transition moment occurs at 3 ms.

9.5.2   Faulty operation

The proposed converter topology can tolerate the fault in one to three symmetrical coils and/or converter modules for example, coils (1,3,5) or coils (2,4,6)) and their corresponding driving converter modules (see Fig. 9.1). If a fault occurs in one coil or one converter module, the other coils/converter modules symmetrical with that coil/converter module are turned off for equal magnetic pull on the bearing [17] and the drive can continue working with the three remaining healthy coils/converter modules. Fig. 9.19 illustrates the converter configuration in case of fault in coil1 or/and coil3 or/and coil5 or any of their corresponding driving converter modules. All the reconfiguration switches and all the converter modules driving coils (1,3,5) are turned off. The required torque is produced from coils (2,4,6) only. But, to get the full output torque of 3Nm at faulty condition, the cooling system has to be re-designed to allow up to 8A rms coil current.
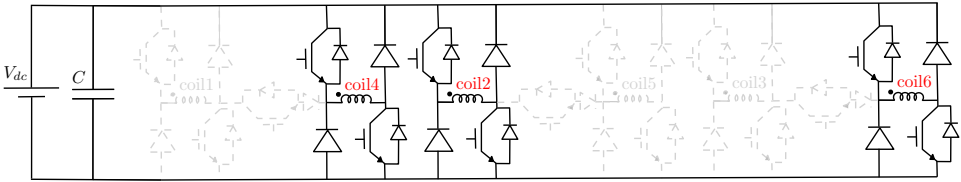
Figure 9.19: Configuration of the proposed converter in case of fault in coil1 or/and coil3 or/and coil5 or any of their corresponding driving converter modules.

The PWM signals of the main switches and reconfiguration switches and the output phase voltage in case of fault in coil1 and/or coil3 and/or coil5 or one of their associated driving converters are shown in Fig. 9.20. The reconfiguration switches remain off in this mode, and hence, their duty cycle remains zero. The duty cycle of the main switches of the converter modules driving the symmetrical healthy coils designated (duty 4, duty 2, duty 6) in Fig. 9.20 is compared with a carrier waveform with a frequency equivalent to the switching frequency of the converter to generate the switching pulses of the main switches of the converter modules. The pulses of the main switches of the converter modules driving coil4, coil2 and coil6 are designated pulses 4, pulses 2 and pulses 6 in Fig. 9.20. These pulses are the same but shifted by θ_{sh}. The duty cycle of the switches of the inactive modules (shown in dashed grey) in Fig. 9.20 remains zero until the fault is cleared. The resulting coil voltage of active symmetrical coils is bipolar and swinging from V_{dc} to -V_{dc} as shown in Fig. 9.20.

Fig. 9.21 (a) and (b) shows the phase currents and torques at 3Nm and 5500 rpm with the converter working in the conventional driving mode up to the moment of 2.7 ms. At 2.7ms, a short/open circuit fault (in both cases, the faulty coil is disconnected along with the other symmetrical coils) occurs in coil 1. The converter automatically disconnects coil 1, coil 3 and coil 5. The output torque of 3Nm can
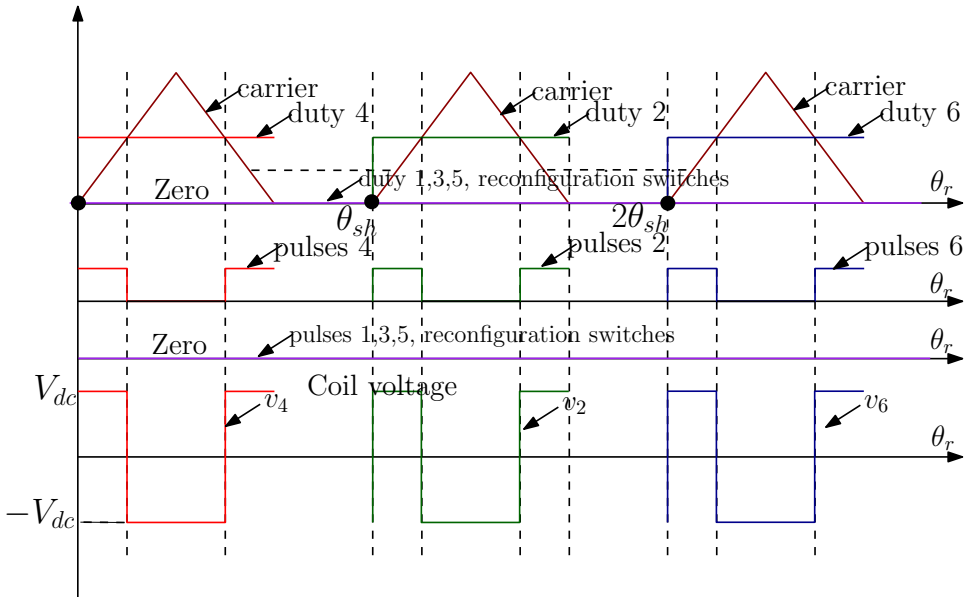
Figure 9.20: PWM signals of the main switches and reconfiguration switches and the output phase voltage in case of fault in coil1 and/or coil3 and/or coil5 or one of their associated driving converter modules. (duty 4, duty 2, duty 6) are the duty cycles of the power devices of the modules driving coils 4, 2 and 6 respectively. θ_{sh} is the shift angle between pulses of the different coils. The waveforms of coils 4, 2 and 6 are shown in red, green and blue respectively.

still be obtained from coils (2,4,6).

Fig. 9.22 (a) and (b) shows the phase currents and torques at 3Nm and 12000 rpm with the converter working in the modular driving mode up to the moment of 1.22ms. At 1.22ms, a fault occurs in coil 1. The converter automatically disconnects coil 1, coil 3 and coil 5. The output torque of 3Nm can still be obtained from coils (2,4,6) at that high speed but with higher torque ripples.

Fig. 9.23 shows the torque ripples in case of fault in one, two or three symmetrical coils/converter modules up to the rated torque of 3Nm and rated speed of 12000rpm. The maximum torque ripple is 40% occurring at rated torque and a high speed of 10500 rpm. It worth mentioning that with the fault-tolerance strategy proposed in this paper, the rated torque can still be obtained with a little bit higher torque ripple (40%) compared to the healthy case of (35%). This is an indication of the effectiveness of the fault-tolerance operation of the proposed converter.

Fig. 9.24 shows the map of the RMS current of the DC-link capacitors in case of fault in case of fault in one, two or three symmetrical coils/converter modules up to the rated torque of 3Nm and rated speed of 12000rpm. The maximum ca-
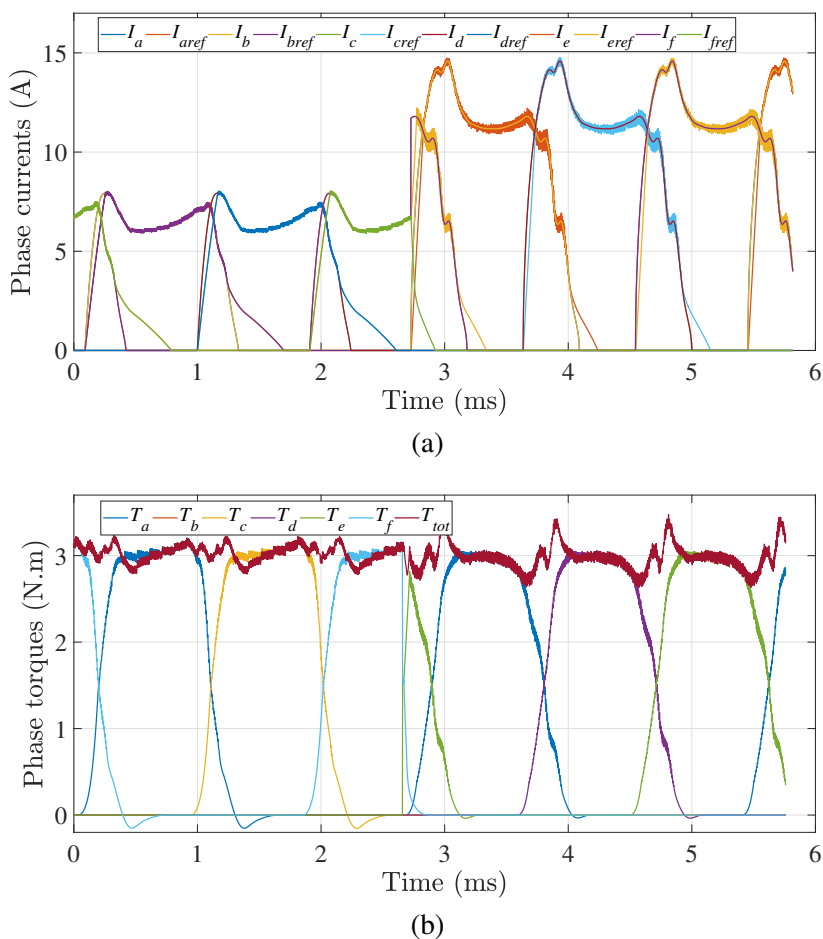
Figure 9.21: (a) Phase currents, (b) shaft and phase produced torques at 3Nm and 5500 rpm with a fault in coil 1 occurring at the moment of 2.7ms. This figure considers conventional mode of operation at healthy condition.

pacitor RMS current is 15A occurring at rated torque and 500 rpm. This value is even lower than the maximum DC-link capacitor rms current which is 18A in case of healthy modular operation. The value of the turn-on and turn-off angles are definitely influencing the RMS value of the DC-link current. The values of the turn-on and turn-off angles that minimize the torque ripple are different for the conventional, modular and faulty cases as shown in Fig. 9.9.
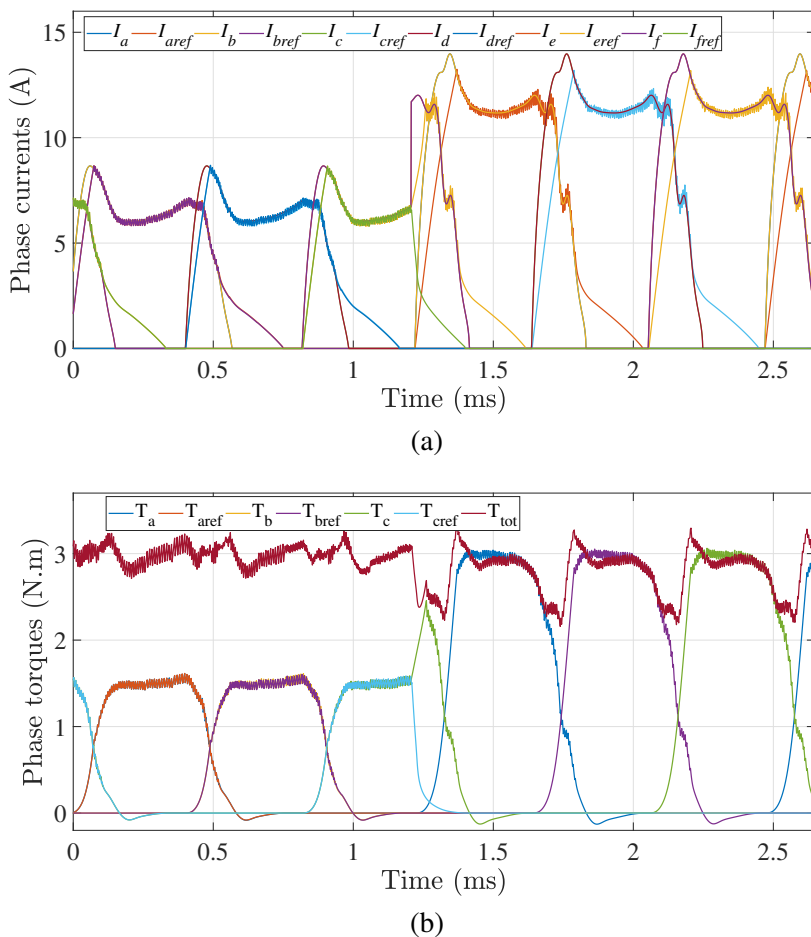
Figure 9.22: (a) Phase currents and (b) shaft and phase produced torques at 3Nm and 12000 rpm with a fault in coil 1 occurring at the moment of 1.22ms. This figure considers modular mode of operation at healthy condition (the only possible mode at this speed).

9.6 Experimental validation

Fig. 9.25 shows the pictures of the implemented asymmetric H-bridge modules with and without reconfiguration switches.

The polygon retrofitted SRM integrated setup explained in Chapter (6) section (6.4) is equipped with six asymmetric H-bridge modules. Half of them are implemented with reconfiguration switches (Fig. 9.25) (a) and the other half without (Fig. 9.25) (b). This setup is used to validate the simulation results of the reconfig-
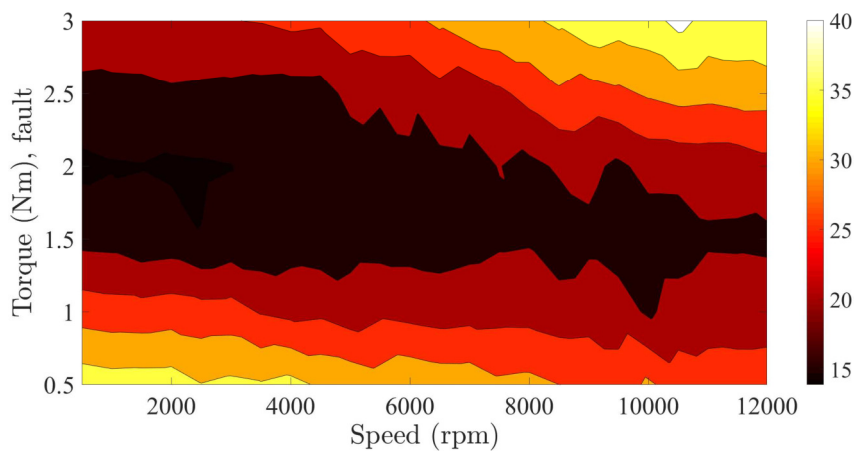
Figure 9.23: Peak-to-peak torque ripple map (%) in case of fault in one, two or three symmetrical coils/converter modules up to the rated torque of 3Nm and rated speed of 12000rpm.
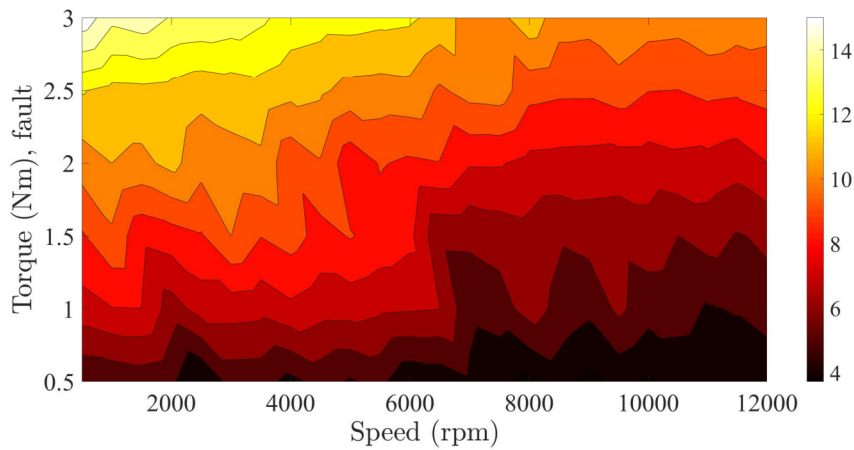
Figure 9.24: RMS current (A) of the DC-link capacitors in case of fault in one, two or three symmetrical coils/converter modules up to the rated torque of 3Nm and rated speed of 12000rpm.

urable asymmetric H-bridge.

9.6.1   Performance comparison

The performance of the drive in the conventional and the modular modes of operation is measured at (0.5,1,1.5,2) Nm shaft torque and 1000 rpm. The measured

(a)

(b)
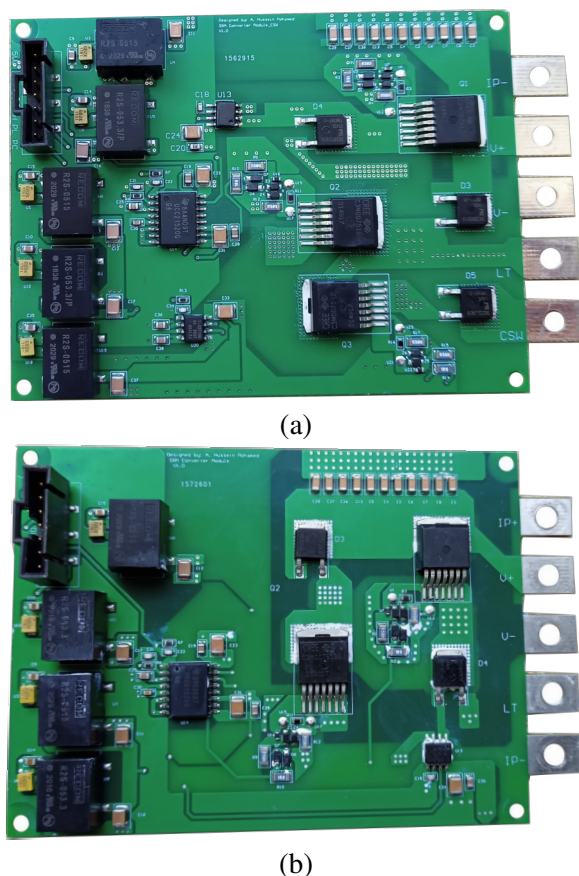
Figure 9.25: The implemented SiC based asymmetric H-bridge inverter module.(a) with reconfiguration switch, (b) without reconfiguration switch.

phase currents and torques are shown in Fig. 9.26 (a) and (b) for the conventional driving method at (2 Nm, 1000 rpm). Fig. 9.27 (a) and (b) shows the measured phase currents and torques in case of modular driving method at (2 Nm, 1000 rpm). From Fig. 9.26 (b) and Fig. 9.27 (b), the peak-to-peak torque ripple is 9.5% and 18.3% for the conventional and the modular driving methods respectively.

It can be noticed from Fig. 9.26 (a) and Fig. 9.27 (a) that the peak value and the steady-state value of the current required for each phase for producing 2 Nm torque in case of conventional driving are a bit lower than the peak value and the steady-state value of the current required for each coil to supply half of that torque in case of modular driving. This means that the change of the co-energy of a single coil with respect to the rotor position is half of the change of the co-energy of two diagonally opposite coils with respect to the rotor position. This relation depends

on the turn-on angle of both driving methods and the state of saturation of the magnetic circuit.

(a)

(b)
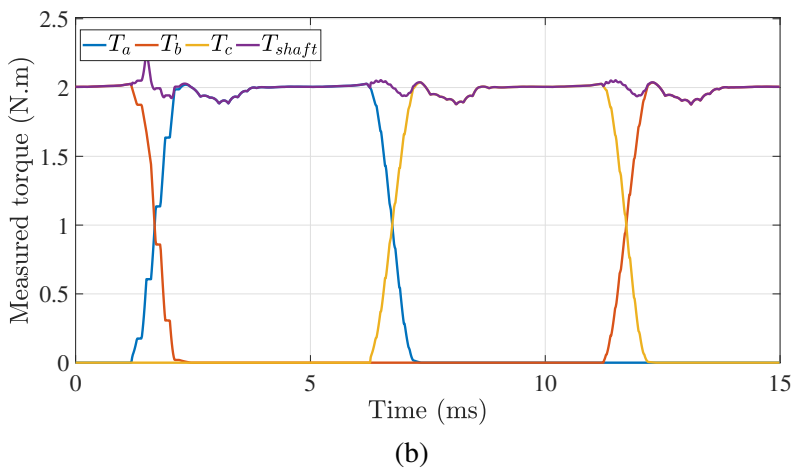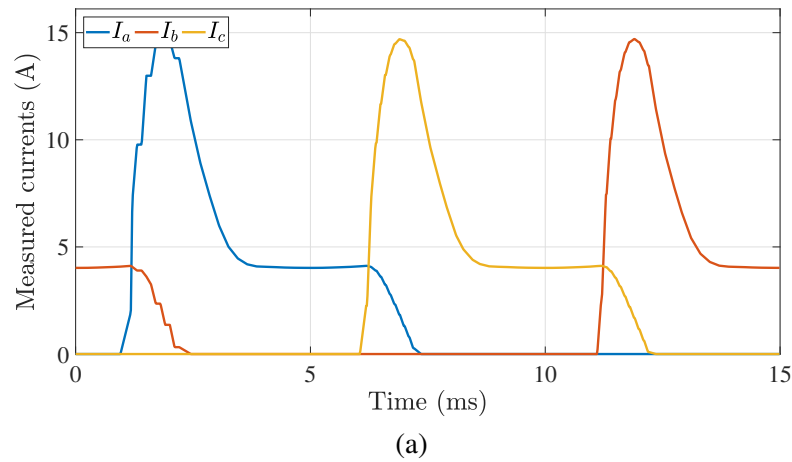
Figure 9.26: The measured phase currents (a) and torques (b) at 2 Nm and 1000 rpm in case of conventional driving.

The DC-link current waveforms for the conventional and the modular driving methods are shown in Fig. 9.28 (a) and (b). The rms of the DC-link ripple current is 5.26A and 9.2A for the conventional and the modular case respectively. The measured DC-link capacitors rms current in case of modular operation is 1.7 times higher than the conventional case.

The input DC-source power and the output shaft power at (2 Nm, 1000 rpm) are reported in Fig. 9.29 (a) and (b) respectively for the conventional driving method. The average input power is 436 W while the average output power is 208 W. The

(a)

(b)
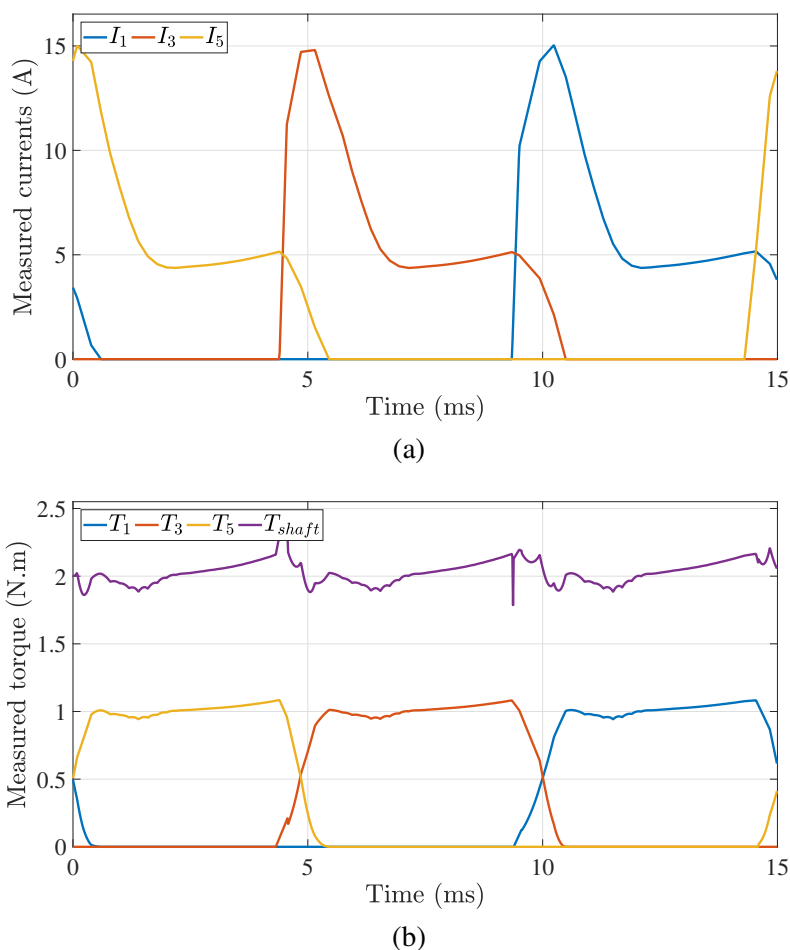
Figure 9.27: The measured coil currents (a) and torques (b) at 2 Nm
and 1000 rpm in case of modular driving.

total drive loss is 228 W.

The input DC-source power and the output shaft power at (2 Nm, 1000 rpm)
are reported in Fig. 9.30 (a) and (b) respectively for the modular driving method.
The average input power is 667 W while the average output power is 213 W. The
total drive loss is 454 W.

Table 9.1 contains the measured values of the peak-to-peak torque ripple, the
DC-link capacitor rms current and the total drive loss values at 1000 rpm and the
torque values (0.5,1,1.5,2) Nm for both the conventional and the modular driving
techniques. It is observed from the measurement values that the performance of
the conventional driving method is much better than the modular one. The main

(a)

(b)
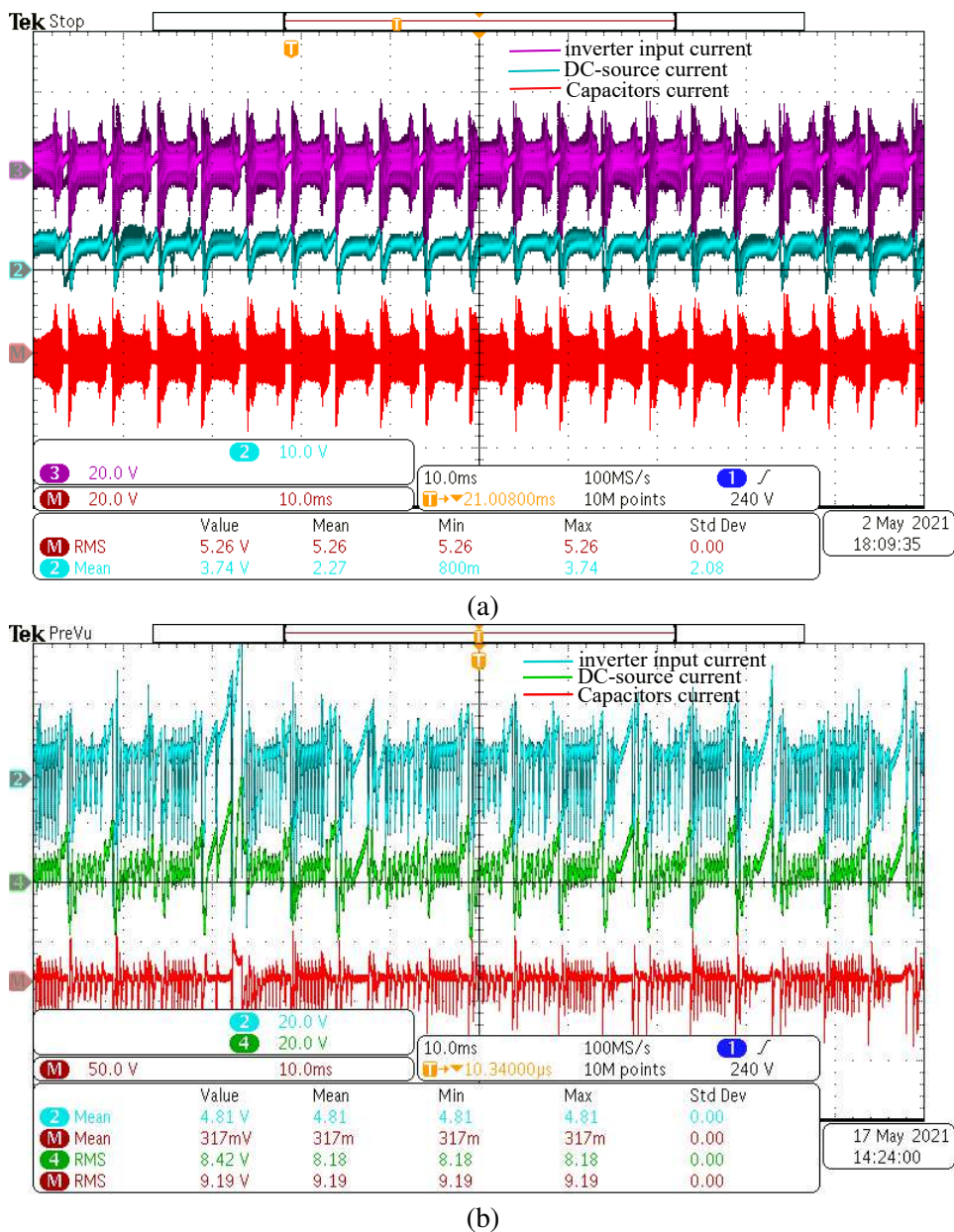
Figure 9.28: The measured DC-link currents at 2 Nm and 1000 rpm
(a) conventional case b) modular case.

reason behind that is the switching of similar but double the number of the current
waveforms needed in the conventional case.

(a)

(b)
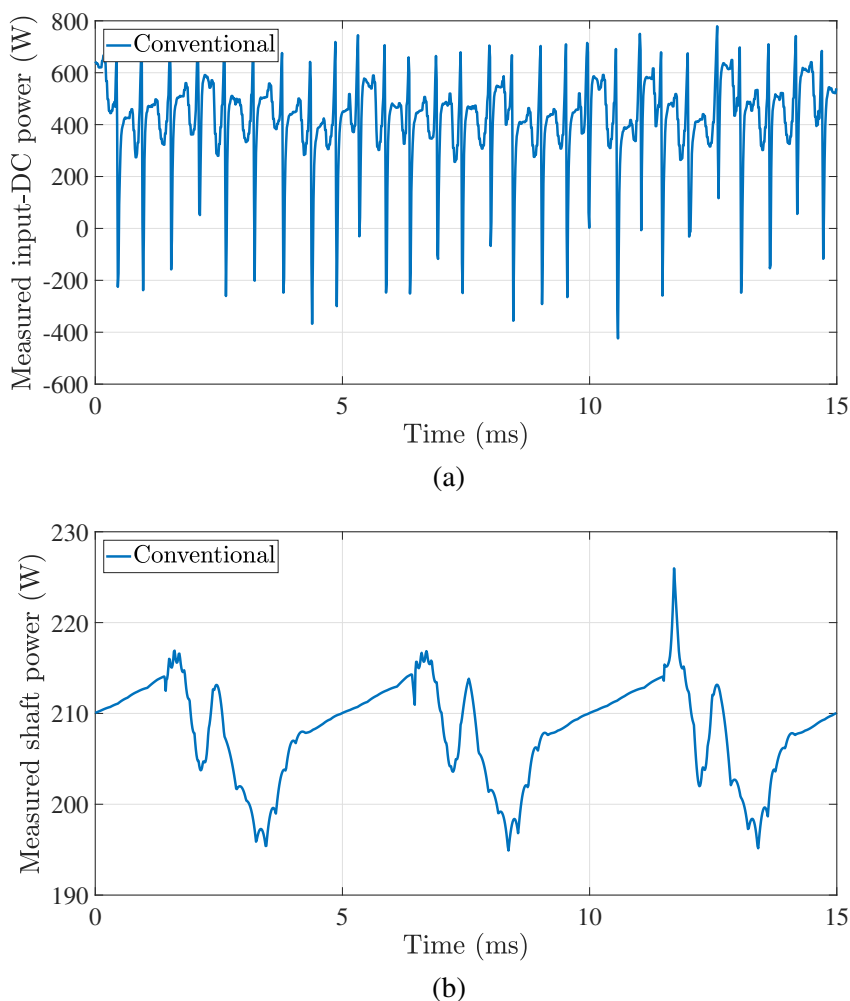
Figure 9.29: The measured input DC-source power (a) and the measured shaft power (b) at (2 Nm, 1000 rpm) for the conventional driving method.

9.6.2   Transition performance

The measured phase currents at (0.5 Nm, 1000 rpm) are shown in Fig. 9.31 with modular healthy operation from 0 to 15 ms and faulty operation with three working coils from 15 ms to 30 ms. It can be noticed that the fault occurs during the conduction of only one phase and the current transitions rapidly at the fault moment. As the fault occurs in a position and at a current at which the core is saturated and the phase inductance is small, fast current transition can be noticed. A higher coil
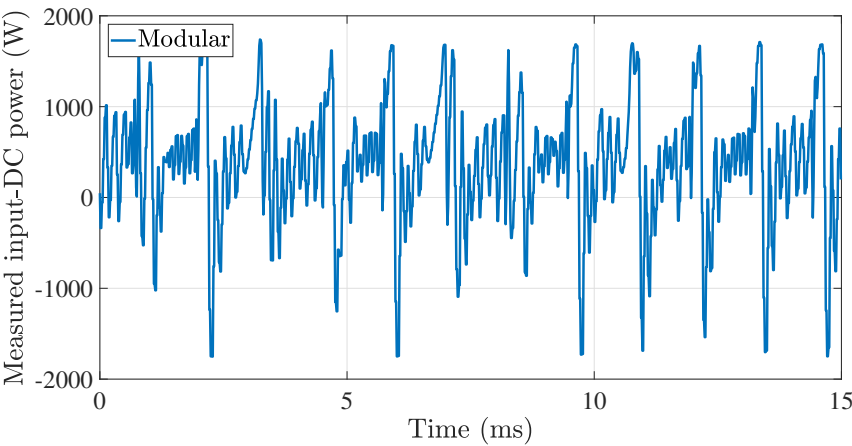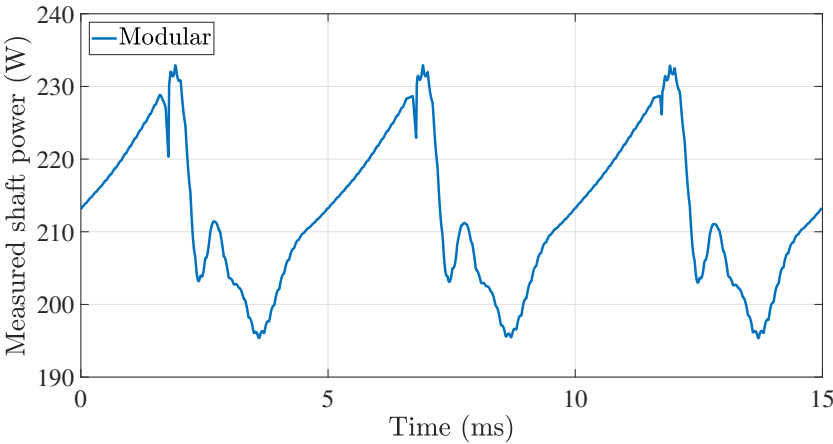
Figure 9.30: The measured input DC-source power (a) and the measured shaft power (b) at (2 Nm, 1000 rpm) for the modular driving method.

current results in case of fault as each coil is required to produce double the torque needed in case of healthy operation.

A picture for the scope visualized coil current and input power in case of fault mode at (0.5 Nm, 1000 rpm) is shown in Fig. 9.32. The switching ripples of the coil current can be noticed. These ripples are not detected by the dSpace sampled waveform as the current is sampled with a rate equal to the PWM frequency.

The measured phase torques at (0.5 Nm, 1000 rpm) are shown in Fig. 9.33 with modular healthy operation from 0 to 15 ms and faulty operation with three

Table 9.1: Performance comparison at 1000 rpm and different shaft torques for the conventional and the modular driving methods

Torque (Nm)	Conventional			Modular		
	Torque ripple (%)	Capacitor rms current (A)	Drive loss (W)	Torque ripple (%)	Capacitor rms current (A)	Drive loss (W)
0.5	14.7	1.92	87.5	21.7	4.35	181
1	14.7	2.82	125	23.34	5.92	217
1.5	13.3	3.52	179.5	20.34	7.5	355
2	9.5	5.26	228	18.5	9.2	454
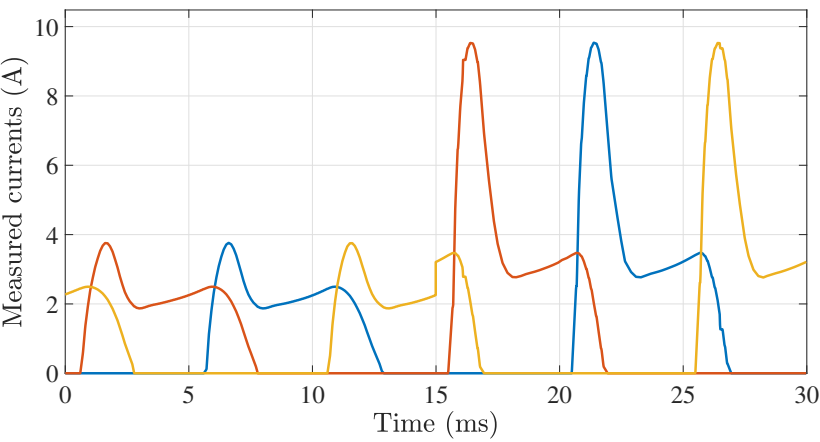
Figure 9.31: The measured coils currents at (0.5 Nm, 1000 rpm) with modular operation until 15 ms and faulty operation from 15 ms to 30 ms.

working coils from 15 ms to 30 ms. The peak-to-peak torque ripple increases from 21.7% in case of healthy operation to 34.5% in case of faulty operation.
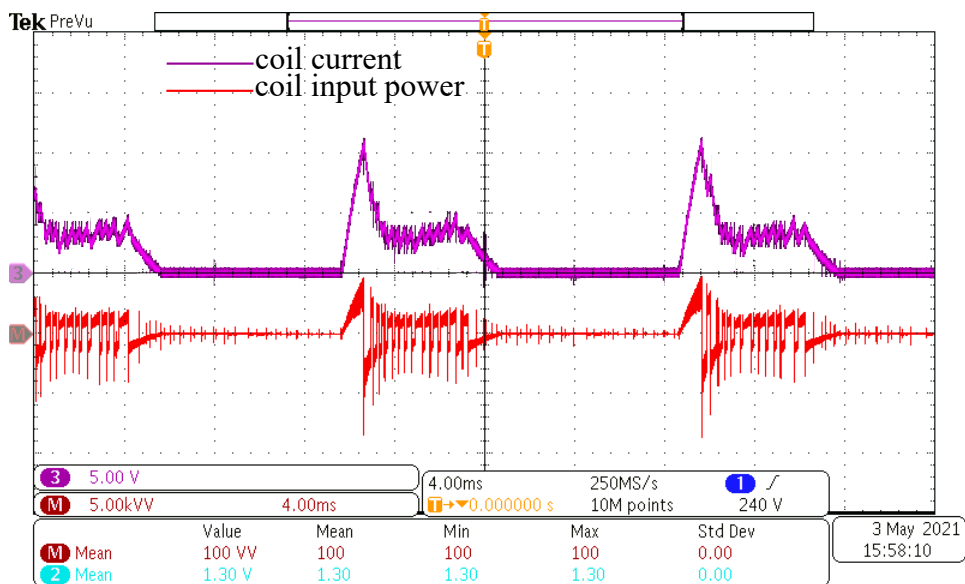
Figure 9.32: The measured coil current and input power at (0.5 Nm, 1000 rpm) with faulty operation.
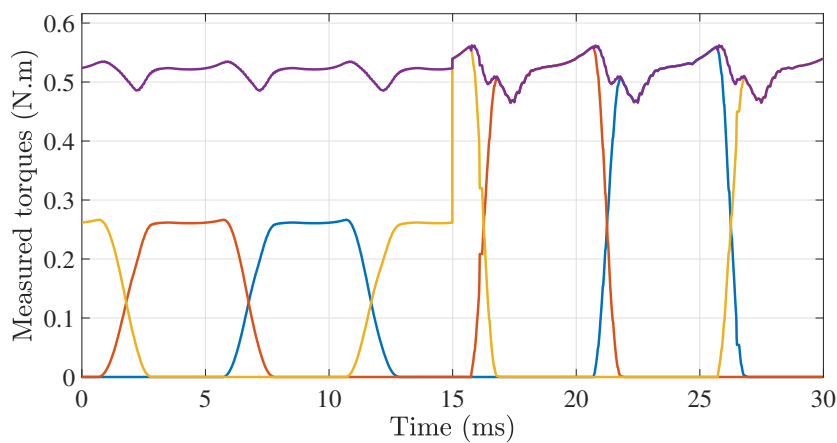
Figure 9.33: The measured coil torques at (0.5 Nm, 1000 rpm) with modular operation until 15 ms and faulty operation from 15 ms to 30 ms.

9.7 Conclusion

In this chapter, a reconfigurable converter topology for SRMs is proposed. The topology can be configured to work in the conventional and the modular driving ways so that the benefits of both driving methods can be obtained. The conventional driving method is applicable in low speed ranges with better performance in terms of torque ripple (11% lower than the modular method), the rms current ripple of the DC-link capacitors (50% lower than the modular method), and the total converter losses (58% lower than the modular case).

In the modular mode, the speed range of the constant torque region of the SRM is extended to double the value that can be reached with the conventional method. In low speeds with conventional driving, the maximum peak-to-peak torque ripple is 24%, the maximum converter loss is 75 W and the maximum rms current of the DC link capacitors is 9 A.

In high speeds with modular driving, the maximum peak-to-peak torque ripple is 2% higher than the corresponding one in the conventional mode of operation, the maximum converter loss is 1.9 times higher than the corresponding one in the conventional mode of operation, the maximum rms current of the DC link capacitors is 1.6 times higher than the corresponding one in the conventional mode.

The converter can tolerate the fault in one to three symmetrical stator coils and/or converter modules. In case of fault, the converter can still supply the rated torque if the cooling of the machine allows for double the rms current in case of healthy operation. Smooth transition from conventional and modular mode of operation to the fault mode of operation is noticed. The simulation results are validated by experimental measurements.

Chapter 10

Conclusions and Future Work

10.1   Conclusions

This thesis focuses on the modelling and design of novel integrated modular motor drive (IMMD) topologies. Two novel IMMD topologies are proposed, extensively modelled and applied on two different electric machines: a yokeless and segmented armature (YASA) axial flux permanent magnet synchronous machine and a switched reluctance machine (SRM). For the two topologies, prototypes are built and extensive experimental measurements are conducted.

The first topology for which the integration methodology is studied, is the YASA machine. The idea of the integration topology applied on the YASA machine is to redesign the housing of the machine by replacing the outer circular cross-sectional area by its circumscribing polygon. By doing this step, a flat surface extending in the axial direction is created. This flat surface is utilized in mechanical mounting of the converter modules. Now, the heat generated by the electric machine flows radially outward and the heat generated by the converter modules flows radially inward. To decouple this heat, a cooling channel is introduced in the designed shared cooling structure through which a cooling fluid is pumped. The heat generated by the machine and the power converter is evacuated by the cooling fluid. This integration topology is named circumscribing polygon (CP) integration topology.

Electromagnetic and thermal models of the YASA and its GaN based integrated half-bridge inverter are crucial for optimal design of the CP drive. Analytical electromagnetic models developed by former PhD colleagues for the YASA machine are used. Both Finite element and lumped parameter thermal network (LPTN) models are built for the YASA machine. The LPTN model provides much faster solution for the temperature field than the finite element model while maintaining a good accuracy. These models are used to select the optimal geometrical parameters of the YASA machine. Average and instantaneous loss models are built for the GaN switch. Electromagnetic and thermal finite element models are developed for

the GaN half-bridge module. These models are used for optimal design of the half-bridge inverter module. The instantaneous losses and junction temperature of the inverter module are evaluated. A temperature difference of a few degrees Celsius between the peak and the average junction temperature is noticed. This difference results mainly from the large instantaneous switching losses during short time intervals in the fundamental period.

A CP integrated YASA drive is built to validate the integration concept and the developed models. The experimental measurements prove the validity of the CP integration concept and the built models.

The volumetric and the mass power density of the CP integrated YASA drive are computed and several optimization techniques are proposed to boost the power density. These techniques incorporate the optimal selection of the integrated module materials and the optimization of the geometry. The proposed optimization techniques boosted the power density by a factor 2 from 1.12 kW/litre to 2.14 kW/litre. A compromise between the power density and the efficiency is noticed. The efficiency of the CP integrated drive reduces by 18.5% after doubling the power density.

A novel integrated DC-link structure is designed for the CP integrated YASA drive. This DC-link structure combines both the bus-bar and the capacitors, and nevertheless doesn't increase the outer diameter of the integrated machine/converter drive. Electromagnetic and thermal finite element models have been built for this DC-link structure. Using the electromagnetic model, the parasitic parameters of the bus-bar are extracted. It is shown that the designed bus-bar structure has a small per module AC parasitic inductance of and a relatively higher DC inductance. This small AC inductance reduces the overall commutation loop inductance which means lower voltage spikes on the switch during commutation. The relatively higher DC inductance is smoothing the input DC-current, which reduces the electrical stresses on the input source. Using the electromagnetic model of the bus-bar, the loss density distribution over the bus-bar is computed. It is shown that the highest loss density occurs at the input DC-terminals. The temperature distribution over the bus-bar is calculated using the thermal model. A hot-spot is noticed at the input terminals. This hot-spot can be eliminated by distributing several input terminals around the bus-bar instead of concentrating them at one position along the circumference. An analytical design methodology for the DC-link capacitors is provided. The DC-link structure design is validated by experimental measurements.

The second topology for which the integration methodology is studied, is the SRM. The idea of the integration topology applied on the SRM is to design a 3D aluminium part with outer flat surface for mounting of the converter module PCB and an inner cylindrical surface. The part's inner surface is designed in such a way that it is retrofitted with the already existing water jacket cooled SRM. The heat generated by the SRM and the heat generated by the converter modules are both flowing radially towards the water jacket. The equivalent convection coef-

ficients over the SRM's outer surface and the 3D aluminium part's inner surface are computed using CFD simulations. This integration concept is named polygon retrofitted (PR) integration concept.

A dynamic simulation model is built for the whole SRM drive. This model includes the SRM, the asymmetric H-bridge converter and the closed loop controller. The instantaneous torque control is implemented using sinusoidal torque sharing function (TSF). This model is built to compute the exact current waveform of the SRM windings and the converter power devices. These current waveforms are used as input to the electromagnetic model of the SRM and the loss model of the asymmetric H-bridge.

Both electromagnetic and thermal models for the SRM and its asymmetric H-bridge driving converter modules are required for the study of the PR integrated SRM drive. An electromagnetic finite element model is built for the SRM. It is found that the magnetic field density is unipolar in the stator pole and DC-biased bipolar in the rest of the stator and rotor core. The frequency of the magnetic flux density waveform in the stator core is the same as the excitation current frequency. The frequency of the magnetic flux density in the rotor equals the excitation current frequency divided by the number of rotor poles. The flux density achieves the highest local values on the rotor and stator pole sides. The highest local core loss density is noticed on the sides of the rotor poles. The total loss in the stator core is higher than the total loss in the rotor core due to the smaller mass of the rotor. Both 3D thermal finite element model and LPTN model are built for the SRM. Good agreement between the results of both of them is observed. It is noticed that at the beginning of the SRM heat-up, the heat transfers from the stator to the airgap then to the rotor until the steady-state moment of the stator windings. After that, the rotor temperature rises above the airgap temperature and the heat transfer direction becomes from the rotor to the airgap and then to the stator. For the asymmetric H-bridge, a temperature difference of a few degrees Celsius between the peak and the average junction temperature of the switch and the diode is noticed due to the large instantaneous switching losses.

A PR integrated SRM setup is built to validate the integration concept and the modelling of the integrated drive. The measurements prove the validity of the integration concept and the introduced modelling.

A final contribution of the PhD is a novel converter structure capable of reconfiguring the SRM machine to work either in the conventional or in a modular driving mode. The conventional driving method provides better performance of the SRM in terms of efficiency and torque ripple compared to the modular mode of operation. Nevertheless, the conventional mode of operation doesn't provide fault-tolerance capability. Therefore, switching from the conventional to the modular mode of operation is needed in case of faults. A smooth transition from conventional to modular mode using the proposed converter structure is observed. The converter is capable of tolerating a fault in one converter module or one stator phase. In addition, a smooth transition from the healthy mode of operation to the

faulty mode of operation using the proposed converter structure is observed. The converter performance is validated by experimental measurements.

10.2   Future Work

This work was focusing on the modelling and design of two novel integrated modular motor drives for a YASA axial flux machine and a switched reluctance machine. A novel integrated DC-link structure for the YASA drive is designed. A novel reconfigurable fault-tolerant converter topology is also designed. The following research topics are suggested for further study of the two introduced integrated modular motor drives.

A reconfigurable fault-tolerant converter topology can be designed for the integrated YASA drive so that it can be used in safety critical applications like electric vehicles.

An integrated DC-link structure for the polygon retrofitted SRM drive can be designed to further reduce its electromagnetic noise and to have a completely integrated drive.

The electromagnetic interference (EMI) performance of both the circumscribing polygon and the polygon retrofitted integration topologies can be studied.

Different inverter topologies such as current source inverter and multi-level inverter can be studied for integration with the YASA machine.

Advanced cooling techniques such as pumped two-phase cooling can be considered to further increase the power density of integrated modular motor drives.

Bibliography

[1] A. M. El-Refaie, "Integrated Electrical Machines and Drives: An Overview," in *2015 IEEE International Electric Machines & Drives Conference (IEMDC)*. IEEE, Feb 2016, pp. 350–356.

[2] R. Abebe, G. Vakil, G. L. Calzo, T. Cox, S. Lambert, M. Johnson, C. Gerada, and B. Mecrow, "Integrated motor drives: State of the art and future trends," *IET Electric Power Applications*, vol. 10, no. 8, pp. 757–771, 2016.

[3] M. Maerz, M. Poech, E. Schimanek, and A. Schletz, "Mechatronic Integration into the Hybrid Powertrain-The Thermal Challenge," *International Conference on Automotive Power Electronics (APE)*, pp. 1–6, 2006.

[4] M. Maerz, E. Schimanek, and M. Billmann, "Towards an Integrated Drive for Hybrid Traction," *CPES Annual Conference*, pp. 1–5, 2005.

[5] M. Ugur and O. Keysan, "Multi-physics design optimisation of a GaN-based integrated modular motor drive system," *The Journal of Engineering*, vol. 17, no. 17, pp. 3900–3905, 2019.

[6] M. Schiestl, F. Marcolini, M. Incurvati, F. G. Capponi, R. Starz, F. Caricchi, A. S. Rodriguez, and L. Wild, "Development of a High Power Density Drive System for Unmanned Aerial Vehicles," *IEEE Transactions on Power Electronics*, vol. 36, no. 3, pp. 3159–3171, 2021.

[7] M. D. Hennen, M. Niessen, C. Heyers, H. J. Brauer, and R. W. De Doncker, "Development and control of an integrated and distributed inverter for a fault tolerant five-phase switched reluctance traction drive," *IEEE Transactions on Power Electronics*, vol. 27, no. 2, pp. 547–554, 2012.

[8] O. Wen and T. A. Lipo, "Multiphase modular permanent magnet drive system design and realization," *Proceedings of IEEE International Electric Machines and Drives Conference, IEMDC 2007*, vol. 1, pp. 787–792, 2007.

[9] P. Brockerhoff, Y. Burkhardt, K. Egger, and H. Rauh, "Highly integrated drivetrain solution: Integration of motor, inverter and gearing," *2014 4th*

International Electric Drives Production Conference, EDPC 2014 - Proceedings, 2014.

[10] J. Wang, Y. Li, and Y. Han, "Evaluation and design for an integrated modular motor drive (IMMD) with GaN devices," *2013 IEEE Energy Conversion Congress and Exposition, ECCE 2013*, no. Immd, pp. 4318–4325, 2013.

[11] W. Lee, S. Li, D. Han, B. Sarlioglu, T. A. Minav, and M. Pietola, "A Review of Integrated Motor Drive and Wide-Bandgap Power Electronics for High-Performance Electro-Hydrostatic Actuators," *IEEE Transactions on Transportation Electrification*, vol. 4, no. 3, pp. 684–693, 2018.

[12] G. Pellegrino, A. Vagati, B. Boazzo, and P. Guglielmi, "Comparison of induction and PM synchronous motor drives for EV application including design examples," *IEEE Transactions on Industry Applications*, vol. 48, no. 6, pp. 2322–2332, 2012.

[13] S. Chowdhury, E. Gurpinar, G. J. Su, T. Raminosoa, T. A. Burress, and B. Ozpineci, "Enabling Technologies for Compact Integrated Electric Drives for Automotive Traction Applications," *ITEC 2019 - 2019 IEEE Transportation Electrification Conference and Expo*, 2019.

[14] A. L. Fuerback, T. B. Soeiro, M. J. Jacoboski, M. L. Heldwein, and A. J. Perin, "Integrated motor drive design for an all-electric boat," *PCIM South America*, no. October, 2014.

[15] A. Tenconi, F. Profumo, S. E. Bauer, and M. D. Hennen, "Temperatures evaluation in an integrated motor drive for traction applications," *IEEE Transactions on Industrial Electronics*, vol. 55, no. 10, pp. 3619–3626, 2008.

[16] N. R. Brown, T. M. Jahns, and R. D. Lorenz, "Power converter design for an integrated modular motor drive," *Conference Record - IAS Annual Meeting (IEEE Industry Applications Society)*, pp. 1322–1328, 2007.

[17] J. J. Wolmarans, M. B. Gerber, H. Polinder, S. W. De Haan, J. A. Ferreira, and D. Clarenbach, "A 50kW integrated fault tolerant permanent magnet machine and motor drive," *PESC Record - IEEE Annual Power Electronics Specialists Conference*, pp. 345–351, 2008.

[18] G. J. Su and L. Tang, "A segmented traction drive system with a small dc bus capacitor," *2012 IEEE Energy Conversion Congress and Exposition, ECCE 2012*, pp. 2847–2853, 2012.

[19] M. Schulz, L. Lambertz, and R. Marquardt, "Dimensioning of Modular High Frequency converter for drives," *2013 IEEE ECCE Asia Downunder - 5th*

IEEE Annual International Energy Conversion Congress and Exhibition, IEEE ECCE Asia 2013, pp. 675–680, 2013.

[20] J. Wang, Y. Li, and Y. Han, "Integrated Modular Motor Drive Design With GaN Power FETs," *IEEE Transactions on Industry Applications*, vol. 51, no. 4, pp. 3198–3207, 2015.

[21] G. Choi, Z. Xu, M. Li, S. Gupta, T. Jahns, F. Wang, N. A. Duffie, and L. Marlino, "Development of Integrated Modular Motor Drive for Traction Applications," *SAE International Journal of Engines*, vol. 4, no. 1, pp. 286–300, 2011.

[22] F. Hilpert, K. Brinkfeldt, and S. Arenz, "Modular integration of a 1200 v SiC inverter in a commercial vehicle wheel-hub drivetrain," *2014 4th International Electric Drives Production Conference, EDPC 2014 - Proceedings*, 2014.

[23] T. M. Jahns, "Hardware Integration for an Integrated Modular Motor Drive Including Distributed Contrrol," *2014 IEEE Energy Conversion Congress and Exposition (ECCE)*, pp. 4881–4887, 2014.

[24] F. Magnussen and C. Sadarangani, "Winding Factors and Joule Losses of Permanent Magnet Machines with Concentrated Windings," *IEEE International Electric Machines and Drives Conference (IEMDC) 2003*, pp. 1–7, 2006.

[25] J. K. Tangudu and T. M. Jahns, "Comparison of interior PM machines with concentrated and distributed stator windings for traction applications," *2011 IEEE Vehicle Power and Propulsion Conference, VPPC 2011*, 2011.

[26] "Things in Motion: Selecting the best pole and slot combination for a BLDC (PMSM) motor with concentrated windings." [Online]. Available: https://things-in-motion.blogspot.com/2019/01/selecting-best-pole-and-slot.html

[27] I. Boldea, L. N. Tutelea, L. Parsa, and D. Dorrell, "Automotive electric propulsion systems with reduced or no permanent magnets: An overview," *IEEE Transactions on Industrial Electronics*, vol. 61, no. 10, pp. 5696–5711, 2014.

[28] Z. Q. Zhu and D. Howe, "Electrical machines and drives for electric, hybrid, and fuel cell vehicles," *Proceedings of the IEEE*, vol. 95, no. 4, pp. 746–765, 2007.

[29] Y. Guan, Z. Q. Zhu, I. A. Afinowi, J. C. Mipo, and P. Farah, "Comparison between induction machine and interior permanent magnet machine for

electric vehicle application," *COMPEL - The International Journal for Computation and Mathematics in Electrical and Electronic Engineering*, vol. 35, no. 2, pp. 572–585, 2016.

[30] L. De Lillo, B. Ahmadi, L. Empringham, M. Johnson, J. Espina, and R. Abebe, "Next Generation Integrated Drive, NGID: A Novel Approach to Thermal and Electrical Integration of High Power Density Drives in Automotive Applications," *2018 IEEE Energy Conversion Congress and Exposition, ECCE 2018*, pp. 1228–1232, 2018.

[31] J. Hornberger, A. B. Lostetter, K. J. Olejniczak, T. McNutt, S. M. Lal, and A. Mantooth, "Silicon-carbide (SiC) semiconductor power electronics for extreme high-temperature environments," *IEEE Aerospace Conference Proceedings*, vol. 4, pp. 2538–2555, 2004.

[32] A. N. Lemmon and R. C. Graves, "Comprehensive Characterization of 10-kV Silicon Carbide Half-Bridge Modules," *IEEE Journal of Emerging and Selected Topics in Power Electronics*, vol. 4, no. 4, pp. 1462–1473, 2016.

[33] S. Tiwari, O. M. Midtgard, and T. M. Undeland, "SiC MOSFETs for future motor drive applications," *2016 18th European Conference on Power Electronics and Applications, EPE 2016 ECCE Europe*, 2016.

[34] K. Shirabe, M. Swamy, J. K. Kang, M. Hisatsune, Y. Wu, D. Kebort, and J. Honea, "Advantages of high frequency PWM in AC motor drive applications," *2012 IEEE Energy Conversion Congress and Exposition, ECCE 2012*, pp. 2977–2984, 2012.

[35] A. Morya, M. Moosavi, M. C. Gardner, and H. A. Toliyat, "Applications of Wide Bandgap (WBG) devices in AC electric drives: A technology status review," *2017 IEEE International Electric Machines and Drives Conference, IEMDC 2017*, pp. 1–8, 2017.

[36] S. Hazra, S. Madhusoodhanan, S. Bhattacharya, G. K. Moghaddam, and K. Hatua, "Design considerations and performance evaluation of 1200 V, 100 a SiC MOSFET based converter for high power density application," *2013 IEEE Energy Conversion Congress and Exposition, ECCE 2013*, pp. 4278–4285, 2013.

[37] C. Klumpner, F. Blaabjerg, and P. Thøgersen, "Evaluation of the Converter Topologies suited for Integrated Motor Drives," *Conference Record - IAS Annual Meeting (IEEE Industry Applications Society)*, vol. 2, pp. 890–897, 2003.

[38] ——, "Converter topologies with low passive components usage for the next generation of integrated motor drives," *PESC Record - IEEE Annual Power Electronics Specialists Conference*, vol. 2, pp. 568–573, 2003.

[39] J. Salmon and D. Koval, "Improving the operation of 3-phase diode rectifier using an asymmetrical half-bridge DC-link active filter," *Conference Record - IAS Annual Meeting (IEEE Industry Applications Society)*, vol. 4, no. c, pp. 2115–2122, 2000.

[40] M. Ugur, H. Sarac, and O. Keysan, "Comparison of Inverter Topologies Suited for Integrated Modular Motor Drive Applications," *Proceedings - 2018 IEEE 18th International Conference on Power Electronics and Motion Control, PEMC 2018*, pp. 524–530, 2018.

[41] R. A. Torres, H. Dai, W. Lee, T. M. Jahns, and B. Sarlioglu, "Current-Source Inverters for Integrated Motor Drives using Wide-Bandgap Power Switches," *2018 IEEE Transportation and Electrification Conference and Expo, ITEC 2018*, pp. 513–518, 2018.

[42] P. W. Wheeler, J. C. Clare, L. Empringham, K. J. Bradley, S. Pickering, D. Lampard, and M. Apap, "A fully integrated 30kW motor drive using matrix converter technology," *PESC Record - IEEE Annual Power Electronics Specialists Conference*, vol. 2005, pp. 2390–2395, 2005.

[43] S. Norrga, L. Jin, O. Wallmark, A. Mayer, and K. Ilves, "A novel inverter topology for compact EV and HEV drive systems," *IECON Proceedings (Industrial Electronics Conference)*, pp. 6590–6595, 2013.

[44] G. J. Su, L. Tang, C. Ayers, and R. Wiles, "An inverter packaging scheme for an integrated segmented traction drive system," *2013 IEEE Energy Conversion Congress and Exposition, ECCE 2013*, pp. 2799–2804, 2013.

[45] G. Engelmann, M. Kowal, and R. W. De Doncker, "A highly integrated drive inverter using DirectFETs and ceramic dc-link capacitors for open-end winding machines in electric vehicles," *Conference Proceedings - IEEE Applied Power Electronics Conference and Exposition - APEC*, vol. 2015-May, no. May, pp. 290–296, 2015.

[46] P. Thelin, *Design and evaluation of a compact 15 kW PM integral motor*, 2002, vol. 2002:02. [Online]. Available: http://urn.kb.se/resolve?urn=urn:nbn:se:kth:diva-3322

[47] ABB, "The Integral Motor: A new motor drive," pp. 1–5, 2000.

[48] "AC drives — Danfoss." [Online]. Available: https://www.danfoss.com/en/products/ac-drives/?sort=default{_}sort

[49] VARMECA, "Variable speed motors VARMECA General information Variable speed motors VARMECA Mounting positions VARMECA motors with foot mounted," pp. 1–18. [Online]. Available: http://www.hasmak.com.tr/leroysomer/asenkron/4-Varmeca-en.pdf

[50] "Yaskawa." [Online]. Available: https://www.yaskawa-global.com/newsrelease/product/38942

[51] "Siemens." [Online]. Available: https://www.greencarcongress.com/2014/10/20141017-siemens.html

[52] "Integrated Motor Drive - Motion Control." [Online]. Available: https://acim.nidec.com/motors/motion-control/products/integrated-motor-drive

[53] J. F. Gieras and N. Bianchi, "Electric motors for light traction," *EPE Journal (European Power Electronics and Drives Journal)*, vol. 14, no. 1, pp. 12–23, 2003.

[54] H. Shimizu, T. Okubo, I. Hirano, S. Ishikawa, and M. Abe, "Development of an integrated electrified powertrain for a newly developed electric vehicle," *SAE Technical Papers*, vol. 2, 2013.

[55] D. K. Perovic, "Making the impossible, possible-overcoming the design challenges of in wheel motors," *World Electric Vehicle Journal*, vol. 5, no. 2, pp. 514–519, 2012.

[56] S. Loddick, "Active Stator, a new generator topology for direct drive permanent magnet generators," *IET Conference Publications*, vol. 2010, no. 570 CP, 2010.

[57] H. Vansompel, A. Hemeida, and P. Sergeant, "Stator heat extraction system for axial flux yokeless and segmented armature machines," *2017 IEEE International Electric Machines and Drives Conference, IEMDC 2017*, 2017.

[58] H. Vansompel, P. Leijnen, and P. Sergeant, "Multiphysics Analysis of a Stator Construction Method in Yokeless and Segmented Armature Axial Flux PM Machines," *IEEE Transactions on Energy Conversion*, vol. 34, no. 1, pp. 139–146, 2019.

[59] C. Du-Bar, "Design of an axial flux machine for an in-wheel motor application," *Chalmers Reproservice, Göteborg*, pp. 1–2, 2011. [Online]. Available: http://webfiles.portal.chalmers.se/et/MSc/DubarChristian.pdf

[60] L. N. Tutelea, S. I. Deaconu, I. Boldea, and G. N. Popa, "Dual rotor single-stator axial air gap PMSM motor/generator drive for high torque vehicles applications," *IOP Conference Series: Materials Science and Engineering*, vol. 57, no. 1, 2014.

[61] I. Boldea, L. N. Tutelea, S. I. Deaconu, and F. Marignetti, "Dual rotor single-stator axial air gap PMSM motor/generator drive for HEVs: A review of comprehensive modeling and performance characterization," *Electrical Systems for Aircraft, Railway and Ship Propulsion, ESARS*, vol. 1, 2012.

[62] A. Ferreira, A.P., Silva,A.M., Costa, "Prototype of an Axial Flux Permanent Magnet Generator for Wind Energy Systems Applications Department of Electrical and Computer Engineering , FEUP Keywords."

[63] N. Zabihi and R. Gouws, "A review on switched reluctance machines for electric vehicles," *IEEE International Symposium on Industrial Electronics*, vol. 2016-Novem, pp. 799–804, 2016.

[64] S. S. Ramamurthy and J. C. Balda, "Sizing a switched reluctance motor for electric vehicles," *IEEE Transactions on Industry Applications*, vol. 37, no. 5, pp. 1256–1264, 2001.

[65] H. Vansompel and P. Sergeant, "Extended End-Winding Cooling Insert for High Power Density Electric Machines with Concentrated Windings," *IEEE Transactions on Energy Conversion*, vol. 35, no. 2, pp. 948–955, jun 2020.

[66] P. Nance, "Thermal Modeling of Power-electronic Systems," Infineon, Munich, Tech. Rep., 2000.

[67] D. Chiozzi, "Electro-thermal simulation methodologies for automotive power electronic systems," Ph.D. dissertation, Di Parma University, 2017.

[68] B. Andersson, "Lumped Parameter Thermal Modelling of Electric Machines: Analysis of an Interior Permanent Magnet Synchronous Machine for Vehicle Applications," Ph.D. dissertation, Chalmers University, 2013.

[69] J. Pyrhönen, T. Jokinen, and V. Hrabovcová, *Design of Rotating Electrical Machines*, 2008.

[70] J. Nerg, M. Rilla, and J. Pyrhönen, "Thermal analysis of radial-flux electrical machines with a high power density," *IEEE Transactions on Industrial Electronics*, vol. 55, no. 10, pp. 3543–3554, 2008.

[71] E. Barbisio, F. Fiorillo, and C. Ragusa, "Predicting loss in magnetic steels under arbitrary induction waveform and with minor hysteresis loops," *IEEE Transactions on Magnetics*, vol. 40, no. 4 I, pp. 1810–1819, jul 2004.

[72] A. Hemeida and P. Sergeant, "Analytical modeling of surface PMSM using a combined solution of Maxwell-s equations and magnetic equivalent circuit," *IEEE Transactions on Magnetics*, vol. 50, no. 12, dec 2014.

[73] H. Vansompel, P. Sergeant, L. Dupré, and A. Van Den Bossche, "Axial-flux PM machines with variable air gap," *IEEE Transactions on Industrial Electronics*, vol. 61, no. 2, pp. 730–737, 2014.

[74] A. Hemeida, "Electromagnetic and Thermal Design of Axial Flux Permanent Magnet Synchronous Machines," Ph.D. dissertation, Ghent University, 2017.

[75] G. Bertotti, "General Properties of Power Losses in Soft Ferromagnetic Materials." *IEEE Transactions on Magnetics*, vol. 24, no. 1, pp. 621–630, jan 1987.

[76] A. Hemeida, P. Sergeant, and H. Vansompel, "Comparison of methods for permanent magnet eddy-current loss computations with and without reaction field considerations in axial flux PMSM," *IEEE Transactions on Magnetics*, vol. 51, no. 9, sep 2015.

[77] W. Jiang and T. M. Jahns, "Coupled Electromagnetic-Thermal Analysis of Electric Machines Including Transient Operation Based on Finite-Element Techniques," *IEEE Transactions on Industry Applications*, vol. 51, no. 2, pp. 1880–1889, mar 2015.

[78] TDK, "Neodymium-Iron-Boron Magnets NEOREC series," *Application Note*, no. May, 2010.

[79] "Temperature Effects on Neodymium Iron Boron, NdFeB, magnets — Stanford Magnets." [Online]. Available: https://www.stanfordmagnets.com/temperature-effects-on-neodymium-iron-boron-ndfeb-magnets.html

[80] S. Nategh, A. Krings, O. Wallmark, and M. Leksell, "Evaluation of impregnation materials for thermal management of liquid-cooled electric machines," *IEEE Transactions on Industrial Electronics*, vol. 61, no. 11, pp. 5956–5965, 2014.

[81] LOCTITE, "STYCAST 2850FT / Catalyst 9," pp. 0–1, 2010.

[82] A. Bejan, *Heat transfer, second edition*, 1995.

[83] D. Staton, A. Boglietti, and A. Cavagnino, "Solving the more difficult aspects of electric motor thermal analysis in small and medium size industrial induction motors," *IEEE Transactions on Energy Conversion*, vol. 20, no. 3, pp. 620–628, sep 2005.

[84] D. A. Howey, A. S. Holmes, and K. R. Pullen, "Measurement and CFD prediction of heat transfer in air-cooled disc-type electrical machines," *IEEE Transactions on Industry Applications*, vol. 47, no. 4, pp. 1716–1723, jul 2011.

[85] D. A. Howey, P. R. Childs, and A. S. Holmes, "Air-gap convection in rotating electrical machines," *IEEE Transactions on Industrial Electronics*, vol. 59, no. 3, pp. 1367–1375, mar 2012.

[86] W. R. Canders, J. Ho, and M. Henke, "Cooling technologies for high power density electrical machines for aviation applications," *Energies*, vol. 12, no. 23, 2019.

[87] P. Romanazzi, S. Ayat, R. Wrobel, and D. A. Howey, "3D homogenisation of concentrated windings with rectangular conductors," in *2017 IEEE International Electric Machines and Drives Conference, IEMDC 2017*. IEEE, 2017, pp. 1–8.

[88] N. Simpson, R. Wrobel, and P. H. Mellor, "Estimation of equivalent thermal parameters of impregnated electrical windings," *IEEE Transactions on Industry Applications*, vol. 49, no. 6, pp. 2505–2515, nov 2013.

[89] L. Siesing, A. Reinap, and M. Andersson, "Thermal properties on high fill factor electrical windings: Infiltrated vs non infiltrated," *Proceedings - 2014 International Conference on Electrical Machines, ICEM 2014*, pp. 2218–2223, 2014.

[90] L. Idoughi, X. Mininger, F. Bouillault, L. Bernard, and E. Hoang, "Thermal model with winding homogenization and FIT discretization for stator slot," *IEEE Transactions on Magnetics*, vol. 47, no. 12, pp. 4822–4826, 2011.

[91] P. H. Mellor, D. Roberts, and D. R. Turner, "Lumped parameter thermal model for electrical machines of TEFC design," *IEE Proc. B Electr. Power Appl.*, vol. 138, no. 5, p. 205, 1991. [Online]. Available: http://digital-library.theiet.org/content/journals/10.1049/ip-b.1991.0025

[92] R. Wrobel and P. H. Mellor, "A general cuboidal element for three-dimensional thermal modelling," *IEEE Transactions on Magnetics*, vol. 46, no. 8, pp. 3197–3200, aug 2010.

[93] D. Kuehbacher, A. Kelleter, and D. Gerling, "An improved approach for transient thermal modeling using lumped parameter networks," *Proceedings of the 2013 IEEE International Electric Machines and Drives Conference, IEMDC 2013*, pp. 824–831, 2013.

[94] A. Rasekh, P. Sergeant, and J. Vierendeels, "Fully predictive heat transfer coefficient modeling of an axial flux permanent magnet synchronous machine with geometrical parameters of the magnets," *Appl. Therm. Eng.*, vol. 110, pp. 1343–1357, 2017.

[95] ——, "Development of Correlations for Windage Power Losses Modeling in an Axial Flux Permanent Magnet Synchronous Machine with Geometrical Features of the Magnets," *Energies 2016, Vol. 9, Page 1009*, vol. 9, no. 12, p. 1009, nov 2016. [Online]. Available: https://www.mdpi.com/1996-1073/9/12/1009/htmhttps://www.mdpi.com/1996-1073/9/12/1009

[96] R. Krishnan, *Switched reluctance motor drives: Modeling, simulation, analysis, design, and applications*, 2017.

[97] X. D. Xue, K. W. Cheng, J. K. Lin, Z. Zhang, K. F. Luk, T. W. Ng, and N. C. Cheung, "Optimal control method of motoring operation for SRM drives in electric vehicles," *IEEE Transactions on Vehicular Technology*, vol. 59, no. 3, pp. 1191–1204, 2010.

[98] A. M. Omekanda, "A new technique for multi-dimensional performance optimization of switched reluctance motors for vehicle propulsion," *Conference Record - IAS Annual Meeting (IEEE Industry Applications Society)*, vol. 1, pp. 22–26, 2002.

[99] K. M. Rahman and S. E. Schulz, "High-performance fully digital switched reluctance motor controller for vehicle propulsion," *IEEE Transactions on Industry Applications*, vol. 38, no. 4, pp. 1062–1071, jul 2002.

[100] A. C. Pop, V. Petrus, C. S. Martis, V. Iancu, and J. Gyselinck, "Comparative study of different torque sharing functions for losses minimization in Switched Reluctance Motors used in electric vehicles propulsion," *Proceedings of the International Conference on Optimisation of Electrical and Electronic Equipment, OPTIM*, pp. 356–365, 2012.

[101] I. Husain, "Minimization of torque ripple in SRM drives," *IEEE Transactions on Industrial Electronics*, vol. 49, no. 1, pp. 28–39, feb 2002.

[102] X. D. Xue, K. W. Cheng, and S. L. Ho, "Optimization and evaluation of torque-sharing functions for torque ripple minimization in switched reluctance motor drives," *IEEE Transactions on Power Electronics*, vol. 24, no. 9, pp. 2076–2090, 2009.

[103] I. Husain and M. Ehsani, "Torque ripple minimization in switched reluctance motor drives by PWM current control," *IEEE Transactions on Power Electronics*, vol. 11, no. 1, pp. 83–88, 1996.

[104] N. C. Sahoo, J. X. Xu, and S. K. Panda, "Low Torque Ripple Control of Switched Reluctance Motors Using Iterative Learning," *IEEE Power Engineering Review*, vol. 21, no. 12, p. 66, 2001.

[105] M. Ilic-Spong, T. J. Miller, S. E. MacMinn, and J. S. Thorp, "Instantaneous Torque Control of Electric Motor Drives," in *PESC Record - IEEE Annual Power Electronics Specialists Conference*. IEEE, 1985, pp. 42–48.

[106] P. Kjaer, "Very high bandwidth digital current controller for high-performance motor drives," *1996 Sixth International Conference on Power Electronics and Variable Speed Drives*, pp. 185–190, 2005.

[107] V. P. Vujičić, "Modeling of a switched reluctance machine based on the invertible torque function," *IEEE Transactions on Magnetics*, vol. 44, no. 9, pp. 2186–2194, sep 2008.
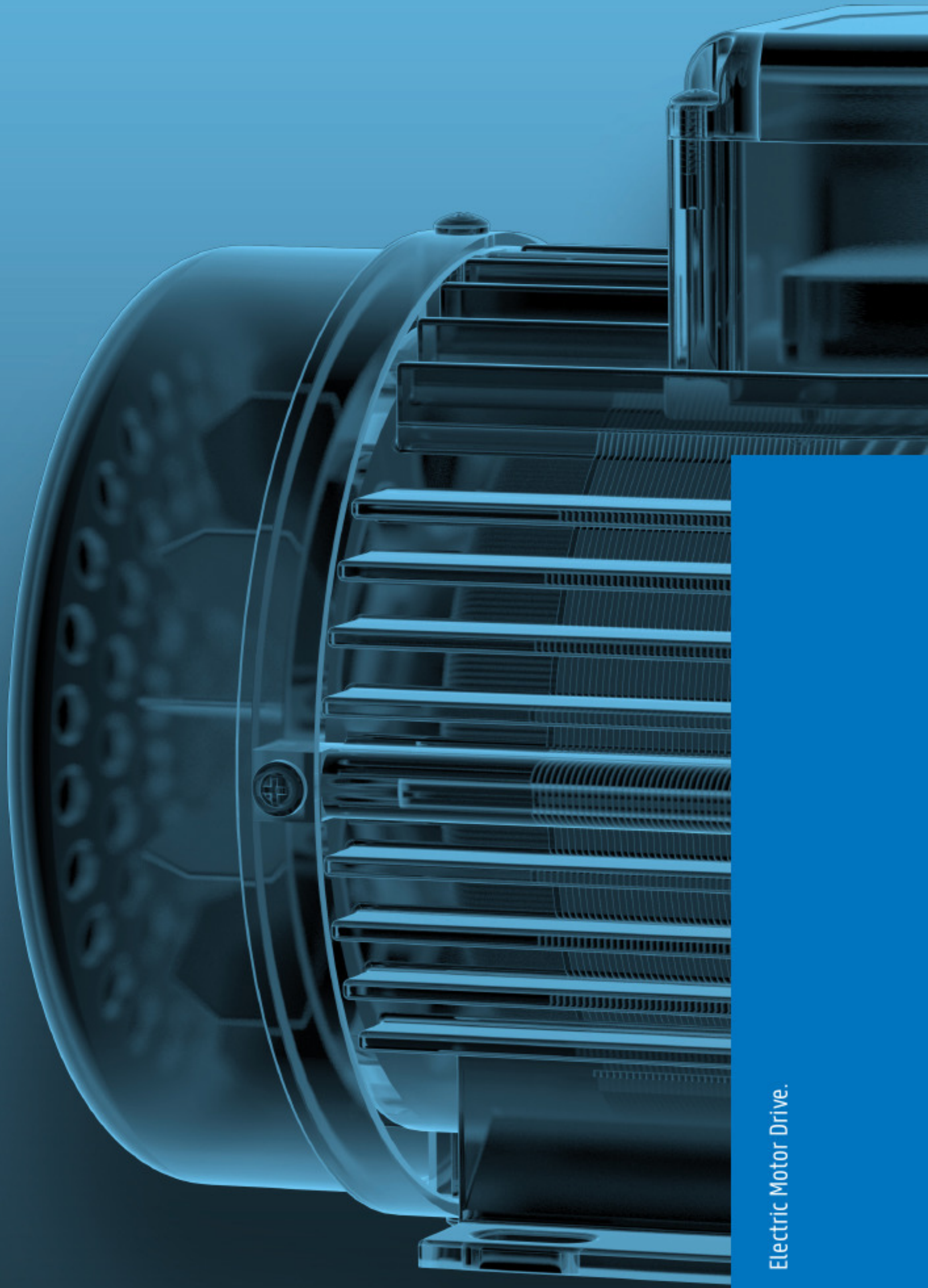
[108] T. J. Miller, "Optimal design of switched reluctance motors," *IEEE Transactions on Industrial Electronics*, vol. 49, no. 1, pp. 15–27, feb 2002.

[109] N. K. Sheth and K. R. Rajagopal, "Estimation of core loss in a switched reluctance motor based on actual flux variations," *2006 International Conference on Power Electronics, Drives and Energy Systems, PEDES '06*, 2006.

[110] P. N. Materu and R. Krishnan, "Estimation of Switched Reluctance Motor Losses," *IEEE Transactions on Industry Applications*, vol. 28, no. 3, pp. 668–679, 1992.

[111] L. Chen, H. Chen, and W. Yan, "A fast iron loss calculation model for switched reluctance motors," *IET Electric Power Applications*, vol. 11, no. 3, pp. 478–486, 2017.

[112] J. Faiz, B. Ganji, C. E. Carstensen, K. A. Kasper, and R. W. De Doncker, "Temperature rise analysis of switched reluctance motors due to electromagnetic losses," *IEEE Transactions on Magnetics*, vol. 45, no. 7, pp. 2927–2934, 2009.

[113] C. D. Ghildyal, "Stability of a viscous liquid contained between two rotating cylinders," *Journal of Applied Mathematics and Mechanics*, vol. 39, no. 12, pp. 473–476, 1959.

[114] P. Romanazzi and D. A. Howey, "Air-gap convection in a switched reluctance machine," *2015 10th International Conference on Ecological Vehicles and Renewable Energies, EVER 2015*, pp. 1–7, 2015.

[115] G. Wang, J. Mookken, J. Rice, and M. Schupbach, "Dynamic and static behavior of packaged silicon carbide MOSFETs in paralleled applications," *Conference Proceedings - IEEE Applied Power Electronics Conference and Exposition - APEC*, pp. 1478–1483, 2014.

[116] S. Maniktala, *Switching Power Supplies A to Z*, 1st ed.   ELSEVIER, 2016.

[117] J. Guo, "Modeling and Design of Inverters Using Novel Power Loss Calculation and DC Link Current Ripple Estimation," Ph.D. dissertation, McMaster University, 2017.

[118] P. Haaf and J. Harper, "Understanding Diode Reverse Recovery and its Effect on Switching Losses," *Fairchild Power Seminar*, pp. 23–33, 2007.

[119] Silicon Labs, "Si827x Data Sheet," pp. 0–42, 2015.

[120] R. Künzi, "Thermal design of power electronic circuits," *CERN Accelerator School: Power Converters, CAS 2014 - Proceedings*, vol. 003, no. May 2014, pp. 311–327, 2018.

[121] Y. C. Gerstenmaier, W. Kiffe, and G. Wachutka, "Combination of thermal subsystems by use of rapid circuit transformation and extended two-port theory," *Microelectronics Journal*, vol. 40, no. 1, pp. 26–34, 2009.

[122] Texas Instruments, "Ringing Reduction Techniques for NexFET," *Application Note*, no. November, pp. 1–18, 2011. [Online]. Available: https://e2echina.ti.com/cfs-file/ {_}{_}key/communityserver-discussions-components-files/24/8244. Ringing-Reduction-Techniques-for-NexFET-high-performance-mosfets. pdf

[123] Y. Shen, H. Wang, F. Blaabjerg, H. Zhao, and T. Long, "Thermal modeling and design optimization of PCB vias and pads," *IEEE Transactions on Power Electronics*, vol. 35, no. 1, pp. 882–900, 2020.

[124] Renesas, "P9038 Layout Guide," *Application Note*, pp. 1–16.

[125] O. Ellabban and H. Abu-Rub, "Switched reluctance motor converter topologies: A review," in *Proceedings of the IEEE International Conference on Industrial Technology*.   Institute of Electrical and Electronics Engineers Inc., sep 2014, pp. 840–846.

[126] S. Vukosavic and V. R. Stefanovic, "SRM inverter topologies: A comparative evaluation," *IEEE Transactions on Industry Applications*, vol. 27, no. 6, pp. 1034–1047, nov 1991.

[127] X. Pei, W. Zhou, and Y. Kang, "Analysis and Calculation of DC-Link Current and Voltage Ripples for Three-Phase Inverter With Unbalanced Load," *IEEE Transactions on Power Electronics*, vol. 30, no. 10, pp. 5401–5412, 2015.

[128] J. M. Guichon, J. Aimé, J. L. Schanen, C. Martin, J. Roudet, E. Clavel, M. Arpillière, R. Pasterczyk, and Y. Le Floch, "Busbar design: How to spare nanohenries?" *Conference Record - IAS Annual Meeting (IEEE Industry Applications Society)*, vol. 4, pp. 1865–1869, 2006.

[129] M. Chiadò Caponet, F. Profumo, R. W. De Doncker, and A. Tenconi, "Low stray inductance bus bar design and construction for good EMC performance in power electronic circuits," *IEEE Transactions on Power Electronics*, vol. 17, no. 2, pp. 225–231, 2002.

[130] M. Salcone and J. Bond, "Selecting film bus link capacitors for high performance inverter applications," *2009 IEEE International Electric Machines and Drives Conference, IEMDC '09*, pp. 1692–1699, 2009.

[131] J. Kolar and S. Round, "Analytical calculation of the RMS current stress on the DC-link capacitor of voltage-PWM converter systems," *IEE Proceedings-Electric Power Applications*, vol. 153, no. 4, pp. 535–543, 2006. [Online]. Available: https://ieeexplore.ieee.org/document/1650869

[132] B. Rubey, A. Patzak, F. Bachheibl, and D. Gerling, "DC-link current harmonics minimization in ISCAD multi-phase inverters with interleaving," *2017 IEEE Vehicle Power and Propulsion Conference, VPPC 2017 - Proceedings*, vol. 2018-Janua, pp. 1–7, 2018.

[133] S. Bhattacharya, D. Mascarella, and G. Joos, "Interleaved SVPWM and DPWM for dual three-phase inverter-PMSM: An automotive application," *2014 IEEE Transportation Electrification Conference and Expo: Components, Systems, and Power Electronics - From Technology to Business and Public Policy, ITEC 2014*, 2014.

[134] M. Ugur and O. Keysan, "DC link capacitor optimization for integrated modular motor drives," *IEEE International Symposium on Industrial Electronics*, vol. i, pp. 263–270, 2017.

[135] A. D. Callegaro, J. Guo, M. Eull, B. Danen, J. Gibson, M. Preindl, B. Bilgin, and A. Emadi, "Bus Bar Design for High-Power Inverters," *IEEE Transactions on Power Electronics*, vol. 33, no. 3, pp. 2354–2367, 2018.

[136] S. Tiwari, O. M. Midtgård, and T. M. Undeland, "Design of low inductive busbar for fast switching SiC modules verified by 3D FEM calculations and laboratory measurements," *2016 IEEE 17th Workshop on Control and Modeling for Power Electronics, COMPEL 2016*, 2016.

[137] R. J. Pasterczyk, C. Martin, J. M. Guichon, and J. L. Schanen, "Planar busbar optimization regarding current sharing and stray inductance minimization," *2005 European Conference on Power Electronics and Applications*, vol. 2005, 2005.

[138] A. M. Hava, U. Ayhan, and V. V. Aban, "A DC bus capacitor design method for various inverter applications," *2012 IEEE Energy Conversion Congress and Exposition, ECCE 2012*, pp. 4592–4599, 2012.

[139] C. Dong, Y. Qian, Y. Zhang, and W. Zhuge, "A Review of Thermal Designs for Improving Power Density in Electrical Machines," *IEEE Transactions on Transportation Electrification*, vol. 6, no. 4, pp. 1386–1400, dec 2020.

[140] K. Wang, Z. Y. Gu, C. Liu, and Z. Q. Zhu, "Design and Analysis of a Five-Phase SPM Machine Considering Third Harmonic Current Injection," *IEEE Transactions on Energy Conversion*, vol. 33, no. 3, pp. 1108–1117, sep 2018.

[141] C. Gan, J. Wu, Y. Hu, S. Yang, W. Cao, and J. M. Guerrero, "New Integrated Multilevel Converter for Switched Reluctance Motor Drives in Plug-in Hybrid Electric Vehicles with Flexible Energy Conversion," *IEEE Transactions on Power Electronics*, vol. 32, no. 5, pp. 3754–3766, may 2017.

[142] H. Li, B. Bilgin, and A. Emadi, "An Improved Torque Sharing Function for Torque Ripple Reduction in Switched Reluctance Machines," *IEEE Transactions on Power Electronics*, vol. 34, no. 2, pp. 1635–1644, 2019.

[143] K. M. Rahman, B. Fahimi, G. Suresh, A. V. Rajarathnam, and M. Ehsani, "Advantages of switched reluctance motor applications to EV and HEV: design and control issues," *IEEE Transactions on Industry Applications*, vol. 36, no. 1, pp. 111–121, 2000.

[144] M. Takeno, A. Chiba, N. Hoshi, S. Ogasawara, M. Takemoto, and M. A. Rahman, "Test results and torque improvement of the 50-kw switched reluctance motor designed for hybrid electric vehicles," *IEEE Transactions on Industry Applications*, vol. 48, no. 4, pp. 1327–1334, 2012.

[145] J. Borg Bartolo, M. Degano, J. Espina, and C. Gerada, "Design and Initial Testing of a High-Speed 45-kW Switched Reluctance Drive for Aerospace Application," *IEEE Transactions on Industrial Electronics*, vol. 64, no. 2, pp. 988–997, feb 2017.

[146] W. Ding, S. Yang, and Y. Hu, "Performance Improvement for Segmented-Stator Hybrid-Excitation SRM Drives Using an Improved Asymmetric Half-Bridge Converter," *IEEE Transactions on Industrial Electronics*, vol. 66, no. 2, pp. 898–909, 2019.

[147] M. Balaji, C. A. Vaithilingam, and V. Kamaraj, "Torque ripple minimization in switched reluctance motor drives," *IEE Conference Publication*, vol. 1, no. 1, pp. 104–107, 2004.

[148] A. Labak and N. C. Kar, "Designing and prototyping a novel five-phase pancake-shaped axial-flux SRM for electric vehicle application through dynamic FEA incorporating flux-tube modeling," *IEEE Transactions on Industry Applications*, vol. 49, no. 3, pp. 1276–1288, 2013.

[149] H. Eskandari and M. Mirsalim, "An improved 9/12 two-phase e-core switched reluctance machine," *IEEE Transactions on Energy Conversion*, vol. 28, no. 4, pp. 951–958, dec 2013.

[150] J. Liang, D. H. Lee, G. Xu, and J. W. Ahn, "Analysis of passive boost power converter for three-phase SR drive," *IEEE Transactions on Industrial Electronics*, vol. 57, no. 9, pp. 2961–2971, sep 2010.

[151] Y. G. Dessouky, B. W. Williams, and J. E. Fletcher, "A novel power converter with voltage-boosting capacitors for a four-phase srm drive," *IEEE Transactions on Industrial Electronics*, vol. 45, no. 5, pp. 815–823, 1998.

[152] J. Liang, D. H. Lee, G. Xu, and J. W. Ahn, "Analysis of passive boost power converter for three-phase SR drive," *IEEE Transactions on Industrial Electronics*, vol. 57, no. 9, pp. 2961–2971, sep 2010.

[153] W. Cai and F. Yi, "An integrated multiport power converter with small capacitance requirement for switched reluctance motor drive," *IEEE Transactions on Power Electronics*, vol. 31, no. 4, pp. 3016–3026, apr 2016.

[154] L. Szabo and M. Ruba, "Segmental stator switched reluctance machine for safety-critical applications," *IEEE Transactions on Industry Applications*, vol. 48, no. 6, pp. 2223–2229, 2012.

[155] A. H. Mohamed, H. Vansompel, A. Hemeida, and P. Sergeant, "Wide Bandgap Based Modular Driving Techniques for Switched Reluctance Motor Drives," in *IECON Proceedings (Industrial Electronics Conference)*, vol. 2020-Octob. IEEE Computer Society, oct 2020, pp. 1120–1125.

Electric Motor Drive.